Probing the resistance switching mechanism in silicon suboxide memory devices

Mark Buckwell

Thesis submission for the degree of doctor of philosophy

Supervisor: Professor Anthony J. Kenyon

Final submission date: 17 April 2018

Department of Electronic and Electrical Engineering

University College London, UK

Declaration

I, Mark Buckwell, confirm that the work presented in this thesis is my own. Where information has been derived from other sources, I confirm that this has been indicated in the thesis.

17 April 2018

Abstract

Redox-based resistive random access memory has the scope to greatly improve upon current electronic data storage, though the mechanism by which devices operate is not understood completely. In particular, the connection between oxygen migration, the formation of conductive filaments and device longevity is still disputed. Here, I used atomic force microscopy, scanning electron microscopy and x-ray photoelectron spectroscopy to characterise the growth of filaments and the movement of oxygen in silicon-rich silicon oxide memory devices. As such, I was able to establish some of the chemical and structural differences between states of different resistance, which would correspond to binary data storage states. The oxide active layer is reduced simultaneously to the appearance of surface distortion and volumes of high conductivity in an otherwise-insulating material. These results support the established model of a resistance switching mechanism that relies on the migration of oxygen ions under an electrical bias, forming conductive pathways in the switching material. Notably, I demonstrate a reduction in the active layer stoichiometry as a result of electrical stress and show for the first time the presence of multiple filamentary growths in three dimensions in an intrinsic switching material. In addition, I have proven the efficacy of an extension to the method of profiling conductivity variations in insulators in three dimensions using conductive atomic force microscopy. However, in this case my findings conflict with the status quo of this methodology. In particular, I demonstrate that the measurement process significantly affects the scanning probe, leading to the likelihood of data inaccuracy. This highlights the needed for further development of the technique and careful analysis of the data obtained.

Contents

List of acronyms

AFM – Atomic force microscopy

CAFM – Conductive atomic force microscopy

CMOS – Complimentary metal-oxide-semiconductor

RRAM – Resistive random access memory

SEM – Scanning electron microscopy

SiO_x – Silicon suboxide

QNM – Quantitative nanomechanical mapping

RMS – Root-mean-square

XPS – X-ray photoelectron spectroscopy

Acknowledgements

To my surprise and delight, I've written a thesis. The last four years have been amazing. I've learned so much, scientific and personal, yet I'm sure I'm still clueless. However, I couldn't have come this far without support from a lot of great people, who deserve my thanks and respect.

Firstly, to my supervisor, Tony, who gave me this opportunity, offered me his guidance and has been wholly supportive of every aspect that I've thought to explore, thank you so much. And, surely more importantly, thank you for showing me how to play the Purdie shuffle. To my examiners, Dr. Romans and Dr. Kemp, thank you for taking the time to read what I've written and be a part of this process, I'm extremely grateful. I would also like to thank the Engineering and Physical Sciences Research Council and the Worshipful Company of Scientific Instrument Makers for their generous funding of this project and, therefore, me and my scientific career.

To Wing and Richard, thanks for inspiring me and being interested in what I've aspired to do. To Luca, Adnan, Steve, Sarah and all my colleagues in London, thanks for being great to work with and fantastic to spend time with. To the rest of my colleagues worldwide, all those I've met through my doctorate and especially to Mario, thanks for listening to me, questioning me, believing me, disagreeing with me and allowing me to reciprocate.

To my bandmates, thanks for putting up with my workload when it's gotten in the way of our music and for always being supportive and understanding. To those friends I've not been able to see so much recently, I'm sorry. I hope I can make up for it now. To AB, thank you for maintaining a level of anti-scientific belligerence that has always kept me on my toes. In case you're wondering, I'm close to the truth now and I'm pretty sure the potato is a hoax. Time to buy a blue fleece.

To my parents, thanks for always supporting me wholeheartedly in everything I've pursued, from professional skateboarding to rock stardom. I couldn't have done this without you. The same goes to my grandparents; grandpa, sorry you weren't able to see the end of it. And to the rest of my family, thanks for putting up with my nonsense for so long. Particularly you, Joe, for always being my brother.

Finally, to MH, sorry for so often being boring and thanks for always understanding. In case you don't get round to reading all the way through this thesis, it's ultimately about pigs and bears.

1. Introduction

1.1 Electronic memories and switching

Electronic memories are vital to modern technology. There is an ever-increasing demand for larger data storage volumes in smaller packages and a drive toward ensuring that new components are adequately efficient and reliable to meet technological advances.[1] To store electronic data long-term, memory devices must be non-volatile, retaining information after their power source is removed. The state-of-the-art is currently flash memory, fabricated in high-density device arrays with fabrication costs kept low by using silicon as a base material.[2]

Flash is based on field-effect transistor technology, storing information via trapping and removing electrons from a thin conductive layer between a gate and channel.[3] This layer is known as the floating gate and is insulated from the device terminals, as shown in **Figure 1.1**. Charge stored on the floating gate creates a field that opposes normal operational gate voltages, raising the threshold voltage of the channel. Thus, the floating gate charge is used to set the transistor into different operational states, such as 'on' and 'off', or '1' and '0'.

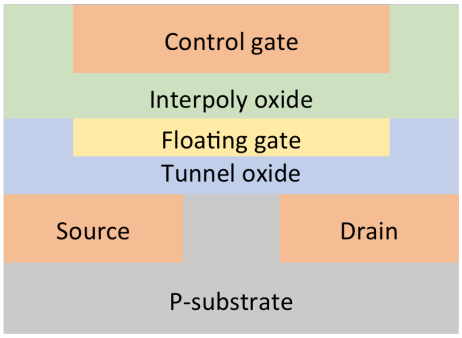

Figure 1.1. Schematic of a flash memory cell.[3] As with standard single-gated transistors, a voltage applied to the control gate opens a conductive channel between the source and drain. However, in a flash cell, electrons can be trapped on the floating gate by applying a field between the control gate and drain. Thus, the threshold voltage of the device is increased and its state set to '1'. A high voltage at the source facilitates electron tunnelling through the tunnel oxide when the other terminals are grounded, setting the device to '0'.

To meet the continuing demand for more highly-integrated consumer technologies, the size of individual memory elements must decrease. However, through improvements in fabrication methods, flash memory has steadily been approaching its miniaturisation limit.[4] In fact, semiconductor component sizes have been decreasing since the advent of the first integrated circuit. In 1965, Gordon Moore quantified the rate of device shrinkage and discussed its implications for technology.[5,6] He predicted that

integrated circuit component density would double every 18 months, a trend that allowed for affordable home and mobile computing. However, he also predicted complications with packing more components into smaller spaces. Namely, reliability, heat dissipation, fabrication, yield and cost would become increasingly problematic with decreasing device size. However, “Moore’s Law,” has held true to the present day, with successive device generations building upon one another to overcome these issues.

Flash memories are based on transistor technology and are thus subject to Moore’s Law. In particular, the thickness of individual layers such as the tunnel oxide is reduced. For a consistent voltage, this greatly increases the strength of the electric field across the layer. As such, the risk of electrical breakdown is higher in smaller devices and can result in short-circuiting and irreparable damage.[7,8] As insulating layers in flash devices approach and progress below 8 nm, there is a significant increase in ‘leakage’ currents and so the device reliability is reduced.[9] Therefore, new types of memory must be developed to enable further technological progress. One proposed alternative to flash is resistive random access memory (RRAM).

RRAM devices store information through physical changes in a thin film rather than charge trapping. Such devices are non-volatile and offer improved efficiency over flash, having shown faster switching times, lower power consumption and the potential for integration into highly-scalable, three-dimensional memory architectures.[4,10,11]

Most generally, RRAM devices exploit the phenomenon of resistance switching in a thin, insulating layer sandwiched between conductive electrodes. Applying electrical biases between the electrodes, across the active insulator, causes the device to switch rapidly between distinct, non-volatile states of resistance. The final state of the device is dependent upon the voltage and current supplied during biasing.

1.2 Motivation for study

A number of resistance switching mechanisms have been studied and in some cases integrated into functional device arrays.[4] Predominantly, however, these use metal oxide active layers or rely on the diffusion of metal ions into the active layer. While such devices promise stability and reliability, their integration into consumer electronics is problematic; each case would require costly modifications to industrial fabrication. Additionally, for ion diffusion systems, there is significant risk of unwanted metal diffusion and thus short circuits, reducing the semiconductor architecture reliability.

For straightforward integration of new component designs into existing technologies, compliance with existing infrastructure is desirable. Thin films of non-stoichiometric silicon suboxide, SiO_x, sandwiched between highly conductive electrodes have displayed suitable properties for information storage in RRAM.[12-15] The active layers

of such devices may be fabricated from silicon and oxygen alone. This makes them extremely promising for industrial integration, as silicon and silicon dioxide remain prominent within current complementary metal-oxide-semiconductor (CMOS) technologies.[13,16,17]

Broadly, the aim of this project is to contribute to the development of efficient, reliable, CMOS-compatible, silicon oxide-based memory arrays. In particular, this might be achieved by providing insight into and thus an improved understanding of the mechanisms of switching in SiO_x. Generally, device operation is thought to rely on oxygen drift and diffusion within the active layer. This is coupled with morphological changes reflecting the changes in oxidation states. Specifically, the aims of this project are: *i)* to use spectroscopic techniques to probe the role of oxygen in chemical changes occurring in electrically-stressed SiO_x-based RRAM devices and; *ii*) to use microscopic techniques to measure the resulting morphological changes, namely distortions on the surface of devices and conductive filamentary pathways in the SiO_x bulk. In order to incorporate RRAM devices into functional, commercial electronic architectures, the exact processes governing switching must be understood. Characterisation of structural and compositional change is therefore of particular interest in developing a comprehensive understanding of the switching mechanics of RRAM devices.

1.3 Outline

In chapter **2** I will introduce the concepts and history of resistance switching, from its origins to the present day. I will also put SiO_x-based devices into context, relative to other materials in the literature. In chapter **3**, I will explain the theory and practice of the experimental methods employed to carry out my work. In chapter **4** I will describe my samples and in chapter **5** I will state the specific measurement instrumentation used.

In chapter **6** I will begin the discussion of my experimental work, looking at the changes occurring on the device scale. I use microscopy to image distortions at the device surface and spectroscopy to demonstrate the need to study the active layer directly. In chapter **7** I will show my findings from direct study of the active layer, again using microscopy to image distortions occurring at the SiO_x surface. I then use spectroscopy to demonstrate that the stoichiometry of the active layer is reduced, indicating oxygen migration. In chapter **8** I move to the scale of individual conductive pathways, using microscopy to first study distortions at the SiO_x surface and then to perform tomography on individual filaments within the bulk. I conclude this chapter with a discussion of some of the concerns with the tomographic method.

Finally, in chapter **9** I present my conclusions and their relation to the fields of resistance switching and measurement methodology.

2. The development of resistance switching

2.1 Resistance switching phenomena

Resistance switching is the phenomenon by which a dielectric layer may be electrically cycled between two or more states with distinct conductivities. The change from a more insulating 'off' state to more conducting 'on' state is a 'set' operation. The subsequent switch from on to off is a 'reset' operation. Note that the on state is often referred to as the low resistance state and the off state the high resistance state.

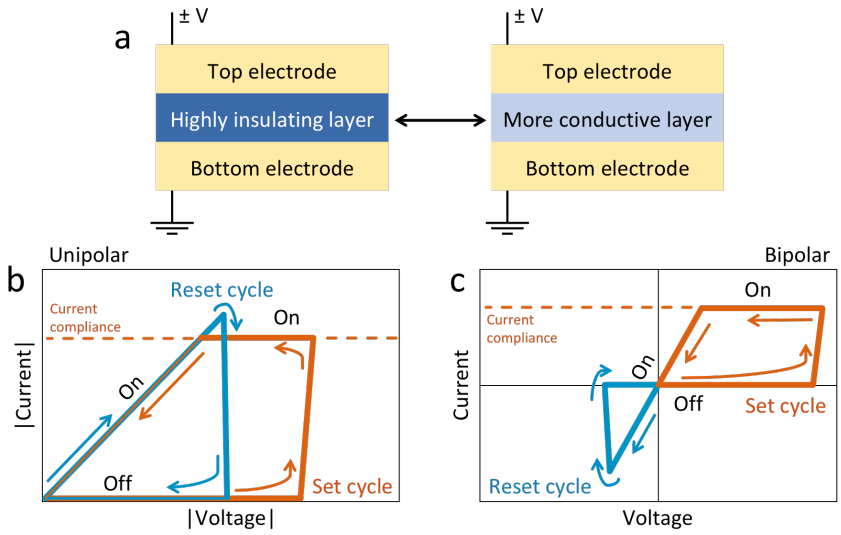

Figure 2.1. Generalised resistance switching device and operational modes. (**a**) Schematic of a resistance switching device with an insulating layer sandwiched between a pair of conductive electrodes. The device may be cycled between at least two distinct states of conductivity by changing the resistance of the sandwiched active layer. (**b**) and (**c**) representative current-voltage curves for unipolar switching and bipolar switching, respectively.[18] For both devices in the off state, increasing the voltage to a threshold value will cause the device to jump to the on state, characterised by a low resistance and thus greater current. This is a set cycle, with current compliance used to limit the current and prevent hard dielectric breakdown. In the off state, compliance is removed in order for the voltage to drive a current whose magnitude eventually exceeds the previous limit. This causes the device to jump to the high resistance, off state. For a unipolar device, both these cycles are made with the same voltage polarity. Conversely, for a bipolar device the set and reset cycles are of opposite polarity. In each case, the polarity is dependent on the materials used.

Generally, the active insulating layer is thin, between 5 nm and 100 nm, and sandwiched between top and bottom electrodes, as shown in **Figure 2.1.a**. Changes in resistance are induced by applying an electric field between the electrodes. Most

generally, resistance switching devices have two operational regimens, unipolar and bipolar, as shown in **Figure 2.1b** and **c**. Bipolar devices require electric fields of opposite polarities for set and reset operations, whereas unipolar devices use only a single field polarity.[18] Typically, as the voltage is changed, the current will show rapid, discrete changes, as demonstrated in **Figure 2.1b** and **c**. Such 'jumps' correspond to the transitions between off and on states. When the voltage is returned to 0 V these changes are retained, indicating that the device state is non-volatile.

A relatively low voltage is used to 'read' the state of the device. This voltage is not high enough to induce further change but sufficient to distinguish the resistance state of the device from the measured current.[18] Ideally, the difference in read current between distinct states should be large. This allows them to be reliably distinguished from each other, giving a high on/off current ratio.[2] A suitably large ratio enables the device to function as memory, allowing binary and, when a number of distinct programmable states are available, multi-level storage in a single device.[19]

Some active layer materials do not exhibit resistance switching in their pristine state; suitable voltages for set and reset processes do not notably affect the resistance of the device. In these cases, an electroforming process, sometimes referred to as a 'form' or 'forming' step, is required to prepare the virgin insulator for subsequent switching operations.[20] Forming, in general, constitutes applying a field greater than that of any subsequent switching operation. Following this, it is not possible to return the material to its pristine state of conductivity.

Forming is considered a soft dielectric breakdown, as the electrical changes may be at least partially reversed. This is in contrast to irreversible conductivity changes which are well-documented and associated with hard dielectric breakdown.[21] For efficient device operation, hard breakdown must generally be avoided. As a result, it has been studied extensively since the 1960s, with some work dating back to the 1920s.[22]

Hard dielectric breakdown of an electrically stressed insulator ultimately depends on the energy transferred to charge carriers in the system by the electric field.[23,24] The field generates a space-charge accumulation below the more negative electrode, leading eventually to instability in the current. Above a threshold voltage, an electron avalanche occurs, causing irreversible damage to the dielectric.[25] Thus, resistance switching devices can be considered as requiring a given quantity of energy to reach the point of hard dielectric breakdown. Some of this is provided by the field and some is thermal, as a result of current-driven Joule heating.[21] Thus, hard breakdown may be avoided by limiting the current in a device. This is often achieved with electrical measurement instrumentation, which lowers the applied voltage to prevent the current exceeding a limit known as the current compliance level. In some systems, the

compliance level determines whether the device is operates in a unipolar or bipolar mode. As bipolar operation typically requires a lower forming compliance than unipolar, it is sometimes possible to convert a bipolar device into a unipolar. However, bipolar behaviour is typically not recoverable.[26]

2.2 Filamentary switching mechanism

To date, a variety of resistance switching phenomena have been studied, including ferroelectric, phase change, molecular, nanomechanical, thermochemical, redox and electrochemical mechanisms.[27] The behaviour depends on the device materials, but may be generalised to two categories. Intrinsic systems rely only the composition of the active layer in its pristine state. Extrinsic devices require external species to enter the active layer. Generally, these are metal ions, migrating from one or other electrode or an additional dopant layer.

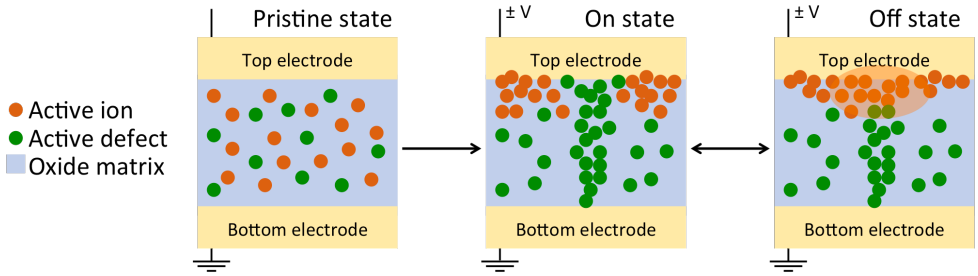

Figure 2.2. Schematic of generalised filamentary switching. In the pristine state, the switching layer is a matrix, usually an oxide, of active species and defects. Here, ions and their counterpart vacancy defects are presented. Upon electroforming to the on state, ions drift toward one electrode, leaving behind a localised conductive filament of defects that bridges the electrode pair. In switching to the off state, a small portion of the filament is disrupted, introducing an insulating region at one end of the filament. Thus, the device resistance increases but does not return to the initial, pristine resistance.

Of particular interest are devices in which resistance changes result from the generation of a thin, bridge-like conductive filament between the pair of electrodes, shown schematically in **Figure 2.2**. Filaments are difficult to study directly, owing to their small size and structural instability.[28] However, a filamentary mechanism is expected because the resistance of individual devices of the same composition is independent of the device area, defined by the overlap of the top and bottom electrodes.[29,30] This indicates that a single, very narrow conductive component is responsible for the behaviour of each device.

This report is principally concerned with devices exhibiting filamentary intrinsic resistance switching. Many materials exhibiting this behaviour have been investigated

for use in RRAM devices. Among these, transition metal oxide active layers, for example titanium dioxide, hafnium oxide, tantalum oxide and nickel oxide, have displayed promising switching properties.[31-35] However, the focus of this report is on another promising binary oxide, SiO_x, that is additionally well-suited for integration into existing fabrication infrastructure, as discussed in chapter **1.2**.

2.3 Resistance switching in silica

Full studies of resistance switching in silicon oxide are relatively recent, although non-volatile switching in silica films has been investigated since the 1960s.[14,25,36-41] Such studies have included stoichiometric silicon oxide, SiO, silicon dioxide, SiO_2, and non-stoichiometric SiO_x, where x is a non-integer between zero and two. In early work, the possibility of using bistable materials for memory was understood, but reliable control of electrical behaviour was not a focus and devices were significantly larger than those of today.[37] For example, in 1967 Simmons and Verderber discussed memory effects in SiO devices with electrode surface areas of a few square centimetres.[36] Later, in 1974, Shatzkes *et al* presented work on device areas of several square millimetres. These are in contrast to more recent sub-millimetre and sub-micron diameter devices [42] such as those presented in this report. However, this change in focus is most likely due to recent advances in semiconductor technology in line with the predictions of Moore's Law.[5,6]

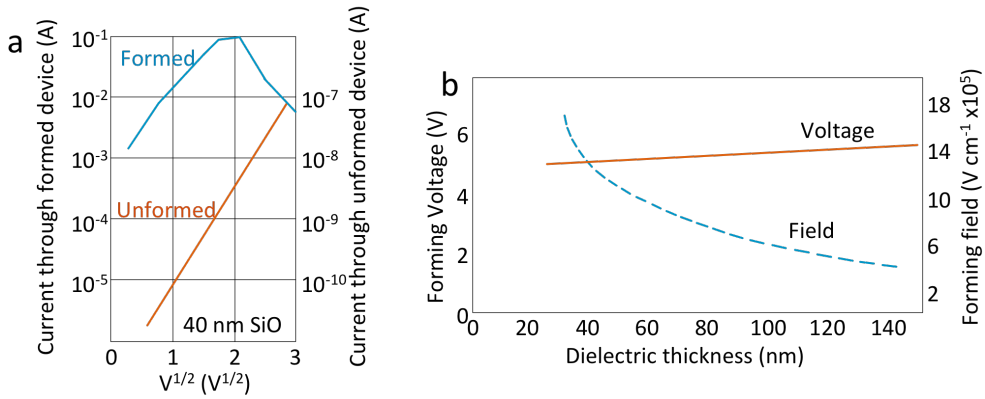

Figure 2.3. Early studies of resistance switching, reproduced after refs [36] and [43]. (**a**) Example SiO device exhibiting differential negative resistance. The formed device has a lower resistance than the unformed, but after 4 V its resistance becomes negative, evidenced by the change from a positive to a negative slope. (**b**) Example of thickness-independent forming voltage. Although the voltage required to form the device is relatively consistent with dielectric thickness, the field increases rapidly as the thickness decreases. This phenomenon was not fully explained, though one model suggested it might indicate a field-independent impurity ionisation process, assuming a high impurity concentration in the dielectric.

Early switching behaviour was termed differential negative resistance.[36,43] As shown in **Figure 2.3a,** this describes phenomena in which an increasing applied voltage decreases the resistance of a material. For a formed switching device as in **Figure 2.3a**, the current decreases after a threshold voltage. Conversely, the current in the unformed case is much lower but continues to increase after this threshold. Of particular interest in ref [43], as in **Figure 2.3b**, was that the independence of the forming voltage on the thickness of the switching layer, despite the electric field increasing rapidly with decreasing thickness. Notably, this conflicts with more recent observations of thickness-dependent forming voltages.[44]

One model presented in ref [43] suggested the formation process constituted impurity ionisation within the switching layer, which, assuming a high impurity concentration, is voltage-driven above a threshold value and independent of the field. Another model conflicted with this, suggesting the presence of very thin regions of dielectric resulting from variations in its thickness due to the roughnesses of the device materials. However, a further model based on metal injection from one electrode was presented, a mechanism now commonly known as an electrochemical metallisation memory.[44]

Several models were presented in ref [43] to explain the forming process, though no comprehensive explanation was given. However, thickness-independent current-voltage characteristics were also observed in later devices, though only in the low resistance state.[25] Here, it was suggested that the conductive region formed between the electrodes dominated the conduction, with the background field between them having little influence on the current. This is in better agreement with more recent observations.[44] Given this discrepancy in the literature, it is reasonable to speculate that all the abovementioned effects, namely impurity ionisation, thickness variation and metal injection, contributed to the forming process discussed in ref [43]; perhaps the fabrication, structure and composition of the materials used was not so well-understood in earlier devices, making a comprehensive explanation difficult to settle on.

The model of early devices that is possibly most coherent with current literature is electrochemical metallisation, as operational temperature and choice of electrode materials continue to determine the efficacy of switching behaviour. Specifically, devices were and are operable when comprising an electrode material whose ions are mobile in the active layer. For example, aluminium/SiO/aluminium devices discussed in [36] would not switch, whereas those with one or two gold electrodes would. The authors suggested that this was a result of the relatively high mobility of gold in SiO, enabling the formation of conductive filaments of gold ions. However, gold is typically considered as an inert electrode in more recent reports, with copper often used in metallisation memories.[44] In addition, given ion mobility is thermally-dependent, the

inhibition of switching at lower temperatures supported a metallisation mechanism. For a formed device, high temperatures reduced the conductivity, suggesting the filament would be disrupted as ions move away once supplied with sufficient thermal energy.

The structure, formation, rupture and conduction of filaments is still not fully understood, despite having been imaged in some devices, as will be discussed in chapter **2.6**. The existing model for intrinsic oxide-based RRAM devices, including SiO_x, describes switching in relation to structural and compositional defects and oxygen migration under electrical stress.[13,18,26,29] Oxygen vacancies are of particular interest. These are defects in the dielectric where oxygen should be bound to silicon but instead the bond is unsaturated and positively charged.

In silica, oxygen vacancies present mid-band gap energy states for electron capture.[40,46] As shown in **Figure 2.4a**, electrons in the anode are captured if its Fermi energy is greater than or equal to the defect energy. A filled defect induces a highly localised restructuring of the matrix, thus its energy is lowered as it relaxes. For the electron to leave the trap and enter the cathode, a bias is applied to bring its Fermi level below the relaxed trap level. This conduction mechanism is known as trap assisted tunnelling.[47]

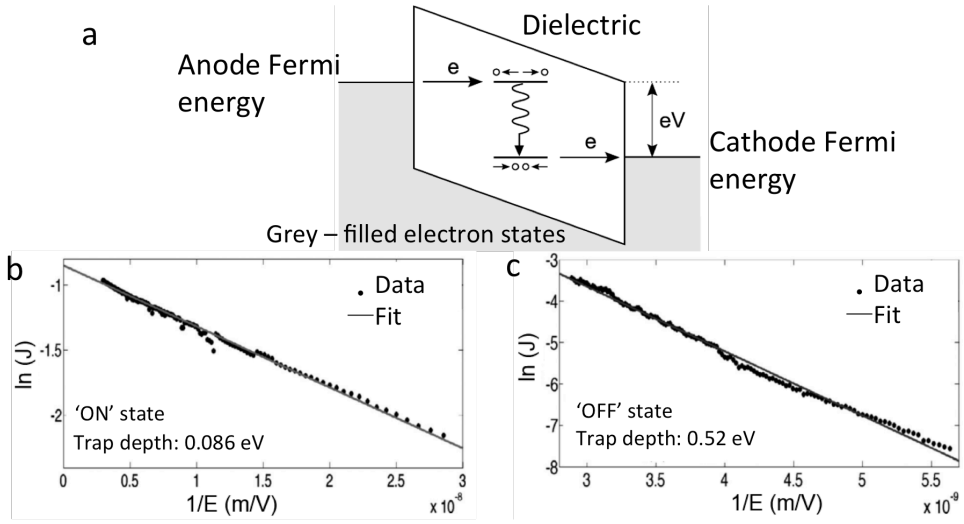

Figure 2.4. Trap assisted tunnelling in silica. (**a**) Schematic of an electron moving from anode to cathode, through a dielectric, by filling and emptying trap states in the dielectric band gap, reproduced from [45]. (**b**) and (**c**) trap assisted tunnelling fits for SiO_x devices in on and off states, respectively, reproduced after ref [13]. The trap depth is lower in the on state, indicating a greater concentration of available traps, in line with **Equation 6.1**.

Small currents can flow in pristine silica as a result of trap assisted tunnelling between intrinsic defects. However, for a significant current, such as might flow in a device in the on state, the defect concentration must increase. In silica RRAM, electroforming is

believed to drift oxygen ions from bonding sites towards the cathode, leaving behind oxygen vacancies. This field-driven dissociation increases the defect density. With sufficient dissociation, an aggregated, filamentary chain of oxygen vacancies bridges the active layer. As such, the trap assisted tunnelling current increases and the device enters the on state. To reset the device into the off state, some vacancies are thermally re-oxidised by the relatively high current and the filamentary chain is disrupted, reducing the device conductivity. In both states, oxide RRAM devices operate under relatively high fields of a few megavolts per centimetre, a regime in which trap assisted tunnelling dominates the conductivity.[45] As is shown in **Figure 2.4b** and **c**, the conduction in SiO_x devices may best be fitted with a trap assisted tunnelling model,[13,14] following that of Huong *et al* [45] and described by

$$J_s = J_0 \exp\left[-\frac{8\pi\sqrt{(2qm^*)}}{3hE}\Phi_t^{3/2}\right] \qquad (6.1)$$

where J_s represents the tunnelling current density, q the electron charge, m^* the effective mass of an electron in the active layer, h is Planck's constant, E the applied field strength and Φ_t the trap barrier height, defined as the difference in energy between the trap and the dielectric conduction band. From **Equation 6.1**, it is possible to extract the trap depth and thus the capability of the system to support a trap assisted tunnelling current. Lower trap depths suggest a more conductive dielectric, due to greater defect density. As shown in **Figure 2.4b** and **c**, the trap depth is lower in the on than the off state, indicating increased capability for trap assisted tunnelling in the on state. A full, schematic model for this conduction mechanism is shown in **Figure 2.5**.

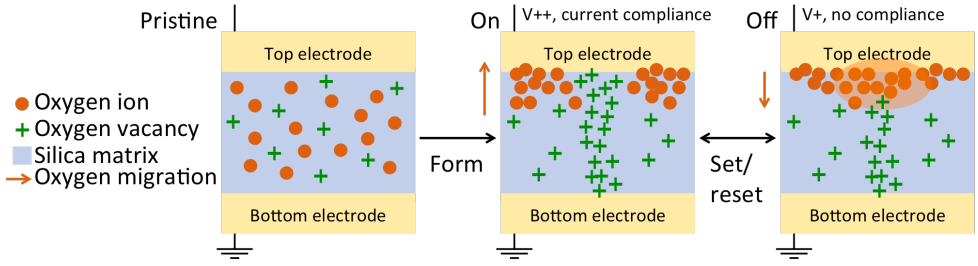

Figure 2.5. Switching model schematic in unipolar SiO_x devices. The pristine active layer contains some intrinsic oxygen vacancy defects. A large voltage, V++, with a current compliance limit, liberates oxygen from silicon-oxygen bonds, drifting it toward the top electrode. This leaves a bridge of defects between the electrodes, enhancing trap assisted tunnelling. With current compliance removed, a smaller voltage, V+, induces Joule heating locally to the filament and some ions diffuse back to vacancy sites, disrupting the filament. Thus the device resistance increases, but does not reach the pristine state.

The removal of oxygen from silicon-oxygen bonds is a reduction reaction, thus the nomenclature of oxide-based resistance switching often refers to redox-based

memories.[18] As the filament grows, field-driven oxygen vacancy creation within the active layer accelerates, effectively decreasing the distance between the electrodes. This filamentation process constitutes a soft dielectric breakdown of the insulator.[48] If cycling causes continued filament growth, eventually the size of the filament prevents it being broken.[49] For example, it may not be possible to supply sufficient current to reset a particularly large filament, thus reset operations will produce further field-driven effects and filament growth. This might be considered hard dielectric breakdown, as the device state can no longer be changed.[50]

It has been suggested that intrinsic structural defects may facilitate the dissociation and migration of ions within dielectric films.[13,15,32,51] As a result, many redox-based dielectrics are intentionally amorphous, structurally defect-rich material.[52] Notably, a structural defect is difficult to define for an amorphous material. However, they are often described as intrinsic density variations or distinct microstructures, as these are thought to facilitate filamentation.[53]

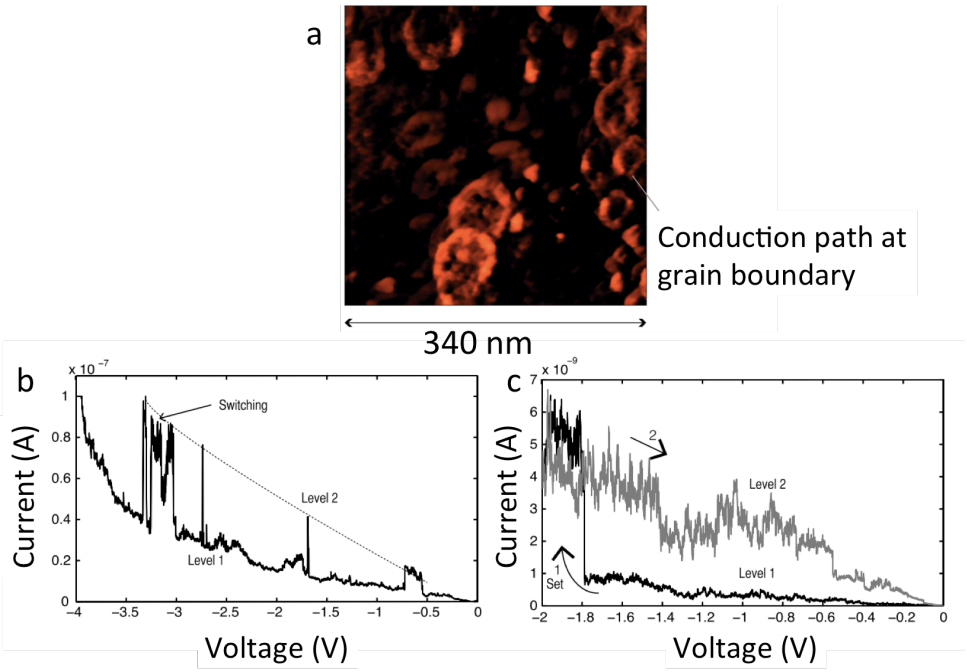

Figure 2.6. Switching activity in relation to grain-like edges in SiO_x, reproduced after ref [14]. (**a**) Scanning tunnelling microscopy image of switching layer surface, indicating increased conductivity at grain edges compared to off-grain areas. (**b**) and (**c**) each demonstrate evidence of switching behaviour when voltages are applied to the edge of a grain using the scanning probe tip.

Notably, scanning tunnelling microscopy of the SiO_x film in intrinsic devices exhibiting both unipolar and bipolar operation demonstrated a grainy surface appearance.[12,14] The edges of the grain features showed increased conductivity and exhibited switching behaviour relative to the rest of the film, as shown in **Figure 2.6**. The devices did not require a vacuum environment or exposed SiO_x edge to function, thus a redox-based,

trap assisted tunnelling mechanism was an appropriate model for their operation.[7] Together, these observations support the notion that structural defects might encourage filament formation, at least in SiO_x.

An important defect is the silicon dangling bond, as shown in **Figure 2.7**.[40] The operation of unipolar platinum/SiO_x/platinum devices was attributed to this defect and its increasing concentration under an applied electric field. Dangling bonds are unsaturated silicon valences, which includes oxygen vacancies. As with oxygen vacancies, dangling bonds may be created by an electric field and can capture electrons. As previously discussed, the device resistance decreases as the defects aggregate into a filament. Resetting is then achieved by thermal re-oxidation of the dangling bonds near the biased electrode. Here, it was also suggested that the external environment might supply the oxygen needed recombine at vacancy sites and break the filament during reset.

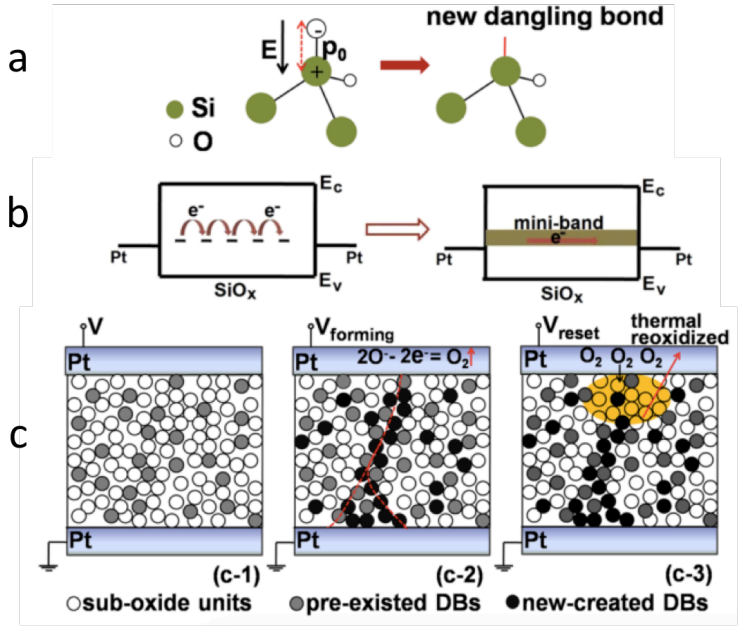

Figure 2.7. Dangling bond conduction in SiO_x, reproduced from [40]. (**a**) Schematic of dangling bond formation. The applied field, E, stresses the silicon-oxygen dipole, dissociating the oxygen. (**b**) Schematic of dangling bonds generating a 'mini-band' of electron states within the band gap, across the switching layer. (**c**) Filament formation in platinum/SiO_x/platinum devices. During forming, the creation of new dangling bonds increases their concentration until they bridge the electrodes. During reset, Joule heating induces reoxidation of dangling bonds in a portion of the filament near the top electrode.

The critical nature of oxygen in redox RRAM device is most evident during reset, when it must migrate to disrupt the filament.[29] Typically, as there must be sufficient Joule heating during reset to re-oxidise some of the filament, current compliance is removed

and a lower voltage used than for the set, as discussed in chapter **2.1**.[54] However, further field-driven changes might still occur, such as filament growth. Thus the active layer would continue to lose oxygen, suggesting an eventual depletion that might prevent sufficient reoxidation to reset the device. It is therefore important to consider the effect of the environment that the device is operated in.

Evidence that bulk resistance switching devices require an oxygen source for operation, in particular for reset, comes from results on operation in different atmospheres.[29,31,40,55] For air and oxygen environments, switching is stable and devices cycle reliably, particularly in an oxygen-rich environment. In a vacuum, however, performance is drastically worse and it becomes more likely that a reset will fail. This suggests that environmental oxygen might enter the switching layer during reset and thermally re-oxidise dangling bonds in the filament.

An alternative mechanism of resistance switching in SiO_x involves the formation of a crystalline silicon surface region, between the electrodes.[1,17,56] Devices operation is governed by an exposed, switchable nanogap region of SiO_x between amorphous carbon electrodes, as shown in **Figure 2.8d**.[56] These devices also have a lower set voltage than reset and can require up to eight successive form steps to reach optimal behaviour. However, they have a high on/off current ratio, in the order of 10^6.

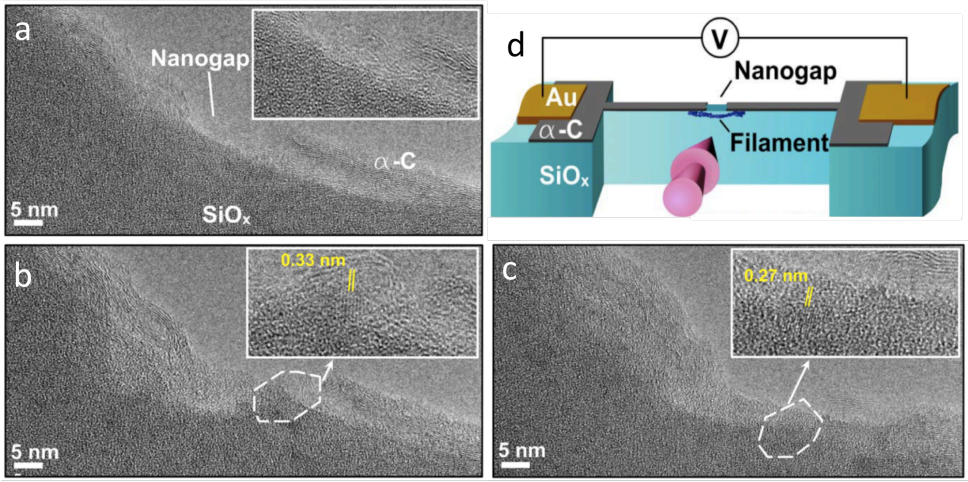

Figure 2.8. Transmission electron microscopy images showing crystallisation of a silicon filament, reproduced from ref [57]. (**a**) Pristine active nanogap SiO_x region between the amorphous carbon, α-C, electrodes. **(b**) Formed device, showing a crystallised region of the SiO_x. The formation of nanocrystals is evident in the inset, which shows features consistent with the lattice spacing of the silicon (111) and (220) planes. These create a conductive bridge between the electrodes. (**c**) The crystalline region is disrupted and the device enters a more insulating state. (**d**) Schematic of the device and exposed nanogap region.

Transmission electron microscopy imaging at 10^{-8} Torr enabled direct imaging of the conductive filament between a pair of amorphous carbon electrodes, separated by 4 nm of SiO_x surface, as shown in **Figure 2.8**.[57] Thus, rather than bulk resistance switching behaviour relying on ion migration, the exposed SiO_x edge appears to govern device behaviour. Edgeless SiO_x were also produced but showed no switching, also suggesting that it is the exposed active layer that enables switching. Further evidence for this was that device must be operated in a vacuum of at least 10^{-5} Torr, likely to prevent oxidation of the silicon filament as it crystallises. However, it is not always practical for a device to require a vacuum for operation. This is particularly important for integration into consumer technology, where vacuum operation is difficult to implement.

2.4 Silicon oxide-based devices relative to the state of the art

To successfully integrate RRAM devices into consumer technology, they must demonstrate stable and reliable switching, as mentioned in chapter **1.1**. Endurances of 10^{11} cycles have been demonstrated, although the on/off resistance ratio of such devices was low, around one order of magnitude.[58] In contrast, devices with four orders of magnitude resistance contrast have been fabricated, but with an endurance of only 10^6 cycles.[59] Practically, this implies that the former devices would have a longer lifetime but the resistance state of the latter is more likely to be read correctly. However, tungsten/SiO_x/carbon devices have been fabricated and demonstrate more than 10^7 cycles with a resistance contrast of four orders of magnitude at up to 260˚C.[60] Thus, silicon oxide-based devices might overcome the apparent and undesirable compromise between stability and reliability present in other devices. To better illustrate this relation to other materials, and also to flash memory, **Figure 2.9** presents collated data from the literature.

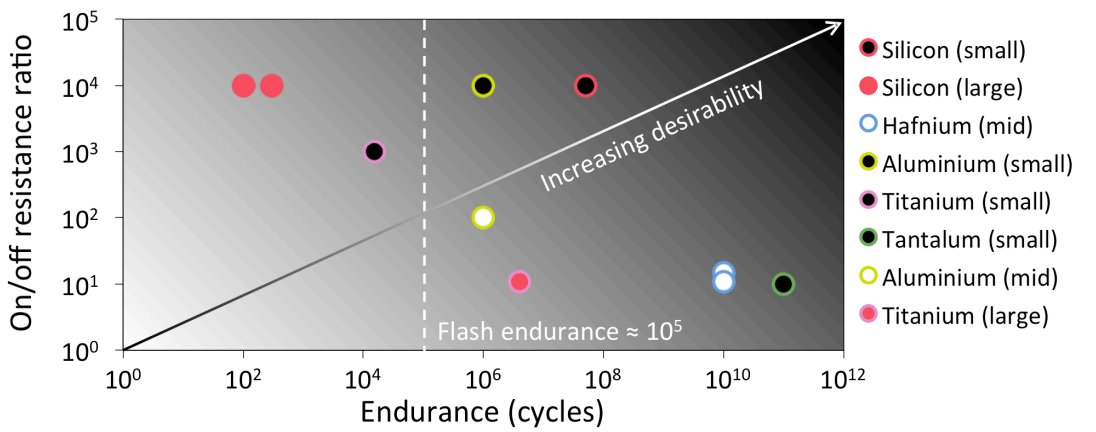

Figure 2.9. Illustration of the functionality of silicon oxide-based devices [17,60,61] in relation to the state of the art in hafnium,[58,62] aluminium,[59,63] titanium,[64,65] and tantalum [66] oxide-based devices. Black-filled circles indicate 'small' device diameters, below 100 nm. White-filled circles indicate 'mid' sizes, between 100 nm and 1 μm. Red-filled circles indicate 'large' devices, greater than 1 μm. The greyscale fill of the plot area indicates the desirability of device parameters, with black indicating the most desirable region of the plot. Devices exhibiting higher endurance tend to have lower on/off ratios, compromising the reliability of reading data. Devices with larger on/off ratios show lower endurance, although it is generally greater than that of flash. Silicon oxide-based devices appear to offer the most desirable compromise; endurance over two orders of magnitude greater than flash and a competitively large on/off ratio. In addition, such devices have been fabricated with 70 nm diameter, making them suitable for integration into densely packed device architectures known as crossbar arrays.

In addition to demonstrating desirable switching behaviour, emergent devices must be scalable. RRAM requires only two terminals for operation, thus crossbar arrays may be used to pack memory elements more densely than three-terminal flash memory.[67] Recently, silicon/silicon dioxide/silicon crossbars have been fabricated with a 5 μm by 5 μm crosspoint area [61] and titanium/SiO_x/carbon crossbars with crosspoint areas of 70 nm by 70 nm have also been produced.[60] These successes suggest that silicon oxide-based devices are competitively scalable, in addition to their demonstration of highly desirable switching behaviour.

2.5 Observation of structural transformations

Alongside changes in resistance, dynamic structural transformations have been observed in RRAM devices during operation. In particular for silicon oxides, these are often protuberances of varying size on the top electrode and switching layer. Early reports showed crater-like distortions, thought to be correlated with high currents, as shown in **Figure 2.10a** and **b**.[25] More recently, larger devices demonstrated the

appearance of snaking, discoloured regions whose area of coverage increases with larger currents, as shown in **Figure 2.10c**.[40] This behaviour was attributed to oxygen release through the top electrode, although no further evidence was presented.

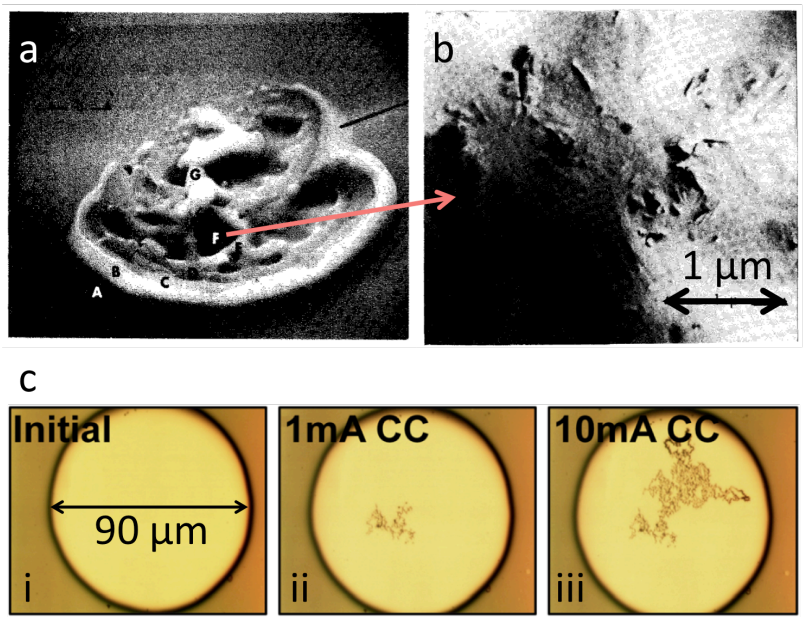

Figure 2.10. Deformations of silicon oxide-based devices. (**a**) Cratering on an aluminium/silicon dioxide/silicon device, reproduced after ref [25]. (**b**) Close-up of area F in **a**, demonstrating small cracks on the exposed silicon dioxide surface. (**c**) Protuberances on the top electrode of a platinum/SiO_x/platinum device, reproduced after ref [40]. **i** –pristine state, **ii** – following electroforming at 1 mA current compliance and **iii –** electroforming a second time, at 10 mA current compliance.

Structural changes have also been observed in other binary oxide RRAM devices. Often, these are bubble-like deformations, as shown in **Figure 2.11**. In particular, these have appeared on the top electrode it is positively biased.[26] In general, the set process induces bubble formation, thus local reduction of the active layer near the cathode has been proposed as a cause. Copper/tantalum suboxide/platinum crossbar array devices, with a 35 μm^2 crosspoint area, have displayed optically visible, bubble-like structural deformations, as shown in **Figure 2.11a**.[68] Interestingly, smaller, 10 μm^2 devices, showed no deformation. Similarly, bubble formation was observed on 25 μm^2 platinum/titanium dioxide/platinum devices, as shown by atomic force microscopy (AFM) in **Figure 2.11b** and **c**, but not on smaller, 50 nm wide devices.[29] In this case, it was suggested that this difference resulted from the greater volume of active layer participating in switching larger devices. Reduction of the oxide would produce a comparatively high gas pressure, causing damage as oxygen is released. Smaller devices might also more readily out-diffuse oxygen at their edges without damage.

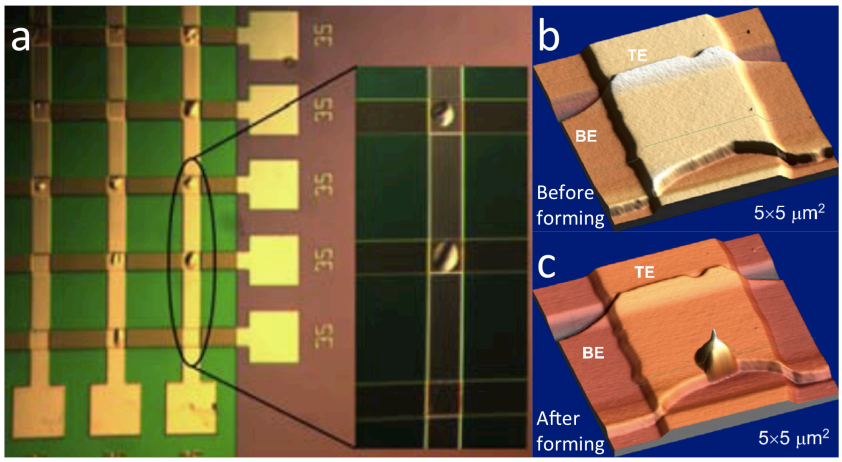

Figure 2.11. Structural changes in binary oxide resistance switching devices following electrical operation. (**a**) Optical images of bubbles on tantalum suboxide-based crossbar devices, reproduced from [68]. (**b**) and (**c**) AFM images of a bubble-like deformation on titanium dioxide-based devices, reproduced from [29].

In 60 μm wide devices, similar to those of **Figure 2.11b**, the polarity of the applied voltage determined whether bubbles would persist once the electrical stress was removed.[29] It was suggested that the bubbles contain oxygen, forming at the interfaces electrode and active layer. If they are able, they then diffuse to the edge of the electrode and escape. Thus, bubbles formed at the bottom interface persist, as they are unable to pass through the blanket oxide and electrode layers. However, bubbles formed at the top interface should more readily be released.

Deformations such as those shown in **Figure 2.11** have been attributed to the migration of oxygen. However, this is not generally confirmed experimentally, as mentioned in relation to the silicon oxide-based device in **Figure 2.10c**. Correlation between surface distortions and localised conductivity enhancement has been shown with conductive atomic force microscopy (CAFM), as in **Figure 2.11a** to **d**. This might indicate that dissociated oxygen is responsible for changes in both structure and conductivity, although it is not direct evidence.[31,69]

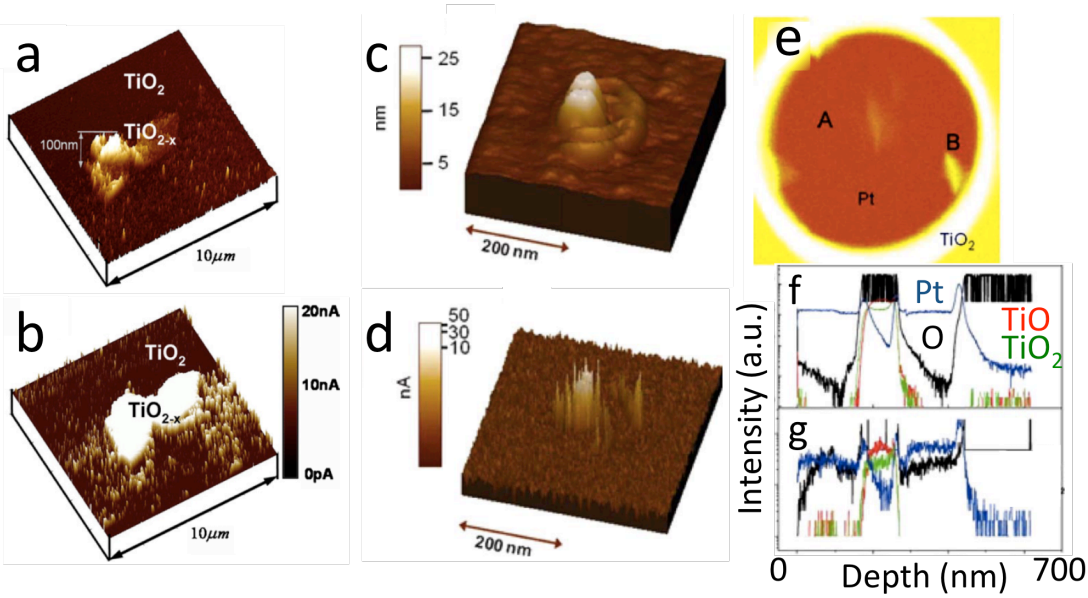

Figure 2.12. Switching-induced structural and compositional changes in titanium dioxide-based devices. (**a**) and (**b**) CAFM topography and current maps, respectively, from the active layer following removal of the top electrode, reproduced from [69]. (**c**) and (**d**) topography and current maps, respectively, from the active layer following electrical stress, reproduced from [31]. (**e**) Secondary ion mass spectroscopy surface map of the platinum top electrode of a device following forming, in which bright areas indicate a higher oxygen concentration, reproduced from [31]. (**f**) and (**g**) depth profiles at positions A and B, respectively, from **e**, indicating oxygen migration from the active layer into the electrodes, reproduced after ref [31].

Notably, changes in oxygen concentration have been observed in titanium dioxide-based devices.[31] As shown in **Figure 2.12e** to **g**, the top electrode of a formed device showed regions of increased oxygen relative to the rest of the active layer. Depth profiling revealed that the active layer in these regions was depleted of oxygen, whereas both electrodes appeared to contain more oxygen than in their pristine state. This suggested that oxygen is liberated from the active layer during electroforming and also that it accumulates in the electrodes.

Bubbling has been noted on manganite-based RRAM and attributed to oxygen ion migration under bias, as shown in **Figure 2.13a**.[70] The formation and shape variation of bubbles on titanium/gold electrodes was attributed to the reduction of sub-stoichiometric titanium oxide at the interface, although no further evidence of oxygen mobility was presented. Notably, however, evidence has been presented for a change in stoichiometry at the location of a surface deformation in a perovskite RRAM device.[55] Following a single switching event, setting the device into a low resistance state, the top electrode of the device was removed and a few-micrometre deformation

observed, as shown in **Figure 2.13b**. This was correlated with a reduction of the titanium and oxidation of the strontium in the strontium titanate active layer, demonstrated in **Figure 2.13c** and **d**,

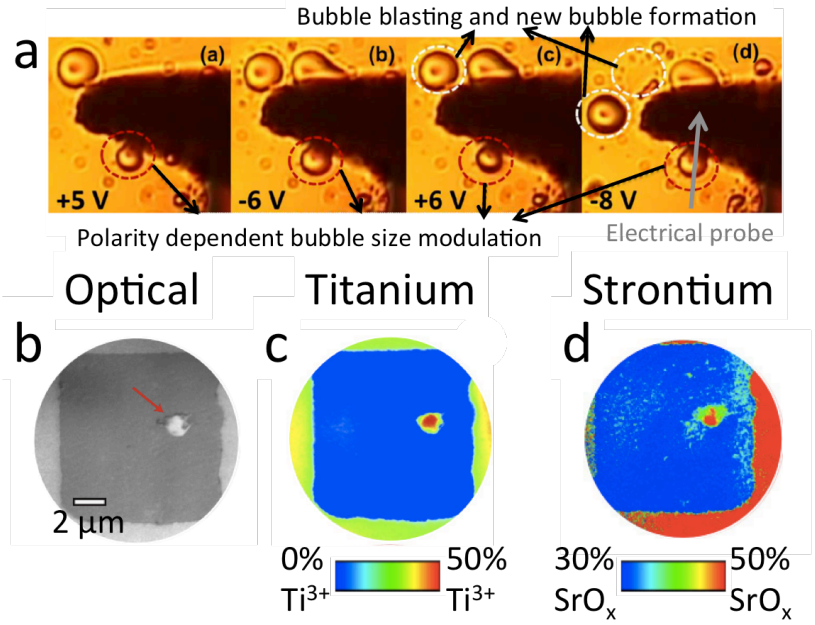

Figure 2.13. Structural changes in manganite and perovskite resistance switching devices. (**a**) Optical images of the appearance and disappearance of bubbles in close proximity to the electrical probe on the top electrode of a lanthanum-strontium-manganese-oxide device, reproduced from [70]. (**b**) to (**d**) observed deformation, indicated by the red arrow, following removal of the top electrode and correlated with a change in the stoichiometry of the active layer of a strontium titanate device, reproduced after ref [55].

The formation of bubbles and the suggestion that switching depends on oxygen migration implies a possible physical limit on RRAM device endurance. If oxygen is gradually removed from the active layer and not replenished, then the device will become oxygen deficient and no longer function. As discussed in chapter **2.3**, environmental oxygen might be a crucial oxygen source for resetting. In addition, it has been suggested that varying the switching polarities to reduce oxygen loss might improve device lifetimes, although the uniformity of on and off states may be degraded.[49] Such a scheme and the underlying phenomena govern the variety of switching behaviours noted for different resistance switching materials, as discussed in chapter **2.4**.

2.6 Observations of filaments

Large structural changes, such as bubbles, provide an insight into the effect of resistance switching on a device. However, the more localised phenomenon of filamentation, as discussed in chapter **2.2**, governs switching and ultimately enables

larger device deformation. Filaments have been imaged by transmission electron microscopy and CAFM in some devices, as shown in **Figure 2.14**. In extrinsic devices, filaments have been observed to grow and rupture as a result of electrical operation and the conductive pathway has been revealed in three dimensions, as shown in **Figure 2.14a** and **c**. In intrinsic devices, it has been demonstrated that filaments are composed of distinct, conductive phases, such as the Magnéli phase in titanium dioxide and silicon rich channels in silicon dioxide.

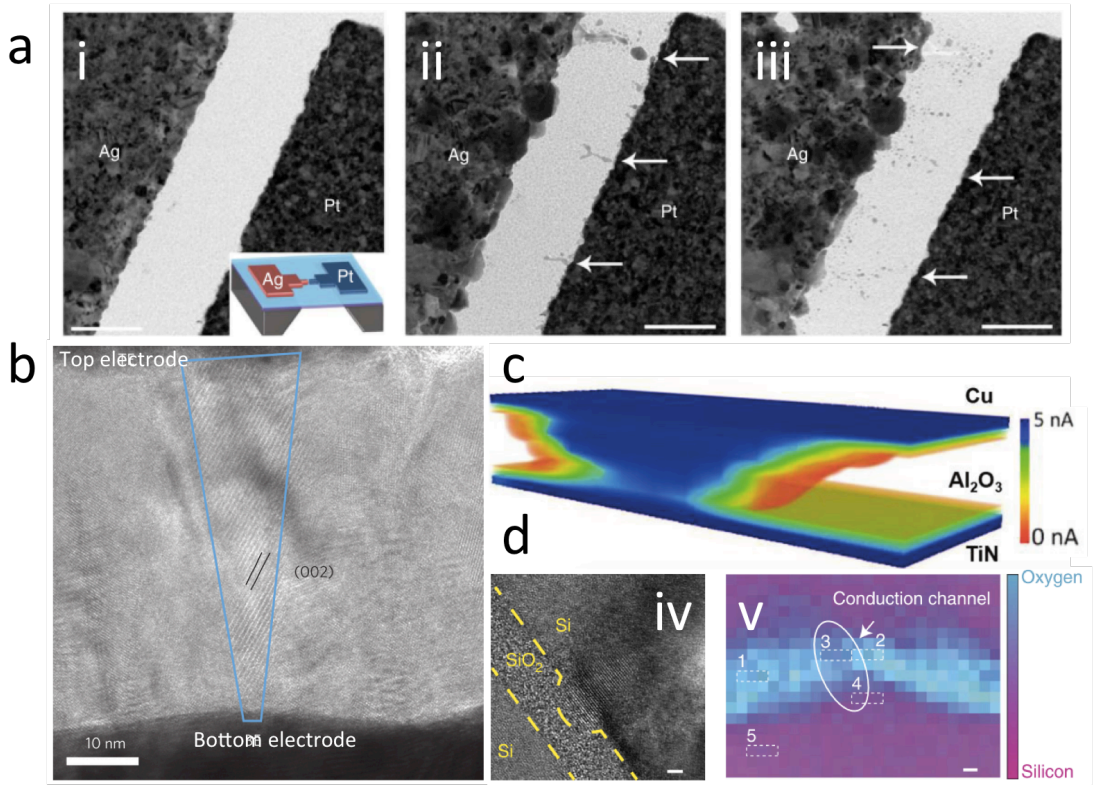

Figure 2.14. Observations of conductive filaments in RRAM devices. (**a**) Transmission electron microscopy images of filament growth and rupture in silver/silicon dioxide/platinum devices, in which mobile silver ions bridge the top and bottom electrodes, reproduced from [71]. **i** – pristine device, **ii** filament growth, **iii** – filament rupture. (**b**) Transmission electron microscopy image of the conductive, Magnéli phase of titanium dioxide that composes the filament in a platinum/titanium dioxide/platinum device, reproduced from [48]. (**c**) Three-dimensional CAFM image showing the conductive profile of a filament of copper ions in a copper/aluminium oxide/titanium nitride device, reproduced from [28]. (**d**) **iv** – transmission electron microscopy image of a conductive region in a silicon/silicon dioxide/silicon device and **v** – associated electron energy loss spectroscopy map demonstrating that this region is silicon rich, reproduced from [61].

The conductive pathways, or filaments, shown in **Figure 2.14** are a few to tens of nanometres in diameter. These are promising findings, as they indicate that RRAM

devices should be scalable down to similar sizes. However, these observations have analytical limitations. For transmission electron microscopy, measurements require a thin device cross-section and the resulting image is a flattened projection of this sample volume. Thus, the true structure of the filament is convoluted by the measurement. For CAFM measurements, although three-dimensional information is produced, very little detail is present. As a result, the image shows the general shape of the filament but it does not indicate any of the internal structure that is evident in transmission electron microscopy images.

2.7 The gap in understanding

Bubble formation and damage has been cited as a direct confirmation of the diffusion of oxygen ions and vacancies within intrinsic RRAM active oxide layers, as discussed in chapter **2.5**. In the case of perovskite devices, evidence for stoichiometric changes as a result of switching has been presented. In titanium dioxide, oxygen was observed to move from the active layer into the electrodes. However, such confirmation of oxygen drift during switching in silicon oxide-based devices does not appear in the literature. Furthermore, there is a lack of evidence correlating oxygen migration with structural changes in intrinsic devices, although this has been reported for extrinsic devices. Thus, there is a gap between the interpretation and understanding of switching-related changes in SiO_x.

Despite the knowledge gap, it seems plausible that device operation is reliant upon oxygen drift, given the apparent morphological changes. In addition, it is reasonable to suppose that those changes occurring on the device scale might indicate electrically driven restructuring on a smaller scale, within the device layers. Thus, to advance RRAM toward incorporation into commercial electronic architectures, it is useful characterise switching-related material changes in order to better understand device operation. The properties of the active layer and electrodes might then be optimised for energy consumption, endurance, retention and size.

This reasoning underpins my work on SiO_x devices in this report. I aim to better characterise the relation between structural, compositional and electronic changes in a highly commercialsable material system. Namely, I hope to provide convincing evidence that oxygen migration occurs when my devices are operated electrically and that this behaviour correlates with morphological changes at the device scale down to filamentation at the nanoscale.

3. Characterisation methods

3.1 Electrical measurements

The primary method for characterising resistance switching devices is through electrical measurement. By monitoring the current while a voltage is applied between the top and bottom electrodes, it is possible to discern the behaviour of a device, as illustrated in **Figure 3.1**.

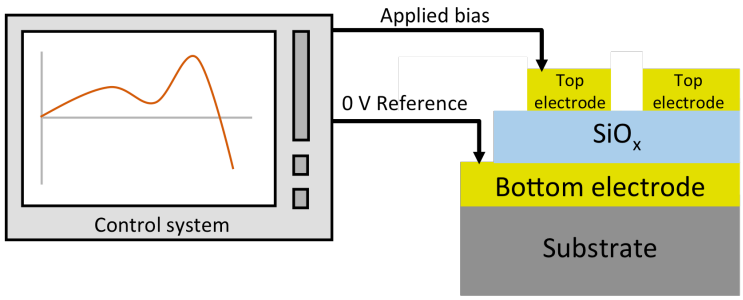

Figure 3.1. Keithley 4200-SCS electrical measurement system schematic.[72] The integrated control system is capable of applying voltage sweeps between a pair of output leads. Here, the leads are connected to the top electrode and bottom electrode of the device via tungsten needles, with the bottom electrode held at 0 V relative to the bias applied to the top electrode.

Tungsten probes connect the semiconductor parameter analyser, a Keithley 4200-SCS,[72] to the devices. This is shown schematically in **Figure 3.1**. Using built-in software, voltages are applied between the output probes and the current measured over time. This generates current-voltage spectra characterising the resistance switching behaviour of the test device.

3.2 Atomic force microscopy

AFM is a scanning probe technique used for collecting maps of the topography of samples. To do so, it exploits variations in the energy between nanoscale objects in close separation; namely features on the sample surface and a sharp probe that is raster scanned across this surface.[73] The Lennard-Jones potential, U_{LJ}, approximates this interaction as a function of the inter-object separation, r,[74] given by

$$U_{LJ} = 4\varepsilon\left[\left(\frac{r_0}{r}\right)^{12} - \left(\frac{r_0}{r}\right)^{6}\right] \qquad (7.1)$$

where ε is the maximum depth of the potential well, where U_{LJ} is most negative and the attractive forces dominate, and r_0 is the separation at which the potential is zero. **Figure 3.2a** shows the form **Equation 7.1**. At relatively large separations, represented by the second term in **Equation 7.1,** the objects experience the attractive van der Waals forces of chemical bond formation. As the objects become closer, their electron

clouds eventually try to overlap. As such, the electrons attempt to occupy the same states. This is forbidden according to the Pauli Exclusion Principle, so the repulsive force tends to infinity, as described by the first term in **Equation 7.1**.[75]

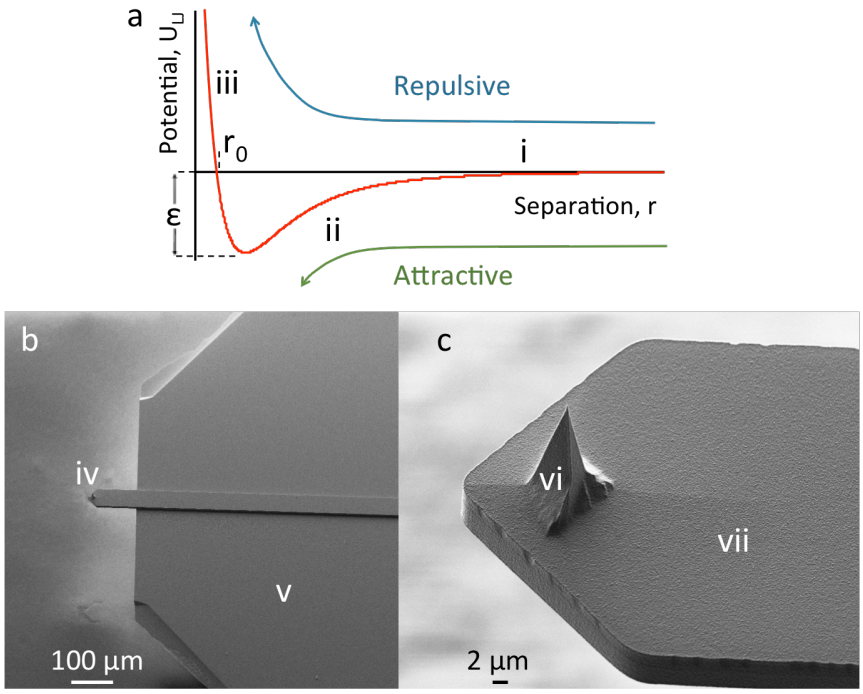

Figure 3.2. Fundamentals of AFM. (**a**) The Lennard-Jones potential, describing the energy of interaction, U_{LJ}, of two nanoscale objects as a function of their separation, *r*. **i** – long-range attractive van der Waals and Coulombic forces, **ii** – short-range attractive chemical bonding forces, **iii** – short-range repulsion of electron cloud overlap, as described by the Pauli Exclusion Principle. (**b**) Top-down SEM image of an AFM probe. **iv** – cantilever and probe tip, **v** – silicon chip on which the cantilever is mounted. (**c**) Side-on SEM image of the probe tip. **vi** – the tip tapers to a sharp apex. **vii** –silicon cantilever on which the tip is mounted.

Figure 3.2b and **c** show scanning electron microscopy (SEM) images of a typical AFM probe. The probe is mounted in the AFM instrument, allowing the user to control its position and motion. To study topography, the probe is brought toward the sample so that the apex experiences the interaction potential from atoms on the surface.[76] As the probe moves across the sample, the surface height changes and therefore so does the separation, causing a deflection of the cantilever. Depending on the method used to measure the deflection, forces in the order of piconewtons can be detected.[77]

Figure 3.3 illustrates typical AFM instrumentation.[78] Most commonly, to measure cantilever deflection, a laser beam is reflected from the back of the cantilever onto a quadrant photodiode, producing four distinct voltage signals. By comparing variations in incident intensity, and thus voltage, on each quadrant, the response of the probe to the sample topography can be tracked. Other methods include incorporating

piezoelectric or piezoresistive elements into the cantilever, or using it as a capacitor plate, such that deflections produce measureable changes in its electrical properties.[79]

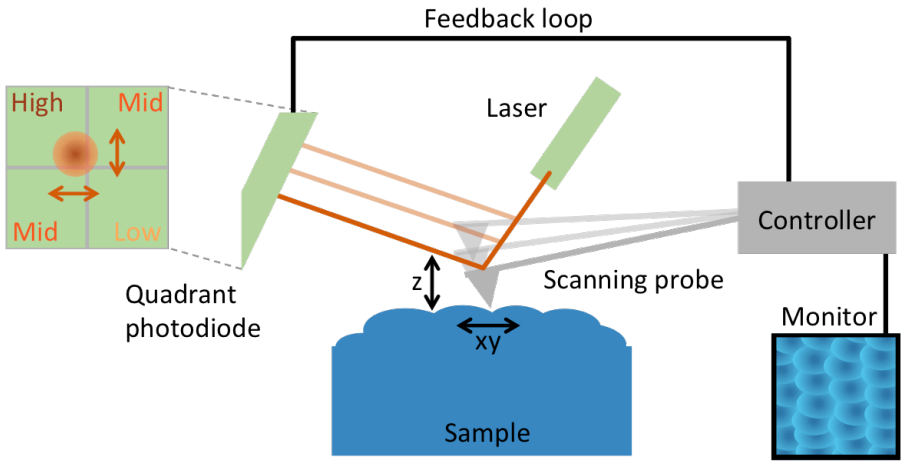

Figure 3.3. Schematic of AFM operation.[78] Piezoelectric controllers actuate the probe, raster-scanning it across the sample. The tip responds to changes in surface height, causing the cantilever to deflect. The deflection is monitored by a quadrant photodiode that detects a laser reflected from the cantilever. The beam intensity varies between quadrants, allowing the height and tilt of the cantilever to be tracked. A feedback loop controls the actuators in order to maintain constant photodiode signals or scan parameters. The feedback process produces topographical data that can be mapped to produce an image of the surface features.

AFM instruments generally operate using a feedback loop, whereby a particular parameter is maintained at a value known as the setpoint, while another is measured.[80] Often, and in the case of the measurements discussed in this report, the tip-sample separation is maintained. This is best achieved by exploiting region **ii** of the Lennard-Jones potential, shown in **Figure 3.2a**. In this range, small changes in the surface height of the sample will produce relatively large deflections in the cantilever, as the change in interaction energy is also large. The cantilever behaviour is analogous to a mass on a spring; the force on the tip is proportional to the tip-sample separation. At greater separations, the cantilever will not deflect so much when the apex encounters changes in height. For smaller separations, the tip will be forced into contact with the sample and both may be damaged.

Maintenance of a constant tip-sample separation is generally achieved in one of two ways. In contact mode, as illustrated in **Figure 3.4a**, the feedback loop attempts to keep the photodiode signal constant by actuating changes in the cantilever height as the tip moves over surface features. In tapping mode, as demonstrated in **Figure 3.4b**, the cantilever is made to oscillate at its resonant frequency, producing a sinusoidal

photodiode voltage. As the tip approaches the sample, the oscillation amplitude is enhanced and the voltage range changes. The feedback system attempts to maintain a fixed maximum voltage in order to keep the oscillation amplitude, and thus the tip-sample separation, constant. In addition, the phase of the oscillation is perturbed by the surface, in particular by changes in composition and contact area, such as when the apex encounters a slope.[81] Although the cantilever phase data is difficult to quantify, it may used to complement the topography data. Notably, contact-mode scanning can dislodge loose objects from the surface, but tapping-mode allows imaging without this risk.[82] This is because the tip does not make shear movements in contact with the sample during tapping-mode scans.

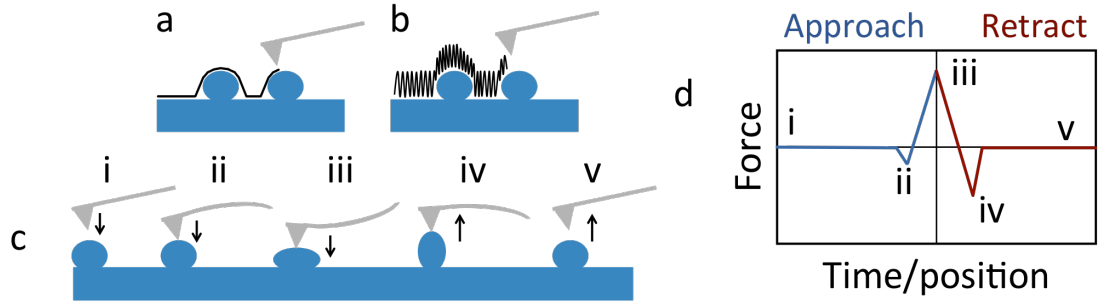

Figure 3.4. Schematics of AFM measurement modes. (**a**) In contact mode, the tip-sample separation is maintained. (**b**) In tapping mode, the oscillation amplitude of the cantilever is held constant. (**c**) and (**d**) the process and resulting plot, respectively, for a force-distance measurement. **i** – as the tip approaches the surface, it experiences small forces from coulombic interactions. **ii** – when nearing the surface, there is a sudden pull-in as the tip experiences chemical bonding forces. **iii** – when pushed further into contact, the cantilever must bend according to its spring constant as the apex and sample surface may not occupy the same space. **iv** – as the tip is pulled out, it also pulls on the surface and both may deflect. **v** –the tip is released from the surface and again experiences only relatively weak forces.

Contact mode can also be used to study mechanical properties by pressing the probe tip into the sample and then moving it back, away from the surface. The corresponding cantilever deflection is tracked, producing a plot whose shape characterises the interaction between the tip and sample and the spring constant of the cantilever. This is known as a force-distance spectrum, shown schematically in **Figure 3.4b** and **d**. The differences in force between the tip and sample during approach and retract can be used to ascertain mechanical properties of a point on the surface. This technique may be extended to quantitative nanomechanical mapping (QNM) mode, wherein multiple force-distance spectra are gathered at each point on an area of the sample surface. This produces maps of, for example, the energy dissipated by the cantilever during the

interaction, the adhesion force between the tip and sample, the energy dissipated in the tip-sample interaction, the degree of deformation of the surface and its Young's modulus.[83] The relation between these properties and force-distance spectra is illustrated in **Figure 3.5**.

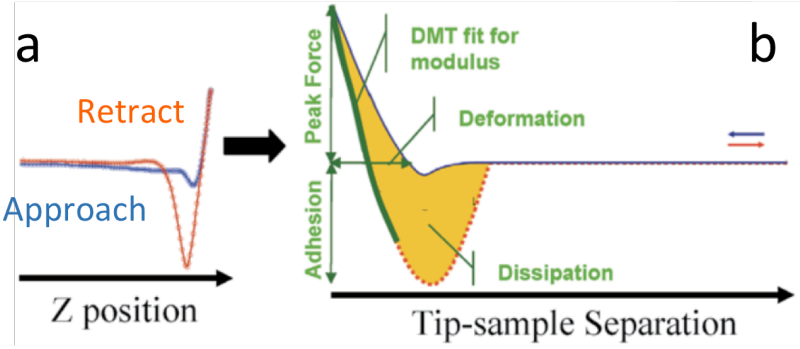

Figure 3.5. QNM metrics, reproduced from [84]. (**a**) Typical force-distance spectrum, demonstrating the difference in approach and retract data. (**b**) Mechanical properties of the sample may be extracted from force-distance data. Deformation is a measure of how far the surface displaces under the force of the probe, in its direction movement. Practically, this is the difference between the vertical position of the probe controller and the measured deflection of the cantilever. Energy dissipation is the integral of the difference between approach and retract data. More energy is dissipated on a flexible surface because the cantilever bends less than on a hard surface. Likening the system to a spring, this means less energy is stored in the flexing cantilever, instead being dissipated in the surface displacement. Adhesion is the most negative force, indicating the pull of the surface on the probe as it retracts. The DMT modulus corresponds to the Derjaguin-Muller-Toporov model for estimating the Young's modulus of a surface under an interaction governed by the Lennard-Jones potential.[85][86][87] The peak force is a measure of the maximum gradient of the spectrum. This is determined by the spring constant of the cantilever and is used in QNM-mode to automatically optimise the scan parameters for each pixel.

Conductive coatings, such as platinum/iridium or boron-doped diamond can be applied to a silicon probe so that the electronic properties of a sample might be studied.[77] With CAFM, a voltage may then be applied between the probe and AFM stage, with the sample closing the circuit between them, as shown in **Figure 3.6**.[88] Thus, regions of the sample that short the circuit will demonstrate a measurable current, enabling synchronous study of topography and conductivity. Additionally, current-voltage measurements, similar to those described in **3.1**, can be made at selected locations on the sample surface. In some cases, probe tips are fabricated wholly from metals or

single-crystal, boron-doped diamond. However, for each material, the mechanics of the interaction between the tip and sample are affected.[89]

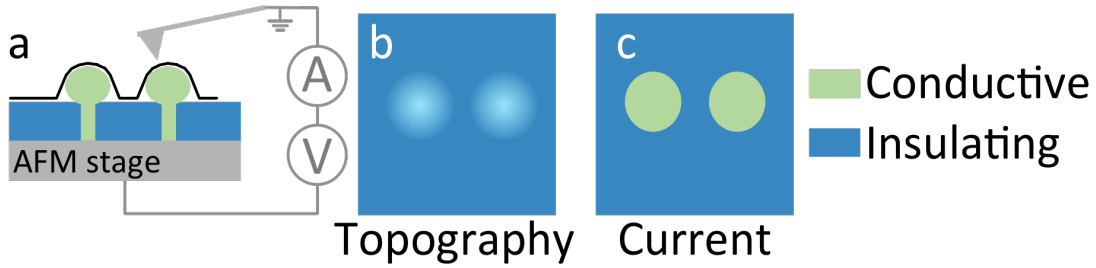

Figure 3.6. CAFM schematic. (**a**) The sample is mounted on the conductive AFM stage, to which the bias, V, is applied while the probe is grounded during scanning. This configuration maximises current sensitivity, measured by the detector, A, on the probe-side of the circuit, by injecting electrons into the sample from the tip. (**b**) In the topography image, the sample surface height is shown. (**c**) The current map demonstrates the correlation between the topography and conductivity, as the features are well-aligned.

Measuring topography with a scanning probe necessarily means that tip convolution occurs, whereby the geometry of the apex is projected onto topographic features. Ideally, the apex should be infinitely sharp, although in practice the best case would be narrower than the smallest feature on the sample.[90] For a hemispherical apex, the resolution limit of the probe is its radius of curvature, typically around 10 nm for a standard silicon tip.[91] Notably, for a conductive probe, the electrical contact area is significantly lower than radius of curvature because the conductivity will be dominated by a single prominent point on the apex.[86] However, the radius of curvature will be larger than that of a standard probe, from 20 nm to over 100 nm, due to the conductive coating.[92]

All probes are damaged during AFM measurements, although the rate of wear is dependent on the tip and sample materials. The metal coating on a CAFM probe tends to wear relatively quickly, whereas diamond coatings are very durable.[93] A tip that is not durable may be blunted such that is becomes unsuitable for measurement, particularly when imaging with a high CAFM voltage or on a hard material. Blunted tips produce inaccuracies in measurements and a poorer understanding of the tip-sample interaction; the true size and shape of surface features are lost, although they should be no larger their convoluted appearance.[94]

Figure 3.7 demonstrates the effect of tip wear and convolution on AFM images. Two topography maps are shown, the second taken after twenty minutes of continuous scanning. Notably, after this time, the detail of the surface is lost and the size of the

smallest features increases. In addition, each bump on the surface has the same shape. These observations suggest that the apex is worn, resulting in tip convolution.

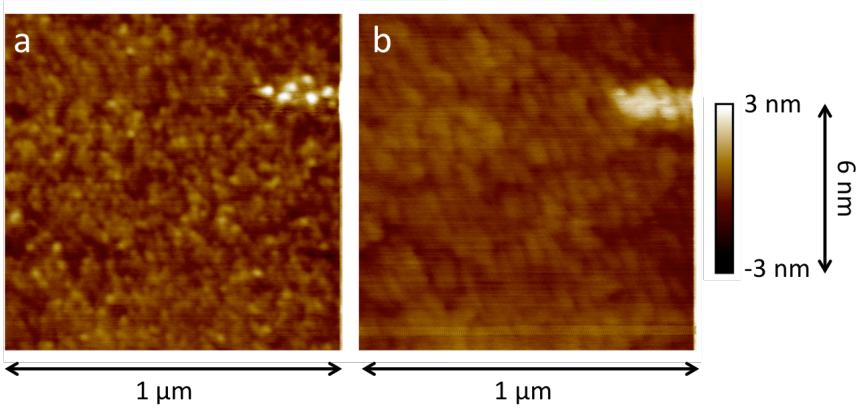

Figure 3.7. AFM images of the surface of a thin film of SiO_x, demonstrating tip artefact. (**a**) Initial image, showing small, grainy features. The smallest bumps in the image are roughly circular, suggesting the tip apex is fresh and imaging at its resolution limit. (**b**) Final image, taken after twenty minutes of continuous scanning on the same area. The tip has degraded and so there is less detail than in **a**. The features show a repeated oblong shape, likely a tip convolution artefact. Note that the height scale may be represented by two distinct values or by a range, as shown. Both formats will be used in this report, according to which is most appropriate for the figure.

A worn AFM probe tip will not have an ideal shape. Rather, the apex will often become oblong, triangular or elliptical. This shape will be projected onto surface features as the tip moves over them, which is particularly evident on very rough surfaces or features with high aspect ratios. In the case of conductive probes, the coating will often wear at a different rate to the silicon below. This can lead to convolutions in both topography and also current mapping; the tip-sample electrical contact properties may be modified by tip wear.

3.3 Scanning electron microscopy

SEM is a technique for imaging a samples using an electron beam.[95] Its principle was first proposed in 1935 and, by 1942, a microscope resembling those currently in use had been developed.[96,97] To acquire images, the electron beam is raster scanned across the sampling area, producing an output electron current with intensity dependent on the properties of the sample and electron beam.[98] Most often, SEM is used to study surfaces, although the detected electrons originate in a volume whose depth depends on the incident beam energy.[98,99]

Electrons incident on a material, referred to as primary electrons, produce certain measurable effects, including secondary electrons, backscattered electrons and x-

rays.[98] SEM is used to induce, detect and map these outputs, each of which describes different sample properties. Backscattered electrons result from elastic interactions with the electric field of atomic nuclei in the sample. Here, incident electrons are deflected back out of the sample with typically more than half their initial energy. Secondary electrons have a relatively low energy and are produced by inelastic interactions between primary or backscattered electrons and the electric field of atoms in the sample or sample chamber. When an electron from a higher energy level fills a vacancy created by secondary electron emission, an x-ray is produced that characterises this electron energy transition. These interactions are shown schematically in **Figure 3.8**.

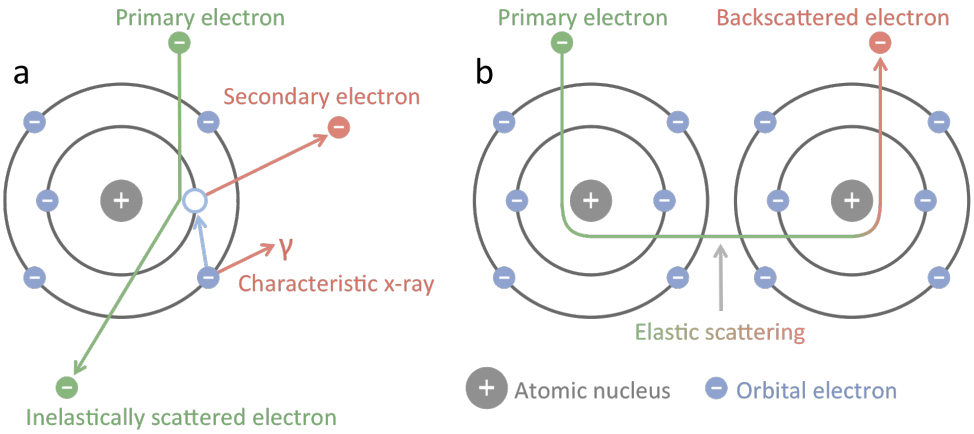

Figure 3.8. Electron interactions with sample atoms.[98] (**a**) Secondary electrons are produced by inelastic interactions between primary electrons and orbital electrons. When an orbital electron of a higher energy level fills the hole left by an emitted secondary electron, a characteristic x-ray is produced. (**b**) Primary electrons that are scattered back out of the sample as a result of elastic interactions with atomic nuclei are known as backscattered electrons.

SEM is generally performed under vacuum in order to maximise the mean free path of the primary and output electrons. The primary electrons are typically generated by field emission from a sharp tungsten filament, as illustrated in **Figure 3.9a**. A potential difference is applied between the filament and an anode under ultra high vacuum, 10^{-10} Torr or below, producing an electric field that is concentrated at the tip of the filament. As such, the work function of the tungsten is reduced and electron emission occurs. In order to accelerate the electrons toward the sample, another electric field is set up between the filament and a second anode.[98]

An SEM instrument is shown schematically in **Figure 3.9**. The electron beam is accelerated from the gun toward the sample. In its path are two lensing systems, the condenser and objective. Together, these try to achieve the desired interaction volume and sampling plane by narrowing the beam and focusing it on the sample. The

interaction volume is determined by the accelerating voltage, the atomic number of the sample and the tilt of the sample stage. Higher voltages increase the interaction volume, whereas higher atomic number nuclei will reduce it. The sample may also be moved closer to the objective lens, decreasing the working distance and so increasing the magnification.[100] In addition, the stage may be rotated and tilted to best image the desired features.

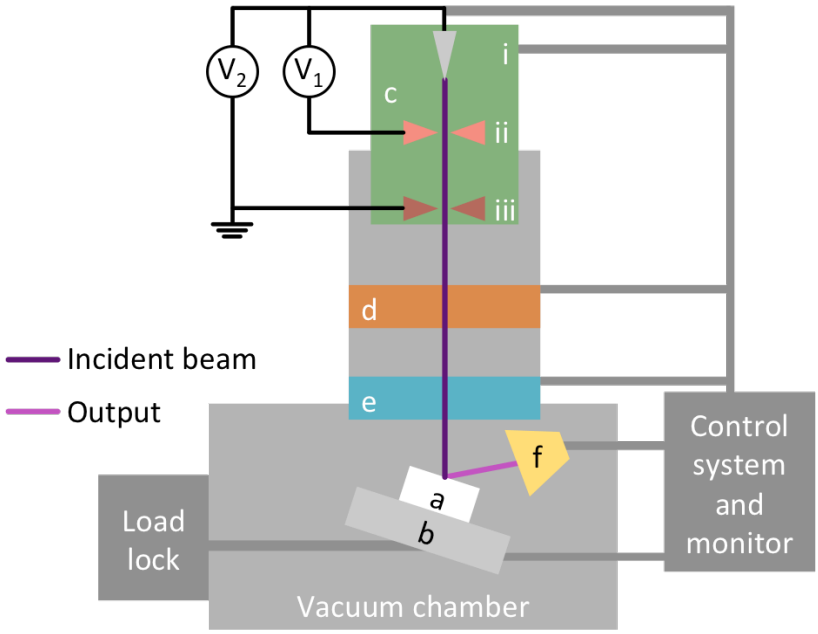

Figure 3.9. Schematic of an SEM.[98] (**a**) The sample is loaded into the vacuum chamber via the load lock. (**b**) The sample stage is used to control the position of the sample relative to the objective lens. The stage may also be used to tilt and rotate the sample (**c**) The electron gun is the source of electrons for illuminating the sample. The potential difference, V_1, between the tungsten filament, **i**, and the first anode, **ii**, induces field emission of electrons from the filament. The potential difference, V_2, between the filament and the second anode, **iii**, accelerates the electrons toward the sample. (**d**) The condenser lensing is used to demagnify the beam, reducing its diameter. (**e**) The objective lensing is also used to demagnify the beam, as well as to focus it on the sample surface. (**f**) The incident electrons produce a variety of outputs for detection. These include secondary electrons, backscattered electrons and x-rays. The control system is used to adjust the microscope parameters and collect data from the detector.

The lenses in SEM instrumentation are electromagnetic, using the magnetic field produced by a current in a copper coil to augment the electron beam.[98] As these systems are imperfect, a number of aberrations must be corrected for in order to acquire high quality images. Spherical aberrations, caused by variations in magnetic force as electrons moves through the field, limit the resolving power of the microscope. Apertures may be used to address this by reducing the beam width. Chromatic

aberrations result from the energy spread of the electron beam, as lower energy electrons will experience a smaller magnetic force in passing the lenses. This is difficult to correct for and is particularly problematic at low acceleration voltages. Astigmatism results from machining imperfection in the lens, causing the beam to have an asymmetric cross-section. A ring of stigmator coils can be placed around the objective lens in order to produce a field that forces the beam to have a more symmetric cross-section.

Where the properties of a sample vary, the intensities of output electrons and x-rays will change and so the variations in the sample will be detected and mapped.[95] Contrast in SEM images is therefore correlated with sample composition and topography. The backscattered electron intensity is dependent on the atomic number of atoms in the sample, thus this signal gives compositional information.[98] Likewise, the x-ray emission spectrum depends on electron transitions and so also provides compositional information. However, SEM is most often used to display topographic information. This is usually shown with the secondary electron signal as it is surface sensitive and depends strongly on the surface morphology.[95]

Figure 3.10 shows a set of secondary electron SEM images demonstrating some typical features. The intensity of inelastically scattered electrons is correlated with the local incidence angle, so variations in topography are clearly shown by contrast variations.[95] Flat surfaces, such as the AFM cantilever in **Figure 3.10ai**, appear relatively dark. The tip on the end of the cantilever appears brighter than its immediate surroundings, as indicated by the blue arrows, despite both being composed of diamond. This is because the pyramidal tip presents steep angles to the incident beam and thus the secondary electron signal is higher here. Similarly, as indicated by the green arrows in **Figure 3.10a** and **b**, feature edges often show bright contrast. This is because secondary electrons more readily escape at edges owing to the increased proximity to the vacuum and thus detection; less material is present to cause perturbations.

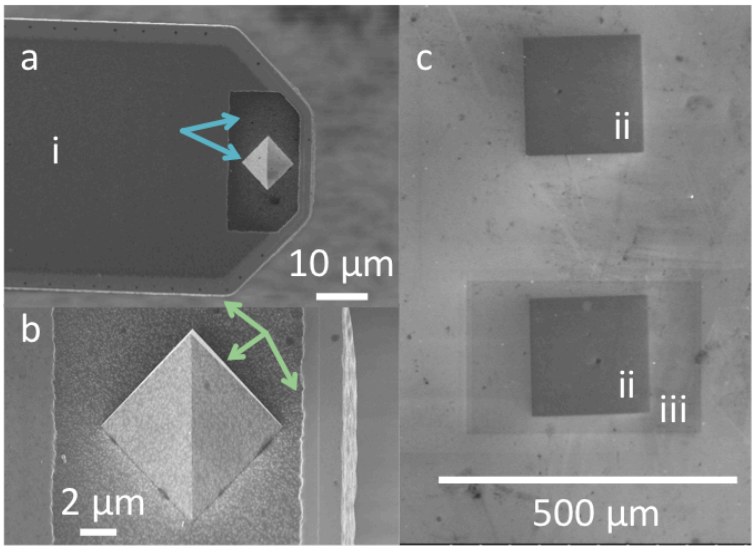

Figure 3.10. Examples of typical SEM image features. (**a**) Single-crystal diamond AFM probe. **i** – nickel cantilever. The blue arrows indicate flat and sloped regions of diamond. The pyramidal tip shows bright contrast, likely because it presents four slanted facets to the incident beam. (**b**) Side-on image of the probe, taken with a sample tilt of 45˚. The green arrows indicate contrast enhancement at feature edges. (**c**) Titanium nitride squares on SiO_x. Although the squares, **ii**, are raised, they are darker than the oxide. This is likely because the oxide is charged under electron illumination, enhancing further scattering. The darkened region, **iii**, indicates a region that was imaged prior to the image shown. Here, the electron beam may have removed some surface contamination, reducing the charging artefact and so brightening the contrast.

Contrast is also produced by variations in sample conductivity.[98] **Figure 3.10c** shows some dark squares of titanium nitride, **ii**, on a brighter SiO_x layer. This difference in contrast occurs because the SiO_z is more insulating than the titanium nitride, thus incident electrons are trapped in the sample, enhancing scattering and increasing the secondary electron signal. This effect is known as a charging artefact. There is also a darker region, **iii**, around the lower square. This square was imaged separately before both were imaged together, meaning that the total electron dose on this region was higher. As a result, insulating contaminants might have been removed from the sample surface. The dark region has therefore likely occurred due to a reduction of the charging artefact in this region.

3.4 X-ray photoelectron spectroscopy

X-ray photoelectron spectroscopy (XPS) is a surface-sensitive technique to study composition, in particular the elements and bonding configurations present in a sampled volume.[101] Photoelectron spectroscopy in general exploits the photoelectric effect, originally discovered by Heinrich Hertz, whereby electromagnetic illumination

liberates electrons from atoms. These are thus referred to as photoelectrons and their kinetic energy depends on the frequency, and thus the energy, of the incident photons.[102] This effect was explained by Albert Einstein for the case of ultraviolet light incident on metals.[103,104]

High-energy, short-wavelength radiation is required to generate photoelectrons because atomic ionisation energies tend to be in the order of a few electronvolts. Ultraviolet photons with wavelengths below 200 nm are often used to study outer-shell valence electrons that participate in chemical bonding. These photons have energies above 6 eV, for example a helium discharge lamp produces 58.43 nm wavelength photons with a corresponding energy of 21.22 eV, suitable for liberating relatively weakly-bound electrons.[105]

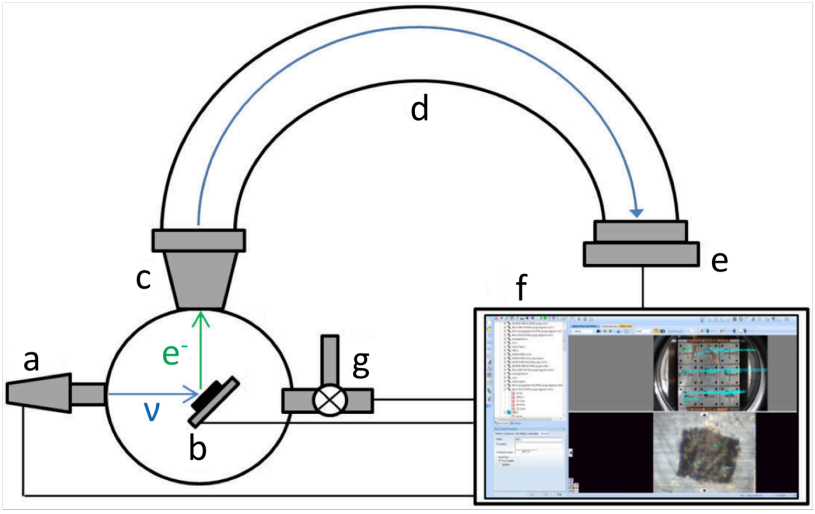

Figure 3.11. XPS instrument schematic.[105,107] An x-ray source, **a**, illuminates the sample in a vacuum chamber, **b,** with photons of frequency v. Photoelectrons, $\mathbf{e^-}$, pass through electronic lensing, **c**, whose voltage is adjusted to select electrons of a particular kinetic energy. These are focussed into the analyser, **d**, and their velocity impeded such that they are able to pass through. The hemispherical analyser is a pair of curved, charged plates with an electrostatic field between them. The fields permit the passage of photoelectrons of a selected energy, known as the pass energy. The electron detector, **e**, measures the photoelectron flux at the specified pass energy. The acquisition system, **f**, controls the experimental parameters and records data. An energy spectrum is created by sweeping the lens voltages over a range of electron energies to measure the variations in flux at the detector. Vacuum pumps, **g**, are controlled and monitored by the acquisition system.

XPS is a form of photoelectron spectroscopy used to expel electrons from the core shell of atoms, where the bond strength is greatest.[106] Measurements are performed in ultra-high vacuum to maximise the photoelectron mean free path and reduce sample

contamination.[101] It is not possible to generate spectra from gases, liquids or solids with a low vapour pressure, as they will be extracted by the vacuum pumping. Hydrogen and helium do not appear in XPS spectra due to their low emission probabilities; hydrogen shares its single electron in bonding and helium does not readily form any solid that may be sampled.[101] An XPS instrument is shown schematically in **Figure 3.11**.

To eject a photoelectron from an atom, the incident photon energy must be at least as great as the ionisation energy of the sample material.[105] This is the energy required to promote an electron from its orbit to the vacuum level, defined as the energy of an electron at rest in a vacuum, at a large distance from any other objects.[108] For core shell electrons, this energy is referred to as the binding energy, E_b. If the photon energy, hv, where h is Planck's constant and v the photon frequency, is greater than E_b, then the photoelectron will have non-zero kinetic energy, E_k. This is because momentum is conserved in the ionisation process.[109] The energetics of this interaction are described by [101]

$$E_k = hv - E_b \qquad (7.2)$$

For spectroscopic measurements, v is known and h is a constant. Hence, E_k may be measured to find E_b. Since the atoms of each element have distinct values of E_b for their core electrons, peaks characterising the elemental composition of the sample will be present in XPS measurements. Note that in **Equation 7.2** additional terms such as the work function of the sample material and the interaction energy of the atom with its neighbours have been incorporated into E_b for a simplified description of the photoemission process.

Although x-rays have a high penetration into matter, photoelectrons have a short inelastic mean free path of up to a few nanometres. This ensures that only those generated close to the surface will escape with sufficient kinetic energy to contribute to the measured spectrum, although the sampling depth depends on the sample material.[110] As electrons are removed by x-ray illumination, localised charging of the sample surface occurs. It is necessary to compensate for this in order to avoid experimental inaccuracies such as binding energy shifts and peak broadening, caused by perturbations of the photoelectrons by the surface charge.[111] An ion gun is typically used to flood the vacuum chamber with electrons, neutralising the surface for improved photoelectron emission. The pass energy of the detector determines the final energy of detected electrons and the energy resolution of the detector.[97] For lower pass energy, the resolution will be increased but the photoelectrons must be

decelerated by a larger amount, lowering the sensitivity due to increased noise in the data as higher-energy electrons scatter from the analyser walls.

A typical survey spectrum from a SiO_x sample is shown in **Figure 3.12**. Survey spectra are low-resolution scans with a large binding energy range, useful for a general indication of the elemental makeup of the sample. Each element present in the sample will produce a characteristic photoelectron peak, where the intensity is proportional to the quantity of that element present. However, each instrument will have a different elemental sensitivity, so care must be taken in analysing elemental ratios and stoichiometries. Relative sensitivity factors may be used to scale the data obtained and correct for the instrumental sensitivity.[112]

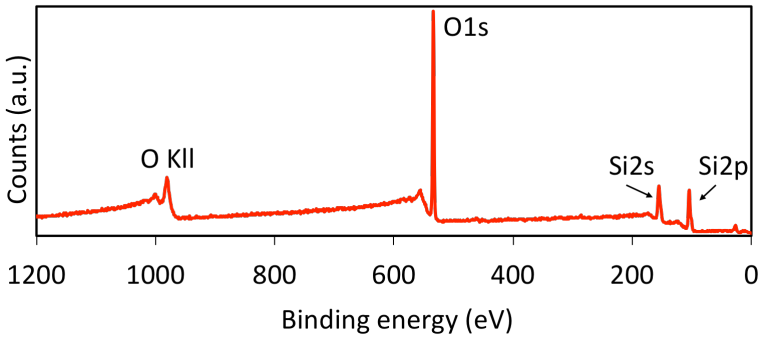

Figure 3.12. Example XPS survey spectrum from a SiO_x surface**.** The x-axis scale is typically reversed as it corresponds to binding energy rather than kinetic energy. The y-axis displays photoelectron counts pet second. Several features and a clear background trend are apparent. The most notable features are the three narrow peaks centred at around 100 eV, 150 eV and 530 eV corresponding to emission from silicon, Si2p and Si2s, and oxygen, O1s, respectively. Other notable features are the step-like feature at 978 eV corresponding to Auger emission. All peaks are imposed on a background that is predominantly produced by inelastic photoelectron scattering and electrons excited by x-ray Bremsstrahlung radiation.

Auger peaks, such as that of oxygen labelled O KLL in **Figure 3.12**, appear at higher binding energies those of photoelectrons. These result from electrons of a higher energy shell filling the hole created by photoemission.[113] In heavier atoms, the energy liberated in this process tends to cause x-ray emission. More generally, an additional electron is ejected from the atom with kinetic energy independent of the initial incident radiation energy.[101]

The background count of an XPS spectrum results from photoelectrons that are scattered inelastically and electrons excited by x-ray Bremsstrahlung radiation [114]. Scattered electrons generally originate far from the surface have a low probability of escaping without a collision, thus their kinetic energy is reduced if they do escape. The

instrument interprets these electrons as having a high binding energy because their kinetic energy is low.[101] Bremsstrahlung-excited electrons are liberated by photons decelerating as they propagate through the sample.[115] These have a high kinetic energy because they originate at the sample surface and so are interpreted as being from low binding energy orbitals.

Although core electrons do not participate in bonding, small shifts occur in the peak positions and widths as a result of neighbouring atoms and bonds. The electronegativity of bound elements will affect the charge distribution across their bond, with the more electronegative atom drawing the valence electron density towards itself.[116] This reduces screening of the nucleus of the less electronegative atom, increasing the measured binding energy of photoelectrons, as they are perturbed by the redistributed charge.[101,105]

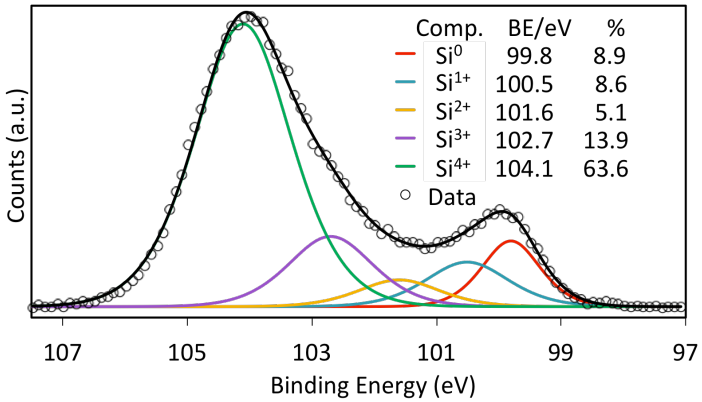

Figure 3.13. High-resolution Si2p XPS spectrum from a SiO_x surface. By fitting an appropriate model to the data, the sample structure may be assessed. The peak shape is determined by the full width at half maximum and is dependent upon the peak element, in this case silicon. The contribution (%) of a sub-peak component (Comp.) with a particular bonding configuration to the full peak indicates the relative presence of that bond. It can be seen here that the spectrum may be divided into five components in order to fit the data.

As a result of the mixture of bonds of a particular element in a sample, the peak for that element will be a convolution of multiple, narrower sub-peaks. Each sub-peak will be shifted in binding energy, depending on the bond it characterises, and have a full width at half maximum determined by the distribution of lengths of that bond.[117] High-resolution scans of small energy ranges are required to assess these small shifts, as shown in **Figure 3.13**.

Elemental spectra must be deconvoluted, whereby a modelled combination of sub-peaks is fitted to the data. It is necessary to have some prior knowledge of the sample composition so parameters for the positions and widths of the sub-peaks may be

reliably designated. The sub-peak ratios provide an insight into which bonds the element is part of. For example, SiO_x XPS spectra are often characterised in terms of five oxidation states of silicon, as shown in **Figure 3.13**. These are Si^0, Si^{1+}, Si^{2+}, Si^{3+} and Si^{4+}. The superscript indicates the degree of oxidation of the silicon, with Si^{4+} a silicon atom bound to four oxygen atoms.[40,106,118,112] The presence of a suboxide phase may be confirmed by the presence of Si^{1+}, Si^{2+} and Si^{3+} peaks, whereas Si^0 indicates elemental silicon. Si^{4+} describes fully oxidised silicon.[119]

XPS instruments are often used to perform depth profile measurements. This is typically achieved by interleaving spectral measurements with ion beam milling of the sample. This scheme produces a data set characterising changes in the sample composition with depth as material is gradually removed by the milling. The effect of ion milling is controversial; older reports consider silicon dioxide stable under milling [120] whereas more recent work suggests crystalline silicon dioxide would amorphise and that oxygen is preferentially removed.[121]

4. Description of samples

4.1 Sample fabrication

The samples I used in this work were metal-insulator-metal RRAM devices; an insulating layer sandwiched between a pair of metallic electrodes. They were fabricated on a 500 µm thick, p-type silicon wafer covered by a 200 nm isolation layer of thermally grown silicon dioxide, as illustrated in **Figure 4.1**. As I did not fabricate the devices, I will present only a brief description of their fabrication and will not detail the development of the specific recipes used.

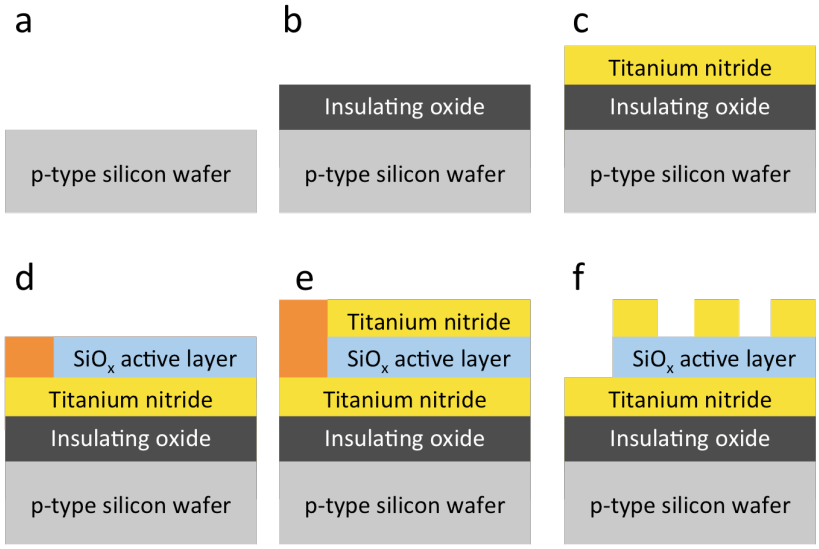

Figure 4.1. Sample fabrication schematic. (**a**) Samples were fabricated on a p-type silicon wafer. (**b**) Firstly, an insulating layer of silicon dioxide was grown. (**c**) Subsequently, the titanium nitride bottom electrode was sputter-deposited. (**d**) The active layer was then sputter-deposited, with an area of bottom electrode masked (orange) to enable electrical probe access. (**e**) The top electrode was sputter-deposited. (**f**) Finally, the titanium nitride top electrode was patterned using photolithography and the mask removed to expose an area of bottom electrode.

The isolating oxide prevented unwanted electrical stress from being applied via the wafer to the devices during measurements. The bottom electrode of the devices was deposited by sputtering 100 nm of titanium nitride from a titanium nitride target to cover the wafer. A section of this layer was kept clear of further deposition in order to allow electrical access to the bottom electrode. Subsequently, the active layer was fabricated by magnetron cosputtering silicon and silicon dioxide in an argon plasma environment to cover the wafer in a 37 nm thick layer of SiO_x. The value of x was unknown, but was determined as part of this work. Finally, the 100 nm thick top electrodes were produced by sputter-depositing titanium nitride and patterning this layer into squares of various sizes using optical lithography.

4.2 Sample preparation

The sample wafer was cleaved into smaller portions for measurements. Each piece contained a number of labelled sets of devices of varying size. The scheme for the layout and group labelling of the devices is shown in **Figure 4.2**. To perform resistance switching, a tungsten needle was used to contact individual top electrodes and apply electrical stress to the volume of the switching layer below that top electrode. Such a scheme constitutes device operation.

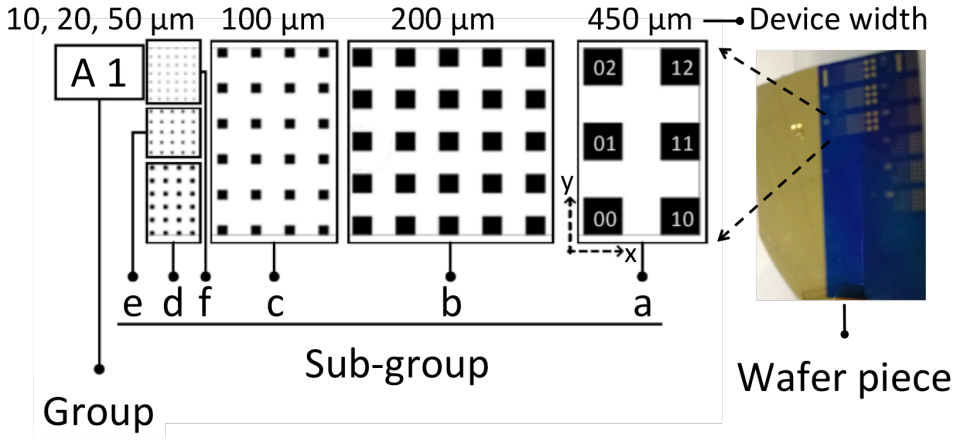

Figure 4.2. Device map and photograph of a piece of sample wafer. In the photograph, blue regions correspond to exposed SiO_x surface and gold-coloured regions the top layer of titanium nitride. Groups of devices were labelled with a letter and number. Sub-groups were pattered into squares of different widths. The wafer contained about forty groups of devices.

Prior to measurements, the samples were cleaned using ultrasonication in organic solvents. For electrical measurements, the tungsten needles were also cleaned. Firstly, de-ionised water was used for fifteen minutes to remove large particulates adhered to the sample and needle surfaces, such as dust and dirt.[122] Acetone was then used for fifteen minutes to remove grease from human contact.[123] Finally, isopropanol was used for fifteen minutes to remove residual acetone and other hydrocarbons, as well as residual dust.[122] The ultrasonic treatment assists the cleaning effect of the solvents by causing cavitation, improving removal and transport of debris from the surface.[124]

Although some SiO_x devices exhibit bipolar operation,[13,60] the devices in this report are unipolar, thus all voltages are positive and applied to the top electrode, with the bottom electrode held at ground. It has previously been shown for these devices that their electrical behaviour is independent of their area.[19,125] This is because the resistance switching mechanism is believed to be filamentary, as discussed in **2.2**. Therefore, I have considered my results to be independent of the device area and thus the electrode size.

5. Instrumentation

I used a Keithley 4200 semiconductor parameter analyser with tungsten needles for electrical measurements. The sample was loaded into a Signatone probe station connected to the analyser and two probes were used to apply biases. One probe was placed in contact with the exposed area of the bottom electrode and another contacted individual device top electrodes. The probing station also comprises an optical microscope. I processed data using MATLAB R2013a [126] and Excel 2011.[127]

I performed AFM and CAFM measurements using Veeco Dimension 3100 and Bruker Icon microscopes. The photodiode signal was set to 0 V in the horizontal and -2 V in the vertical for contact-mode scans, including CAFM, and 0 V in both axes for tapping-mode scans. The contact mode and CAFM setpoint was set between -1.9 V and -1.7 V, unless otherwise stated. The tapping mode setpoint was between 160 mV and 260 mV. QNM-mode measurement parameters were automated, the system optimising them at each pixel. Silicon probes were used for contact, tapping and QNM-mode scans. Conductive measurements were performed in contact mode using platinum/iridium-coated silicon probes. Conductance tomography measurements were made using boron-doped, diamond-coated probes and single-crystal, boron-doped diamond probes. I processed data using NanoScope Analysis v1.5,[128] MATLAB R2013a [126] and 3D Slicer.[129,130]

I used a Thermo Scientific K-Alpha with a monochromated aluminium source at 10^{-8} Torr for XPS measurements. The x-ray energy was 1486.68 eV and an ion flood gun was used for charge compensation during all measurements. The pass energy was set to 200 eV for survey spectra and 20 eV for elemental spectral. The survey spectra were averaged from three measurements, each with a sampling time of 10 ms at 1 eV binding energy resolution. Carbon spectra were extracted from the survey spectra. Elemental spectra were averaged from twenty scans, each with a sampling time of 100 ms at 0.1 eV binding energy resolution. The exception to this was oxygen, which was averaged from ten measurements with 50 ms sampling time due to the high instrumental sensitivity to oxygen. Ion milling was performed with a 2 nA argon beam for five seconds per depth level at either 2 keV or 3 keV. Thermo Advantage software was used to collect data.[95,96] I used CasaXPS v2.3.16 to process the data, using a least squares fit to minimise the residual signal between the fitted components and the data, in line with the chosen fitting parameters.[131,132] A Shirley background was subtracted from all spectra to account for Bremsstrahlung photoelectrons.[133,134]

SEM images were taken at 10^{-7} Torr with a Gemini microscope mounted in a Zeiss Crossbeam instrument. All SEM images herein display the secondary electron signal.

6. Behaviour observed at the device surface

6.1 Chapter introduction

As discussed in chapter **2.5**, RRAM devices generally demonstrate structural transformations as a result of operation. Some changes, such as those observed with transmission electron microscopy, occur within the active layer.[61,135,136] Other changes are more readily observed on outer surfaces using techniques such as optical microscopy and AFM.[29,40,50]

I began this project operating devices normally and observing the most pronounced changes. Techniques that require a relatively simple setup, such as optical microscopy and AFM, offer a quick means of qualifying resistance switching phenomena. Thus, an appropriate foundation for developing an understanding of device behaviour and the underlying phenomena is to look at readily observed effects. Data gathered this might then be used to inform further study.

In this chapter I will introduce measurements made at the device scale, using optical microscopy, AFM, CAFM and SEM to investigate the structural deformation observed at the surfaces of devices following operation. In addition, I will present XPS results indicating that the electrode composition is not consistent with depth and may undergo further changes as a result of electrical stress.

6.2 Normal switching operation

Typical switching characteristics for a single 100 µm by 100 µm device are shown in **Figure 6.1**. Electroforming requires a voltage just over 7 V, with around 2 V and 3 V required for reset and set operations, respectively. The set voltage is lower than that of electroforming because resetting does not return the oxide to its initial state, indicating the conductive changes are not fully reversed. The reset data demonstrates that the current reaches around 5 mA, exceeding the compliance of 3 mA used to prevent hard breakdown during forming and setting. As discussed in chapter **2.3**, this current is believed to promote sufficient Joule heating to induce an increase in resistance.[13,137]

As shown in **Figure 6.1b**, switching was repeated for five cycles without failure and gave a consistent on/off current ratio of two orders of magnitude when reading the state with 0.5 V. Notably, attempting to operate the device with sweeps of opposite polarity was less successful; devices could be electroformed but not cycled. I did not investigate this thoroughly although I speculate that it might be related to the asymmetry of the devices; the switching layer covers the bottom electrode, which in turn covers the entire sample wafer. This means that the significantly larger bottom

electrode may be a better electron source that the top electrode, making operation preferential for a positive top electrode bias. In addition, if it is assumed that oxygen movement governs device behaviour, then the large switching layer/bottom electrode interface might hinder the oxygen migration mechanism when a positive bias is applied to the bottom electrode.

It should be mentioned that the focus of this project was to better understand the switching mechanism rather than to study or optimise the electrical parameters. Thus, a detailed report on the polarity dependence, cyclability and lifetime of devices will not be presented. However, the devices have been cycled up to 150 times with voltage sweeps and thousands of times with voltage pulses.[19] My work focuses on changes resulting from voltage sweeps using a positive top electrode polarity, although there will be some discussion negative polarity and pulsed operation, particularly in chapters **7** and **8**. The sweeps used in this work varied from a few to tens of seconds for an entire cycle, unless otherwise stated. Notably, this is longer than the duration of pulses sometimes used to quantify device performance, which can have durations in the microsecond or nanosecond range.[60] However, it has previously been shown that the sweep rate does not effect the switching behaviour of similar SiO_x-based devices.[13]

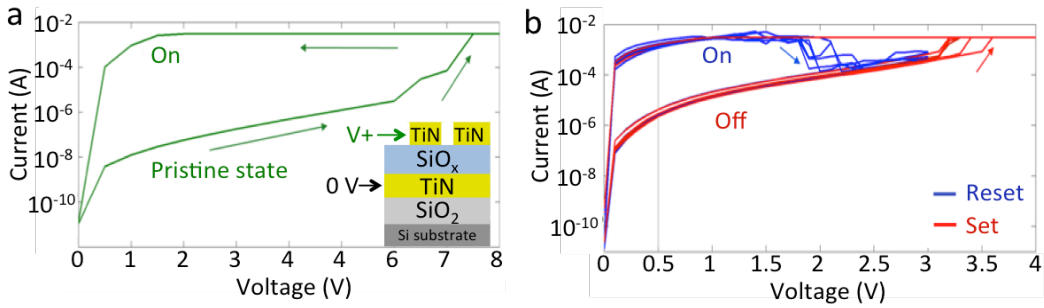

Figure 6.1. Current-voltage curves for normal device operation. (**a**) A voltage sweep of the high resistance, pristine device yields an electroforming current jump around 7.5 V. This state is retained as the voltage returns to 0 V. Inset – device schematic. Note the switch to low resistance is not sharp due to the low sampling resolution, 0.5 V, between points. (**b**) Five on/off cycles are shown. In the on state, the reset sweep without current compliance induces a switch to the off state around 2 V. In the off state, the set sweep produces a switch to the on state around 3 V. The on/off current ratio for reading at 0.5 V is around two orders of magnitude, as indicated by the grey line. 3 mA current compliance was used for form and set operations.

6.3 Optical observations of top electrode distortions

As expected for normal RRAM behaviour, such as in **Figure 6.1**, I readily observed structural changes on devices as a result of electrical operation. **Figure 6.2a** and **b** demonstrate the appearance of a darkened region on a 100 µm by 100 µm device,

following cycling until it became stuck in the high resistance state. **Figure 6.2c** and **d** demonstrate two further observations of discoloured, stained top electrodes. Again, in each case, the device had stopped working properly when the stain was observed. The size and shape of the discolouration is variable, yet the colour is similarly dark in each instance and the features appear rough.

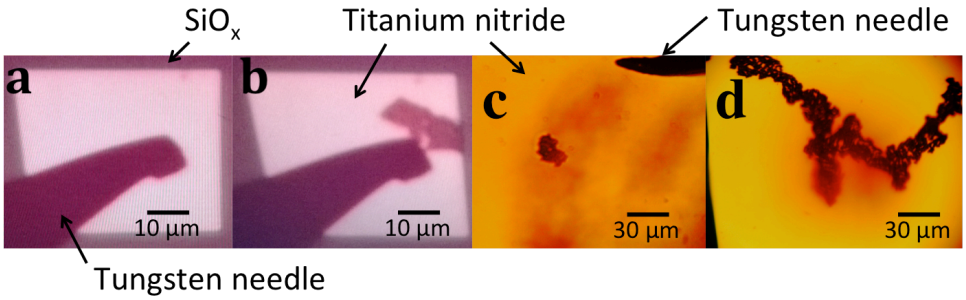

Figure 6.2. Optical microscope images demonstrating the appearance of discolouration on the top electrode. (**a**) The pristine electrode appears clear of staining. (**b**) Following operation, a large, dark region appears. (**c**) A stain of a similar diameter to the probe used to contact the device. Here, the probe has been moved away from the discoloured region, which was found at the point of contact. (**d**) A stain demonstrating a snaking form.

Resistance switching behaviour appeared not to be possible after stain formation, thus I was interested in any correlation between staining and device lifetime. The top electrode stains shown so far were found after the device had failed; devices were not observed until all electrical operation had finished. However, subsequent observations of top electrodes during cycling demonstrated that the stains were dynamic. They grew by discrete areas from small regions as more cycles were made, sometimes starting at the probe contact point and sometimes growing towards it.

Figure 6.3 shows the progression of a stain on a 50 µm by 50 µm device. Over the course of 146 cycles, a discoloured region appeared on the upper edge of the electrode and expanded until it covered the contact point of the probe. Interestingly, the stain did not grow continuously with time or cycles. Rather, every few to tens of cycles a new area a few to tens of micrometres in diameter would develop, adjoined to the rest of the stain, progressing towards the probe. Such behaviour might track the path of the current through the device, indicating perhaps the greatest degree of oxygen migration or heating, leading to structural deformation.

The device shown in **Figure 6.3** was no longer switchable after 146 cycles, having become stuck in the high resistance state. However, moving the probe away from the stain revealed that the contact point was an island-like region surrounded by discolouration, as shown in **Figure 6.3f**. Contacting the electrode away from the

stained area, it was possible to resume switching until the stain once again encompassed the probe contact. Thus, the loss of functionality might have resulted from the probe losing electrical contact with the electrode, having become isolated from the rest of the titanium nitride by the stain.

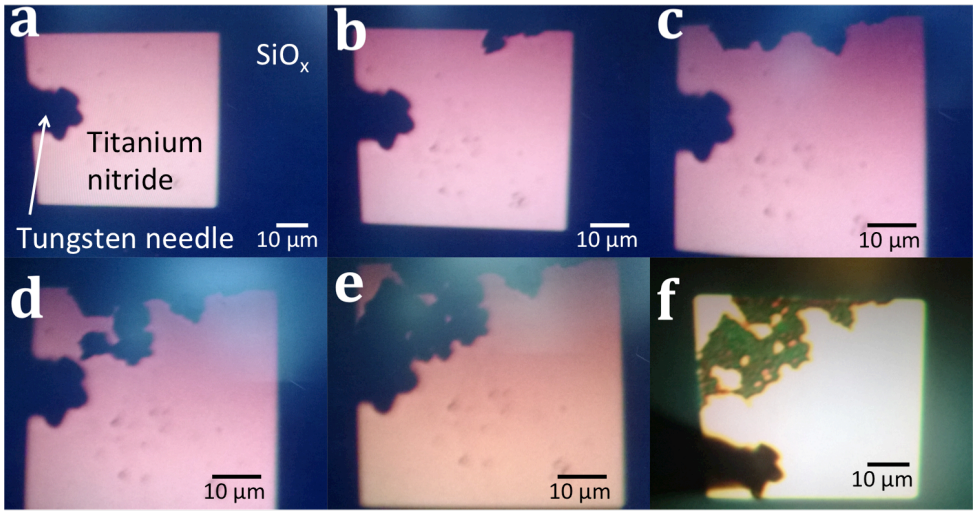

Figure 6.3. Optical images showing a stain develop across an electrode, eventually reaching the contact point of the probe. (**a**) Initially, the electrode is clear of the dark spots that indicate staining. The dark area on the left hand side of the device is the tungsten probe. (**b**) to (**e**) The stain increases in area while the device is cycled, until it is no longer operable. (**f**) With the probe moved away from the stain, a bright area of unaffected top electrode can be seen at the point of contact, suggesting the probe had become electrically isolated from the device.

It was not always possible to recover device functionality by moving the probe to contact a new region of titanium nitride. In general, when the discoloured region seemed to contain the contact point of the probe, the device would be stuck in the high resistance state. However, when the discolouration did not reach the probe, if the device became stuck it would be in the low resistance state. This suggested that the stains were insulating. It is worth noting that this behaviour might be addressed or overcome with the use of crossbar devices, which are addressed via contact pads at a relatively large distance from the device area. Thus it might be possible to continue to electrically stress a stained device without needing to reposition the probe.

6.4 Atomic force microscopy of top electrode stains

Considering that stains seemed to isolate probes from devices, it was necessary to better understand their structural and electronic nature. I therefore performed optical microscopy, AFM and CAFM to study their topography and conductivity, as shown in **Figure 6.4** for a device that had become stuck in the low resistance state.

Figure 6.4a shows an AFM image of a pristine device, the surface of which appears smooth. **Figure 6.4b** shows an AFM image of a stained device, shown optically in **Figure 6.4c**. The optically dark, stained regions appear to correlate with the tallest features in the AFM image. These features are up to 200 nm above the surface of the top electrode, and appear rough. The electrode is 100 nm thick, thus some of the deformations are taller than the electrode is thick.

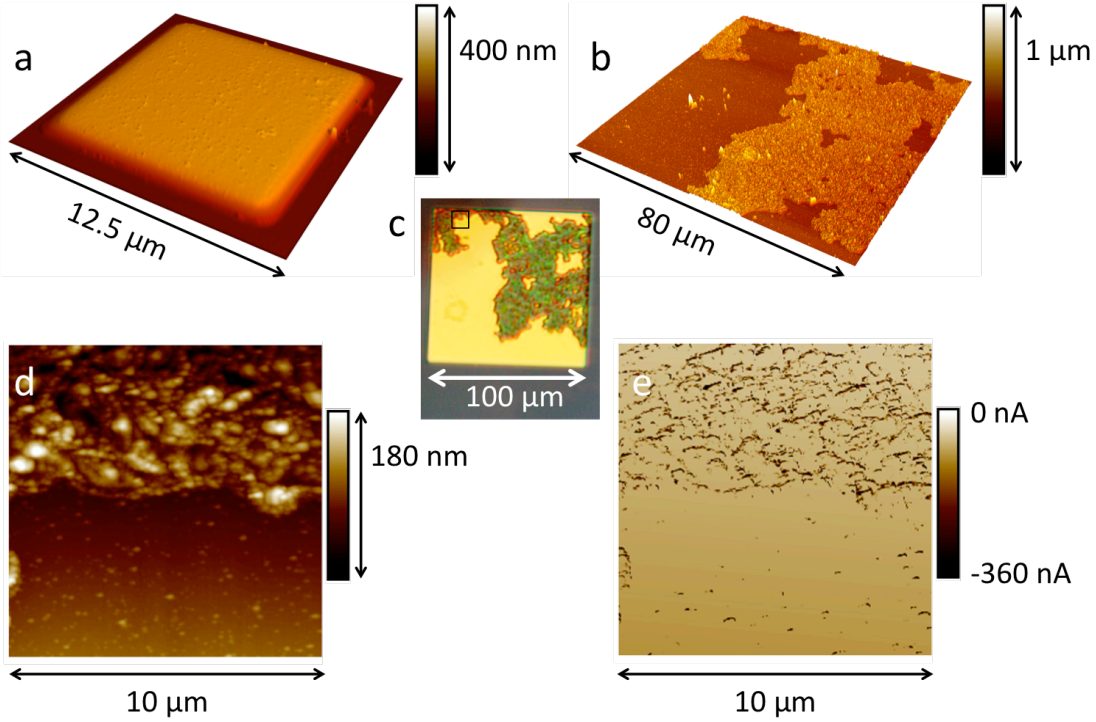

Figure 6.4. Various images of a stain on a device as a result of cycling. (**a**) Tapping-mode AFM topography image of a pristine top electrode. (**b**) QNM-mode topography AFM image of the top electrode stain shown in **c**. The stain is composed of bubble-like protrusions taller than the thickness of the top electrode. (**c**) Optical microscope image of the stain. (**d**) and (**e**) CAFM topography and current maps, respectively, showing the region of the stain indicated by the black box in **c**. The scan was performed with a sample bias of -1.15 V. The smoother area on the bottom half of the images corresponds to unstained titanium nitride. Note the tip convolution artefact in **d;** the individual bubbles appear triangular. The CAFM current indicates the electrode contains conductive regions, which appear dark, though most of the sampling area is not conductive. Interestingly, little current is measured on the unstained electrode, despite the device being in a low resistance state.

In general, the root-mean-square (RMS) roughness is used in discussing AFM roughness data.[138] Sometimes, the roughness average is used, though is has a different physical meaning. RMS roughness is the standard deviation of the height, whereas roughness average is the mean height in a sampled area.[139] The RMS

value is more susceptible to very high or low features. Only RMS roughness will be discussed in this work, given its common usage in relation to AFM.

The pristine electrode in **Figure 6.4a** has a roughness of 2.54 nm. This increases to 34.5 nm for the stained electrode in **Figure 6.4b**, although the neighbouring regions, those that are not dark in **Figure 6.4c**, are of a comparable area to the stain. Evaluating only the apparently rough, dark area gives a roughness of 28.3 nm, whereas the smoother regions give 7.6 nm. It therefore appears that the stained areas are parts of the electrode that have become deformed and are much rougher. In addition, the unstained areas are slightly rougher than the pristine surface. Electrical stress thus appears to roughen intermediate areas along with stained regions.

In the AFM images of **Figure 6.4b** and **d**, the stains seem to be composed of many distinct, bubble-like protrusions with diameters from tens to hundreds of nanometres. However, the triangular form of the individual bubbles may not be accurate. It is unlikely that the features are all of the same shape; rather they may reflect the geometry of the scanning tip as a result of convolution. Tips with a triangular pyramid apex, such as those used in this work, often have a triangular footprint on tall features or if they are blunted, as discussed in chapter **3.2**.**Figure 6.4e** shows a conductivity map of the region of top electrode indicated by the black box in **Figure 6.4c**. Most of the sampled area is insulating, but there are many dark, narrow features indicating conductivity. The correlation between conductivity and topography is difficult to determine, thus three-dimensional plots are more informative.

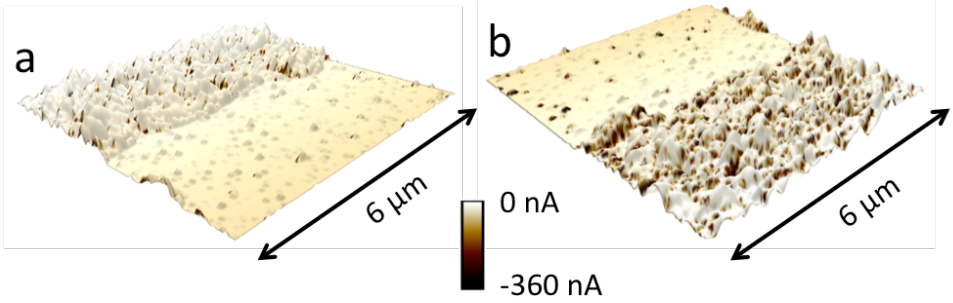

Figure 6.5. Three-dimensional plots of topography with current overlaid from the data in **Figure 6.4**. (**a**) and (**b**) show the same data with 180˚ rotation between them. The dark, conductive regions are sparse and small compared to the size of the bubble-like features and the stained region. As is particularly evident in **b**, the conductive areas are generally between the bubbles; some conductive areas in **a** are hidden by the bubble topography.

Figure 6.5a shows a three-dimensional plot of the topography data in **Figure 6.4d** with the current data from **Figure 6.4d** overlaid. Some small, dark areas are present, indicating conductivity. However, these are quite sparsely located. In contrast, rotating

the plot by 180˚, as in **Figure 6.5b**, reveals a denser arrangement of conductive regions. In both cases it appears that the tops of the bubble-like features are not conductive with the lower, intermediate areas showing conductivity.

The rotation between the plots in **Figure 6.5a** and **b** demonstrates a pattern of conductive regions. In general, they are in the same place with respect to the bubble-like features on which they are situated. Specifically, in **Figure 6.5b**, the lower edges of the bubbles are conductive, so in **Figure 6.5a**, these regions are hidden by the bubble topography. Given the regularity of this feature, it is reasonable to suppose it is an artefact rather than a true representation of the conductivity distribution. This may be a result of CAFM edge convolution, as discussed in chapter **3.2**. Following this, it is interesting that most of the less rough region, corresponding to unstained titanium nitride, shows no current aside from some small spots. It may be that the CAFM probe setpoint was insufficient for good electrical contact with the sample on flat regions. On rougher areas, such as the bubbles, the apex topology might be such that the electrical contact area is increased or the probe moves closer to the surface.

I found CAFM measurements were generally prone to transient current artefacts, likely due to random telegraph noise from trapping and detrapping defects on the sample and probe,[140] combined with apex geometry, contact and Coulombic forces. As a result, the location of the measured current did not always persist between scans, sometimes appearing in areas that were not previously conductive or disappearing from those that were. In order to determine the reliability of the conductive mapping in **Figure 6.4** and **Figure 6.5**, I scanned a stained region of the top electrode multiple times at different voltages, as shown in **Figure 6.6**.

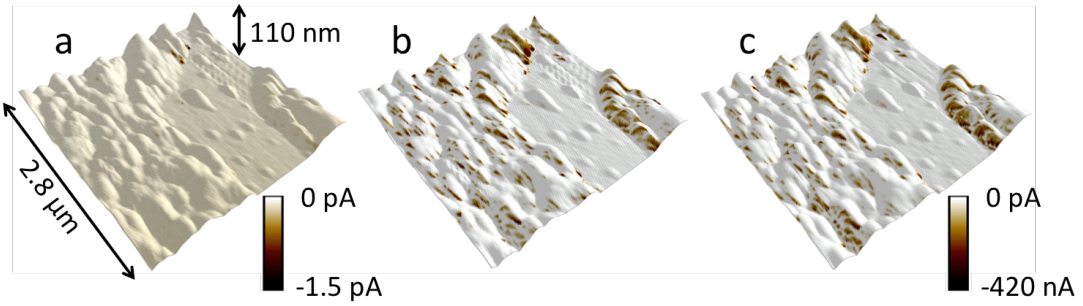

Figure 6.6. Three-dimensional CAFM topography with current overlaid, demonstrating repeatable conductivity mapping. (**a**) Control scan without bias applied; some small, few-picoamp spots of current are present, like due to random telegraph noise. (**b**) and (**c**) were taken on the same area as **a**, ten minutes apart, with a sample bias of -1.15 V. The conductive areas are consistent between the scans, indicating that their locations are likely to be reliable and non-artefactual. Note that the colour scale is the same for **b** and **c** so is only shown once.

Figure 6.6a shows a stained region scanned without a sample bias as a control measurement. Although no bias was applied, some small patches of conductivity with very low currents, around 1 pA, are present; these are likely noise. In addition, most of the image is slightly a darker contrast than 0 pA, indicating a few-femtoamp current over the entire region. Again, this is likely noise or an instrumental offset. **Figure 6.6b** and **c** show the same area scanned with a sample bias of -1.15 V, ten minutes apart. In both images the same locations demonstrate conductivity with currents around five orders of magnitude greater than those detected with 0 V applied. Thus, the conductive areas persist over time and their presence requires an applied bias. This suggests the data is a reliable indicator of the distribution of conductive regions, though the issue of tip convolution and poor electrical contact on flat areas may still influence the mapping.

6.5 Scanning electron microscopy of stained devices

To better understand the structure of the bubble features, I worked with some colleagues to acquire SEM images from stained titanium nitride electrodes. **Figure 6.7** shows a set of six devices of which three have been operated, resulting in staining. The stained regions are bright compared to the rest of the electrode, which may result from the stain height relative to the surrounding material. However, the electrodes are raised features on the switching layer yet they have a darker contrast. This is likely because the switching layer is more insulating than the electrodes and so charges under the electron beam, becoming brighter in the image. Therefore, it is not clear whether the contrast of the stains is due to height or charging.

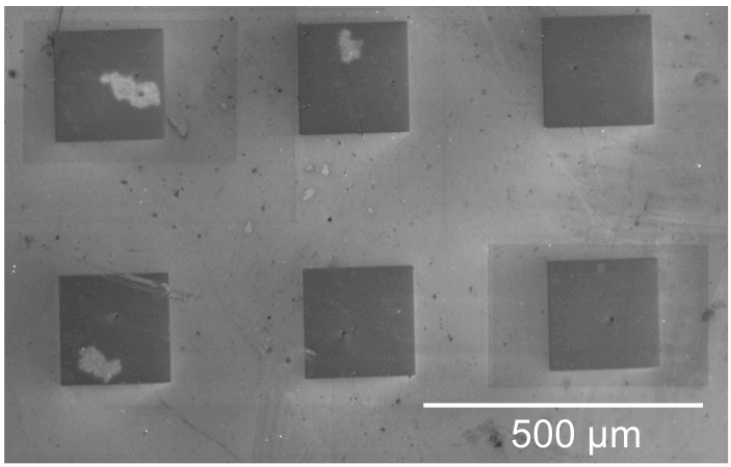

Figure 6.7. SEM image of stained top electrodes, taken with a 20 keV beam. The devices show dark contrast against their surroundings, though three have been used and are stained, evidenced by patches of bright contrast. The electrodes likely appear darkest because they are the most conductive features present, so less charging artefact occurs. There are also some square artefacts around some devices, probably resulting from removal of surface material under previous electron illumination, reducing charging, as discussed in chapter **3.3**.

Figure 6.8a shows an SEM image from a stained region of a device. Note that this is not one shown in **Figure 6.7**. The contrast between the stain and the unstained top electrode, as well as the contrast variations across the stain, is clear. Brighter and darker areas are present, relative to the unstained electrode. As with my previous AFM and CAFM results, the stain appears to be composed of many bubble-like features.

Figure 6.8b shows a close-up SEM image of the stain shown in **Figure 6.8a**. The brightest parts of the image correspond to the edges of the bubbles, evidenced by the adjacency of narrow, dark contrast regions. This is reasonable, given that feature edges generally produce bright SEM contrast as secondary electrons more readily escape from these regions, increasing the detected signal.[98] Conversely, depressions produce dark contrast due to a decrease in the signal. The bright edges may indicate the tallest or sharpest parts of each bubble and the dark regions are suggestive of depressions between bubbles.

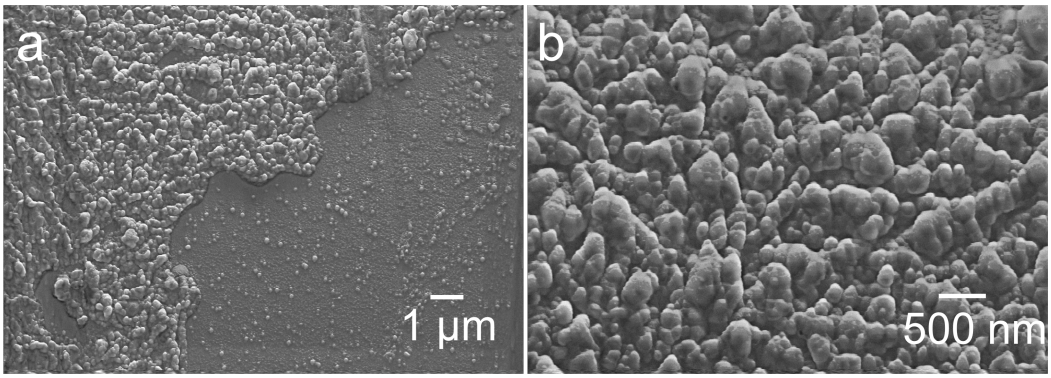

Figure 6.8. SEM images of a top electrode stain, taken with a 5 keV beam. (**a**) A region of top electrode showing stained and unstained areas. The stain is generally brighter than the unstained area, though there are some darker regions. (**b**) Close-up of the stained region in **a**. The stain appears to be composed of many bubble-like features. For each bubble, there is a bright region that seems to correspond with the upper edge, closest to the top of the image. Thus, the geometry of the individual bubbles appears to be correlated with one another.

Interestingly, the positioning of the bright contrast relative to the shape of each bubble appears to be correlated. Specifically, the upper edges of the bubbles, closest to the top of the image shown in **Figure 6.8b**, are brightest. Another way of describing this observation is to note that thin, dark contrast regions are adjacent to, and generally above, the bright contrast. To discern whether this observation was due to the orientation of the sample relative to the detector, the sample was rotated by 45˚ and 180˚ to check whether the correlation of the contrast was maintained. To also check that the correlation was not a charging artefact, retaining bright contrast between

measurements, the time taken between images was at least five minutes so that any accumulated charge would have time to dissipate.

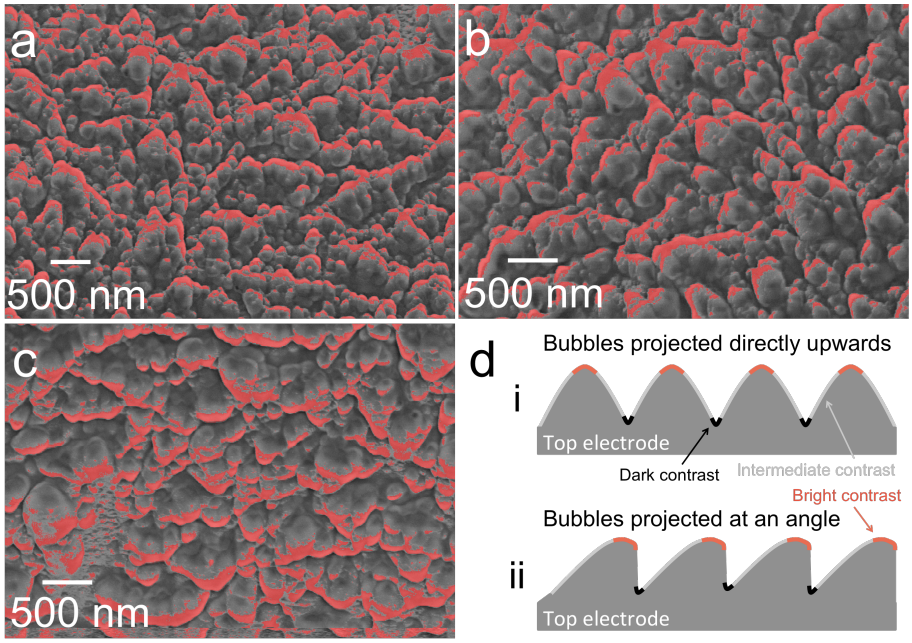

Figure 6.9. Positioning of bubble edges with sample rotation. The red areas correspond to the bright contrast shown in **Figure 6.8**. Adjacent are thin regions of dark contrast. Otherwise, the colouring may be considered intermediate contrast. (**a**) Masked SEM image of a stained region, without rotation. The bubble edges point upwards. (**b**) Masked SEM image of a stained region with an anticlockwise sample rotation of 45˚. The bubble edges point left, anticlockwise relative to those in **a**. (**c**) Masked SEM image of a stained region with a sample rotation of 180˚. The bubble edges point downwards, opposite to those in **a**. The changes in edge orientation suggest this feature is not an artefact and that the bubble structures have a correlated asymmetry. Note the scan area changed between rotations. Thus, **a**, **b** and **c** show different regions although they are all contained within the stained region shown in **Figure 6.8a**. (**d**) Schematic of possible origin of correlated asymmetry. For symmetric bubbles, as in **i**, viewed from above, the bright contrast at the top of each bubble would be separated from dark contrast between bubbles by a region of intermediate contrast. This would be the case regardless of the sample rotation. For asymmetrically correlated bubbles, as in **ii**, viewed from above, bright contrast would be adjacent to dark contrast. This would be true regardless of sample rotation, but the orientation relative to intermediate contrast on the bubble slopes would rotate with the sample.

Figure 6.9a, **b**, and **c** show a stained region at three angles of sample rotation. In each case, the image has been masked such that the brightest areas appear red. To visually distinguish these areas clearly, the mask threshold was set at 47% of the maximum

intensity. The greyscale images have values ranging from 0, black, to 255, white, meaning the masking threshold value was 120. Note that this value was chosen as a qualitative means of highlighting edges and is not intended to quantify any characteristic of the sample. Adjacent to the red regions are thin, dark areas. Otherwise, the contrast may be considered intermediate, as discussed in the caption of **Figure 6.9**. For each angle, it is clear that the bubble edges, defined by the relative positions of the masked area and the adjacent thin, dark contrast regions, rotate with the sample angle.

The consistency of the edge positioning in **Figure 6.9a**, **b**, and **c** suggests the bubbles have some asymmetry in their geometry, yet their geometries are correlated with one another. This is illustrated schematically in **Figure 6.9d**. When viewed from above, symmetric bubbles would show a separation between the bright and dark contrast indicating the peaks and troughs of the bubbles, respectively. This would not change with the sample rotation. Conversely, the adjacent bright and dark contrast of asymmetric bubble edges would rotate with the sample rotation, relative to the intermediate contrast of the bubble slopes.

Given the possible asymmetry of bubble geometry, it is reasonable to suppose that each bubble has a steep side and a gradual side, producing dark and bright SEM contrast, respectively. This may be considered beside my previous CAFM findings. In **Figure 6.5** conductive regions were located on the same edge of each individual bubble, though this may have been artefactual. However, the correlated asymmetry shown in the SEM images does not appear to be an artefact. I now suggest that the CAFM feature is not an artefact. Rather, the bubbles are more conductive on one side than the other. The conductive regions in **Figure 6.5** are generally long and narrow. This form is more in line with the shape of the dark contrast in the SEM images of **Figure 6.9**. Therefore, it seems that the steep regions between bubbles are more conductive than the gentler slopes opposite them. It should be noted that there is some uncertainty in this claim. Although the bubble asymmetry might not be an SEM or CAFM imaging artefact, it may be caused by sample tilt. If the sample was not mounted completely flat, or if its thickness varied linearly from one side to the other, then a consistent tilt angle would be introduced into all features. Such a feature would persist with the scan angle, as shown in **Figure 6.9**, despite being artefactual.

Given that the surface of the top electrode was certainly deformed, it is reasonable to postulate that some change of phase took place in or on the titanium nitride. In particular, a separation of more and less conductive regions corresponding to more and less conductive titanium nitride phases. However, measurements of material chemistry, are necessary to investigate this supposition.

6.6 X-ray photoelectron spectroscopy of stained devices

To better understand the structural chemistry of the devices, I used XPS as it offers high surface sensitivity and detailed information on the bonding present in a sample.[101] I sampled both pristine and stained electrodes as well as the switching layer in order to probe both materials that compose the devices.

In order to sample only the stained portion of the electrode, the elliptical illumination spot was set to a long axis of 30 µm and short axis of 15 µm, smaller than the 200 µm by 200 µm device area in order to minimise the possibility of sampling off-electrode material. When measuring the SiO_x in an electrode-free area, an ellipse with a 300 µm long axis and 150 µm was used as the available area was large enough that there was little risk of sampling unwanted material. **Figure 6.10a** shows an XPS survey spectrum from pristine and stained top electrodes, along with a spectrum from the SiO_x layer, taken from a region away from any top electrodes.

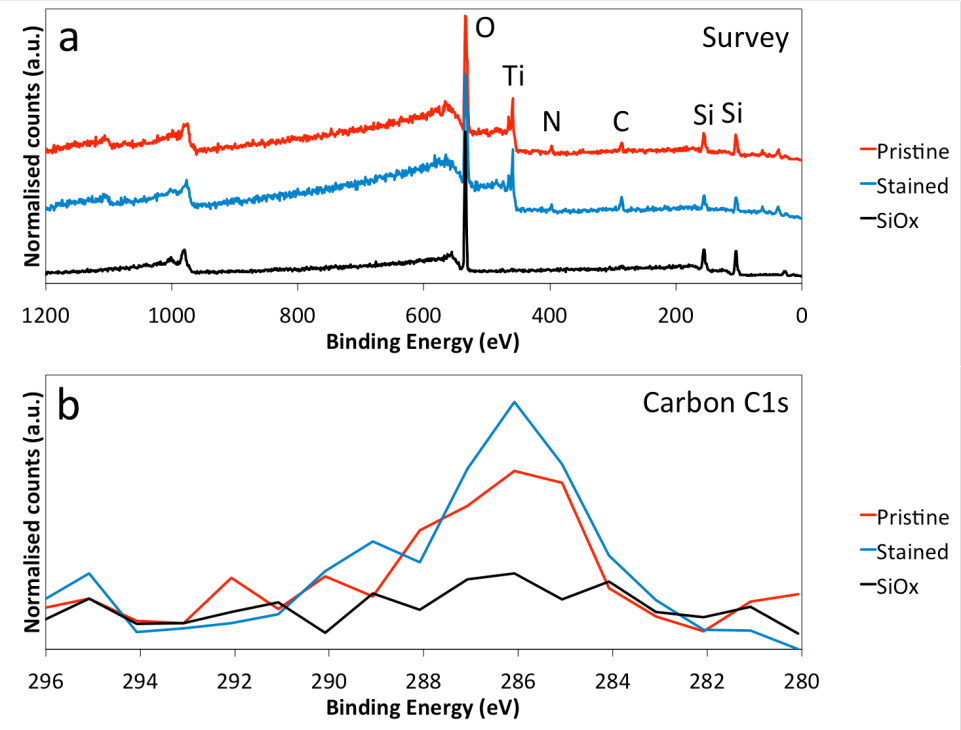

Figure 6.10. XPS of pristine and stained devices and of the switching layer. The spectra have been normalised to their maximum counts. (**a**) Survey spectra, offset for display clarity, demonstrating the presence of oxygen, titanium, nitrogen, carbon and silicon on the devices and silicon and oxygen on the switching layer. (**b**) C1s spectrum, demonstrating that up to 2 eV of shifting may have occurred between stained and pristine devices. Notably, no carbon is present on the SiO_x.

The SiO_x spectrum, shown in **Figure 6.10a,** displays evidence of silicon and oxygen, as expected. The spectra from pristine and stained devices are similar to one another, with no significant differences noticeable. Silicon, carbon, titanium, nitrogen and

oxygen appear in on each device. The titanium and nitrogen signals are small in comparison to those of oxygen, silicon and carbon.

Silicon and oxygen signals are unexpected for the measurements on devices as the sampling area was smaller than the device area. Given the surface sensitivity of XPS, it is unlikely that these signals originate in the active layer below the electrodes. Additionally, the electrode surface is not likely to be contaminated to such a large extent by silicon or silicon oxide, particularly as the wafer was cleaned before measurements were made. It is therefore most likely that there was an instrumental error in the alignment of the sampling area and the incident x-rays. The sampling area is selected using an optical camera whereas the x-ray illumination spot alignment is operated separately. It is therefore possible that the x-ray beam was not properly aligned on the top electrode, sampling the SiO_x along with the titanium nitride.

Sampling misalignment may explain the relatively weak titanium and nitrogen signals from the electrode in comparison to those of silicon and oxygen from the SiO_x. However, another source of oxygen may be the electrode. Sputter-deposited titanium nitride can contain oxygen as a result of native oxidation.[141] After a few minutes in air, a titanium nitride film 100 nm to 150 nm thick may contain around 5% titanium dioxide. This is principally in the first few Angstroms of the surface. Additionally, the bulk will be oxidised by oxygen diffusion at grain boundaries. These aspects may account for some of the oxygen signal shown in **Figure 6.10a**.

The survey spectrum provides information on the sample composition, yet it is difficult to discern small changes in the peaks for each element present. Higher binding energy resolution measurements are required for inspection and must be calibrated to account for shifting in the spectra between samples. Here, the carbon C1s peak was used for calibration of inorganic species because carbon is not of analytical interest and is generally present on surfaces.

Carbon is present in the pristine and stained device spectra of **Figure 6.10a** likely due to surface contamination from storage under ambient conditions, alongside residues from cleaning with acetone and IPA. However, the SiO_x spectrum does not show any carbon, despite being cleaned and stored in air before measurements were made. It is possible that exposing the sample to a 10^{-8} Torr vacuum removed any carbon-containing contaminants that were present.

As shown in **Figure 6.10b**, the C1s spectra from the devices are not identical. However, the maximum value is located at 286.08 eV in both cases. Although the standard C1s binding energy is 284 eV, corresponding to sp^2 carbon. Common organic compounds such as ketones and alcohols can have binding energies up to around 287 eV and are more likely to be found on the sample surface than low-oxygen

materials such as graphene or graphite.[142,143] The binding energy resolution is 1 eV, therefore the true peaks may be somewhere between 285.08 eV and 287.08 eV, at an energy that was not sampled. Although it is possible that little or no instrumental shifting occurred between measurements, this range of possible peak values means there may be up to a 2 eV shift between spectra.

The SiO_x C1s spectrum in **Figure 6.10b** contains no carbon, meaning the binding energy scale cannot be calibrated as the devices were. Considering this, I assumed a similar shift magnitude might be present between the SiO_x and device measurements. This may be an overestimate, however. It is also possible that no shifting occurred and the peak maximum at 286.08 eV for both device samples is accurate. It is strange that no carbon appeared in the SiO_x spectrum, even following cleaning in organic solvents. This may simply indicate a more effective cleaning of the switching layer than the devices, or possibly that the titanium nitride is contaminated to some extent with carbon, at least at its surface. This may have occurred during fabrication.

To understand the extent to which the signal from the active layer contributed to the measurement of the top electrode, the silicon and oxygen spectra must be studied. **Figure 6.11a** and **b** present XPS spectra of the binding energy ranges corresponding to silicon Si2p and oxygen O1s, respectively. **Figure 6.11a** shows that the shape of the Si2p spectrum is similar for all samples. Given that the switching layer was fabricated as a silicon suboxide, SiO_x, a literature search reveals that the two prominent peaks likely correspond to Si^0, elemental silicon, at around 99.5 eV and Si^{4+}, a configuration characteristic of stoichiometric silicon dioxide, around 104.5 eV.[120] The single O1s peak at around 533.5 eV in **Figure 6.11b** indicates that the SiO_x may be similar to silicon dioxide at the surface.[112]

Figure 6.11a demonstrates that there is a small depression between 102 eV and 103.5 eV in the Si2p spectrum from the SiO_x relative to those of the devices. Alternatively, this difference may be due to a shift of the large peak to higher binding energy. However, characteristic titanium silicide peaks occur around 99 eV and 103 eV.[144] It is therefore possible that this difference, along with the peak around 99.5 eV, results from titanium-silicon bonding.

Titanium-silicon bonding may be present in the stained device, should silicon enter the electrode during switching. However, the spectra from both devices are similar in this region and such bonding should not be present at the surface of a pristine top electrode. Therefore it is likely that instrumental binding energy shifts between measurements, as discussed above, are responsible for this difference. In addition, there does not appear to be any difference in the peak at around 99.5 eV between the titanium nitride and SiO_x spectra. Given that no titanium was detected in the SiO_x, as

shown in **Figure 6.14a**, it is unlikely that this peak corresponds to titanium silicide bonding configurations.

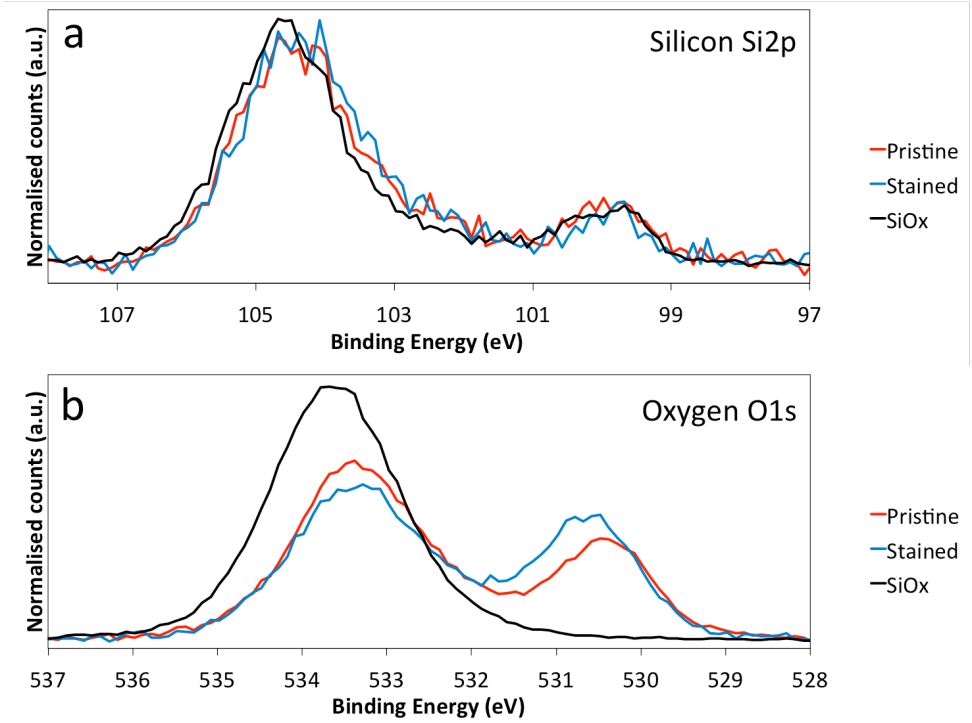

Figure 6.11. (**a**) Silicon Si2p and (**b**) oxygen O1s spectra from pristine and stained devices and SiO_x. The spectra have been normalised to the total counts for each sample for display clarity. The device spectra appear very similar, but there is around 0.5 eV of shift to higher binding energy of the switching layer spectrum relative to those of the devices.

The small Si2p shift between the devices and SiO_x of the Si^{4+} peak around 104.5 eV in **Figure 6.11a** may be due to surface charging and the focus of the x-ray beam. During XPS measurements, the surface is necessarily positively charged by the depletion of electrons, ejected as photoelectrons.[145] As mentioned in **5**, an ion beam was used to compensate for this, but charging may still occur for insulating materials such as silicon dioxide.[146] When sampling the device, although some x-rays would be incident on the SiO_x, the beam focus would be on electrode surface, around 100 nm above. When sampling the switching layer directly, the x-ray focus would be on SiO_x surface. Therefore, the incident x-ray flux on the SiO_x would be greater when sampling the switching layer compared to sampling the device.

With a greater x-ray flux on the switching layer, relatively more photoelectrons would be generated for the same area than when the instrumental focus was on the top electrode. The switching layer would therefore be charged to a greater extent, causing more photoelectron perturbation and a relatively greater peak shift to higher binding energy. However, this does not account for the lack of a shift in the peak at 99.5 eV. It

may be that this peak, as it is of a relatively low intensity, represents deeper material than the silicon dioxide-like outermost part of the surface, represented by the larger peak at 104.5 eV. As such, the 99.5 eV peak would show less charging as it describes oxygen-free silicon and is thus more conductive.

The oxygen spectra in **Figure 6.11b** show some shifting; notably the maximum of the peak around 533.5 eV appears be around 0.5 eV higher for the SiO_x than the devices. There is also a difference around 530.5 eV. Both spectra taken from the top electrode exhibit a small additional peak here, whereas the SiO_x sample does not. Given that the measurement from the top electrode seems to contain a contribution from the switching layer, it may be assumed that the large oxygen peak centred around 533.5 eV is correlated with silicon-oxygen bonding, which is present in all three samples. Thus, the smaller peak at around 530.5 eV likely characterises the state of oxygen at the surface of the top electrode. The peak position is in line with the reported position of peaks corresponding to titanium-oxygen bonding.[147,148] Therefore, the shifting in the peak around 533.5 eV may be due to differences in the surface focus, as with the Si2p spectra in **Figure 6.11a**. Additionally, these observations indicate that the surface of the electrode might be titanium oxynitride rather than titanium nitride.

There is a difference between the pristine and stained devices of **Figure 6.11b** in the magnitude of the 530.5 eV peak. The stained device shows a greater maximum intensity and a small shift to higher binding energy. However, the spectra have been normalised to the total counts for each element, so differences in peak intensities may not be accurately presented. Data must be processed and deconvoluted to study small differences in the spectra, specifically relative intensities and sub-peak positions.

Given the SiO_x O1s spectrum is symmetric about its maximum, it may be modelled with a single component. Though this may be a convolution of smaller sub-peaks corresponding to different bonds, here this is an unnecessary complication; for the purposes of modelling the full SiO_x O1s spectrum, it is reasonable to consider all the possible components as a single peak. This peak was fitted with a Voigt profile, as is typical of XPS data. [149,150] The Voigt lineshape, *V*, is the product of Gaussian, *G*, and Lorentizan, *L*, functions, given by

$$G(x{:}E,F,m) = \exp\left[-4\ln 2\left(1-\frac{m}{100}\right)\left(\frac{x-E}{F}\right)^2\right] \qquad (6.1)$$

$$L(x{:}E,F,m) = \left[1+4\left(\frac{m}{100}\right)\left(\frac{x-E}{F}\right)^2\right]^{-1} \qquad (6.2)$$

$$V(x{:}E,F,m) = G(x{:}E,F,m)L(x{:}E,F,m) \qquad (6.3)$$

where *x* are the binding energy values, *E* the binding energy value for the peak maximum, *F* the peak full width at half maximum and *m* a mixing factor. *m* was set to

0.65, giving a Gaussian:Lorentzian ratio of 7:13, and the full width at half maximum was confined to 1.8 eV. The particular ratio was chosen because it best matched the lineshape of the peak data, as shown in **Figure 6.12a**. The Gaussian component accounts for the behaviour of the instrument, for example the response to the sample and the x-ray beam profile. The Lorentzian contribution represents the photoelectrons, corresponding to the uncertainty in their energy and energy broadening over time.[149,151] Given this complexity and only requiring that the SiO_x O1s spectrum be modelled for use in processing the titanium nitride O1s spectra, the chosen ratio is appropriate.

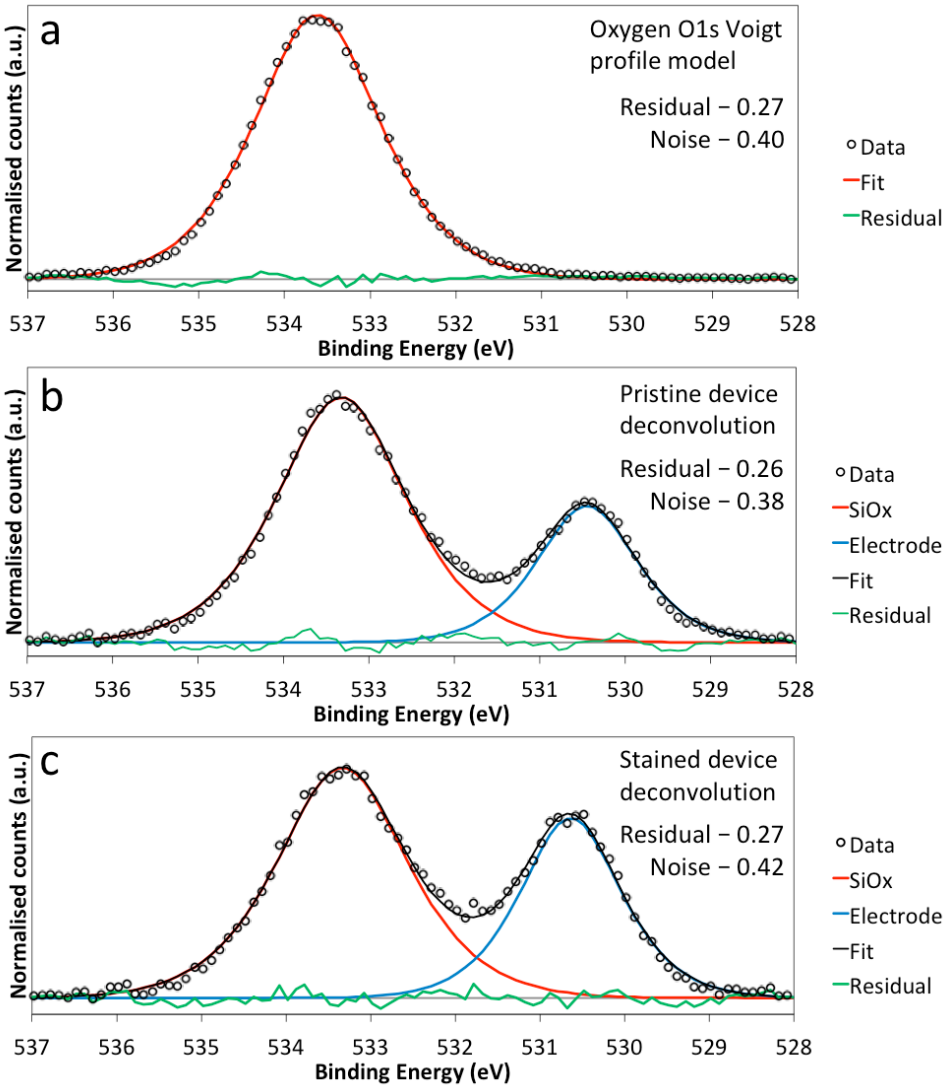

Figure 6.12. Deconvolution of O1s spectra, with normalised standard deviation values for noise and residual indicating the quality of the fit. (**a**) Fitting of Voigt profile to the SiO_x sample data. (**b**) and (**c**) application of the Voigt profile from **a** to the pristine and stained device spectra, respectively. The Voigt model was scaled, shifted and duplicated while the width was retained in order to best fit the data. The small residual signals indicate that the model is a good fit for the experimental data.

To perform a deconvolution of the data, the model peak was applied to the spectra from the devices. Assuming the shift in the O1s peak around 533.5 eV between the devices and the SiO_x is due to surface focus, it is reasonably accounted for by adjusting the position and magnitude of the model to best fit the device peaks. However, the width was confined to within 0.05 eV of the original value in order to maintain the lineshape. For each sample, the fitted peak was then duplicated and the duplicate shifted to around 530.5 eV to model the smaller peak. Again, the magnitude and position were optimised while the width was confined.

A least-squares fit was run multiple times in CasaXPS to adjust the peak positions, widths and magnitudes according to the confinement parameters such that the residual between the data and the fit was minimised.[131] The quality of the fit was determined by comparing the standard deviation of the normalised residual to standard deviation of a normalised portion of the spectrum away from any peaks. In this way, the residual was compared to the noise in the data; the fit was accepted if the residual was of a similar magnitude to the noise. The resulting fitted peaks and residuals, distributed about zero, are shown in **Figure 6.12**. Note the residuals are to the same scale as the fit and data, showing the true difference. When assessing the fit quality, the maximum residual and noise values were used to calculate their normalised standard deviation.

Following fitting of the Voigt profile model to the experimental data, the O1s spectra were scaled by the ratio between the total titanium counts in each sample. Thus, the O1s counts were adjusted such that the same relative quantity of titanium was measured in each sample. The peak at 530.5 eV may then be compared between the pristine and stained devices. To best inspect this peak, the silicon-oxygen bonding peak around 533.5 eV was subtracted from the scaled data, as shown in **Figure 6.13a**.

Figure 6.13a demonstrates that the difference between the O1s peak at around 530.5 eV is less pronounced than that shown in **Figure 6.11b**. Without scaling, the maximum peak intensity appeared to increase for the stained device. However, the scaled data indicates that the maximum intensity is slightly higher for the pristine device. The total counts for the stained device is 3% lower than that of the pristine device, suggesting that the surface of the top electrode becomes reduced, losing oxygen as a result of electrical operation or staining. Additionally, there is a shift of around 0.25 eV to higher binding energy of this peak for the stained device, as was also apparent in **Figure 6.11b**.

The spectra in **Figure 6.13a** appear asymmetric about their maxima, with a knee around 532 eV. Thus it is reasonable to perform an additional deconvolution of the O1s spectra, addressing only the data following subtraction of the silicon-oxygen bonding signal. The binding energy range from around 529 eV to 532 eV corresponds to a

number of titanium-oxygen bonding configurations.[152] In particular, Ti^{2+} and Ti^{3+} are found around 530.1 eV and 530.7 eV, respectively. Given these binding energies are within the width of the peaks centred around 530.5 eV in **Figure 6.13a**, two Voigt profiles with the same separation, 0.6 eV, were used to fit the data.

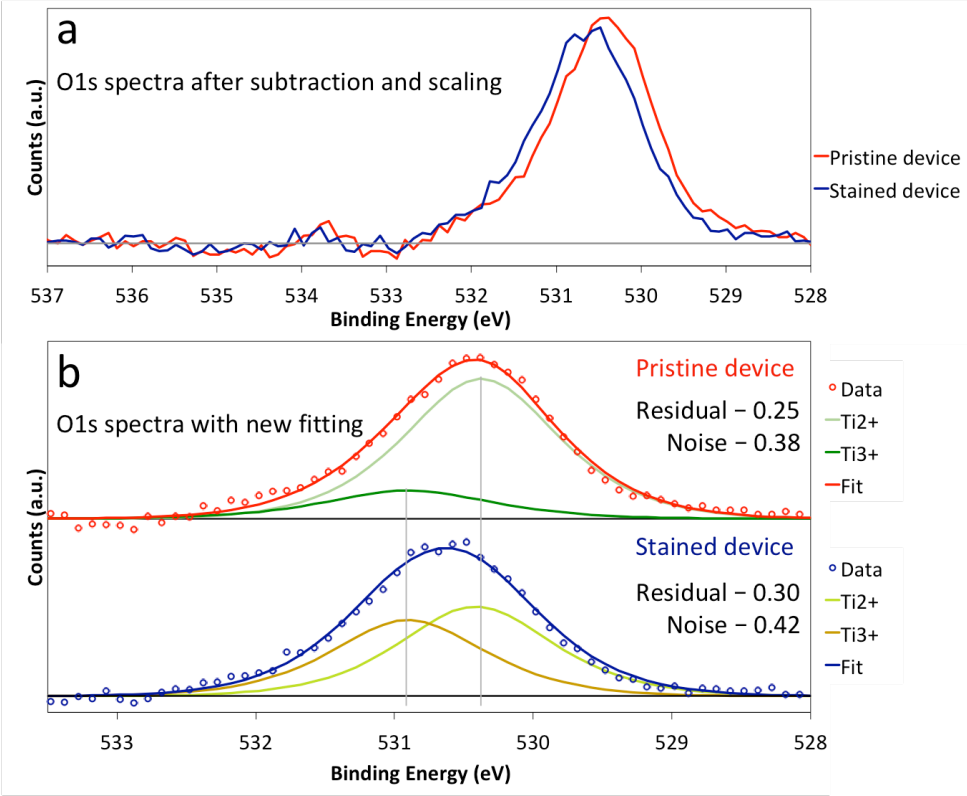

Figure 6.13. O1s spectra following subtraction of the silicon-oxygen bonding peak and scaling relative to the total titanium counts in each samples. (**a**) Both devices exhibit a single peak around 530.5 eV, shifted around 0.25 eV to higher binding energy, with a lower maximum intensity, for the stained device. The total counts for the stained device sample are 3% lower than the pristine sample. (**b**) Second deconvolution of the data, demonstrating two components, Ti^{2+} and Ti^{3+}. The stained device shows an increase in Ti^{3+} relative to Ti^{2+}. Note the residuals are not shown, although the values for the normalised residual and noise standard deviations are given, indicating the quality of the fits.

The fitted peaks are shown in **Figure 6.13b**. The same Voigt profile shape used for the silicon-oxygen bonding was used for the titanium-oxygen bonding, with the width reduced to 1.35 eV ± 0.05 eV to better allow two peaks to fit the data. The width was decreased to account for the reduced range of bond lengths present in Ti^{2+} and Ti^{3+} configurations relative to all the possible silicon-oxygen bond lengths modelled with the wider profile, as discussed in chapter **3.4**. The position of the each sub-peak was held constant between samples and the area varied to fit the data. The maxima are around 0.2 eV higher in binding energy than the positions of Ti^{2+} and Ti^{3+} reported in the

literature. This shift is small and may be accounted for by differences in the sample and instrumentation to those used in the literature. Assuming that the fitted peaks do correspond to Ti^{2+} and Ti^{3+}, the data in **Figure 6.13b** indicates the Ti^{2+} component decreases and the Ti^{3+} component increases. This suggests the electrode has oxidised, which is contrary to the above indication that it is reduced, losing oxygen. Thus, the titanium and nitrogen spectra must be studied in order to determine whether either of these compositional variations is a valid result.

The XPS spectra of titanium and nitrogen for the devices are shown in **Figure 6.14**, alongside the spectra of oxidised titanium nitride from ref [153]. These spectra in **Figure 6.14a** and **c** have been normalised to the same relative titanium counts between measurements. The titanium Ti2p spectra demonstrate three clear peaks, around 455 eV, 459 eV and 465 eV. Titanium nitride is generally characterised by two peaks, at around 455 eV and 462 eV,[153,154,155] although there does not seem to be a peak at 462 eV in the data despite the presence of one at 455 eV. However, there does appear to be a peak at around 461 eV, indicated by an asymmetry on the higher binding energy side of the large peak at 459 eV. The peaks at 459 eV and 465 eV are likely to correspond to titanium-oxygen bonding, possibly in oxidised titanium nitride. As also indicated by the O1s spectra in **Figure 6.12c**, this suggests that the surface of the electrode is titanium oxynitride rather than titanium nitride. This is reasonable, given that the samples were exposed to air, as discussed above, and may account for the discrepancy between the expected and observed peaks at 462 eV and 461 eV.

The titanium spectra shown in **Figure 6.14a** appear to show a small shift for the stained device of around 0.25 eV to higher binding energy of the peak centred around 459 eV, the position of which corresponds to oxidised titanium nitride.[153] This is similar to the shifts observed in **Figure 6.11** and is within the inter-sample shift range. However, for a titanium oxynitride sample, $TiN_{1-x}O_x$, the higher the binding energy of this peak, the closer to 1 the value of x would be. Thus, if the shift is real then it implies that the stained sample is oxidised in comparison to the pristine sample.

Figure 6.14c shows the Nitrogen N1s spectrum characterising the nitrogen at the surface of the electrode. These spectra have been normalised to the same relative titanium signal. The main peak is at 397 eV, corresponding to nitrogen in titanium nitride.[147,156] There may also be a small feature around 400 eV corresponding to oxidised nitrogen.[157] As with the Ti2p spectra in **Figure 6.14a**, there may be a small shift of around 0.25 eV to higher binding energy for the stained sample. Again, this might indicate the surface of the top electrode is oxidised.

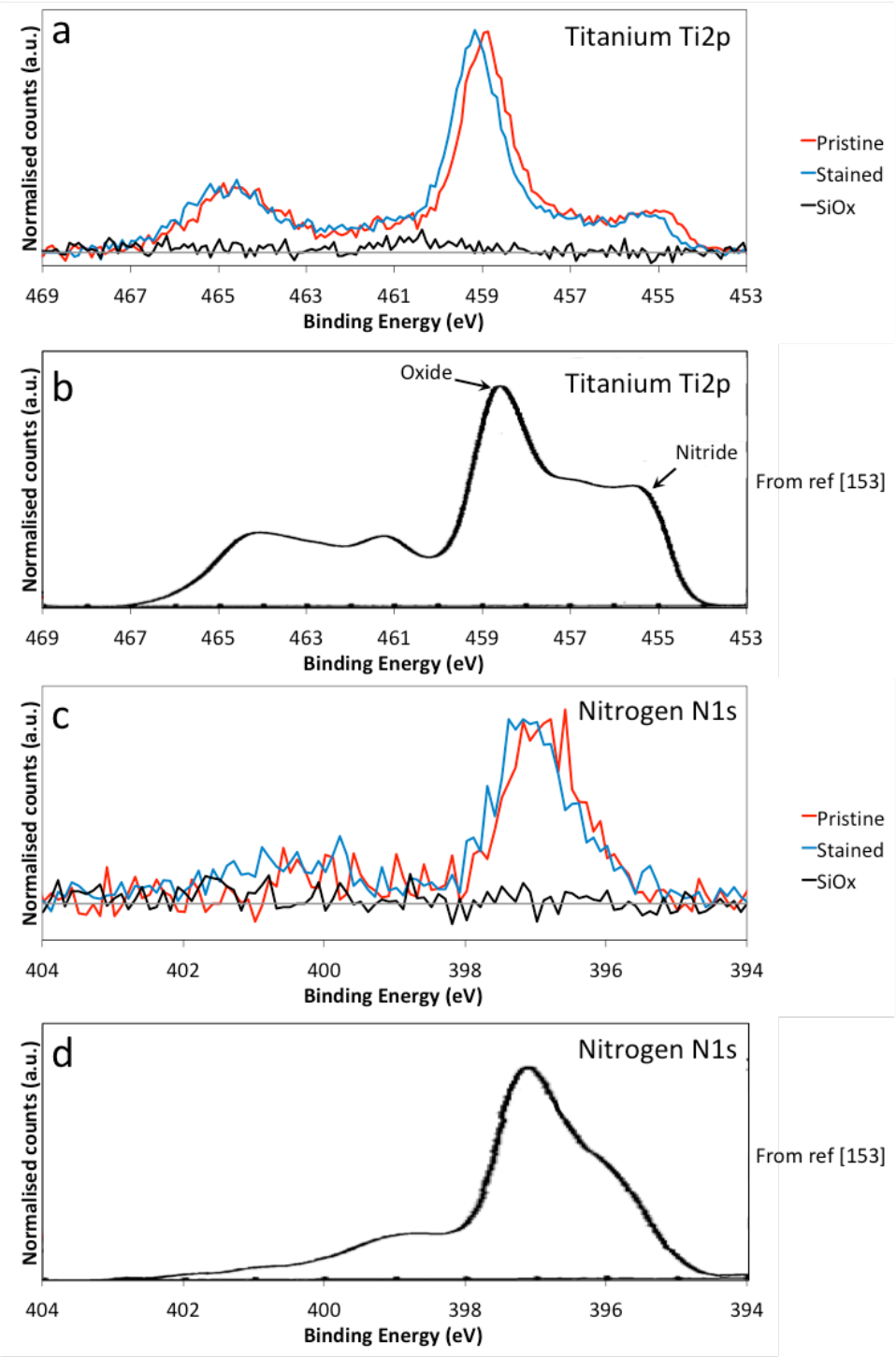

Figure 6.14. Ti2p and N1s XPS spectra from the surface of the pristine and stained electrodes, normalised to reflect the same relative titanium signal in each sample. Oxidised titanium nitride Ti2p and N1s spectra from ref [153] are shown for comparison, demonstrating a good agreement of the data with the literature. (**a**) Ti2p spectra, demonstrating little difference between the two samples. There appears to be a shift of around 0.25 eV to higher binding energy for the stained device. (**b**) Ti2p spectrum from ref [153], showing a similar shape to **a**. (**c**) N1s spectra, also demonstrating little difference between the sampled aside from a shift of around 0.25 eV. (**d**) N1s spectrum from ref [153], showing a similar shape to **c**.

The observations on the titanium and nitrogen signals may be considered along with those from the oxygen spectra. All the peak shifts for the stained electrode are to higher binding energies, indicating oxidation of the surface. However, this is contradicted by the measured decrease in oxygen. This discrepancy may be a result of the surface morphology of the titanium nitride. As discussed in chapter **6.4**, this surface is roughened as a result of electrical operation, which might effect the XPS measurement. This is illustrated schematically in **Figure 6.15**.

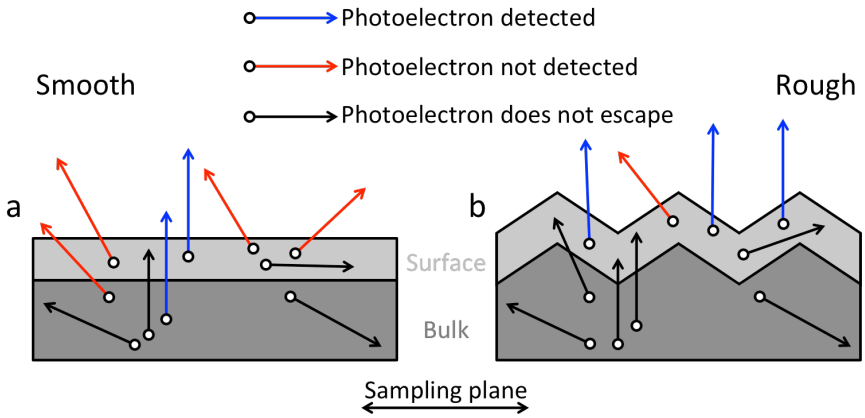

Figure 6.15. Schematic illustration of the effect of surface roughening on photoelectron detection. (**a**) For a flat surface, only photoelectrons escaping normal to the sampling plane are detected. These may include those originating in the surface and in the upper part of the bulk, depending on the photoelectron mean free path in the material. Photoelectrons with other trajectories are either not detected or do not escape the sample. (**b**) For a rough sample, photoelectrons that would have previously had a steep escape angle may be detected as they are now travelling normal to the sampling plane. In contrast, some of those that previously would have been travelling normal to the sampling plane are now emitted and at angle and are not detected. Additionally, some photoelectrons originating in the upper part of the bulk or lower part of the surface may now not escape the sample, even if they are moving perpendicular to the sampling plane. Thus, the measurement becomes more surface-sensitive with roughness.

In general, the photoelectron detector in XPS instruments is most sensitive to emission normal to the sampling plane. For a smooth sample, as in **Figure 6.15a**, photoelectrons originating in the surface or upper part of the bulk may be detected, although those escaping at too shallow an angle may not. Conversely, as shown in **Figure 6.15b**, rough samples increase the detection probability for those photoelectrons that would have had a shallow escape angle from a smooth surface. This is because they would instead travel closer to the normal of the sampling plane. However, some that had detectable trajectories from a smooth surface may have a lower probability of being detected. Additionally, some originating in the bulk or in the

lower part of the surface may have too short a mean free path, around 4 nm in titanium nitride,[158] to escape the rough surface. Thus, the surface sensitivity of the measurement is increased.

Given the influence of surface morphology on XPS measurements, the data in **Figure 6.13b** may not indicate a change in surface composition. Rather, they might reflect the roughened surface. As such, any variations in the electrode surface composition may not be reliably measured by comparing the spectra from the surface. However, the study of sub-surface material might be more suitable for analysis.

6.7 Attempted depth profiling of the top electrode

Having found that the morphology of the stained top electrode surface excluded a reliable analysis of compositional changes, I reasoned that depth profiling with the XPS instrument might be a more suitable approach. Using ion milling to remove material, spectra can be acquired from sub-surface sample material and processed to compose a profile of compositional changes with depth. In addition, changes on the surface of the top electrode are often attributed to processes occurring in the switching layer below, or at the interface between the top electrode and the active layer.[13,159,160,161] This approach may also provide information on such compositional variations.

For consistency, the same sampling parameters were used for depth profiling as for the measurements in chapter **6.6**. The argon beam energy was set to 3 keV, with the milling area set to a 2 mm wide square in order to cover the full x-ray illumination area and avoid artefacts from sampling the edge of the milled square. The sample was milled 32 times, providing 33 sets of spectra for the depth profile.

Figure 6.16a shows XPS survey spectra comparing the first and last measurements taken in a depth profile on a pristine device. These spectra demonstrate the presence of titanium, nitrogen, oxygen, carbon and argon. There is little signal from silicon in **Figure 6.16b**, suggesting relatively less of the SiO_x was sampled than in the measurements of chapter **6.6**. Comparing the spectra of **Figure 6.16a** and **Figure 6.10**, the titanium and nitrogen signals are enhanced. This also suggests improved alignment of the sampling area on the top electrode. The signal from carbon is expected at the surface due to contamination and disappears by the final layer of the depth profile, as demonstrated in **Figure 6.16a**. Argon is present as a result of the milling process, by which ions are implanted into the sample as material is removed.[162]

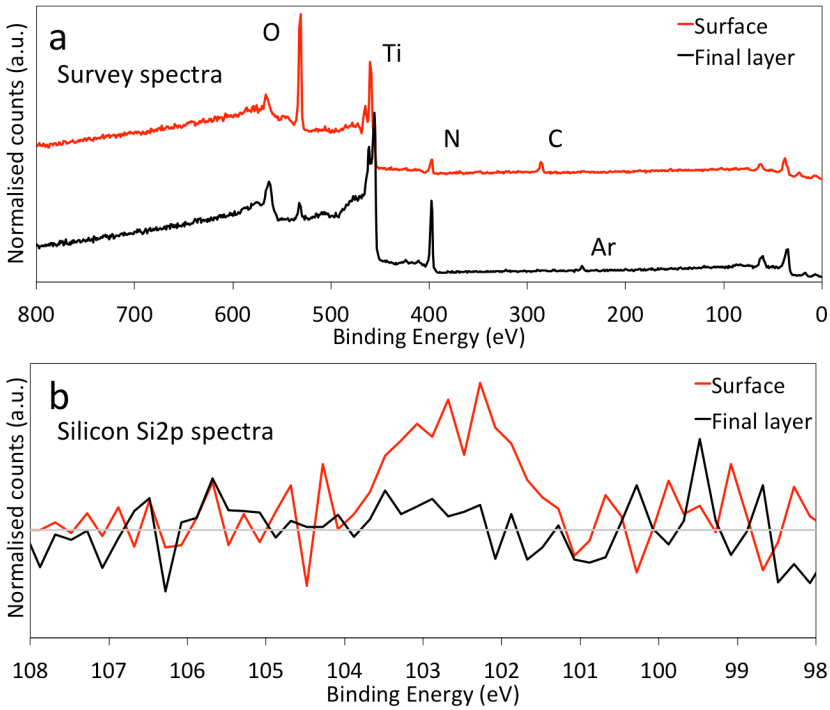

Figure 6.16. Surface and final layer XPS depth profile spectra from a pristine area of top electrode. (**a**) Normalised survey spectra, offset for display clarity, indicating an increase in the nitrogen content and decrease in the oxygen content of the titanium nitride by the final layer. In addition, there is not a significant contribution from silicon. (**b**) Si2p spectra, normalised to the maximum counts in the surface spectrum, demonstrating that a small amount of silicon is present at the surface but none appears to be present in the final layer.

A key feature of the spectra in **Figure 6.16b** is that there is not any silicon in the final layer, indicating the depth profile did not progress all the way through the top electrode to the active layer below. This is likely due to time constraints or poor alignment of the optical camera, x-ray beam and milling beam; each time I attempted this measurement I did not observe an increase in the silicon signal before the experimental session ended. As a result, I did not perform depth profile measurements on a stained top electrode. This would be of interest for follow-up work to better understand the processes occurring in and on the top electrode as a result of switching.

There are notable differences between the surface and final layer in the signals from titanium, nitrogen and oxygen in **Figure 6.16a**, suggesting the bulk composition is different to the surface. **Figure 6.17** shows the spectra of the Ti2p region from each measurement in the depth profile. Notably, at the surface there are three peaks, around 455.5 eV, 459.5 eV and 465 eV. In the bulk, there are two distinct peaks, at 455.5 eV and 461 eV. The transition between the two spectral shapes occurs over the first few layers, with intermediate layers showing no peak at 465 eV and less-pronounced peaks at 455.5 eV and 461 eV than subsequent layers.

The surface Ti2p spectrum is similar to that of **Figure 6.14a**, with peaks at around 459.5 eV and 465 eV suggesting oxidised titanium nitride, or titanium oxynitride. As the depth profile progresses to the bulk, these peaks diminish and lower binding energy peaks around 455.5 eV and 461 eV become dominant, characteristic of titanium nitride.[158] This supports the notion that the surface of the electrode is oxidised and confirms that the bulk is titanium nitride, as expected. This is supported by previous reports of atmosphere-exposed titanium nitride surfaces growing a 4 nm thick native oxide.[158]

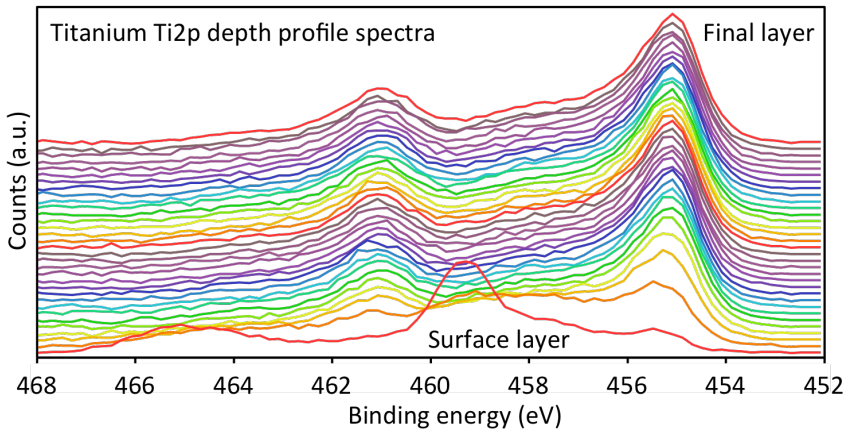

Figure 6.17. Ti2p depth profile spectra from a top electrode. The spectrum at the surface is different from the bulk, in which the peaks at 459 eV and 465 eV have decreased and those at 465 eV and 461 eV have increased. This suggests a transition from oxidised titanium nitride, or titanium oxynitride, to titanium nitride.

In **Figure 6.17**, the spectra appear similar to one another, aside from those of the surface and second layers. Therefore, there should be a depth at which the composition becomes steady. **Figure 6.18** shows the overlaid spectra from titanium, nitrogen and oxygen for the first eight levels, including the surface. In each case, the spectrum appears to reach a steady state after six to eight measurements, indicated by the grey boxes. The titanium tends from a titanium oxynitride signal toward a titanium nitride signal with peaks at lower binding energies. The single nitrogen peak increases and shifts to a slightly higher binding energy. The oxygen signal decreases and the single peak shifts by around 0.5 eV to higher binding energy.

The nitrogen spectra in **Figure 6.18b** demonstrate shifting from around 397 eV to 397.5 eV with increasing depth. This positioning is in agreement with the surface spectra presented in **Figure 6.14b**, so it may be assumed that this peak correlates with titanium nitride, in agreement with the literature.[147,156] There may also be a small feature at around 400 eV, corresponding to oxidised nitrogen,[157] although this is not very prominent. In addition, this feature does not appear to shift with increasing depth although it does increase in magnitude as the larger peak increases.

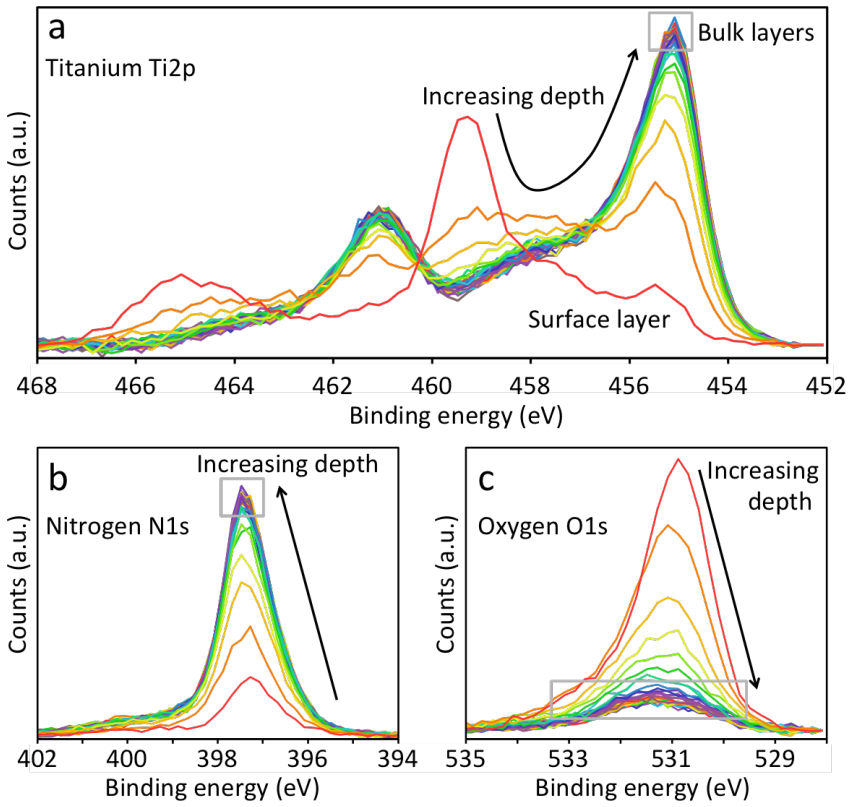

Figure 6.18. XPS depth profile spectra demonstrating the top electrode bulk composition reaching a steady state. (**a**) Ti2p spectra, showing the transition from titanium oxynitride to titanium nitride. (**b**) N1s spectra, demonstrating an increase in the nitrogen signal. (**c**) O1s spectra, demonstrating a decrease in the oxygen signal and a shift by around 0.5 eV to higher binding energy. In each case, the grey box highlights the depth at which the spectra have become steady. The spectra have not been normalised and the raw data is shown.

Considering the XPS findings from **6.6** and **6.7** in relation to the earlier CAFM and SEM observations in **6.4** and **6.5**, a clearer description of electrode staining may be presented. The CAFM data indicated that the bubble edges on stains were conductive and the SEM data indicated that the bubbles appear to have a correlated asymmetry. Combining these observations, I suggested that the asymmetry and conductivity are related, possibly as a result of compositional variations across each bubble. The XPS data indicate that the surface of the electrode oxidised relative to the bulk titanium nitride. Notably, titanium oxynitride is less conductive that titanium nitride.[163] Thus, it may be that the staining exposes regions of conductive material below the relatively less conductive electrode surface and it is these small areas that show a current in CAFM.

The suggestion that the top surface of the titanium nitride is relatively insulating might imply that achieving good electrical contact with the tungsten needle of the probing station was difficult. However, this was not the case as switching was generally

successful when contacting devices in this manner. Such a conflict in the data might be a result of differences between the needle and CAFM probe contact properties. Firstly, the needle contact area would be much larger, around 80 μm^2, compared to around 30 nm^2 for the probe. This would increase the likelihood of the needle making good contact somewhere in this area. Secondly, I controlled the needle motion by hand whereas the probe was operated through software and piezoelectric controllers. The force applied by the needle would therefore be significantly greater than that of the probe. Given also that the needle was composed of tungsten and so was harder than the platinum/iridium-coated probe, the likelihood of the needle scratching the electrode surface would be quite high. This would remove some of the less conductive surface, allowing the needle to make good contact with the exposed titanium nitride below. This might be a reason why, as observed in **6.4**, very little current was observed with CAFM on the unstained regions of a stained top electrode, yet re-contacting these areas with the tungsten needle could restore device functionality.

6.8 Chapter summary and conclusions

In this chapter I have looked at changes occurring at the device surface as a result of resistance switching. In particular, I have presented observations on the stains that appear on the top electrode following device operation.

Optical microscopy allowed me to determine that surface staining was always present on used devices. In some cases, the stain was relatively small, of a similar diameter to the needle probe footprint. In other cases, the stain was much larger, sometimes covering the majority of the electrode. In all cases, devices eventually stopped functioning properly. Sometimes, this was because the needle used to stress the device seemed to lose electrical contact with the device when in physical contact with the stain.

Microscopic measurements indicated that staining changes the surface of the titanium nitride electrode. AFM and CAFM showed that the entire electrode surface becomes rougher and the conductivity of the device is restricted to the edges of the bubble-like features that compose the stains. In some places, the surface is distorted by a greater magnitude than the thickness of the electrode. SEM also revealed an edging effect, correlated with the topography of the bubbles. The CAFM results additionally indicated conductive regions on stains were small and located in the depressions between bubbles. It is therefore reasonable to suppose that staining might displace the tungsten needle of the probing station from good contact with the electrode. Specifically, the tallest points of the bubbles are not conductive. Thus, if the needle rests on top of them it may be isolated from the small conductive areas exposed below the deformed surface.

XPS results showed that the surface of the top electrode is initially titanium oxynitride and that the bulk is titanium nitride. This variation in composition may be correlated with the CAFM and SEM results, suggesting that the surface distortions and conductivity variations characterising staining are related to the exposure of more conductive titanium nitride. This likely occurs as a result of a morphological change in the electrode or material below, although there is not enough data to speculate on what, specifically, this change might be.

As discussed in **2**, features similar to the stains I have presented are seen in many resistance switching devices and are often attributed to the release of oxygen.[29,31,69,70]. In fact, it has been shown for SiO_x that ionised oxygen molecules are dissociated from the active layer and released from the device during operation.[135] If oxygen is mobilised within the device, then it is likely to escape through the surface that is exposed to the environment. The scale of the stains that I have shown may therefore be explained by the motion of and Coulombic repulsion between mobile molecules as they move through the top electrode, causing deformation.

The data I have presented so far support the supposition of oxygen migration governing resistance switching, evidenced by the dynamic changes occurring at the surface of the top electrode. However, this evidence is indirect. There is a lack of information on the processes occurring in the switching layer itself, where oxygen dissociation should occur. In particular, my spectroscopic data is insufficient to draw any conclusions on the compositional changes occurring as a result of switching.

As mentioned in **6.7**, I was unable to successfully depth profile through the top electrode and into the switching layer. Therefore, I was not able to acquire data correlating the effects seen at the surface of the device with processes occurring in the SiO_x. In light of this, I reasoned that examining the active layer directly might provide further insight into the behaviour observed at the device surface.

7. Switching layer structure and transformations

7.1 Chapter introduction

In this chapter I will present observations on the structural changes occurring on the switching layer surface and in its bulk as a result of electrical operation when using a tungsten needle rather than a titanium nitride electrode. I use optical microscopy, AFM and CAFM to demonstrate that the contact point of the needle becomes deformed and that there are delocalised changes at the switching layer surface, indicating a highly energetic process. In addition, I use XPS to demonstrate that oxygen is lost from particular bonding configurations SiO_x under electrical stress, producing a more silicon-rich material.

To directly study the active layer of a device, the top electrode must be removed. However, this would require chemical or mechanical processes that may affect the active layer. Top electrodes also function as a map; locating regions of interest is extremely difficult without them. Notably, the majority of the sample wafer surface is electrode-free SiO_x. I reasoned that addressing this surface with a tungsten needle might be a suitable approach; rather than using the deposited top electrodes, the needle would behave as a mobile electrode. Although this would involve an electrode material with different contact and electrical properties to the titanium nitride studied so far, removing the needle after switching would provide access to the active layer.

7.2 SiO_x surface and adjusted switching parameters

I began looking at pristine SiO_x, before stressing electrically, to better understand the starting material. As discussed in **2.3**, it is often reported that resistance switching is facilitated by the presence of structural defects and inhomogeneities in the switching layer. Features of this nature might provide nucleation sites for structural changes under electrical stress. They may be well-defined, such as crystalline grain boundaries or dislocations,[51,137,164,165] or less well-defined, such as density variations and clustering in amorphous materials.[14,53,166]

Figure 7.1a shows an optical image of the sample where the SiO_x is exposed. It appears almost featureless with some small blemishes. The SiO_x is very thin, 37 nm, and optically transparent, so these spots might be present in the layers below rather than at the surface. The AFM image in **Figure 7.1b** demonstrates that, at higher magnification, the surface appears bumpy. This seems reasonable for a suboxide, as it should be amorphous.[119,167] Such a material would lack long- or short-range order and this appears to be the case in **Figure 7.1b**.

The smallest features in **Figure 7.1b** are around 10 nm in diameter, likely the resolution limit of the AFM probe. Although the surface of the active layer appears rough with these bumps, their height varies by around 4 nm over 4 μm^2. **Figure 7.1c** presents roughness data with a mean value of 0.21 nm, indicating the SiO_x is actually relatively smooth.

Columnar features have been observed in SiO_x as a result of sputtered fabrication.[168,169] In addition, column edges show enhanced conductivity and exhibit switching behaviour.[14] This is likely due to electron-trapping defects, such as intrinsic oxygen vacancies, that allow trap assisted tunnelling conduction.[13,32,51] It is likely the tops of columns produce the bumpy surface structure observed in **Figure 7.1b**. As discussed in **2.3**, resistance switching in SiO_x may rely on the defects associated with intrinsic microstructures such as columns.

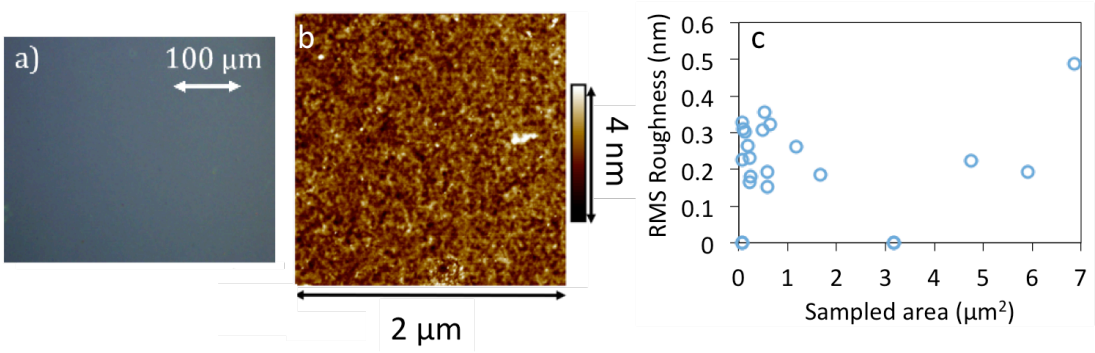

Figure 7.1. Pristine SiO_x surface. (**a**) Optical image; the surface appears smooth. (**b**) Tapping-mode AFM image. The surface has a z range of 4 nm and a grainy, lumpy appearance as a result of sputter deposition. (**c**) From a selection of sample areas, the RMS roughness of SiO_x is 0.21 nm, with a standard deviation of 0.17 nm. Note some data points appear to indicate a roughness of 0 nm, although the lowest value is 10^{-5} nm.

To study the switching properties of the SiO_x with a tungsten needle top electrode, a new surface location was chosen for each attempt at electroforming and cycling. In addition, the areas local to the surface blemishes shown in **Figure 7.1a** were avoided. The tungsten needles of the semiconductor parameter analyser probe station have a nominal few-micrometre circular footprint, so are large relative to the size and distribution of bumps on the active layer surface. Assuming these features correlate with the top of an intrinsic columnar microstructure, the footprint size should ensure that a needle addressing the active layer would contact a large number of preferential switching sites.

The parameters for switching with a titanium nitride top electrode, as in **Figure 6.1**, were not suitable for switching with a tungsten needle. In particular, electroforming was

successful in around 10% of attempts, compared to over 90% with titanium nitride. As shown in **Figure 7.2**, sweeping the voltage as high as 20 V, higher than the typical 7 V to 8 V used, often did not produce the electroforming current jump. Rather, the field capacitively charged the device.

As indicated in **Figure 7.2**, the increasing half of the voltage sweep corresponds to a slightly higher current than on the decreasing half. This suggests that, as the field increases, charge is injected into the device. However, no electroforming occurs. Rather, as the voltage returns to 0 V, further charge injection is inhibited so the current is lower. In a device with a titanium nitride top electrode, lower applied fields would induce electroforming. The work functions of titanium nitride and tungsten are generally reported between 4 eV and 5 eV, so differences of around 1 V in the switching parameters would be expected.[170,171] However, the voltages reached with the tungsten needle in **Figure 7.2** are significantly greater than those required with titanium nitride. Therefore, using a tungsten needle appears to modify the device behaviour to a greater extent than would be expected for a change of electrode material.

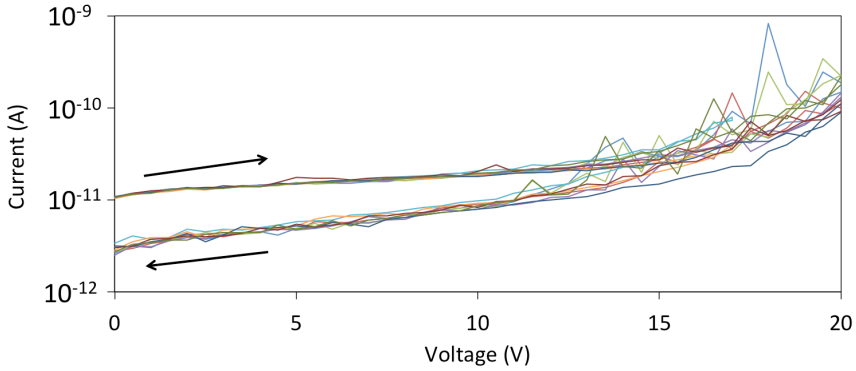

Figure 7.2. Current-voltage curves for switching attempts with a tungsten needle. No electroforming occurs. Rather, there is some capacitive charging of the switching layer. This is evidenced by the lower current when the voltage returns to 0 V, indicated by the arrows.

It is reasonable to suggest that the electrical contact made to the SiO_x by a deposited electrode is better than that of a tungsten needle. The controlled environment required for device fabrication ensures that surfaces are clean when they make contact whereas, in general, surfaces that are exposed to air are oxidised and contaminated. However, the poor switching properties with a tungsten needle are unlikely to be due to surface contamination, as the sample and needle were cleaned before measurements were made. Thus, oxidation of the needle and the switching layer are the most likely causes for the observed behaviour.

Native oxidation of SiO_x surfaces occurs for samples stored in air, such as those in this work. Unstable or weakly bound surface groups are replaced over time with

atmospheric oxygen-hydrogen ions. These split as their oxygen incorporates into silicon-oxygen-silicon bonding structures. Over time, this drives silicon atoms from the bulk to the surface, growing an oxygen-rich native oxide layer under the continued incidence of ions on the surface.[172,173] This layer is insulating, imposing a barrier that increases the field strength required for switching.

7.3 SiO_x switching with a tungsten needle: cratering

To perform structural studies on the SiO_x, observable switching-related changes were required. However, this was hindered by the lack of success in switching with a tungsten needle. There was no apparent correlation between the area chosen and the electroforming success rate, suggesting that effective contact between the probe and sample was difficult to achieve. Therefore, I employed an exploratory approach, using a selection of voltage sweep ranges and current compliances, as well as a variety of contact locations on the switching layer.

Generally, larger fields were required with a needle than with a titanium nitride electrode. As a result, I was concerned that I might overstress the oxide and cause device failure through hard dielectric breakdown. This occurs through a combination of charge injection, defect generation and Joule heating when the device is in a low resistance state.[21] These processes are driven by the applied electric field and can result in catastrophic material deformation.[174]

Instantaneous implementation of current compliance should prevent breakdown-induced device failure, regardless of the applied field. However, implementation is not instantaneous because the semiconductor parameter analyser must measure the resistance, determine the current and then decide whether the applied voltage must be reduced in order to reduce the current. Thus, the current will likely exceed the limit for some time. For the voltages used in normal operation, the unrestricted current may not damage the device. At higher voltages, such when switching with a needle, damage and failure becomes more likely. I therefore used lower current compliances to account for the overshoot in the current.

Figure 7.3a demonstrates successful cycling with a tungsten needle. The oxide was formed, reset, set and reset again. For electroforming and setting, the voltage was swept from 0 V to 20 V. For the first reset, the voltage was swept to 6 V. The first attempt at a second reset, which is not shown, was not successful. The voltage was then swept to 20 V, resulting in a reset and device failure. This was evident as no current jumps were observed when trying to set after the second reset. The current compliances were 100 µA and 1 µA for form and set, respectively. During resetting, the

current reached around 50 mA. The voltages and compliance values were chosen empirically, in this case producing four distinct switching events.

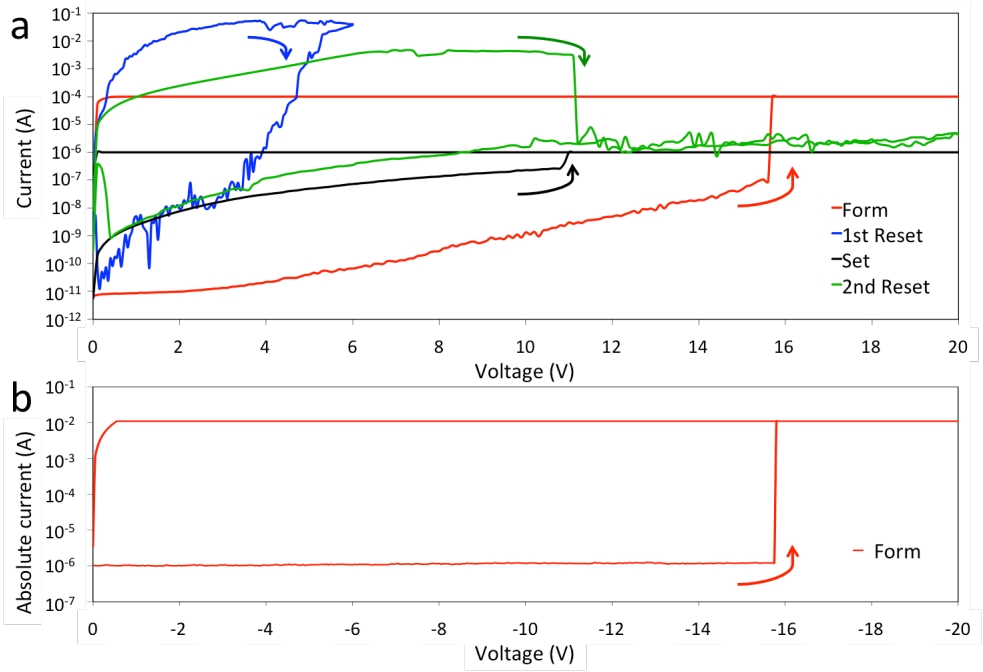

Figure 7.3. Switching SiO_x directly with a tungsten needle. (**a**) Positive needle polarity. Electroforming and set operations used sweeps of 0 V to 20 V with compliances of 100 µA and 1 µA, respectively. The first reset used a sweep to 6 V, reaching a current of around 50 mA. The second reset operation caused the device to fail into a state of low resistance. (**b**) Negative needle polarity. Forming occurred just before -16 V. In contrast to **a**, the pre-forming current is constant with increasing voltage and is relatively large, around 1 µA. The current compliance of 10 mA for this sweep was higher than those used for the positive operation in **a**.

Interestingly, the on state following forming at 100 µA compliance in **Figure 7.3a** appears to be around an order of magnitude lower in resistance than that of the set at 1 µA. This is evident in the currents of around 50 mA and 0.5 mA for the first and second resets, respectively. Such compliance-dependent resistance in RRAM devices has previously been attributed to variations in the size of the conductive region formed in the active layer.[175,176]

Following the cycling shown in **Figure 7.3a**, the oxide was significantly deformed. As demonstrated in **Figure 7.4a**, a crater-like feature was present at the point of contact. Surrounding this were many orange spots, although fewer were present closer to the crater. Crucially, the area covered by the crater and spots is much larger than the footprint of the tungsten needle. Thus, the effect of the electrical stress is not confined to the point of contact.

I also attempted switching with a negative tungsten needle polarity. Electroforming was around half as successful as with a positive-polarity, but the SiO_x could not be reset or cycled. I speculate that the reason for this is similar to that discussed in chapter **6.2**, that it is easier to inject electrons from the bottom electrode and migrate oxygen with a positive top electrode bias. In addition, the energy barrier at the tungsten/SiO_x interface might by rectifying, further hindering operation with a negative top electrode bias. An example of negative electroforming is shown in **Figure 7.3b**. Note the compliance is 10 mA. This is high in comparison to those for a positive polarity in **Figure 7.3a**. Such a high value was chosen to explore cratering, given that cycling was not possible.

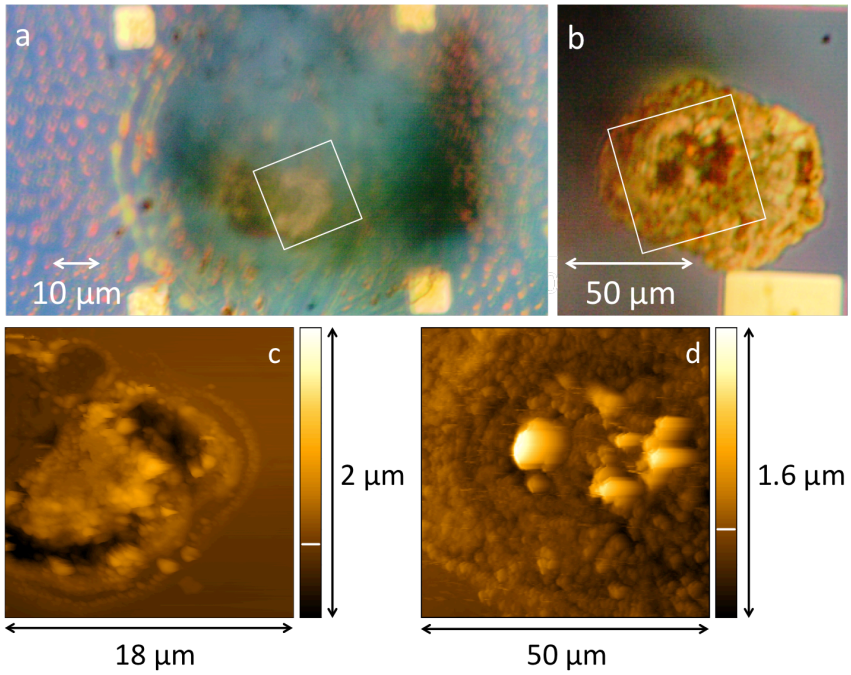

Figure 7.4. Images of SiO_x following electrical stress with a tungsten needle. (**a**) Optical image of a crater and associated orange spots following switching with positive needle polarity. (**b**) Optical image of a crater, with no orange spots, following forming with negative needle polarity. (**c**) Tapping-mode AFM image of the area indicated by the white square in **a**. (**d**) Tapping-mode AFM of the area of the white square in **b**. In both AFM images, the tallest points of the craters are more than 500 nm above and the lowest points more than 100 nm below the SiO_x surface, the colour of which is indicated by the white lines on the scale bars.

For the negative electroform in **Figure 7.3b**, the current stays relatively consistent at around 1 µA before jumping to the compliance level. This is in contrast to positive operation, in which the current is initially lower, around 10 pA, and gradually increases before the jump. This suggests that negative charge is more readily injected from the needle, but dissipates rather than being stored, as observed with a positive voltage in **Figure 7.2** and **Figure 7.3a**.

As shown in **Figure 7.4b**, switching with a negative needle polarity produced a crater-like feature, similar to **Figure 7.4a**, at the point of probe contact. However, no orange spots were present in the surrounding area. This suggests that the appearance of spots may depend on the switching polarity whereas the crater is produced regardless of the field or current polarity.

Figure 7.4c and **d** present AFM images of the craters shown optically in **Figure 7.4a** and **b**. Both are tall in comparison to the 37 nm thick SiO_x, with maximum heights are around 500 nm and 1 µm above the oxide surface for positive and negative bias, respectively. These are hundreds of nanometres greater than the height of the stains observed on titanium nitride electrodes, such as in **Figure 6.4**. Crucially, however, the craters also extend down to around 300 nm below the SiO_x surface. Similar behaviour was not observed on devices with a titanium nitride top electrode and indicates that the cratering has affected both the bottom electrode and the silicon dioxide layer that separates it from the silicon substrate. The lateral extent of the cratering and orange spots suggests a very energetic process. Cratering may thus be a distinct phenomenon from the deformations observed on normal devices at lower operational voltages. Given the extreme depth penetration and surface modification of cratering, it is possible that the active layer is shorted with material from the tungsten needle or bottom electrode. In fact, this material migration may extend through to the thermal SiO_2 layer on the sample substrate.

It is clear from **Figure 7.3** that the maximum reset current is higher during operation with tungsten needle than a normal device, such as in **Figure 6.1**. For a normal device reset, the current reaches around 5 mA, slightly above the 3 mA compliance level. However, for the device operated with a tungsten needle, the maximum is around 50 mA, an order of magnitude higher. This supports the notion that cratering is related to the large fields and currents and may indicate hard dielectric breakdown rather than normal resistance switching behaviour.

On devices with a titanium nitride top electrode, such as in **Figure 6.3**, the staining is confined to the electrode. However, the orange spots shown in **Figure 7.4** are not localised to the needle contact point. In addition, the region roughly 15 µm diameter surrounding the contact point contains fewer orange spots than more distant areas. Radial damage features have previously been associated with heating effects in resistance switching devices,[174] so the spot-free area may indicate that greatest heating during switching is local to the contact point.

It should be noted that the data in **Figure 7.3a** was the only case that a reset was possible after electroforming with a tungsten needle. It is not clear which switching operation caused the cratering and it may have been gradual. However, given that the

negative polarity switching in **Figure 7.3b** caused a similar deformation in a single event with current in the milliamp range, it may have been the second reset in **Figure 7.3a** that caused cratering. It is also possible that this material transformation process is sufficiently powerful to displace the needle, causing it to lose contact with the switching location.

The cratering shown in **Figure 7.4** is more destructive than might be expected for normal devices that operate for hundreds of cycles. As such, a more informative study could focus on less pronounced changes in the switching layer. Electroforming produces the greatest change in resistance that a device will normally undergo. Hence, the most pronounced changes in the SiO_x structure should occur during this step. Smaller deformations than craters would provide an insight into the switching process, more in line with normal device operation. Studies of such features, following only an electroforming step, would also eliminate the risk of a performing destructive reset process and the needle would not need to remain in place.

7.4 SiO_x switching with a tungsten needle: bubbles

To study whether electroforming without causing cratering was possible, a set of voltage sweeps with different current compliances were used and the probe contact point subsequently assessed for optically visible changes. Although some structural changes should occur below the optical limit, this assessment provided a means of quickly determining whether or not a location had undergone extreme deformation, uncharacteristic of normal switching behaviour.

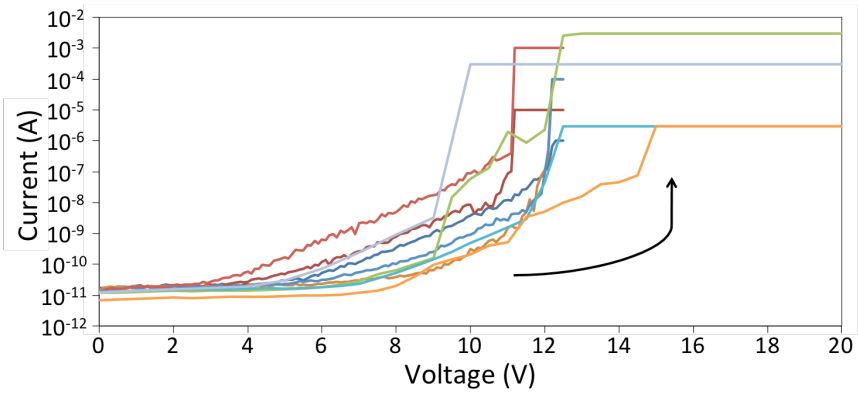

Figure 7.5. Electroforming of the SiO_x with a tungsten needle, using a variety of current compliances. Measurements finished at the maximum voltage, without sweeping back to 0 V. The mean forming voltage is 11.7 V, with a standard deviation of 1.1 V.

Figure 7.5 shows the variation in the forming voltage for sweeps with a tungsten needle. A variety of ranges were tested, applying the voltage only until its maximum value was reached. This was done to minimise stress on the oxide by reducing its

duration once compliance had been reached. The mean forming voltage was 11.7 V, with standard deviation of 1.1 V. The point of forming is defined as the value half way between the data points before and at which compliance is reached. This is around 5 V greater than with a titanium nitride top electrode.

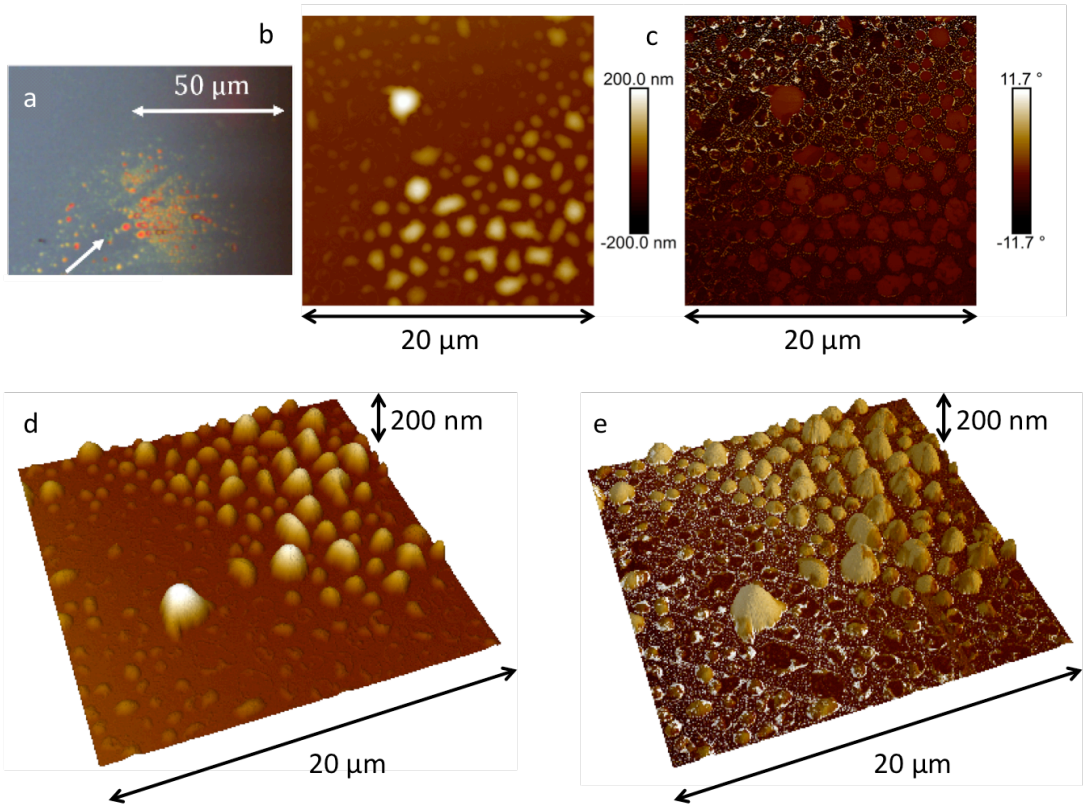

Figure 7.6. Orange spots on the SiO_x surface following electroforming with a tungsten needle. (**a**) Optical microscope image. The contact point is indicated by the white arrow. There are fewer spots local to this point than further away. (**b**) Tapping-mode AFM image of a region containing orange spots. Many tall, bubble-like features are visible, though the interstitial regions appear flat. (**c**) Tapping-mode AFM phase map of the region in **b**, showing small features in the regions that appear flat in **b**. (**d**) Three-dimensional plot of the data in **b**. (**e**) The same plot as in **d**, with the phase data from **c** overlaid. Features between the bubbles are clearer. The upper half of the image shows many intact bubbles whereas the lower half contains many burst bubbles and their residual menisci. Neither **d** nor **e** have scale bars as they are shown in **b** and **c**, respectively.

Following electroforming, there were always optically visible changes on the surface of the SiO_x. In some cases there was a large breakdown crater, although not often for current compliances below 1 mA. Otherwise, there was no apparent correlation between the compliance and the size of the features at the contact point. In cases that did not exhibit cratering, a dark region a few micrometres in diameter was generally present. These observations may indicate that contact between the tip and sample was

inconsistent and not easily controlled. This supports the notion that switching behaviour depends greatly on the contact properties, as discussed in **7.3**.

Figure 7.6a shows an optical microscopy image of an area of SiO_x after electroforming. There is a dark spot at the needle contact point, surrounded by a spread of orange spots covering an area around 50 µm in diameter. This is large in comparison to the few-micrometre needle footprint, again suggesting, as in **7.3**, that the effect of electrical stress is not confined to the contact point. The region closest to the dark spot has fewer orange spots than more distant areas, similarly to **Figure 7.4a**. Again, this may be a thermal effect local to the point of contact.

Figure 7.6b shows the AFM topography for a region of **Figure 7.6a** that contains orange spots. They are up to 200 nm in height and are generally up to a few micrometres in diameter. Notably, some spots are taller than the thickness of the switching layer. The regions between the spots appear flat in the topography image, although the cantilever phase image in **Figure 7.6c** suggests that there are some features. These are likely not clear in the topography data because their height is significantly smaller than the tallest features. As such, they do produce an easily observed height contrast in the colour mapping of the data.

As discussed in chapter **3.2**, the cantilever phase data informs on topography, mostly due to variations in the tip-sample contact area.[81] This helps emphasise changes in the surface slope without being sensitive to height, so is suitable for simultaneously studying features with very different heights. However, the phase is sensitive to sample composition as a result of, for example, variations in the adhesion and viscoelastic properties of the sample.[177] This convolution between topographic and chemical information means quantifying phase data is only suitable for very flat surfaces. Therefore, on an uneven surface such as in **Figure 7.6b**, the phase is only suitable as a qualitative measure. However, for completeness, the scale bar is shown.

To better inspect features of significantly different heights simultaneously, the phase data may be overlaid on the topography. **Figure 7.6d** shows a three-dimensional AFM map of the data in **Figure 7.6b**. In contrast, **Figure 7.6e** shows the same topography with a phase overlay, giving the image its colour contrast. **Figure 7.6d** and **e** show that the orange spots have a bubble-like appearance. As indicated by the phase data in **e**, around half of the imaged region contains intact bubbles whereas the remaining area contains circular features that resemble menisci, perhaps residual from burst bubbles. As with the bubbles, the menisci vary in diameter, from hundreds of nanometres to a few micrometres. It is also evident from the phase data that there is a change in the SiO_x surface morphology in the regions between bubbles and menisci.

Figure 7.7a and **b** show a comparison of pristine SiO_x and the area between bubbles. Small bumps around 10 nm wide, similar to those in **Figure 7.1**, are present on the pristine surface. However, in the bubbled region, these features are not apparent. In this case, there are raised regions up 100 nm in diameter. In both images the height range is less than 10 nm, although the RMS roughness of the surface increased from 0.21 nm to 0.96 nm following electrical stress.

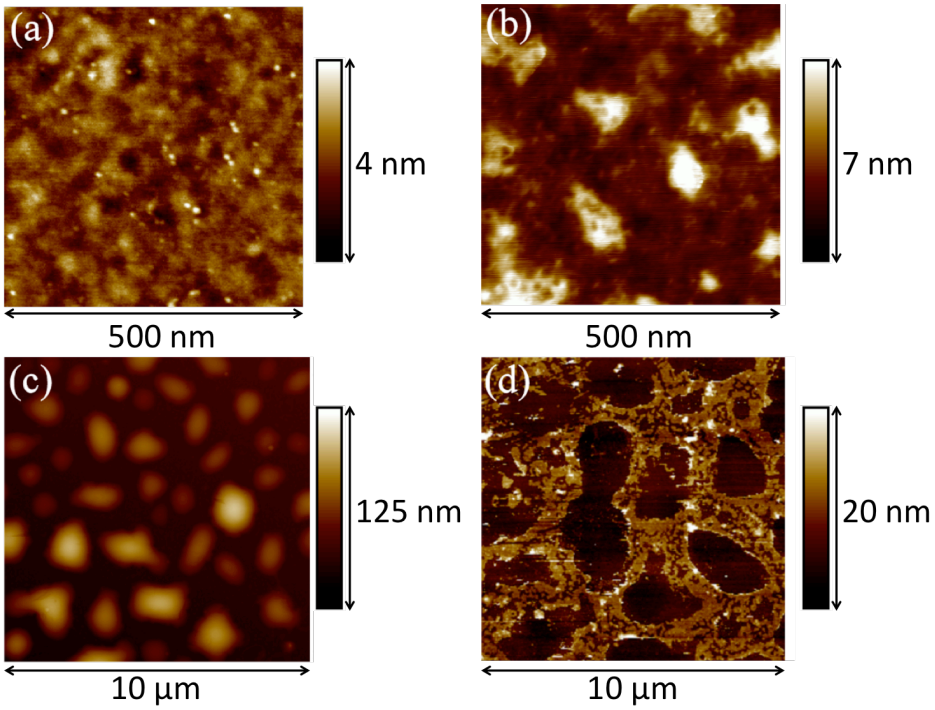

Figure 7.7. AFM images of SiO_x surface changes following electroforming with a tungsten needle. (**a**) QNM-mode topography map of pristine SiO_x, showing characteristic bumpy structure. (**b**) Tapping-mode image of a region between bubbles such as those in **c**. The surface is rougher than pristine SiO_x. (**c**) Tapping-mode image of orange bubbles, which appear unbroken. (**d**) Contact-mode image of orange bubbles, which appear to have burst, likely due to contact with the scanning probe. Thus, only residual menisci appear and are larger than the individual bubbles in **c**. It may be that some bubbles merged before or during bursting, or the menisci have merged afterwards.

Figure 7.7c and **d** demonstrate the difference in AFM images of the bubbles made in tapping and contact modes, respectively. Notably, the bubbles were not measurable with contact mode; only menisci appeared. This indicates that bubbles may have burst and was true of all contact-mode measurements of the bubbles. Thus, the probe may cause bursting. Notably, each meniscus in **d** appears to cover a larger area than the individual bubbles in **c**. This is in contrast to **Figure 7.6e**, in which the menisci and bubbles measured in tapping mode are similar in diameter. This suggests that contact

mode scanning might move bubbles around on the surface, causing them to merge and burst.

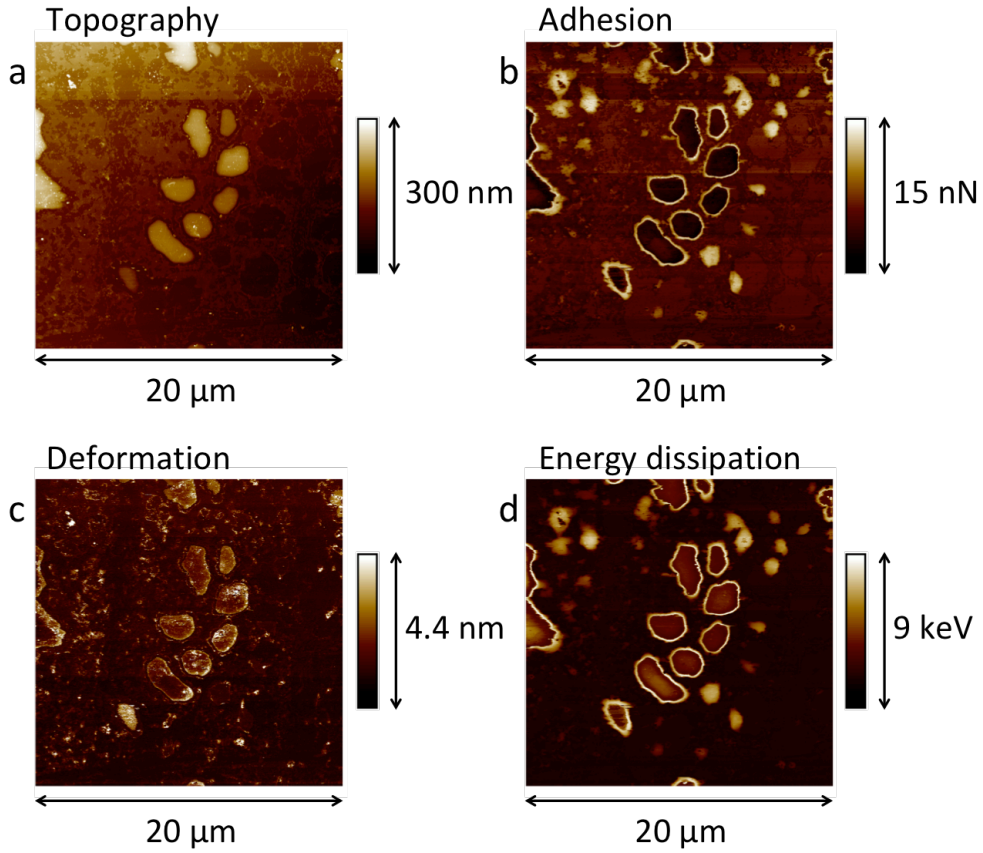

Figure 7.8. QNM mode AFM of orange bubbles on the SiO_x surface following forming with a tungsten needle. (**a**) Topography map, indicating the intact bubbles are around 100 nm tall. There are also some menisci present in the surrounding area. (**b**) Adhesion map, indicating that the tops of bubbles are less adhesive and edges more adhesive than the surrounding material. (**c**) Deformation map, indicating that the tops and edges of the bubbles are deformed more than the surrounding material. The edges are deformed to a greater extent, as indicated by the brighter contrast than on top of the bubbles. (**d**) Energy dissipation map. The tops and edges of the bubbles dissipate more energy than their surroundings. The edges of the bubbles also dissipate more energy than the tops. Note that energy dissipation is given in eV rather than Joules. This is because the keV scale is more appropriate for presentation, whereas the values in Joules would be around sixteen orders of magnitude lower.

I also studied the orange bubbles in QNM mode, to probe their mechanical properties, as shown in **Figure 7.8**. QNM mode is similar to tapping mode in that the probe oscillates to and from the sample. Unlike in tapping mode, however, it also makes contact, pressing into the surface in order to collect force-distance spectra. In contrast to contact mode, however, the probe does not move laterally while in contact. Bubbles

were observed in QNM mode, which suggest that lateral movement while in contact, corresponding to shear force, might burst bubbles. The compressive force applied in QNM mode does not appear to cause bursting, though.

Interestingly, the appearance of the bubbles in QNM mode, as in **Figure 7.8a**, is different from tapping mode, as in **Figure 7.7c**. Surface nanobubbles have previously shown different footprint areas when measured with tapping and QNM modes.[178] This appears to be due to the contact force of QNM, whereas tapping does not involve contact, as suggested above. This may mean that, on the bubbles but away from their edges, compressive QNM measurements at each pixel elicit the same response. Thus, each pixel gives a similar value, leading to apparently flat surfaces on the tops of bubbles. In contrast, the lack of contact in tapping mode may mean a more rounded appearance is observed, as the bubbles are not compressed.

The QNM measurements in **Figure 7.8** demonstrate the bubbles are more flexible than their surroundings. The data, extracted from force-distance measurements, show reduced adhesion but increased deformation and energy dissipation on the bubble tops. The decreased adhesion may indicate a restorative force from the compressed bubble, pushing the AFM probe away from the surface as it retracts. The increased deformation and energy dissipation also suggest that the bubble surface is displaced by the AFM probe during the tip-sample interaction, with the cantilever not storing energy in its flexing during approach.

The scans in **Figure 7.8** indicate increased adhesion, deformation and energy dissipation at the edges of bubbles. This may be due to increased contact area between the tip and sample at feature edges, increasing the cohesive forces but also causing the surface to appear softer. This is because the probe may slip down the side of the bubbles, inducing a measurable height change. However, given that the tops of bubbles are flexible, the edges should also demonstrate flexibility. However, increased adhesion at the edges conflicts with decreased adhesion on top. It is possible that the edge of the bubble deforms as the tip retracts. Thus, rather than providing an additional restorative force to the cantilever, as occurs on top of the bubbles, they may deform outward as the tip retracts, pulling on it and so increasing the adhesion.

As discussed above, contact-mode AFM measurements appear to cause bubble bursting. Further evidence is shown in **Figure 7.9**. The image was taken following AFM measurements on an area of containing bubbles. Some areas have been highlighted, as they appear to show linear gaps and trails in the bubbles. These may correspond to the areas scanned with AFM, traced out as the probe moves bubbles to the edges of the scan. Shear forces may therefore move bubbles around, if not bursting them.

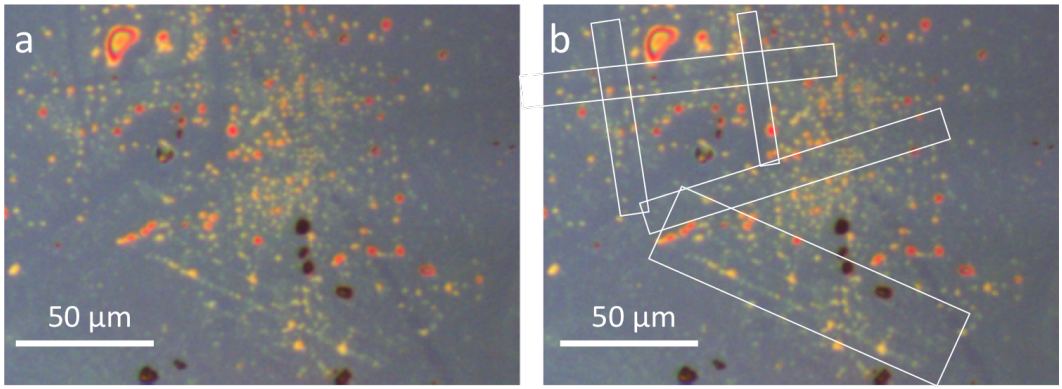

Figure 7.9. Optical microscopy images indicating that the AFM probe may move bubbles around. (**a**) Image of an area of SiO_x containing orange bubbles, after AFM measurements have been made. (**b**) The same area as in **a**, but here some linear features are highlighted as they seem to indicate that bubbles have been dragged by the AFM probe.

Orange bubbles generally covered large areas densely enough to be visible by eye. However, cleaning the sample between measurements removed them. Subsequent inspection of the regions that had contained bubbles indicated that the switching layer surface retained evidence of the electrical stress. **Figure 7.10b** shows the residual markings on the switching layer following cleaning, in contrast to a pristine surface, shown in **Figure 7.10a**. There is a clear, snaking pattern of bright areas with some small dark spots present. The dark spots likely correspond to the needle contact point, as noted earlier in **Figure 7.6a**.

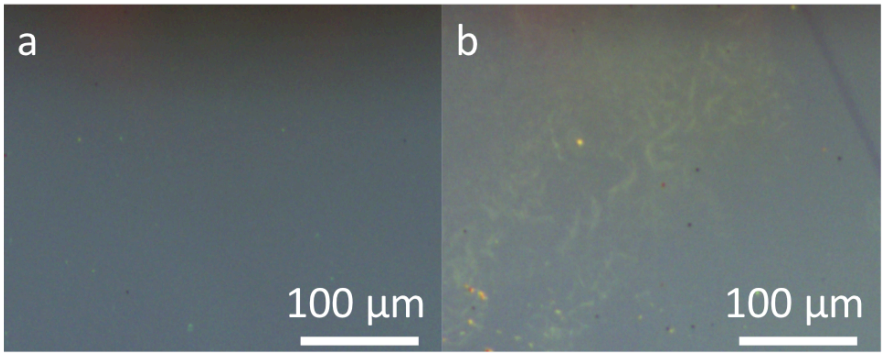

Figure 7.10. Observation of surface marking where orange bubbles were present before the sample was cleaned. (**a**) Pristine region of SiO_x, demonstrating that no snaking features are present, although there are some small light and dark spots. (**b**) Snaking patterns on the surface of the SiO_x following the removal of orange bubbles using ultrasonication in organic solvents. Note that the images in **a** and **b** are not of the same region.

QNM topography, deformation and Young's modulus measurements from the area containing snaking features in **Figure 7.10b** are shown in **Figure 7.11**. Two forms of

feature are present with distinctly different heights. Raised bumps of up to around 160 nm in height are shown in **Figure 7.11a**. The individual bumps appear to be clusters of smaller features, giving them a bubble-like appearance. Snaking patterns around 10 nm in height also appear, branching across the scan area, and are shown more clearly with the reduced height scale **Figure 7.11b**. These have a similar form to the white pattern shown in **Figure 7.10b** and may be the same feature. The deformation and Young's modulus measurements in **Figure 7.10c** and **d**, respectively, show that both the snakes and the bumps are softer than the surrounding SiO_x. Additionally, the bumps are softer and deform more than the snakes.

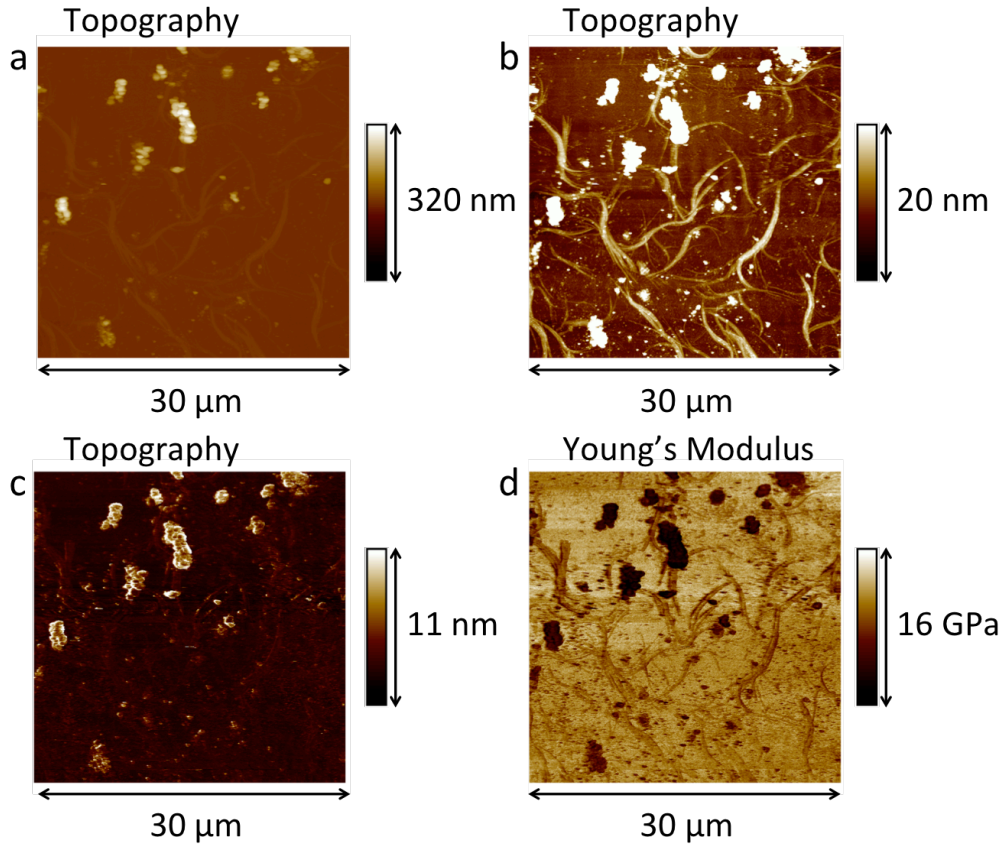

Figure 7.11. QNM mode AFM images of the features observed on a region of SiO_x following the removal of orange bubbles by sample cleaning. (**a**) Topography map showing tall features of up to 160 nm and, less clearly, snaking features with much lower heights. (**b**) Topography map with the data scaled to better distinguish the snaking features. They are up to around 10 nm in height and spread across most of the scanned region, joining one another in many locations. (**c**) Deformation map, indicating that the taller features are deformed by around 10 nm relative to the surrounding material. The snakes deform a few nanometres more than their surroundings, but the contrast is not as pronounced as for the taller features. (**d**) Young's modulus map, indicating that both bubble-like and snaking features are softer than the surrounding material. The bubbles also appear to be softer than the snakes.

The bubbles and snakes in this chapter may be considered alongside observations made on the roughness of stained top electrodes in **Figure 6.4**. Bubbling and snaking features appear to be delocalised, distinct from the dark spots that appear at the contact point of the tungsten needle. Notably, the entire titanium nitride electrode surface appeared to be roughened as a result of electrical operation. However, as discussed in **2.3**, a filamentary region much narrower than the electrode should govern switching. Thus, electrical stress appears to cause deformations that are not confined locally to the filament for both a deposited electrode and a needle probe.

The structural changes discussed in this section may indicate compositional changes within the active layer. As discussed in chapter **2.5**, bubble-like features are commonly seen in resistance switching devices and are thought to be related to oxygen release from the active layer.[10,40,70,179] Additionally, as discussed in **6.7**, the titanium nitride electrodes are deformed following electrical stress. These deformations might result from compositional changes within the switching layer, although the observations made so far in this chapter do not provide a direct insight into such changes.

7.5 XPS of electroformed SiO_x

To probe compositional changes in the SiO_x, I performed XPS depth profiles on pristine and electroformed regions showing orange bubbles. Notably, when attempting to study small features, the alignment of the XPS instrument was unreliable. In particular, spectra from small features were not as expected. For example, spectra from top electrodes tens of micrometres wide would contain only silicon and oxygen signals. This was likely due to an offset between the optical camera, used for selecting the sampling location, and the incidence of the x-ray beam. As such, sampling single electroform features was likely to produce unreliable data.

To account for instrumental misalignment, I reasoned that probing an area containing many features might be practical. If the area was much larger than the x-ray illumination spot then the measurement should sample multiple features. Although there would be significant background signal from the interstitial material, a dense-enough population of features might produce a measurable combined effect.

The largest x-ray illumination spot available was an ellipse with a long axis of 400 µm and a short axis of 200 µm. The sampling area was therefore a region of oxide greater than 500 µm by 500 µm, around 1 mm^2, containing a high density of electroformed spots in a grid-like pattern of roughly 30 µm intervals. These were generated with a tungsten needle, applying voltage sweeps from 0 V to 25 V. To prevent overstressing and damage, 100 µA current compliance was used.

As discussed in chapter **7.4**, cleaning the sample removed the orange bubbles. Therefore, the sample was not cleaned for XPS measurements. However, after the sample was loaded into the 10^{-8} Torr vacuum of the measurement chamber, the orange bubbles were no longer present. This became evident when I tried to locate the region of interest optically to select the sampling area. This suggests that the surface tension of the bubbles was insufficient prevent their rupture at high vacuum pressure. Fortunately, I located the region of interest relative to other noted surface features.

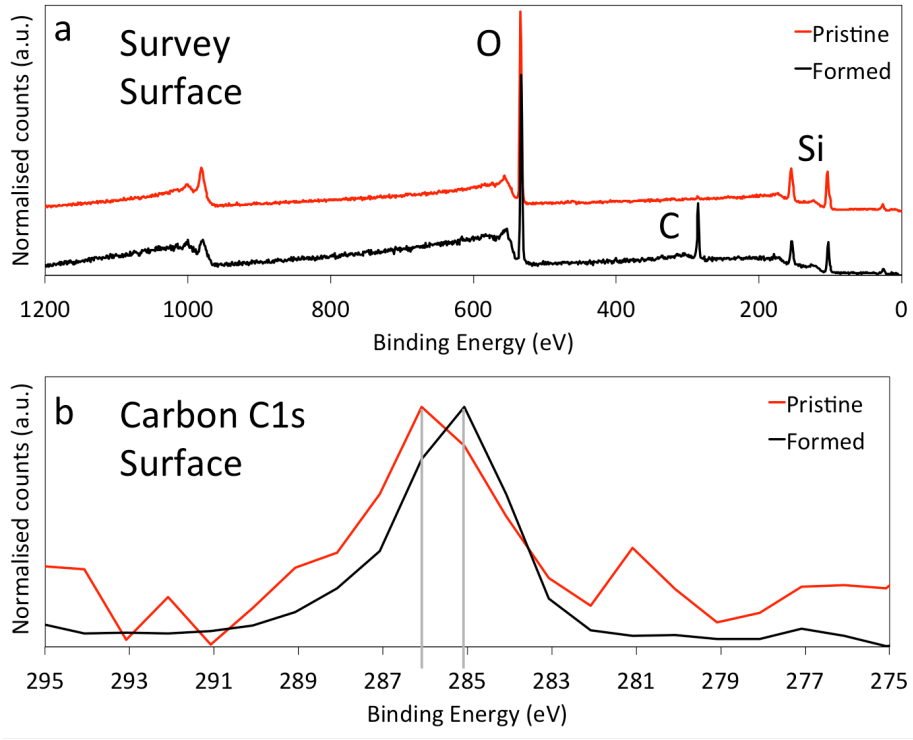

Figure 7.12. Survey and C1s XPS spectra of pristine and formed oxide, normalised and offset to best display and compare the peaks. (**a**) Survey spectra. As expected, silicon and oxygen are present. There appears to be less carbon on the pristine sample than the formed sample, likely because the formed sample was not cleaned. (**b**) C1s spectra showing carbon in both samples. Note the pristine spectrum here has been rescaled to best compare the data.

Figure 7.12a shows a comparison of survey spectra from the surface layer of pristine SiO_x and a region that contained orange bubbles. Silicon and oxygen are present, although the spectra look very similar at this binding energy scale. The main difference is the presence of carbon on the formed sample, likely because it has not been cleaned. The C1s spectrum in **Figure 7.12b** indicates that there may be a shift of up to around 1 eV between the two samples. However, given the resolution of the binding energy scale, as discussed in chapter **6.6**, the true shift may be from 0 eV to around 3 eV.

Figure 7.13 demonstrates Si2p and O1s spectra from the pristine and electroformed samples. As in **Figure 6.11**, the SiO_x surface spectrum suggests a similar composition to stoichiometric silicon dioxide, evidenced by the large peak around 104 eV in the Si2p spectrum. For both the Si2p and O1s spectra, the main peak narrows and shifts by around 1 eV to lower binding energy in the formed sample. This is within the instrumental shift range discussed above. However, in the Si2p spectrum, the smaller peak around 100 eV, corresponding to elemental silicon, does not appear to have shifted by as much. Rather, its intensity has decreased relative to the larger peak at around 103 eV. This suggests the binding energy shift is due to the surface becoming oxygen-rich, rather than an instrumental shift. Additionally, the O1s peak intensity increased, suggesting the surface has become oxidised. However, the shifting of the large peaks to lower binding energy contradicts oxidation, as it usually characterises a reduction process.[101]

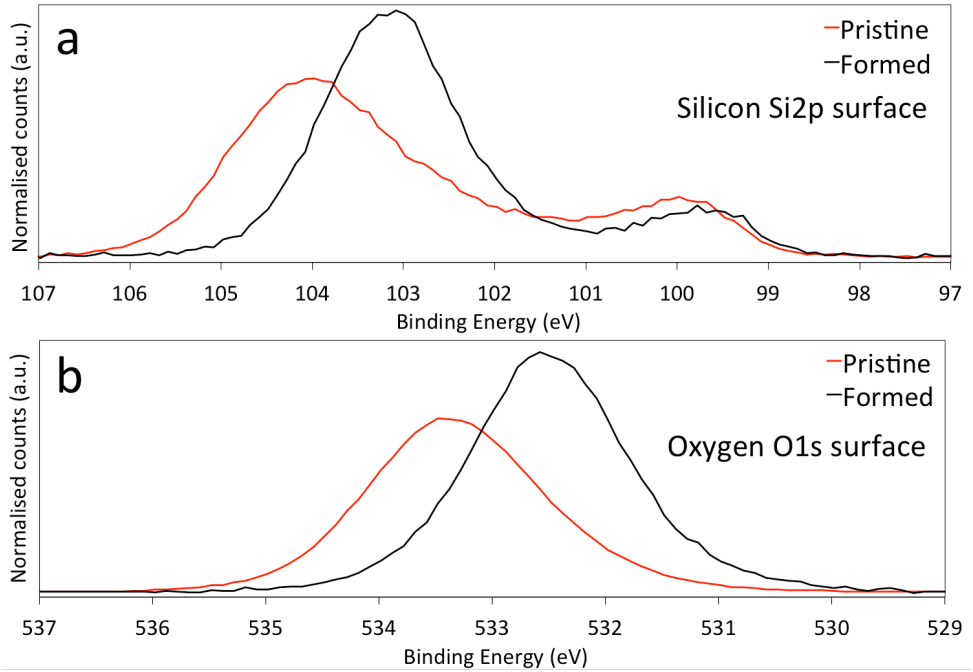

Figure 7.13. Surface Si2p and O1s XPS spectra, normalised to reflect a fixed total silicon signal between each sample. (**a**) Si2p spectra, showing a shift and narrowing of the higher binding energy peak following electroforming. (**b**) O1s spectra, also indicating a shift of the spectrum to a lower binding energy and a narrowing of the peak following electroforming.

The shifts shown in **Figure 7.13** may result from decreased dipole charge across the oxygen-rich surface layer. This dipole is caused by charge accumulation at the surface of insulators during XPS, perturbing photoelectrons during emission. This decreases their kinetic energy, so their measured binding energy is increased.[180] The electroformed sample is more conductive, thus the charging effect should be reduced and the peaks shifted to lower binding energy. However, the shifts are larger than

expected for this effect. Further analysis is needed to discern other possible causes, assuming the shifting is not instrumental.

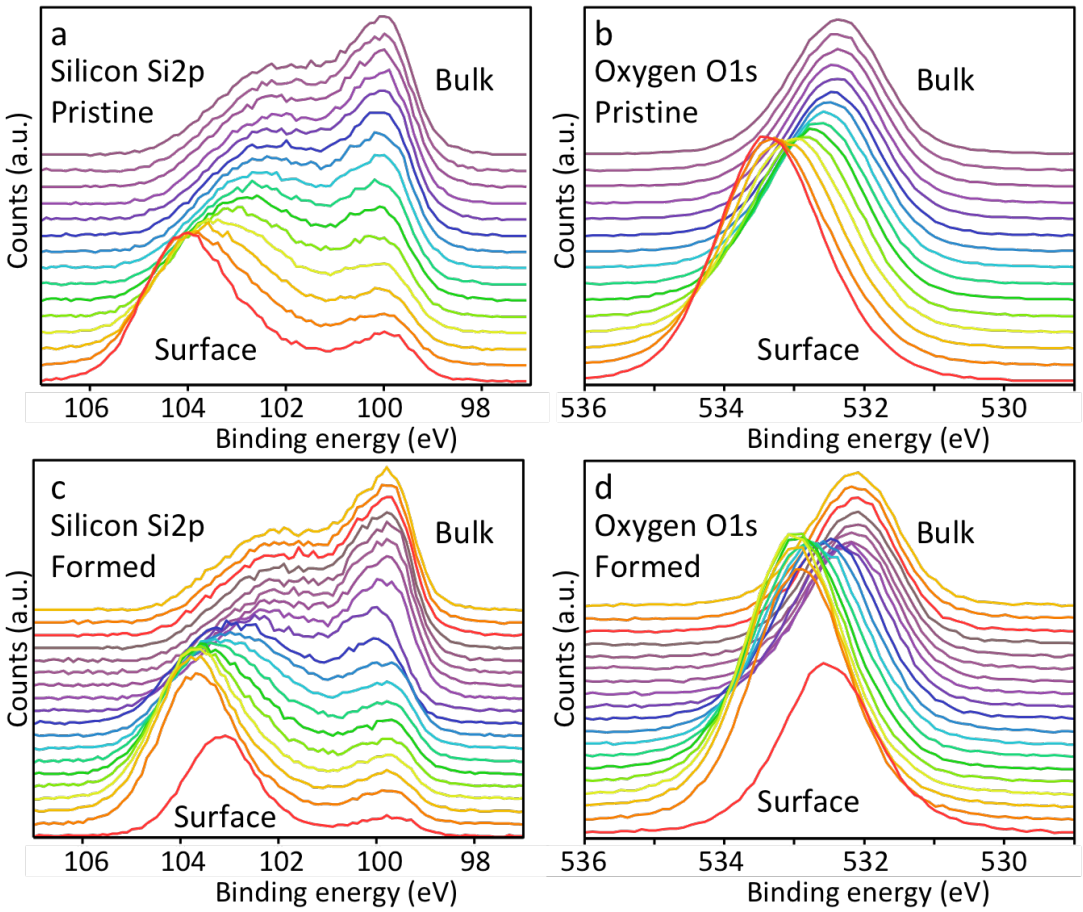

Figure 7.14. Si2p and O1s depth profile spectra from pristine and formed SiO_x, stacked to best display the changes with depth. The spectra have not been normalised. (**a**) Pristine Si2p spectra, demonstrating a gradual decrease in the high binding energy peak and associated increase in the low binding energy peak. (**b**) Pristine O1s spectra, showing a gradual shift to lower binding energy. (**c**) Formed Si2p spectra, demonstrating a gradual decrease in the high binding energy peak and corresponding increase in the low binding energy peak, similarly to **a**. The change from the first to second layer is the most pronounced change between neighbouring levels. (**d**) Formed O1s spectra, showing a gradual shift to lower binding energy, similarly to **b**. As in **c**, the change from first to second layer is the most pronounced.

Figure 7.14 shows all Si2p and O1s depth profile spectra for each sample. In **Figure 7.14a** and **c**, the Si2p peak around 104 eV decreases in intensity with depth and appears to shift to lower binding energy, while the peak at around 100 eV increases in intensity. The 104 eV peak likely corresponds to silicon dioxide-like Si^{4+}, suggesting that the surface is more oxygen-rich than the bulk and so should be more insulating. This may contribute to the high voltages required to electroform the oxide, as

discussed in **7.2**, **7.3** and **7.4**. The O1s spectra in **Figure 7.14b** and **d** show a single peak shifting to lower binding energy with depth. This also indicates reduced oxygen content in the bulk relative to the surface. These observations support the supposition in chapter **6.6** that the Si2p peak between 99 eV and 100 eV represents elemental silicon inclusions below the silicon dioxide-like surface and so demonstrates less charging.

Notably, for the formed sample in **Figure 7.14c** and **d**, the Si2p and O1s peaks from the surface layer are shifted to a lower binding energy relative to the subsequent level. Following this, the peaks shift to lower binding energies, as in the pristine spectra in **Figure 7.14a** and **b**. The difference in the intensity of the surface layer and subsequent layer spectra for the formed sample is also greater than between any other two consecutive Si2p or O1s spectra. This is interesting, as the measurement parameters, including sample area, were the same for each measurement. The signal intensities should show more gradual changes with depth.

Figure 7.12a demonstrates that there is more carbon present on the formed than the pristine sample. The low surface layer Si2p and O1s signals in **Figure 7.14c** and **d** may thus be due to carbon contamination that is removed by the ion milling. Another cause of signal reduction could be poor focusing of the x-ray beam due to an instrumental error in the autofocus. As discussed in chapter **6.6**, if the beam is not focused at the surface, then fewer photoelectrons will be generated and thus their incident intensity at the detector will be reduced.

As demonstrated in **7.4**, SiO_x is deformed by electrical stress, increasing the surface roughness. This may have at least two possible effects. Firstly, the x-ray beam focus at the surface may be poor, decreasing the number of photoelectrons generated. This may be conflated with the instrumental focus discussed above, as roughness can cause poor surface focus. Secondly, the geometry of a rough surface effectively increases the surface thickness, as illustrated in **Figure 6.15**. Over the course of a depth profile, ion milling would smooth the surface, reducing these effects. This appears to happen by the fourth layer for the formed sample, where the peaks around 104 eV for the Si2p and 533 eV for the O1s reach maximum intensity. This contrasts with the pristine sample, in which the surface layer shows the largest intensity for these peaks.

Poor focus, surface roughness, contamination, dipole charging and instrumental shifting may all contribute to the shifting and intensity variations between the pristine and formed SiO_x spectra in **Figure 7.13** and **Figure 7.14**. Thus, comparing the surface composition before and after electroforming may be limited to a discussion of these issues rather than compositional effects. However, the sample bulk may be more

informative because variations in roughness and contamination should be removed or reduced by ion milling. Dipole charging and instrumental shifting might still occur but the former may be analytically relevant and the latter accounted for with a suitable binding energy scale calibration.

To study changes in the switching layer bulk, it is necessary to determine at which sampling layer the bulk has been reached. **Figure 7.15** shows the same data as in **Figure 7.14** with the spectra overlaid rather than stacked. As indicated by the grey boxes, the spectra appear to stabilise by the thirteenth layer for the pristine sample and the fifteenth layer for the formed sample. It is therefore appropriate to compare the fifteenth layer for each sample, to ensure they have received the same dose of x-rays and argon ions.

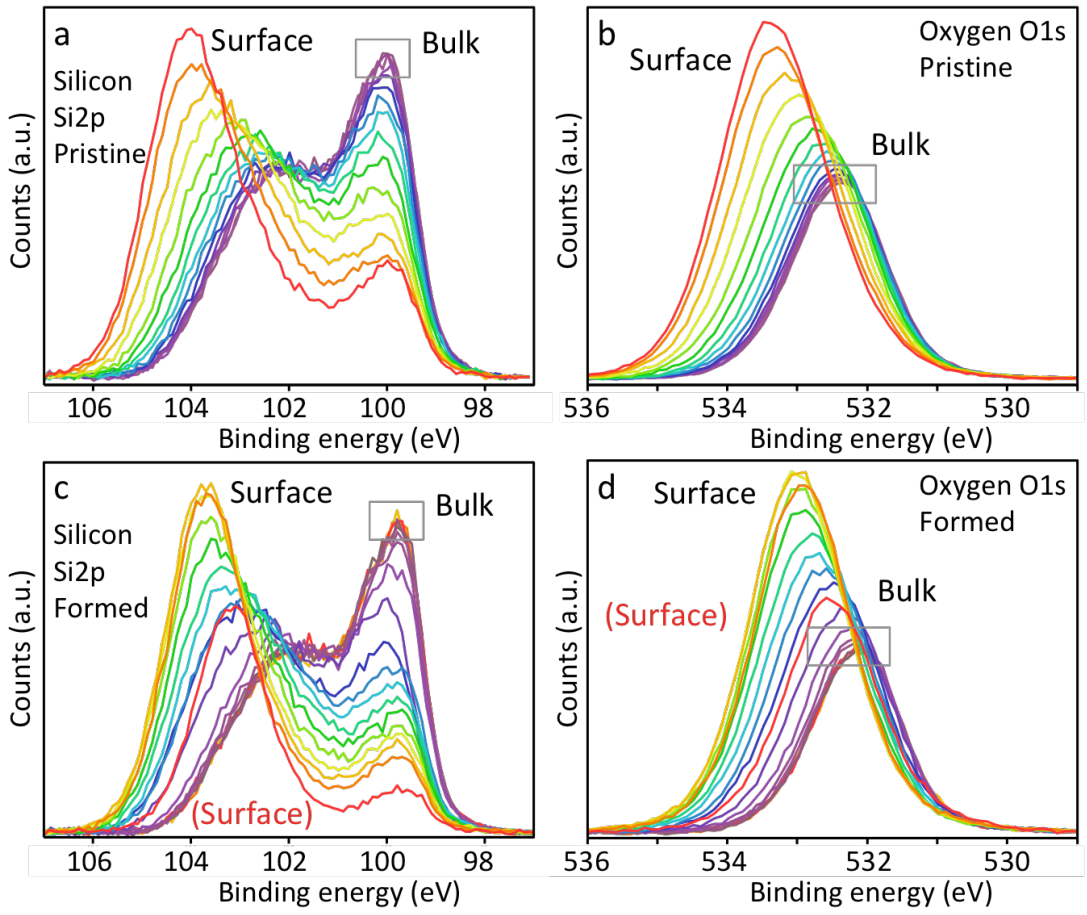

Figure 7.15. Si2p and O1s depth profile XPS spectra, showing the same data as in **Figure 7.14**, but overlaid. The data have not been normalised. (**a**) Pristine Si2p spectra. (**b**) Pristine O1s spectra. (**c**) Formed Si2p spectra. (**d**) Formed O1s spectra. Note that the first measurements in **c** and **d**, the red lines indicated by the red '(surface)' text, are closer to the bulk measurements than the subsequent spectrum, labelled 'surface' in black. The grey boxes indicate the stabilisation of the spectra with depth. In **a** and **b**, the spectra appear stable by the thirteenth layer. In **c** and **d**, the spectra appear to stabilise by the fifteenth layer.

Figure 7.16 shows the Si2p and O1s spectra from the fifteenth layer of the depth profile. There appears to be a small shift for each pair of spectra, with the spectra for the formed sample moving by around 0.2 eV to lower binding energy relative to the pristine sample. It is possible that this shift is instrumental, as this is within the range discussed previously.

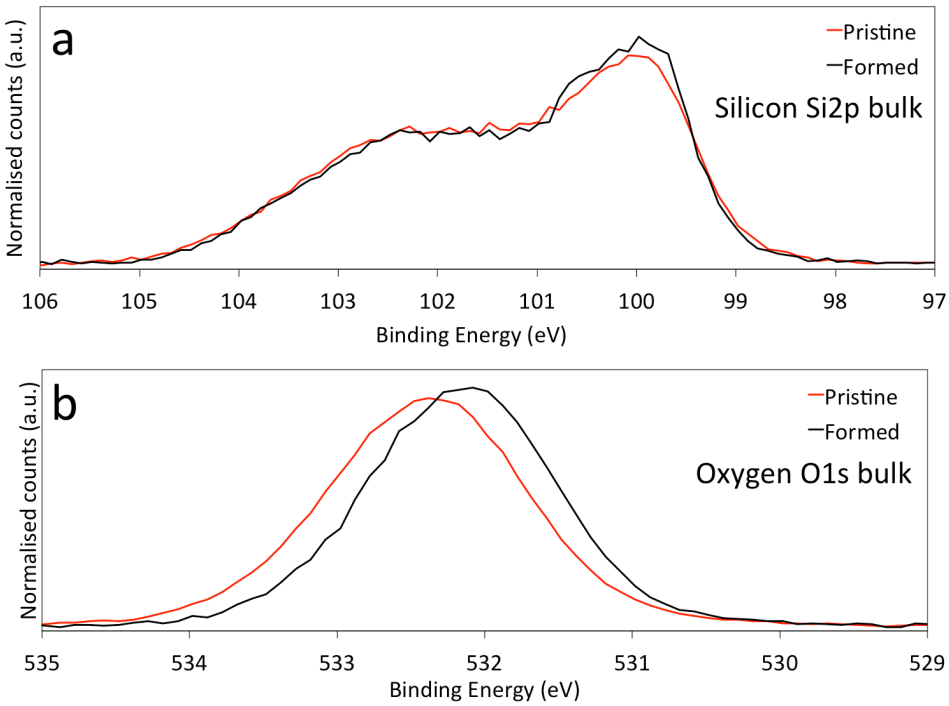

Figure 7.16. Si2p and O1s spectra of the sample bulk, defined as the fifteenth layer from **Figure 7.15**. The spectra have been normalised to reflect a fixed total silicon signal. (**a**) The Si2p spectra have similar shapes, although there appears to be a shift to slightly lower binding energy for the formed sample. (**b**) The O1s spectra have similar shapes, although there is a shift of around 0.5 eV to lower binding energy for the formed sample.

The C1s spectra in **Figure 7.12b** indicated up to 3 eV of shifting might have occurred between measurements. However, no carbon was present in the bulk. It is not appropriate to calibrate bulk spectra using surface measurements, given the artefactual convolutions that have been discussed. However, the ion milling process introduces argon into the sample. As a noble gas, argon is inert so would not readily bond with atoms in the sample.[181] It should be mentioned that argon does form an oxide, though this does not occur under milling conditions.[182] Thus, implanted argon should provide a suitable means of calibrating bulk spectra.

Figure 7.17 shows the argon Ar2p spectra from the pristine and formed samples. There does not appear to be a shift between the samples. The energy resolution of the measurements is relatively low, so the true peaks may be at energies that were not

sampled. However, the similarity in the shapes of the two spectra suggests that this may not be the case and that there has been no instrumental shift.

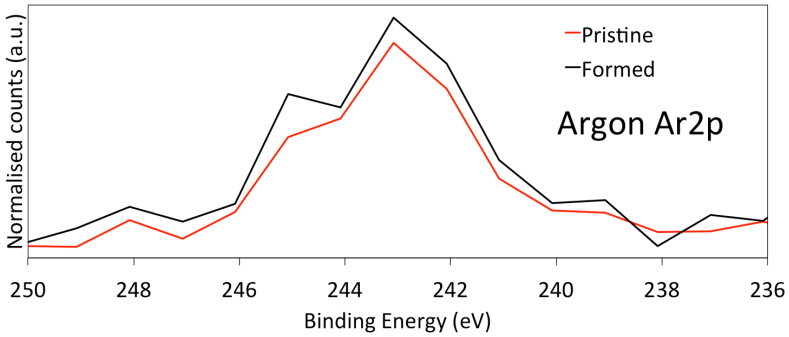

Figure 7.17. Argon Ar2p spectra from the pristine and formed sample bulks. The spectra have not been normalised. The maxima appear to be aligned in the binding energy scale. Additionally, the spectra seem to have similar shapes. This may indicate that there has been no instrumental shifting between the measurements.

Rather than an instrumental shift, another cause for the shifting shown in **Figure 7.16a** could be preferential removal of oxygen by argon sputtering, as discussed in chapter **3.4**, leading to a reduction of the oxide as a result of depth profiling,[121] although this has also been argued against in the literature.[120] However, this effect should be comparable between samples, so would not introduce an inter-sample shift. It is therefore reasonable that the shift resulted from changes to the bulk composition, as expected for an electroformed oxide.

To better understand how the shifting observed in **Figure 7.16a** describes compositional changes, the spectra must be deconvoluted to discern contributions from particular bonding configurations. **Figure 7.18a** and **b** show Si2p XPS spectra of the switching layer in the pristine state and after electroforming, respectively. The spectra have been fitted with five components. Each is separated by around +1 eV in binding energy, corresponding to the increasing oxidation state of silicon, in agreement with the literature.[40,112] Nominally, in order of increasing silicon-oxygen coordination, these are elemental Si^{0}, the sub-oxides Si^{1+}, Si^{2+} and Si^{3+} and the silicon dioxide-like Si^{4+}. As discussed in chapters **3.4** and **6.6**, each component may be modelled by a single Voigt profile. A Gaussian:Lorentzian ratio of 1:1 was used because it was the best fit for the rising edge of the spectrum at around 99 eV. The full width at half maximum of the sub-peaks was 1.35 eV ± 0.25 eV and the shifts 1 eV ± 0.3 eV from the Si^{0} position. The allowed range on the shifts accounted for variations in previously reported binding energies of the components and thus their expected positions. The allowed range on the width accounted for variations in bond length between components, with higher silicon-oxygen coordinations typically showing broader peaks.[117]

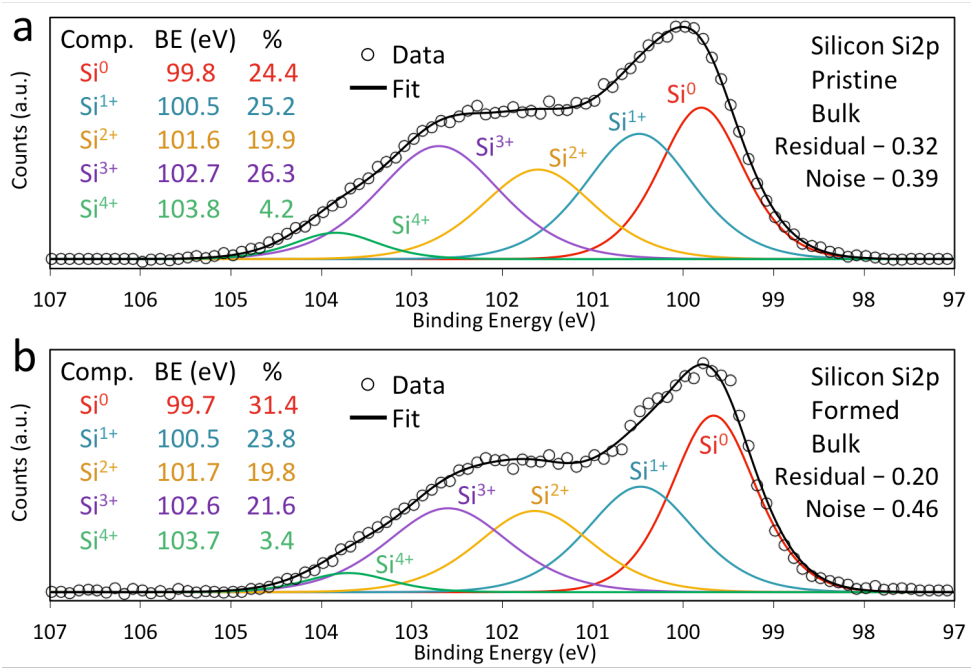

Figure 7.18. Bulk Si2p XPS spectra from the pristine and formed active layer. (**a**) Pristine Si2p spectrum, showing the presence of five component configurations. (**b**) Electroformed Si2p spectrum, showing decreases in the suboxide (Si^{1+}, Si^{2+}, Si^{3+}) and oxide (Si^{4+}) contributions, with a corresponding increase in elemental silicon inclusions, Si^0. The residual and noise normalised standard deviation values are given, indicating that both sets of fitted sub-peaks are of a high quality.

Figure 7.18a demonstrates that the SiO_x is mainly composed of the suboxides Si^{1+}, Si^{2+} and Si^{3+}. Combined with the relatively small contribution from Si^{4+} and large contribution from elemental Si^0, this highlights the non-stoichiometric, silicon-rich nature of the switching layer. In addition, the suboxides suggest that the material should be amorphous, as crystalline silicon or silicon dioxide should be characterised by single, sharp Si^0 or Si^{4+} peaks, respectively.[183]

Following electroforming, as shown in **Figure 7.18b**, the film is reduced. This is demonstrated by the decrease of between 0.1% and 4.7% in contributions from the oxidised silicon components Si^{1+}, Si^{2+}, Si^{3+} and Si^{4+} and an 7% increase in elemental silicon, Si^0. The largest contribution to the spectrum in **Figure 7.18a** is Si^{3+}. As discussed in **7.2**, this is a configuration that has been correlated with dangling bond defects and intrinsic interfaces in SiO_x.[40,112]. Such interfaces may be located between the columns whose tops were observed with AFM in **Figure 7.1**. It has also been suggested that the asymmetric configuration of the oxygen atoms in Si^{3+} predisposes them to electric field-induced dissociation. Interestingly, Si^{3+} shows the greatest decrease of all the components, 4.7%, following electrical stress. Thus, it appears that this configuration is preferentially reduced under electrical stress. This

supports the suggestion that the intrinsic structure of the active layer favours field-driven oxygen dissociation.

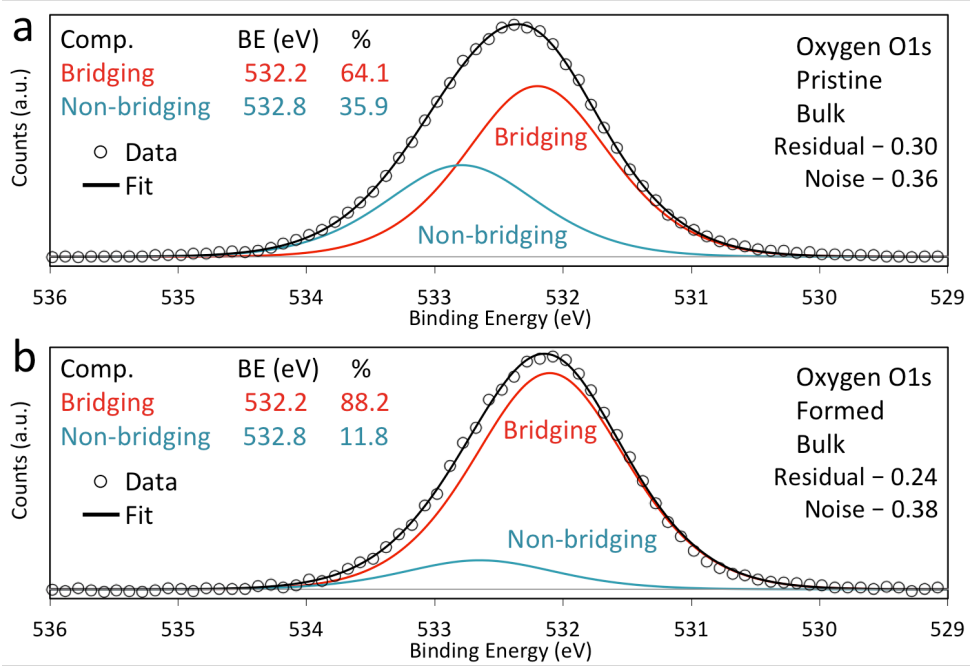

Figure 7.19. Bulk O1s spectra from the pristine and formed active layer. (**a**) Pristine O1s spectrum, demonstrating oxygen in bridging and non-bridging configurations at around 532.2 eV and 532.8 eV, respectively. (**b**) Electroformed O1s spectrum, showing a decrease in the presence of non-bridging configurations relative to bridging, silicon dioxide-like configurations. There is 7% decrease in the total oxygen content of the film. The residual and noise normalised standard deviation values are given, indicating that both sets of fitted sub-peaks are of a high quality.

Figure 7.19a presents the O1s XPS spectrum of pristine SiO_x, showing the presence of two components. Voigt profiles with a Gaussian:Lorentzian ratio of 11:9 and width of 1.45 eV ± 0.05 eV were used to fit the data, with an inter-component shift of 0.6 eV ± 0.25 eV. The lower binding energy component around 532.2 eV is commonly attributed to bridging oxygen in tetrahedral silicon dioxide bonding arrangements.[112,184,185] However, the tetrahedral Si^{4+} contribution in **Figure 7.18b** is only 4.2%, and such bonding is characteristic of crystalline silica.[183] Given the large, non-crystalline suboxide contributions shown in **Figure 7.18a**, it may be that the peak at 532.2 eV corresponds to oxygen bridging two silicon atoms whose bonds do not necessarily have a tetrahedral arrangement. The higher binding energy peak at 532.8 eV is less well reported. However, it seems likely that such a peak might correspond to non-bridging oxygen defects such as interstitial oxygen and peroxy linkages or radicals, which are often reported at higher binding energy than bridging components.[184-187]

As shown in **Figure 7.19b**, the contributions change by 24.1% in favour of bridging oxygen following electroforming. Normalising the data to fixed total silicon intensity in each sample, there is also a 9% decrease in total oxygen, indicating its loss from the film. Accounting for this, the total bridging contribution increases by around 25% and the total non-bridging decreases by 70%. Thus, predominantly non-bridging configurations appear to lose oxygen. In addition, after accounting for the total oxygen loss, these data also suggest that some non-bridging oxygen might be converted to bridging oxygen. Notably, it has been suggested from simulation results that non-bridging oxygen, particularly peroxy linkages, migrates readily in amorphous silicon dioxide under electron injection, such as might occur due to electrical stress.[135] As a result, superoxide ions, O_2^-, are released from the material. This model is supported by the O1s results presented here.

The apparent loss of oxygen from the SiO_x supports earlier suggestions that structural deformations occur during switching as oxygen is released. In particular, deformations of the top electrode and the active layer, as discussed in chapters **6.8** and **7.4**, respectively. Regarding the bubbles discussed in chapter **7.4**, oxygen may accumulate in them until being released when disrupted by an applied force, such as an AFM probe.

The stoichiometry, x, of the SiO_x may be calculated from XPS data. The most appropriate method should be the lineshape fitting method, because it excludes instrumental sensitivities, requiring only the Si2p measurement data.[188] It should be noted, however, that this method relies on the suitability of the fitting parameters used to obtain the component concentrations.

The lineshape fitting method requires the relative component intensities, Si_n, from the Si2p spectrum, each multiplied by its own silicon/oxygen ratio. n defines the silicon oxidation state, where n = 1 corresponds to Si^0 and n = 5 to Si^{4+}. These ratios are described by the relation (n–1)/2, thus the stoichiometry, x, may be calculated using

$$\text{Stoichiometry, } x = \sum_{n=1}^{5} \frac{Si_n(n-1)}{2} \qquad (11.1)$$

The stoichiometry of the pristine SiO_x, according to **Equation 11.1**, is 0.83. In the electroformed sample this value is 0.73, a decrease of 12%. Although this change is likely to be real, the values might be inaccurate if oxygen was preferentially removed from the active layer during depth profiling with argon, as discussed previously in this chapter and in chapter **3.4**. Furthermore, the observations on **Figure 7.18** and **Figure 7.19**, and thus the difference in stoichiometry, might be an underestimate of the localised stoichiometry change for a single electroform. The XPS sampling area was

large in comparison to each needle contact point. It is therefore reasonable to suppose that the change to the film as a whole is not very pronounced, whereas the local changes at the contact point may be much more pronounced than those measured.

7.6 Chapter summary and conclusions

In this chapter I have looked at changes to the switching layer as a result of resistance switching. These included the appearance of bubbles and spots on the surface and a reduction of the SiO_x.

Firstly, I attempted to switch the oxide directly but found this was more difficult than with a titanium nitride top electrode. However, switching was possible, although the standard current compliance of 3 mA resulted in extreme material deformation, visible optically. I found that reducing the compliance reduced the extent of the structural changes. In general, resetting the switching layer in this manner was not possible.

I used optical microscopy to determine the degree of structural change induced with a reduced current compliance. This included large and delocalised distributions of orange bubbles, along with dark spots at the contact point of the tungsten needle. I also found the bubbles were removed by solvent cleaning, leaving snaking surface features.

Using AFM, I determined that the orange bubbles could readily be burst and moved around on the surface of the active layer. The instability of the bubbles made them difficult to measure, though it would be an interesting piece of follow-up work to try and study them with other techniques. Additionally, both the bubbles and the snaking features were softer than the surrounding material. The bubbles appeared softer than the snakes, producing a restorative force when compressed. The pristine SiO_x was bumpy on the nanoscale, suggesting an intrinsic columnar microstructure, and became rougher following electroforming.

My XPS results indicated the pristine SiO_x surface is oxidised in comparison to the bulk, which contains a larger proportion of elemental silicon inclusions and Si^{3+}, a configuration that has been correlated with intrinsic columnar microstructure and may promote oxygen dissociation under electrical stress. Additionally, electroforming reduces the SiO_x, removing oxygen and increasing the proportion of elemental silicon present in the bulk. These results support a correlation between electrical stress, oxygen release and structural deformation.

In this chapter, I have presented studies of areas of the switching layer that are large relative to the expected local changes occurring at the point of contact during electroforming. In particular, conductive filaments in RRAM devices are generally believed to have diameters of a few to tens of nanometres.[32,189-191] Although my data so far enables a discussion of structural and compositional changes resulting from

switching, discerning the extent of localised changes, such as filaments, is not feasible. This particularly limits the discussion of stoichiometric changes. Therefore, further study of the area local to the point of contact should be informative. In addition, the cause of bubble delocalisation from the needle contact point is not clear. Further investigation of local changes might also provide some insight into this phenomenon.

8. Localised structural and conductive changes

8.1 Chapter introduction

In this chapter I will present results that demonstrate a correlation between structural deformation and conductivity changes on the nanoscale, at the positions of individual electroform locations on the SiO_x. Using CAFM, I will then demonstrate that these locations may be mechanically etched to reveal a three-dimensional conductive structure in the bulk. Following this, I will discuss some of the issues that this tomography method faces, namely that the effect of the measurement process on the probe, and thus the data obtained, cannot be disregarded.

As shown in **7.4**, dark spots were typically present on the active layer at the point of contact when electroforming directly with a tungsten needle. These spots varied in size from a few to tens of micrometres. They were also not removed by ultrasonication in organic solvents and persisted in vacuum environments, so were more robust than the orange bubbles discussed in the same chapter. I used AFM to locate and probe these features. The tip and region of interest were not always well aligned, so the most straightforward means of locating the point of contact was to scan a large area at a low resolution while applying a bias. Thus, the region of interest should show up as a conductive spot, or group of spots, in a large, otherwise-insulating area.

8.2 Structural changes at the point of probe contact

Figure 8.1a and **b** present topography and current maps of a tungsten needle contact point following electroforming. There is a roughly circular deformation present, composed of many bubble-like, raised points. Additionally, at the centre of the feature there is a large depression that appears smoother than its surroundings. The raised and depressed areas extend above and below the surface by more than the thickness of the SiO_x. Notably, this feature is very rough, with an RMS roughness of around 70 nm.

Figure 8.1b demonstrates conductivity at the point of contact. However, it is not homogeneous across the deformation, appearing in small spots, lines and curved lines. There are some larger areas but they are small relative to the whole feature. **Figure 8.1c** shows the current map overlaid on a three-dimensional topography plot. The conductive patches are situated between the bubble-like protrusions that compose the deformation. As discussed in chapter **3.2**, conductivity between bubbles may be an artefact of tip wear. However, it may indicate compositional variation, as suggested in chapter **6**. The bubble-like features of **Figure 8.1** are likely of a similar origin to those of

Figure 6.8, where a top electrode was present. Specifically, both are composed of smaller, bubble-like protrusions and are induced by electrical stress.

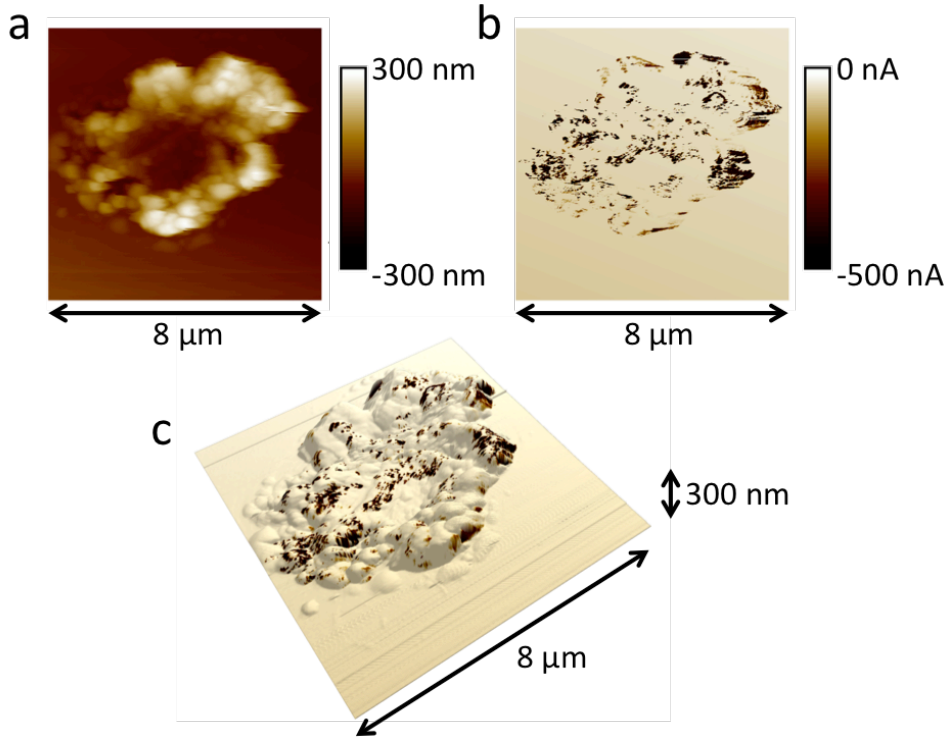

Figure 8.1. CAFM images of oxide deformation at the point of contact of the tungsten needle. (**a**) Topography map. (**b**) Current map of the feature in **a**. (**c**) Three-dimensional plot of the data in **a**, with the current map in **b** overlaid. The deformation appears to be composed of many smaller bubbles. In places, they are taller than the thickness of the switching layer, over 100 nm. Additionally, some areas are depressed to a similar extent. Small conductive regions are present and appear to be confined to the areas between the bubbles.

The heights of the protrusions shown in **Figure 8.1** are greater than the thickness of the switching layer: hundreds of nanometres, in comparison to 37 nm. This suggests either an upthrusting of material from below or an expansion of the SiO_x. In either case, the mechanical properties of the deformation might be different to those of pristine material. In particular, if the SiO_x has expanded then the deformation may be softer or more compressible.

Figure 8.2 presents an AFM force-distance spectrum of a bubble-like protrusion from the SiO_x deformation at the probe contact point. The cantilever spring constant was nominally 0.1 N/m, in agreement with the gradient of the spectrum on pristine SiO_x, as is also shown. The approach curve on the bubble overshoots the SiO_x gradient around 0.2 µm. This implies that, as the tip presses into the bubble, the force on the cantilever does not increase as much as it would do for the same vertical movement on pristine

SiO_x. Interestingly, this occurs at around the same height as the bubble, suggesting sufficient force has been applied to compress it.

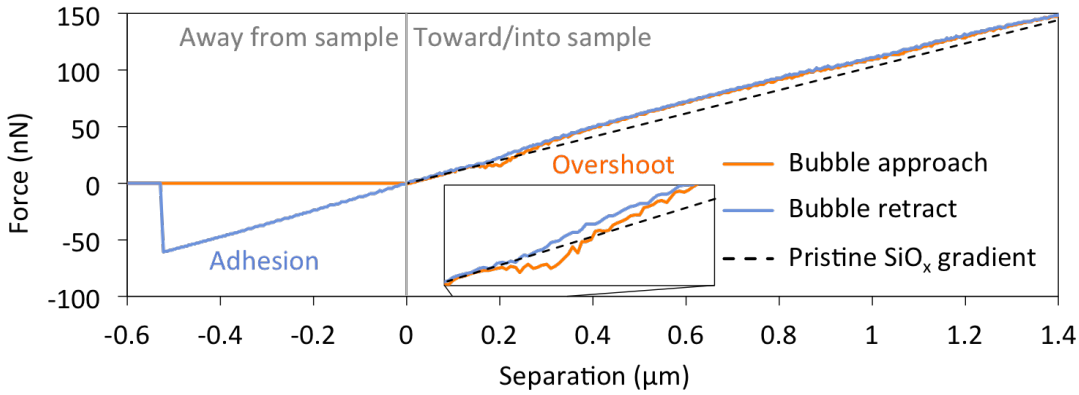

Figure 8.2. Force-distance spectrum of a bubble-like protrusion from the deformation on the active layer shown in **Figure 8.1c**. The probe approached from a setpoint more negative than -0.96 V, not contacting the sample, to a more positive setpoint. In total, the controller moved the probe vertically 2 µm, pressing the tip into the sample and bending the cantilever. The dotted line demonstrates the gradient of the spectrum on pristine SiO_x. There is an approach overshoot around -0.2 µm, also inset, and the spectrum is not a straight line after this until around 1 µm. These features indicate that the AFM tip is encounters a flexible material. The retract data demonstrates adhesion as the tip is moved away from the bubble, although this is not distinguishable from that observed on pristine SiO_x.

The maximum gradient of the approach curve in **Figure 8.2** occurs just after the overshoot at 0.2 µm, as the curve tends towards a similar gradient to the pristine SiO_x. This suggests the bubble bears a restorative force against the probe motion. Following this, both approach and retract are non-linear and deviate to a lower gradient than that of the pristine SiO_x. This indicates the deformed material is softer than pristine SiO_x, as the force from the surface on the cantilever increases more slowly as the separation becomes more positive. Notably, adhesion is evident in the retract curve, as the separation becomes negative with the tip pulling away from the bubble. The force becomes negative for around 0.5 µm. However, this part of the spectrum was not different to that of pristine SiO_x. Therefore, it appears that the bubble does not deform significantly away from the surface, only inwards with the downward probe motion.

Given the observations on the XPS data in **7.5**, it is appropriate to consider surface distortions in relation to oxygen movement. Electroforming reduces the oxygen content of the switching layer, so mobile oxygen is likely to leave through the surface, straining the oxide matrix as it migrates. This strain may cause topographical distortions at the surface as mobile species build up. In particular, as discussed in **6.8**, Coulombic repulsion between charged oxygen molecules might be a factor in the deformations

extending beyond the thickness of the switching layer. With sufficient accumulation the oxygen may be released, leaving bubble-like, flexible features. Notably, following electrical stress, transmission electron microscopy has been used to observe voids at the interface between the active layer and the top electrode.[135] It is therefore reasonable to suggest that deformation of the switching layer under electrical stress is responsible for top electrode deformations such as those discussed in **6.7** and **6.8**.

These observations suggest the morphological changes reported herein result from mobile species causing the switching layer to expand, rather than material from below being upthrust. In particular, the features in **Figure 8.1** are compressible and elicit restorative behaviour when compressed, as shown in **Figure 8.2**. This behaviour should be characteristic of an flexible surface with a less dense interior or internal void.

Figure 8.1 is useful in addressing the suggestion in **7.5** that the SiO_x stoichiometry calculations might be underestimates due to the small area of needle contact relative to XPS sampling. I found the mean area of deformations at the contact point to be around 24 μm^2. With 30 µm separation between neighbouring electroforming points, each point would be in an area of 900 μm^2. This ratio is around 0.026, giving an adjusted stoichiometry decrease of 468% and oxygen loss of 346%. These values are not realistic. Therefore, it is likely that the regions surrounding the electroform spots, where orange bubbles and snakes were present, also contributed to the measured stoichiometry change.

I may now consider why, when electroforming with a tungsten needle, the orange bubbles discussed in **7.4** were not localised to the point of contact. Notably, they did not appear when using a negative needle polarity, suggesting polarity-dependent formation. In addition, I have shown in **7.5** that switching with a positive needle bias causes oxygen to be lost from the SiO_x. I therefore assume that a positive bias drives oxygen toward the surface of the switching layer and that some of this occurs away from the needle contact point.

For a tungsten needle stressing the SiO_x, the electric field is strongest at the contact point. Here, the field may provide accumulated ions with sufficient kinetic energy to rupture the surface, producing larger deformation features such as that shown in **Figure 8.1**. Further from the contact point, where the field is weaker, ions may have less energy and instead produce orange bubbles and smaller features such as the snakes and spots shown in **Figure 7.10** and **Figure 7.11**. However, these features were observed more than 50 µm from the contact point, a large distance for a solely field-driven effect. Therefore, I suggest that, although bubble formation appears polarity-dependent, the current is also crucial to this phenomenon.

The deformability of silicon oxide increases with temperature, in turn reducing the breakdown field strength.[192] Thus, switching with a tungsten needle might produce sufficient Joule heating in the SiO_x to both enable surface deformation at large distances from the needle and reduce the voltage required for breakdown-like effects such as oxygen loss. The latter of these might be responsible for the appearance of bubbles on the surface of the switching layer. It should be noted that this argument is speculative and incomplete. It does not account for the orange bubbles disappearing in a vacuum of 10^{-8} Torr. In addition, it does not provide insight into bubble composition, as I was unable to perform spectroscopic measurements on them.

8.3 Reducing the size of the observed surface deformations

The conditions I have used so far for electroforming the SiO_x with a tungsten needle have not been optimal, resulting in surface features much larger than individual filament sizes quoted in the literature.[14,48,189,193] Furthermore, I applied slow voltage sweeps over tens of seconds, longer than the duration of the short pulses often used to operate high-endurance RRAM devices.[66,166,194-196] As discussed in **7.3**, current compliance is not implemented immediately, so the current likely exceeds it. Despite trying to account for this with lower current compliance levels, I observed large deformations at the point of contact, possibly caused by excess Joule heating from current overshoot. However, this approach allowed me to induce distinct structural changes from which I could study the switching mechanism. This may be likened to a worst-case scenario in which the device is intentionally pushed towards dielectric breakdown by overstressing the active layer.

Structural changes should be considered with respect to device failure and lifetime. Large deformations are inherently bad for performance so should be limited or prevented. Field-driven oxygen migration is unavoidable if, as is established, it is required for the resistance of the active layer to change. However, as mentioned in **8.2**, deformation and breakdown of silicon oxide are more likely with increasing temperature, so it is reasonable to suppose that heating effects induce significant material transformation. In this case, limiting the energy input during switching is necessary, in particular by limiting current and thus Joule heating.

As mentioned, an alternative to voltage sweeps with current compliance is voltage pulses, either with or without current compliance.[194] By controlling pulse duration, the energy input to the device may be controlled; a pulse with a similar duration to the electroforming process, tens of nanoseconds,[194,196] significantly reduces the total current in the filament. This is because electrical stress is, ideally, removed simultaneously to the drop in device resistance, preventing damaging current overshoots and breakdown. Thus, I investigated whether using voltage pulses rather

than sweeps in this work might reduce the feature size at the point of contact, producing changes in the SiO_x more in line with those expected and observed in other devices.

To explore whether voltage pulses reduced the feature size at the point of contact, a colleague electroformed the SiO_x with a tungsten needle, using either +20 V or -20 V pulses for 60 ns without current compliance. Although these voltages are higher than those normally used in switching, they were required to overcome the insulating surface barrier, as discussed in **7.2** and **7.4**. Following electroforming, the contact points were not optically visible and were best located using CAFM, similarly to **8.2**. To locate spots, I made a note of sample features near to the needle location, for example, nearby top electrodes or blemishes.

Figure 8.3 shows CAFM conductivity and QNM energy dissipation maps for the point of contact after pulse biasing. The energy dissipation data for each pixel in the images shown in **Figure 8.3a** and **b** was generated during the QNM-mode scans by averaging five consecutive force-distance spectra at the same location. As discussed in **3.2**, the difference between approach and retract curves of a force-distance spectrum may be integrated to obtain the energy dissipated by the AFM cantilever during the interaction, giving information on the flexibility of the surface. As mentioned in the caption of **Figure 7.8**, the energy dissipation data is given in keV because this scale is more suitable for reading than the value in Joules.

The CAFM scans in **Figure 8.3c** and **d** were made with a sample bias of -5 V. A negative polarity was used to prevent anodic oxidation of the oxide.[135] Notably, this is a high voltage relative to the 0.5 V typically used for reading a device state. However, the resistance of the spots, once formed, was below 200 Ω in each case. Given that the resistance of the CAFM probe was around 2.5 kΩ, the applied voltage is mainly dropped across the probe, such that the bias across the formed location is only around 0.4 V.

Conductive regions are present for both bias polarities and are correlated with the appearance of surface distortions that are more flexible than the surrounding material. The surface deformations shown here are significantly smaller than those presented in the previous two chapters. For both the positive and negative pulse polarity, the lateral dimensions of the features are around 0.5 µm and heights around 40 nm. Crucially, this is roughly equal to the thickness of the switching layer and comparable to observations made with transmission electron microscopy of distortions in SiO_x-based devices.[135] The small size of the features, relative to that of **Figure 8.1**, suggests the oxide was subjected to less stress by pulsing than sweeping. In addition, no other surface

features such as orange bubbles or snakes were observed; the structural change was confined to the small bubbles shown in **Figure 8.3**.

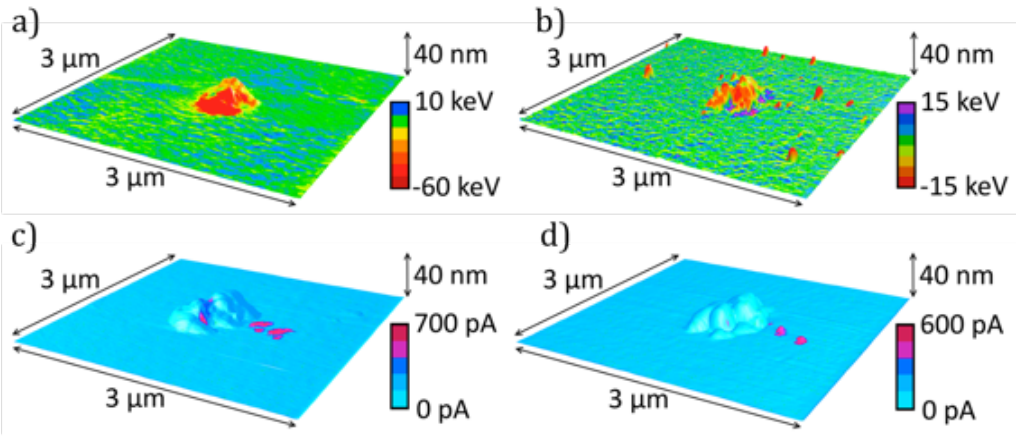

Figure 8.3. AFM images of the SiO_x surface following pulsed electroforming with a tungsten needle. (**a**) and (**b**) energy dissipation mapped onto topography for positive and negative needle polarities, respectively. In each case, the feature is softer than the pristine material, evidenced by increased energy dissipation (red) compared to the surroundings (green). The dispersed points of high dissipation (red) around the central feature in b are likely debris produced during surface deformation. This material is not present in the CAFM image so was likely loose, being measured during the energy dissipation scan but removed during by the tip-sample contact of CAFM. (**c**) and (**d**) CAFM current mapped onto topography for positive and negative needle polarities, respectively. Conductive regions appear on and off the feature. Note CAFM and QNM measurements were made separately.

The colour mapping in **Figure 8.3a** and **b** shows surface flexibility, with pristine SiO_x as baseline. Negative values indicate the surface flexed more than the pristine material, with less energy being stored in the spring of the AFM cantilever. Conversely, positive values indicate the surface became harder. The correlation of red areas with raised surfaces features indicates the switching layer deformed, producing bubble-like, flexible protrusions. Both stress polarities resulted in oxide expansion; this was correlated with increased local conductivity, as evidenced by purple spots in the current maps of **Figure 8.3c** and **d**. The material softened more under a positive than negative bias, dissipating around 60 keV compared to 15 keV more than the pristine surface in the AFM tip-sample interaction. In addition, negative bias also produced hardened regions, dissipating around 15 keV less than pristine SiO_x; the cantilever stored more energy in harder areas.

It is notable that both positive and negative bias produced bubbles. For the former, this might be explained in part by field-driven movement of oxygen to the top surface. However, under negative bias, oxygen should be driven to the bottom interface. I would

therefore expect that, if a distortion appears at the top surface under negative bias, it would be a projection of oxygen accumulation at the bottom interface. Thus, the top surface deformation should be wider and flatter under negative bias than under positive bias, but this is not the case in **Figure 8.3**.

Given that switching in my devices is unipolar, oxygen movement may be dominated by thermal effects.[197] There is current in both polarities and the surface deformations in **Figure 8.3a** and **b** have a similar size and appearance. Thus Joule heating, rather than the electric field, may be responsible for oxygen diffusing to and escaping from the top surface and causing deformations. This may be a different situation to that of bipolar devices in which switching and surface distortions are dominated by field effects.

The current maps in **Figure 8.3** were consistent over multiple scans. This indicates a stable conductive pathway in the active layer, rather than an artefact. However, in both **Figure 8.3c** and **d**, two conductive regions are adjacent to the bubble, closely spaced with similar shapes. This may indicate a tip artefact rather than a true feature shape. Therefore, I suppose that the topography measured with CAFM, at least here, is not reliable and that the current maps are qualitative indications of the presence of conductive pathways. It is possible that the measured size of the conductive regions is an overestimate due to convolution with the scanning tip.

8.4 Collecting three-dimensional conductivity information

The features in **Figure 8.3** demonstrate a correlation between the change in morphology of the switching layer and the presence of a conductive pathway. However, they provide no insight into the three-dimensional structural and electrical changes that might occur within the active layer. Previously, detailed information on the size and shape of conductive regions within switching materials has been obtained from transmission electron microscopy studies of extrinsic systems [189,198] along with intrinsic devices exhibiting bipolar or surface-confined switching.[57,199] Such measurements are difficult in unipolar, bulk-switching intrinsic systems, principally due to poor electron microscopy contrast between conductive, oxygen-depleted regions and surrounding oxide. This is true of SiO_x-based systems,[200] though some progress has been made recently, demonstrating that there is some change in the silicon-oxygen coordination locally to the conductive region, as discussed in chapter **2.6**.[61,135] It is therefore of interest to study the effect of electrical stress below the surface of the switching layer.

As mentioned in chapter **2.6**, Celano *et al* used CAFM to study conductivity variations in extrinsic RRAM systems, namely copper-doped aluminium oxide.[189] They used a

hard, boron-doped, single-crystal diamond probe to etch the sample while measuring current. By pressing the tip into the surface and scanning continuously, sample material is gradually worn down as data is captured. Continuous recording produces a data set mapping current in three dimensions.

My devices were intrinsic, yet I reasoned that this conductance tomography method might be useful for studying filamentation. In addition, the method is in its infancy and might find use in a broad range of applications across materials science, particularly in the study of electronic devices. Although I hoped to better understand the switching mechanism in my samples, I also wanted to determine whether I might be able to contribute to developing the methodology.

Previous measurements were performed under vacuum conditions to prevent exposure of the etched surface to the atmosphere.[201] This helps in preventing oxidation of exposed material but it requires a more complicated setup than normal CAFM. This might prevent researchers from attempting measurements, particularly as many CAFM systems are not vacuum-capable. Further in the interests of accessibility, I used a piece of free medical imaging software, 3D Slicer,[129,130] for data processing. I also used boron-doped, diamond-coated silicon probes, as they are less expensive and more readily available than single-crystal diamond probes.

To probe filamentation in SiO_x, voltage pulses of up to ±20 V were firstly applied directly to the surface with a tungsten needle. Current compliance was set below the normal value of 3 mA as an additional means of reducing stress on the oxide. The resulting surface features were then located similarly to those in chapter **8.2**. The parameters were adjusted to induce etching once a region of interest had been found. The experimental process is shown schematically in **Figure 8.4**.

As shown in **Figure 8.4a**, the point of contact was located with 2 V applied to the sample relative to the CAFM probe, which was held at ground. This was a high enough voltage to locate conductive regions and low enough to not damage the sample or change the state of the formed location; as discussed in chapter, **8.3**, most of the voltage would be dropped across the CAFM probe as it had a significantly greater resistance than the filament. A series resistance of 178 kΩ was also used to reduce transient charging and discharging of defect states in the sample,[202] along with further reducing the electrical stress to the filament during measurement. During etching, the bias was reduced to 50 mV. The maximum current measured in the filaments was around 450 nA, corresponding to saturation of the detector. The true current might have been greater than this.

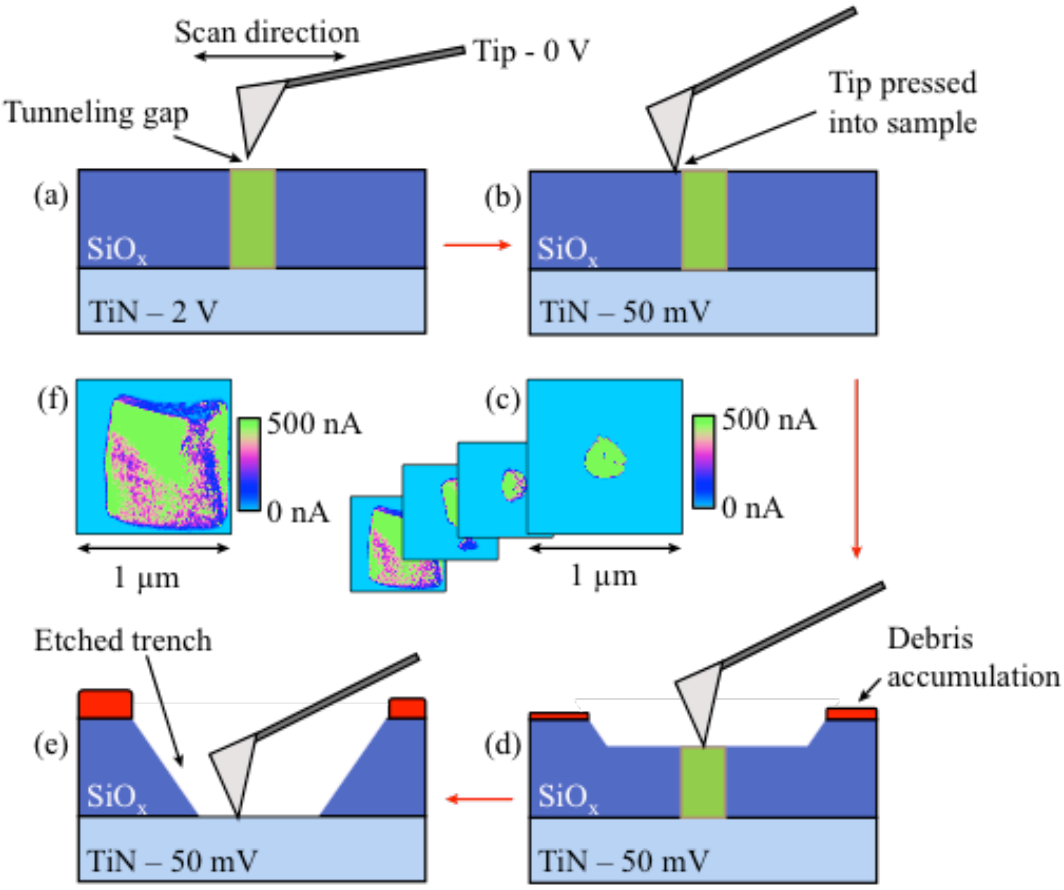

Figure 8.4. Schematic of conductance tomography. (**a**) Filaments are located with CAFM using a low setpoint voltage. Due to relatively small electrical contact area at a low setpoint, and thus low contact force, a high bias is applied. (**b**) Once the filament is located, the setpoint is increased, pushing the probe tip into the sample surface. The electrical contact area increases with setpoint as the contact force increases,[86] so the bias is lowered. (**c**) and (**d**) as the region is scanned, a current map is acquired. With repeated scanning, a trench is etched. Displaced material accumulates at the edge of the scan region. A set of current maps is produced. These may later be rendered into a tomographic image. (**e**) Eventually, the probe reaches the bottom electrode. (**f**) The final current map corresponds to a scan of the conductive electrode.

As shown in **Figure 8.4c** to **f**, continued scanning of the same area with a constant setpoint produced a set of two-dimensional current maps as material was scraped from the SiO_x surface. Eventually, a trench was etched and the current mapping became or approached lateral saturation. The number of slices obtained for each sample location varied greatly, most likely as a result of variations in tip geometry, scan size and tip velocity. Note that a fresh probe was used for each measurement to ensure that it was clean and conductive.

Each slice of each tomogram was composed of 256 scan lines, with 256 samples per line. This gave a maximum lateral resolution between 3.1 and 7.0 nm, depending on the image size. The true scan resolution was dependent on the apex geometry, the local work function of the sample and the pressure applied by the probe.[203] Although the radius of curvature of the diamond-coated CAFM probes was nominally 100 nm, the most prominent point of the tip should be an apex of a single nanodiamond. It is this point that will dominate the conduction of current.[204] This means the electrical contact might be confined to a few square nanometres whereas the mechanical contact, and thus topographical resolution, is tens of nanometres in diameter.

Following etching, I scanned the residual trench to determine how deep the probe had progressed and thus the vertical distance represented by the data. **Figure 8.5a** demonstrates a trench where it can be seen that the etching area is not square and extends vertically by around 95 nm, beyond the thickness of the active layer. This suggests firstly that lateral drift should be considered when examining the rendering of the filament. In addition, the vertical axis of the data set must be calibrated to best represent the thickness of the active layer.

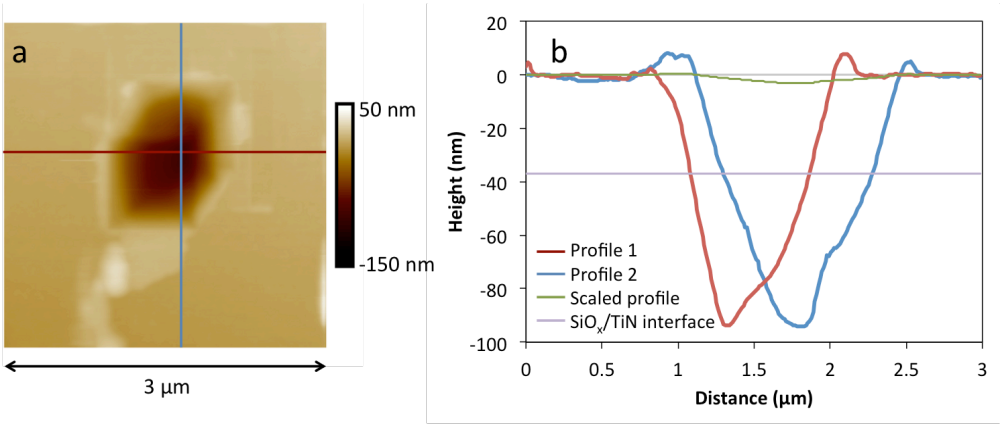

Figure 8.5. Trench produced as a result of performing a tomography measurement. (**a**) CAFM topography image, demonstrating the trench is not a cuboid volume, despite the sampling area being square. This indicates there was some drift in the measurement. (**b**) Cross-sections through **a**, demonstrating the trench extends around 95 nm below the SiO_x surface. This suggests the measurement continued into the bottom electrode and so scaling of the final data must account for this. The aspect ratio of the cross-sections presents the trench with very steep sides. For comparison, a profile is shown with a distance:height aspect ratio of 1:1, showing that the true profile has shallow sides. Also, the SiO_x/titanium nitride interface is indicated at -37 nm, demonstrating that the trench is around 1 µm wide at this point.

The sloped sides of the trench, demonstrated in **Figure 8.5b**, show that the etch area becomes narrower with depth. This is likely due to the CAFM tip geometry convoluting

the edge of the trench, as well as producing a sloped side during etching. This suggests the resulting three-dimensional profile of the filament might not be accurate because the etch area becomes laterally confined. However, as indicated in **Figure 8.5b**, the trench is around 1 µm wide at the SiO_x/titanium nitride bottom interface. Thus, filaments narrower than 1 µm should be accurately represented at least to the interface with the bottom electrode, although at much greater depths the shape of the trench would convolute the current map.

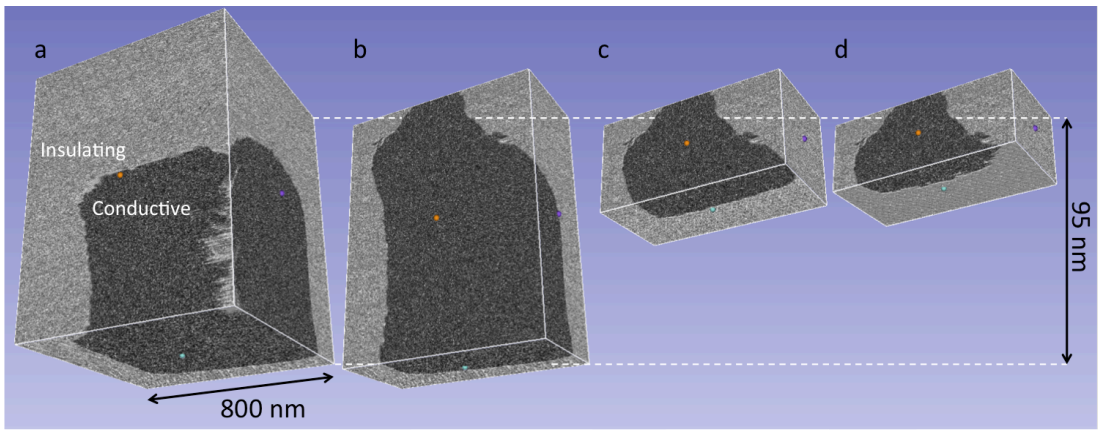

Figure 8.6. Depth scaling and cropping for a tomogram, corresponding to the trench in **Figure 8.5**. The maximum trench depth from the SiO_x surface is 95 nm, so the height scale is set to this. Darker regions indicate conductivity. The white boxes and small coloured spots are software controls, indicating perimeters of the cropped volume. (**a**) The full data volume shows a large conductive region in its lower half. At the base, this region appears roughly square, likely indicating conductivity resulting from etching into the bottom electrode. (**b**) Cropping the volume laterally shows the internal conductive structure. At roughly a third of the depth, the conductive area appears to reach its maximum width and remain consistent for the remaining depth. (**c**) Cropping from the bottom of the volume to leave 37 nm removes most of the large conductive area corresponding to the bottom electrode. However, there is some drift, also evident in **Figure 8.5a**, that might have occurred prior to reaching and then while etching the bottom electrode. (**d**) Cropping to 28 nm starts reducing the cross-sectional area of the conductive region and reveals some lateral detail. This should indicate that the vertical bounds of the volume now correspond to the conductive filament. Thus, the height of the remaining volume may be set to 37 nm.

Following data acquisition, I used 3D Slicer to stack the current map slices, producing a three-dimensional data set of current in the active layer. I then rendered the volume and compared the number of slices with the total etch depth from the measurement of the trench. In each case, the measurement progressed more than 37 nm vertically, into the bottom electrode. The etch rate of titanium nitride should be different to silicon oxide, although I was unable to successfully perform the appropriate calibration

measurements. As a result, I scaled the number of slices in each measurement by its depth to give estimated slices thicknesses between 0.07 nm and 0.3 nm. I then inspected the volume to determine the depth at which the bottom electrode seemed to appear, assuming this would be where the filament cross-sectional area was largest and the current maps became consistent with depth. Considering these two observations together, I cropped the data to best show the expected volume corresponding to the filament, with little or no bottom electrode present, and rescaled the height accordingly. An example of this process, corresponding to the trench in **Figure 8.5a**, is shown in **Figure 8.6**.

Following cropping, I exposed the conductive filament within the bulk insulating material by thresholding the data at around 75 pA to remove the background noise. This produced a solid, three-dimensional rendering of the filament within the switching layer, as shown in **Figure 8.7**. I also applied an anisotropic diffusion filter to the data volume. This is commonly done during image processing to smooth noisy data,[205] in particular with medical images.[206] Briefly, this filter scales the data by its differential in one or more dimensions.[207] My data was filtered only in the z-direction, through the active layer, to reduce noise and smooth the transition between slices while preserving lateral data features in each slice. The effect of filtering may be seen between the unfiltered data in **Figure 8.7b** and the filtered data in **Figure 8.9a**. The filament rendering in the filtered case is much smoother and the structure more readily observed than for the unfiltered data, in which the detail is less clear.

I refer to this technique as conductance tomography. This is because it is a tomographic method generating data that maps conductance in three dimensions. I do not suggest that the true conductance, the inverse of resistance, is measured. Rather, the measurements indicate the extent to which an otherwise insulating sample volume demonstrates conductance. Scaling the data by the inverse of the applied voltage would give the conductance, although this would appear similar to the current because the voltage is constant.[208]

It is important to note that the CAFM measurements undertaken in this chapter do not measure only the current; rather, they measure the connectedness of the exposed sample to the bottom electrode. If there is a very highly conductive layer present that is not connected, unless by tunnelling, to the bottom electrode, it will not be visible using this technique. There is therefore an inbuilt asymmetry in these measurements. This means that, if it were possible to perform conductance tomography starting from the bottom electrode, the three-dimensional conductive profile of the sample might appear different to a profile starting from the surface.

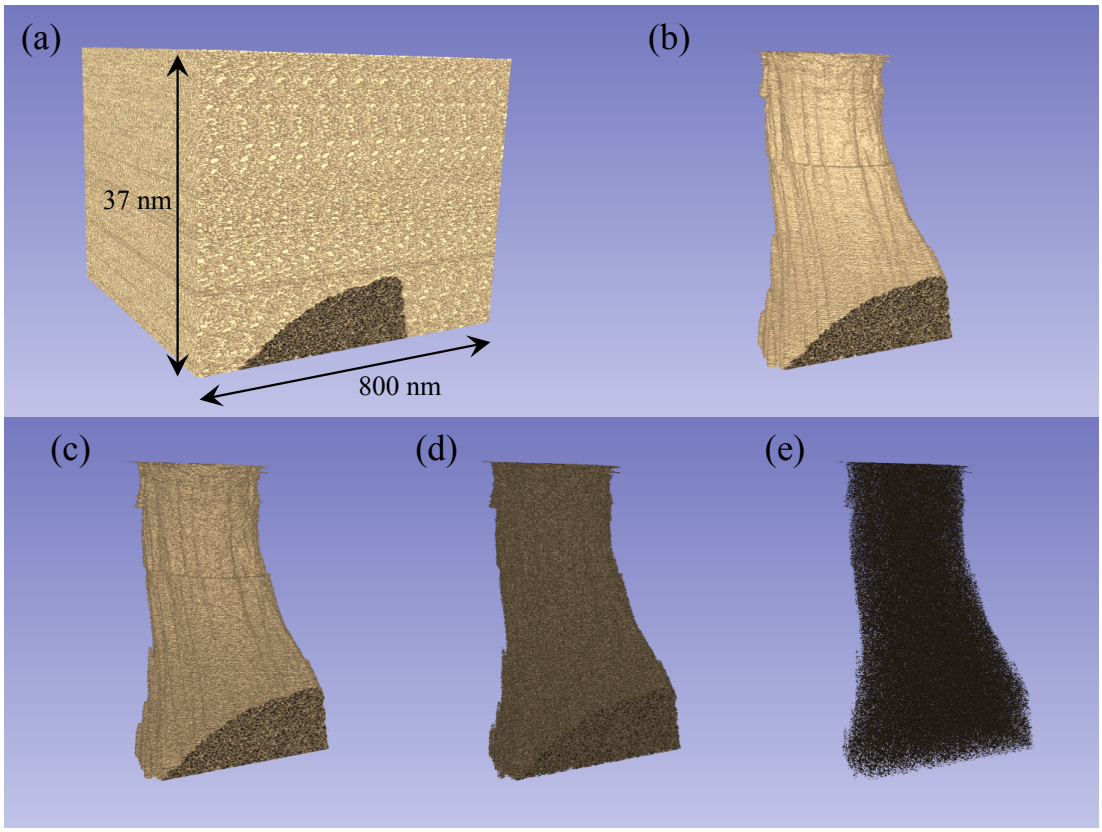

Figure 8.7. The application of different threshold levels to the structure shown in **Figure 8.9**. (**a**) No thresholding applied. No structure is visible in the volume due to background noise. (**b**) Removing the noise floor at 75 pA reveals the internal structure. (**c**) Raising the thresholding to around 50 nA reduces the clarity of the rendering as data at the edge of conductive regions is removed. (**d**) Thresholding at 100 nA removes much of the definition of the filament as more internal regions are removed. (**e**) Thresholding to leave current close to 200 nA produces a very unclear image. Here, only data close to the maximum current is shown, showing the core of the conductive region.

8.5 Conductance tomography results

I performed this conductance tomography on a pristine SiO_x sample, as shown in **Figure 8.8**. There are no conductive regions present in the volume, except near the base, where the bottom electrode has been exposed. This also indicates that the process of pressing into the surface with a hard, conductive probe does not induce the formation of a conductive pathway. In **Figure 8.8** to **Figure 8.12** I have included a selection of corresponding current map slices, none of which have had any thresholding or filtering applied. I did this in order to demonstrate the raw conductivity data. In all tomographic renderings in this chapter, conductive regions are shown in beige and the surrounding, insulating oxide is shown in blue.

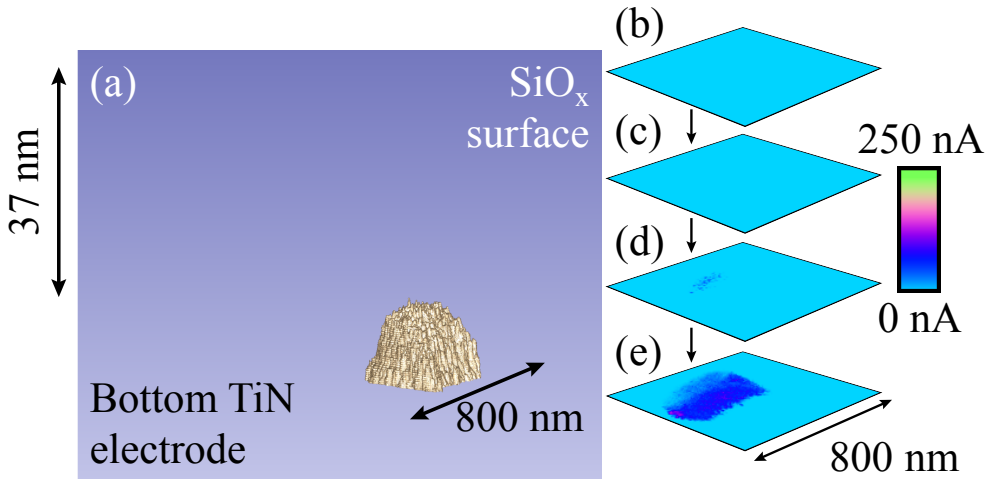

Figure 8.8. Conductance tomography of pristine SiO_x. (**a**) Near the bottom of the etch, a conductive region appears, corresponding to the exposure of titanium nitride by the CAFM tip. The height of the conductive region is large, extending slightly into the SiOx. This may due to tunnelling current as the SiO_x between the tip and bottom electrode thins. The conductive region does not extend over the entire measurement area. This may be a result of tip wear, the accumulation of insulating debris or an inhomogeneity in the titanium nitride thickness. (**b**) to (**e**) cross-sections through the SiO_x, showing the emergence of the bottom electrode. The data were composed of 206 slices with a lateral pixel resolution of 3.1 nm.

Figure 8.9a displays a tomographic rendering of the conductivity slices for a filament formed with +20 V at a current compliance of 0.1 μA. Interestingly, contrary to some suggestions in the literature,[11,49] this filament does not have a conical shape but is instead tubular. It is also evident that there are lateral variations in the current within the filament, possibly a reflection of the intrinsic columnar structure of the SiO_x, as has been discussed in chapters **2.3**, **7.2** and **7.5**. **Figure 8.9b** to **e** show cross-sections depicting the internal structure of the filament. These reveal that the current varies across the filament, with the most conductive regions located toward the centre. There are also some regions in which no current flows. This suggests that the filament has an internal structure following a group of closely located pathways through the SiO_x. Therefore, rather than being a single filament it is possible that a highly localised group of filaments have clustered together. It has previously been suggested that multiple filaments may compete to bridge the active layer.[11,137,209] However, it is not possible to distinguish one filament from another in the case in **Figure 8.9a**, so the single conductive pathway shown may indicate only a single filament.

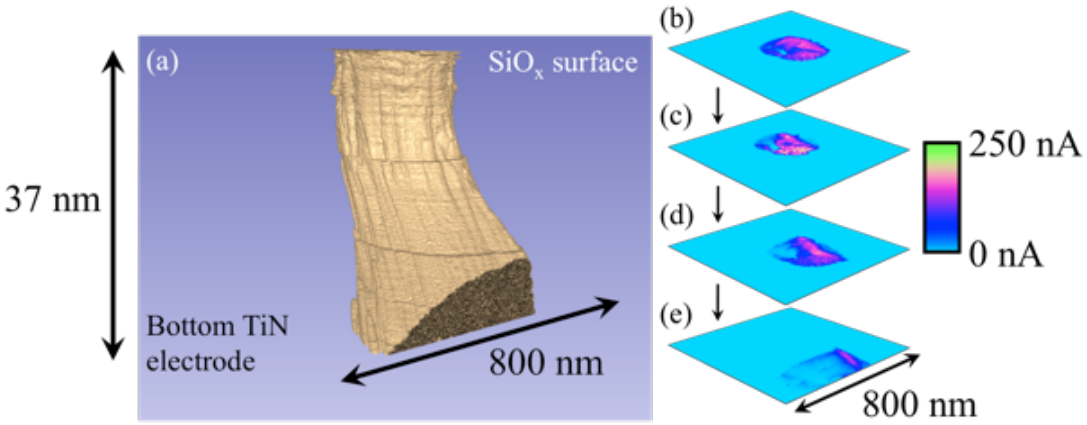

Figure 8.9. Rendering of a filament formed with +20 V at a current compliance of 0.1 μA. (**a**) The filament has a tubular shape that reflects an underlying columnar structure. (**b**) to (**e**) cross-sections through the switching layer, showing the internal filament structure, with clear lateral variations in current at different depths. Note there is some drift evident in the cross-sections that is likely instrumental and caused by the large forces applied to the sample during scanning. As a result of the drift, the filament intercepts the edge of the scan region, causing a flattening of its lower edge. The rendering in (a) has been shown from an angle that best displays the columnar structure rather than the drift. The data were composed of 474 slices with a lateral pixel resolution of 3.1 nm.

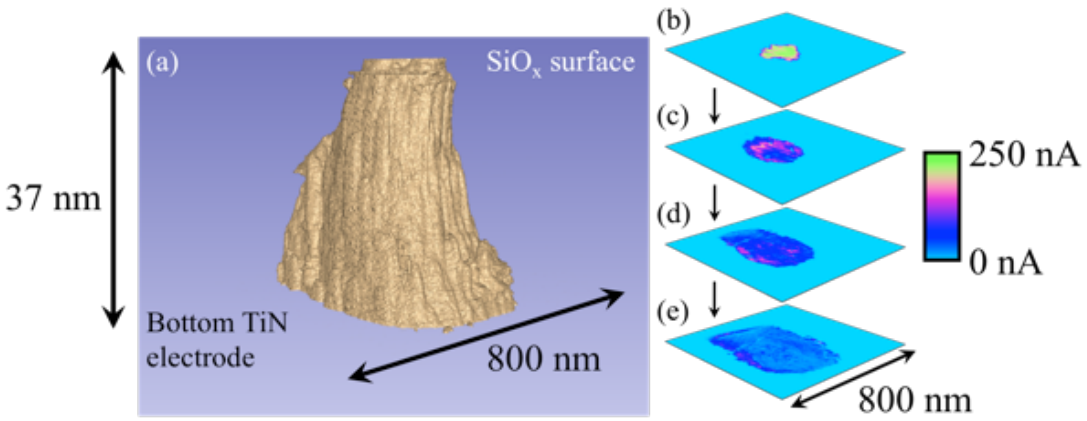

Figure 8.10. Rendering of a filament formed with -20 V at a current compliance of 0.1 μA. (**a**) The shape is more conical than for the positively formed filament in **Figure 8.9a**, yet there is still an underlying structure that might reflect the intrinsic columnar structure of the SiO_x. (**b**) to (**e**) cross-sections showing the lateral variations in the current at different depths into the SiO_x. The data were composed of 224 slices with a lateral pixel resolution of 3.1 nm.

Figure 8.10 presents CAFM measurements of a filament electroformed with -20 V at a current compliance of 0.1 μA. As the rendering shows, the filament shape is more similar to the conical models in the literature than that in **Figure 8.9a**. Again, there is an

underlying columnar structure. It also appears that the conical shape is composed of multiple outer conductive pathways surrounding the main body of the filament. As noted for the positive filament in **Figure 8.9**, it is possible that the structure is a collection of closely packed, smaller filaments that are bunched around a preferential pathway through the oxide. As shown in **Figure 8.10b** to **e**, the filament has an internal structure in which some regions are more conductive than others. Interestingly, although **Figure 8.10a** and **b** show that the central region is the most conductive near the top of the filament, **Figure 8.10d** and **e** demonstrate that, toward the base of the filament, it is actually the outer region that carries the greatest current.

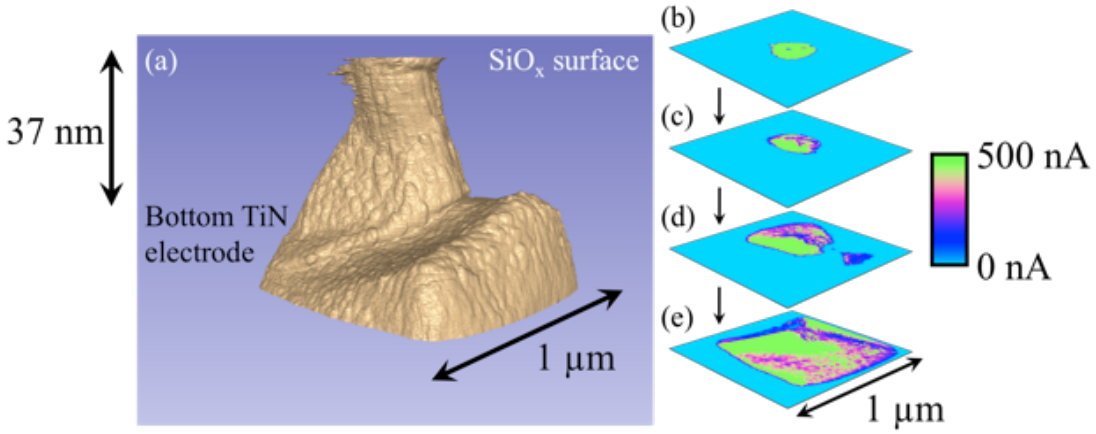

Figure 8.11. Rendering of a filament formed with +12.5 V at a current compliance of 1 mA. (**a**) Near to the bottom electrode, there is a branching of the growth, resulting in a pair of filament peaks. Only one of these bridges the entire active layer, however; the second is likely the appearance of the bottom electrode. (**b**) to (**e**) cross-sections through the SiO_x, showing the emergence of the bottom electrode and its convergence with the main growth pathway. Again, the internal, inhomogeneous structure of the filament is evident. The data were composed of 513 slices with a lateral pixel resolution of 3.9 nm.

Figure 8.11 shows a filament formed with 12.5 V and current compliance of 1 mA. It has a more conical structure than that of **Figure 8.9**. There also appears to be a small second peak adjoining the main filament, with the pair of growths originating from a larger, roughly square region. However, this second peak is most likely the appearance of the bottom electrode during etching, angled away from the horizontal due either to uneven electrode deposition or a scanning artefact. Notably, there is again a correlation between conductivity and the columnar structure of the SiO_x. **Figure 8.11b** to **e** show cross-sections through the filament, highlighting the gradual appearance of the electrode and its eventual saturation of the entire scan area. Interestingly, in **Figure 8.11d** the centre of the filament appears to show a lower current than its surroundings. In addition, the conductive region appears to be split into distinct regions of higher and

lower conductivity. This might be related to the appearance of the bottom electrode, which should be more conductive than the filament.

It has been suggested that filamentation might not involve the generation of a single conductive pathway, as mentioned above. Instead, structural inhomogeneities in the switching layer may present many alterative routes for growth.[11,137,209] Thus filaments might 'compete' to bridge the switching layer, with only a single filament in the end shorting the electrodes. This behaviour has previously been confirmed in extrinsic devices.[71,197] Below, I present findings that support the suggestion of multiple filamentation in intrinsic systems.

Figure 8.12 demonstrates an observation of multiple filaments from electroforming with a voltage of -16 V at a current compliance of 1 µA. It is clear that, aside from the main filament that bridges the SiO_x, there are a number of additional growths extending by various degrees through the oxide. **Figure 8.12b** to **e** highlight the gradual appearance of multiple filaments through the film and their convergence as the CAFM tip approaches the bottom electrode. The internal structure of the conductive pathway is evident here, with higher-conductivity regions appearing more centrally in the filament.

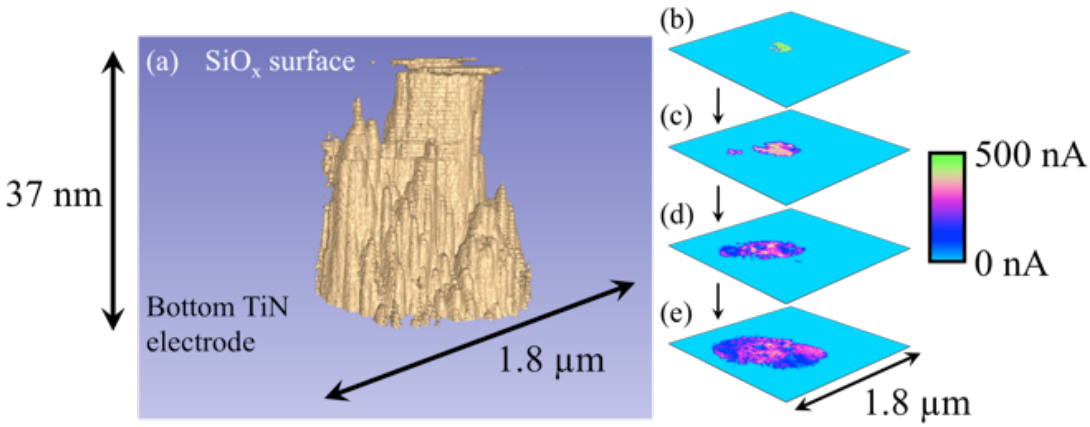

Figure 8.12. Rendering of a filament formed with -16 V at a current compliance of 1 µA. (**a**) There appear to be at least three constituents to the filament, although the smallest of these is only a few nanometres tall. The main filament is very straight, although it becomes broader as it approaches the bottom electrode. Note that a slice has been removed due to high levels of noise that saturated the scan area. (**b**) to (**e**) cross-sections through the filament, showing the appearance and convergence of multiple filaments. The data were composed of 116 slices with a lateral pixel resolution of 7.0 nm.

The presence of multiple filaments, as shown in **Figure 8.12**, suggests that many partial filaments may be produced during electroforming. I have only observed those that occur locally to the main filament, yet it is possible that other, more distant locations in the film between the electrodes would experience some, perhaps

incomplete, filament growth during electroforming. This may be particularly true of devices with larger top electrode areas than the footprint of the tungsten needle that I used. It is reasonable to speculate that only a single filament completes its growth across the active layer, as the electric field will collapse once the electrodes are shorted. At this point there should be no further field-driven growth of secondary filaments. However, with cycling, electrical stress may further develop competing filaments when a voltage is applied across a device in a high resistance state. It is also possible that some growth paths are not suitable for filamentation if they do not propagate through the full oxide thickness. This might allow conductive regions to grow some way into the active layer but not to fully bridge it.

The filaments shown in this chapter are large compared to predictions of nanometres to tens of nanometres.[14,48,189,193] Furthermore, successful resistance switching behaviour has been observed in devices with smaller cross-sectional areas than the filaments shown in this chapter.[32,48,193,210] It is also of note that conductive regions at the SiO_x surface, with sizes of the order of tens of nanometres, have been observed.[202]

It has been suggested that filament size is dependent on the magnitude and duration of the applied bias.[209] Additionally, increased filament conductance has been attributed to filament thickening as a result of increasing operational voltage.[12] The relatively high fields that I used, combined with the time taken for the onset of current compliance, even with a short pulse, may have broadened the filaments produced in this work.

Although a more detailed investigation is required, an interesting aspect of the filaments that I have shown is that their lateral sizes all appear similar, in the order of hundreds of nanometres, despite the application of different electroforming voltages and current compliances. Given the apparent presence of multiple conductive pathways, it may be that filaments continue to grow laterally as these paths converge, until the applied bias is removed, either instrumentally or by shorting the electrodes. A further consequence of this may be that the observed shape of the filaments is not representative of their shape at the time of forming. Notably, the power dissipation in unipolar devices is relatively high, which may explain the much smaller filaments observed using transmission electron microscopy in bipolar systems.[199]

8.6 The effect of measurements on the scanning probe

An aspect of conductance tomography that is particularly relevant to data reliability is that the process is likely to affect the probe. In particular, I would expect that loose debris accumulates on the probe and that the apex become blunted, or obscured by

debris, altering its footprint and conductivity. Additionally, diamond-coated probes have a larger apex than uncoated silicon probes. It is therefore of interest to determine the reliability of the current mapping shown throughout chapter **8.5**.

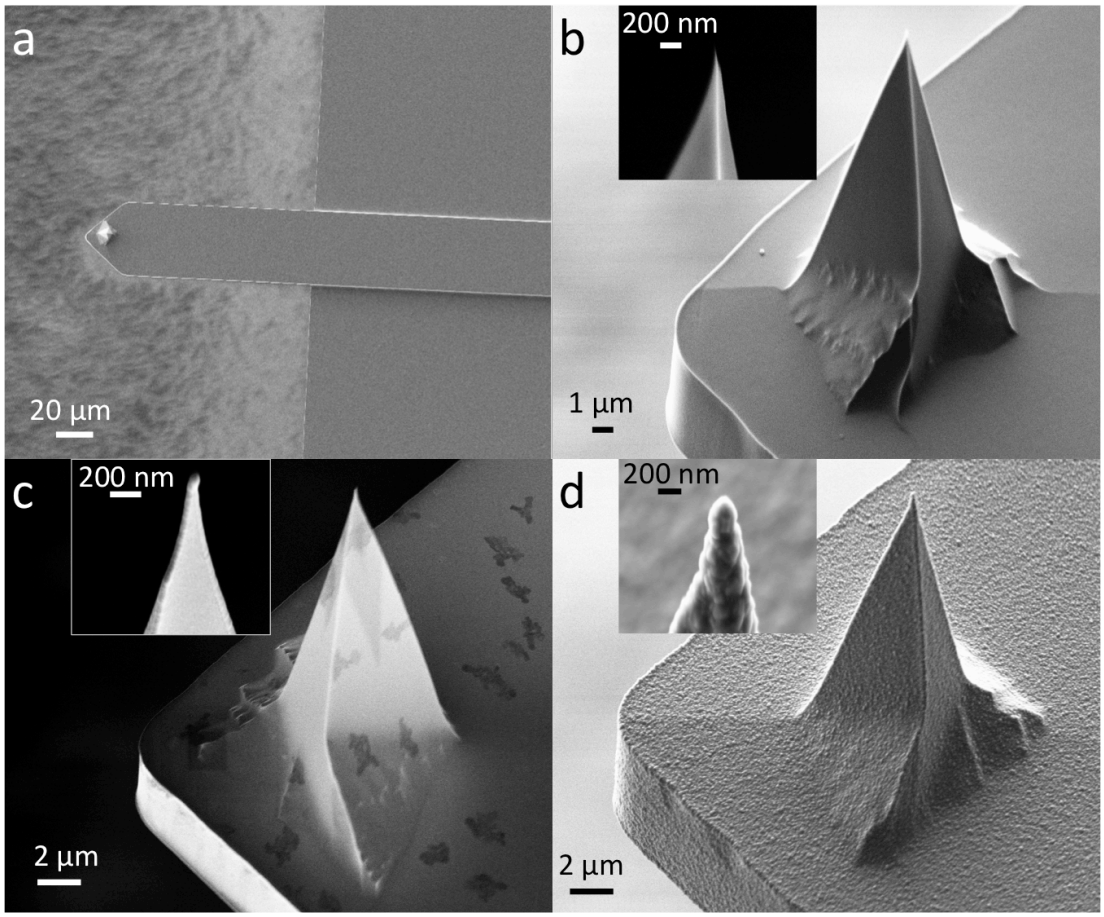

Figure 8.13. SEM images of unused CAFM probes. (**a**) Top-down view of a silicon cantilever with a silicon tip, mounted on a silicon chip. (**b**) Side-view of the tip in **a**. Inset – close-up of the apex, demonstrating its sharpness. The apex is not well defined and appears to be narrower than the resolution of the image, possibly below 10 nm. (**c**) Side-view of a platinum/iridium-coated silicon tip, for comparison. Inset – close-up of the apex demonstrating that it is less sharp than the uncoated probe in **a**. It appears to have a radius of curvature of tens of nanometres. (**d**) Side-view of a diamond-coated silicon tip. Inset – close-up of the apex, demonstrating that it is less sharp than both those in **b** and **c**. Its radius of curvature is above 100 nm, with smaller grains of around 50 nm diameter present.

To discern the effect of the conductance tomography method on the scanning probe, and the apex geometry, a colleague performed SEM on used and unused probes. Using a 3 keV electron bean, we looked at the probes from above and from the side, at 45˚. Images of unused probes are shown in **Figure 8.13**. The diamond-coated probe is not as sharp as the uncoated or metal-coated silicon probes, which have nominal radii of curvature of 8 nm and 20 nm, respectively.[91,92] The diamond-coated probe has a

radius of curvature around 150 nm.[211] This suggests that diamond-coated probes could not resolve topographical features less than 100 nm wide, though the electrical resolution should be much finer.

As discussed in chapter **8.4**, the radius of curvature of the probe is not a good indicator of the electrical contact area as the current is generally dominated by the most prominent point on the apex.[203] For a diamond-coated probe, this might be a vertex of an individual nanodiamond particle. In **Figure 8.13d**, the apex of the probe appears to be a cluster of grains around 200 nm in diameter. This cluster tapers to tens of nanometres, so the lateral resolution should be below 50 nm. However, the smallest features of the current maps in chapter **8.5**, such as in **Figure 8.10b** to **e**, were around 20 nm in diameter. This indicates either that the probe resolution was insufficient to resolve smaller features or there were no smaller features present.

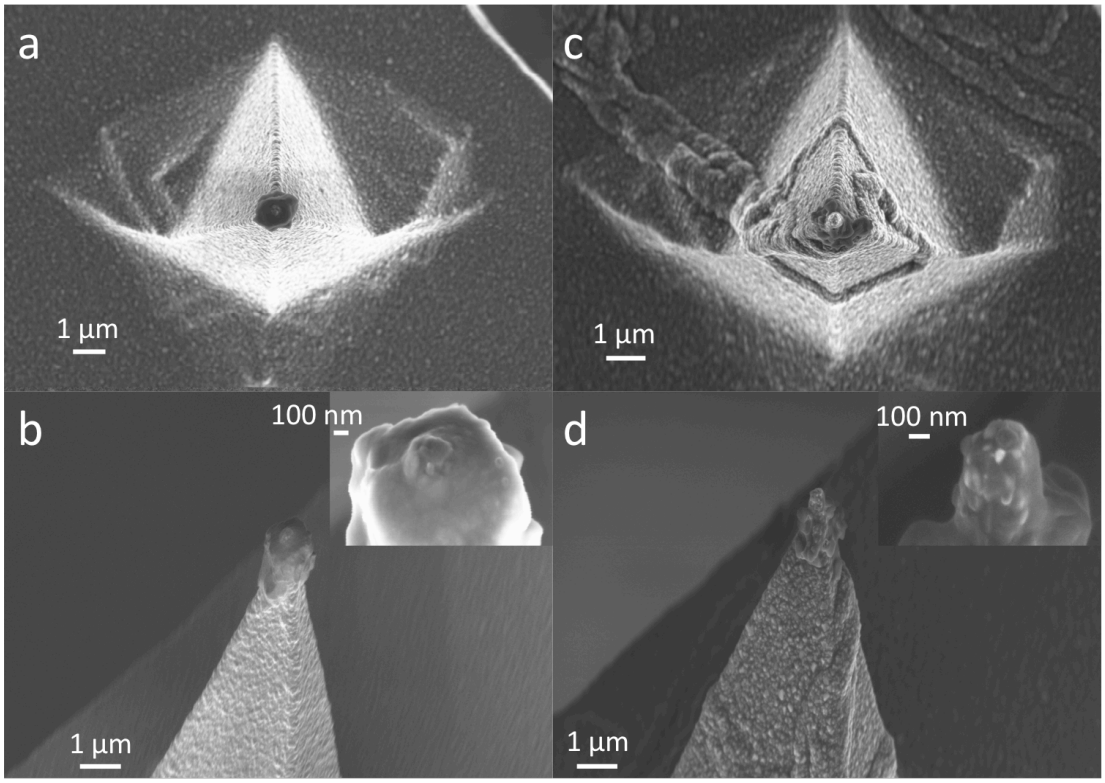

Figure 8.14. SEM images of used diamond-coated CAFM probes. (**a**) Top-down view of a used probe, showing some debris near the apex. (**b**) Side-view of the apex, showing the accumulated debris. However, the apex is still visible and its geometry is retained. Inset – close-up of the apex. (**c**) Top-down view of a used probe tip, showing debris accumulation from the apex to the base of the tip. (**d**) Side-view of the apex, showing the accumulation of debris around the tip. Again, the apex is still visible despite the debris. Inset – close-up of the apex. In both **b** and **d** the apex radii are around 100 nm, with individual grains of smaller diameters present. This suggests that there is no significant change to the apex in comparison to an unused probe, as in **Figure 8.13**.

Figure 8.14 shows two used diamond-coated probes. Material has accumulated on each probe but has not obscured either apex or reduced their sharpness compared to the unused probe in **Figure 8.13d**. Thus, the probes should still be sharp and conductive, providing reliable current maps. These results suggest that using diamond-coated rather than single-crystal diamond probes should not inhibit the tomography technique. In particular, the probe should not be damaged during measurements and so its resolution should be consistent throughout. Additionally, the lateral resolution in current mapping should be sufficient to discern details in the filament structure down to tens of nanometres.

To better compare my tomography results to those in the literature, I also attempted measurements using single-crystal diamond probes. Notably, it has been suggested that diamond-coated probes are not suitable for tomography due to the risk of abrupt breakages and blunting.[204,212] As shown above, this was not to the case with my measurements, so I was interested in determining whether single-crystal probes might produce any improvements in data reliability or accuracy. **Figure 8.15a** and **b** show an unused single-crystal diamond probe. The apex appears to be sharper than that of a diamond-coated probe, so the topographical resolution should be greater. However, these measurements do not inform on whether there would be any difference in the spatial resolution of the current.

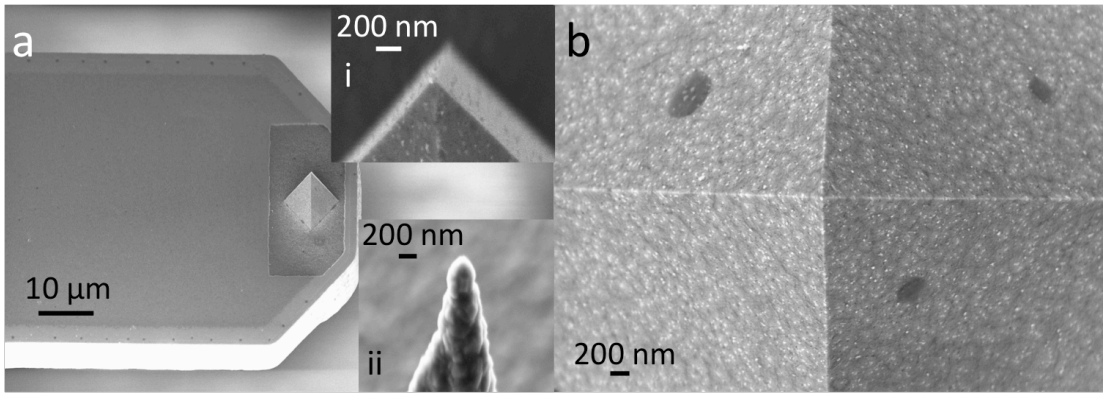

Figure 8.15. SEM images of an unused single-crystal diamond CAFM probe. (**a**) Pristine probe on a nickel cantilever. **i**, close-up of the apex of the tip, demonstrating a radius of curvature of tens of nanometres. **ii**, close-up of a diamond-coated probe, as in **Figure 8.13d**, for comparison. There is an apparent edge enhancement of the secondary electron signal on both tips. The single-crystal probe appears to have the sharper and smoother apex. (**b**) Top-down view of the probe in **a**, demonstrating the apex sharpness.

Interestingly, when attempting to perform conductance tomography with single-crystal diamond probes, I found that it was not possible to etch more than a few nanometres into the SiO_x. In general, the first one to two hours of measuring would produce a

trench but this would not become deeper than around 5 nm, even when leaving the process to continue overnight or for several days. In some cases, such long measurements would not produce any noticeable depression of the surface. This seemed to occur regardless of the scan rate, tip velocity, size of the scan area, setpoint and applied voltage. The only factor that I could discern as having a notable effect on the process was the scan resolution. Scans with 256 lines and 256 samples per line etched the surface by a few nanometres whereas those with more lines did not. This might be due to overlapping paths taken by the probe, resulting in small amounts of material being removed and subsequently moved around, obstructing further etching. For large areas, where overlapping paths should not occur, the inter-path spacing might be great enough to prevent sufficient material from being removed to produce a deep trench.

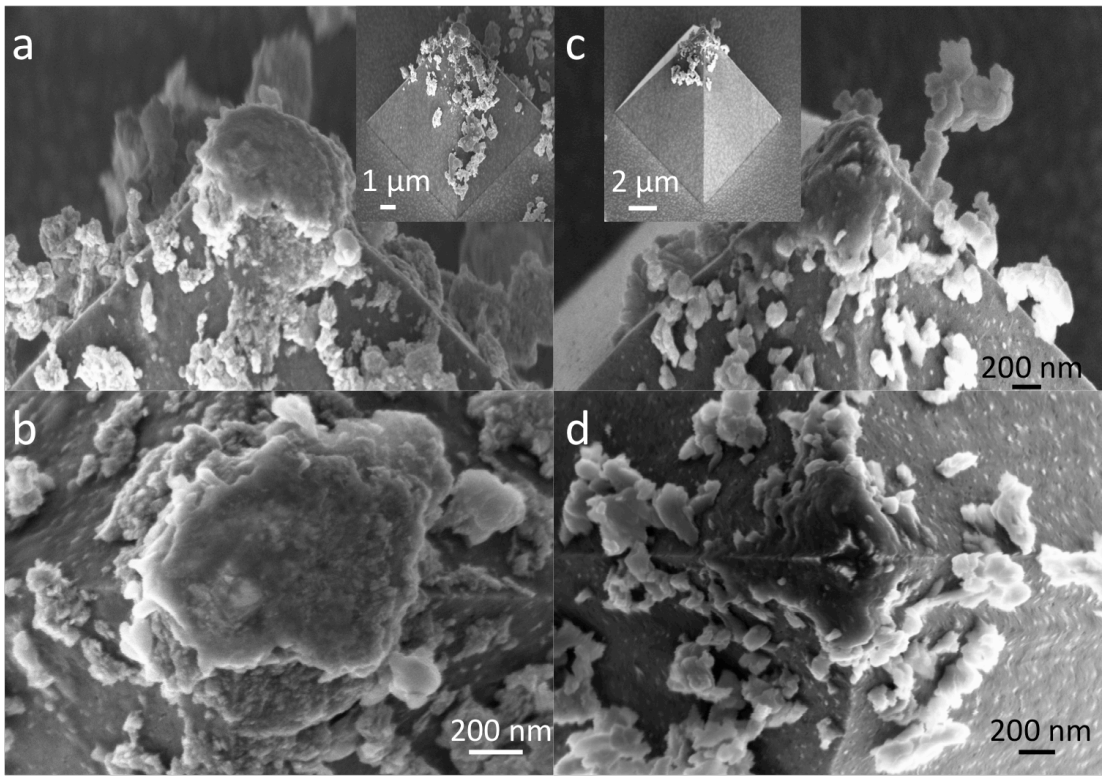

Figure 8.16. SEM images of single-crystal diamond CAFM probes after use in conductance tomography measurements on SiO_x. (**a**) Side-view of a used probe, demonstrating debris accumulation. The apex is obscured, either by debris or blunting. Inset – full view of the tip, showing the distribution of debris. (**b**) Top-down view of the tip in **a**. (**c**) Side-view of a used probe. The apex appears damaged, resulting in multiple protrusions. Inset – full view of the tip, showing that the debris here is confined to the region close to the apex. (**d**) Top-down view of the probe in **c**, demonstrating multiple apexes as a result of crater-like damage.

Figure 8.16a to **f** show two used single-crystal diamond probes following attempted tomography measurements on SiO_x. It can be seen here that the effect on the probes

is much more pronounced than for the diamond-coated probes in **Figure 8.14**. In particular, neither apex remains unchanged following measurement. In **Figure 8.16a** and **b**, the probe appears to have accumulated significant debris or become blunted, as the apex is not visible. In **Figure 8.16c** and **d**, the probe has also accumulated debris, although in this case the apex is still visible. However, there appears to have been some damage, resulting in a crater with a number of apparent protrusions, each less sharp than the pristine probe in **Figure 8.13d** and **Figure 8.15ai**.

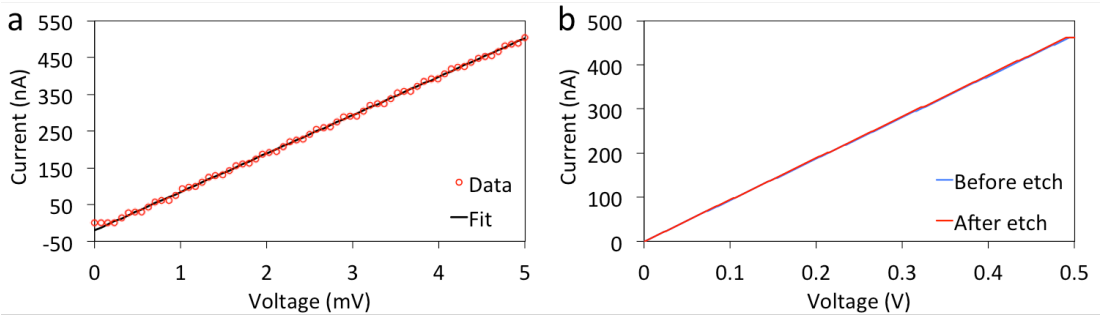

Figure 8.17. Current-voltage spectra of single-crystal diamond probes on the stage and on a gold surface. (**a**) Spectrum taken on the CAFM stage, demonstrating that the system resistance is around 10.5 kΩ. There is a small oscillation present in the data, likely artefactual from the CAFM feedback. (**b**) Spectra taken on a gold film before and after an overnight etching measurement. A 1.06 MΩ series resistance was placed between the gold and the CAFM stage to allow greater voltages to be reached before the current saturated at around 450 nA. Thus, the artefactual oscillation is no longer apparent. Although the data before and after are similar, there is a reduction of around 7 kΩ in the resistance as a result of the etching process.

I further studied the effect of conductance tomography on single-crystal diamond probes by performing current-voltage measurements before and after etching, to ascertain whether their conductivity had changed. A setpoint of 0.5 V was used for current-voltage spectra and the etching was performed overnight with a setpoint of 0 V. The data are shown in **Figure 8.17**. Before etching, the probe showed a linear character, according to Ohm's law,[43] with a small oscillation of the signal, evident in **Figure 8.17a**. The oscillation is likely to be an artefact from the feedback system attempting to keep the probe in a fixed position. However, the linear trend may be used to calculate the system resistance, 10.5 kΩ. To alleviate the oscillations, the measurements were repeated with an additional series resistor of around 1 MΩ. In addition, a gold film deposited on a glass slide was used for the contact point, as it provided a much smoother surface than the stage. This produced more consistent measurements and allowed a greater voltage sweep range before the current saturated

the detector at around 450 nA. The same setup was used for the post-etching characterisation.

Figure 8.17b demonstrates that the pre- and post-etch resistance profiles of the probe are very similar; it is difficult to distinguish differences in the data. However, the total resistance decreases by around 7 kΩ following etching, which is about 70% of the initial value of the system resistance. It is unlikely that any component of the measurement system, other than the probe, changed measurably in resistance during the etching process. Notably, the 66 individual measurements of resistance before the etching gave a mean value of 1.06 MΩ with a standard deviation of 174 Ω. The 66 post-etching measurements gave 1.06 MΩ with a standard deviation of 116 Ω. These deviations are small relative to the total resistance and also to the 7 kΩ change in resistance. Thus, the system was stable, suggesting that it was the probe resistance that changed. Given that CAFM current is proportional to tip-sample contact area, it is possible that the damage to the probe increased the size of the apex.[86] This may indicate that blunting or debris accumulation produced a flatter surface, or that multiple apexes were created, similarly to the probes shown in **Figure 8.17**.

It is interesting that my measurements with single-crystal diamond probes were not successful and that diamond-coated probes were more robust than previously reported.[204,212] This certainly suggests that further investigations must be made on the process and instrumentation of the conductance tomography method. Surely variations in the sample material, probe geometry and composition, microscope and atmosphere must all influence the efficacy of a measurement. In addition, it is difficult to consider that single-crystal probes should be so much less successful than diamond-coated probes. It is possible that my methodology was either inconsistent or inappropriate for both probes; again, further investigation of this behaviour is essential.

Considering my discussion in chapter **8.4** on developing the tomography process to facilitate accessibility, my method successfully addressed this goal. I was able to probe four conductive filaments under ambient conditions using diamond-coated probes. Additionally, 3D Slicer provided a suitable, cost-free platform for data processing and presentation. I have also shown that the diamond-coated probes are not damaged significantly by the etching process, thus they should produce consistent data throughout. In contrast, the single-crystal diamond probes were not suitable for etching and became severely damaged.

Given the success of my method, I suggest that it is suitable for conductance tomography and is more accessible than previous approaches. However, it is not without limitation and is not definitive. Although etching under ambient conditions facilitates the process, it does expose the surface to the possibility of undesirable

chemistry, namely oxidation and contamination. However, it may improve heat dissipation as the tip scratches across the sample and so might help preserve the features of interest and the shape of the probe apex. Single-crystal diamond probes were not suitable in my work, but they have proven efficacy and should not be ruled out. Conversely, I did not observe any breaking or blunting of diamond-coated probes, but it is surely possible for them to be damaged. It may be that the appropriate probe should be chosen for the sample under investigation.

8.7 Chapter summary and conclusions

In this chapter I have shown some of the features at the contact point following electroforming with a tungsten needle. I also demonstrated that their conductivity extends through the switching layer as a filament. Additionally, I have proven the efficacy of a novel method that enabled me to present, for the first time, a rendering of a filament in an intrinsic RRAM device.

Using pulsed stresses, rather than sweeps, I was able to reduce the size of deformations occurring at the point of contact. With AFM and CAFM, I studied the structure of these features, showing that they are conductive and flexible when formed with either a positive or negative needle polarity. Additionally, a negative polarity caused some surface hardening.

Following this, I was able to use conductance tomography to produce tomographic images of intrinsic conductive filaments in oxide RRAM devices. Additionally, I was able to demonstrate success with modifications to the method previously used for CAFM tomography, indicating that the process may be refined further to improve practicality.

My results in this chapter confirm the filamentary nature of conductive pathways in an intrinsic oxide RRAM device. The inhomogeneous oxide structure, discussed in chapter **7**, is reflected in the shape and internal structure of the conductive filaments. Thus, I have demonstrated for the first time that the formation process follows the intrinsic columnar structure of the amorphous material. I have also demonstrated experimentally for the first time that filament formation does not always follow a single pathway in an intrinsic device and that several filaments may grow simultaneously in a device.

8.8 Recent and similar work

It should be made clear that some recent publications appear to conflict with the claims that I have made in chapter **8**. In particular, in **8.5** I claimed to demonstrate the first CAFM tomography results for an intrinsic switching material. Notably, this work was published in published in October 2015.[213] However, it should also be noted that,

more recently but prior to the submission of this thesis, similar work has been presented. Specifically, Celano *et al* published an article in August 2016 demonstrating CAFM tomography measurements on intrinsic hafnium dioxide-based switching devices.[201] As shown in **Figure 8.18**, these results show the shape of the conductive filament, although very little internal structural detail is apparent.

In chapter **8.6** I showed results suggesting that single-crystal diamond probes might not be the most suitable CAFM probes for use tomography on all sample materials. However, more recently than my work and prior to the submission of this thesis, a book has been published that conflicts with my findings. In particular, the authors suggest that single-crystal probes are the most appropriate for use in CAFM tomography.[214] They show probes before and after use, but there is no evidence of damage. It should be noted that their measurements were performed in a vacuum system and not on SiO_x, which might explain the differences in our findings.

Both matters are noteworthy, though they should not affect the validity of my discussion. The novelty of my work is in demonstrating the first CAFM tomography measurements of filaments in an intrinsic switching material, along with evidence for multiple filamentation. In addition, I have contributed to the method by demonstrating success with a technique more readily accessible to researchers without access to vacuum CAFM systems and expensive software.

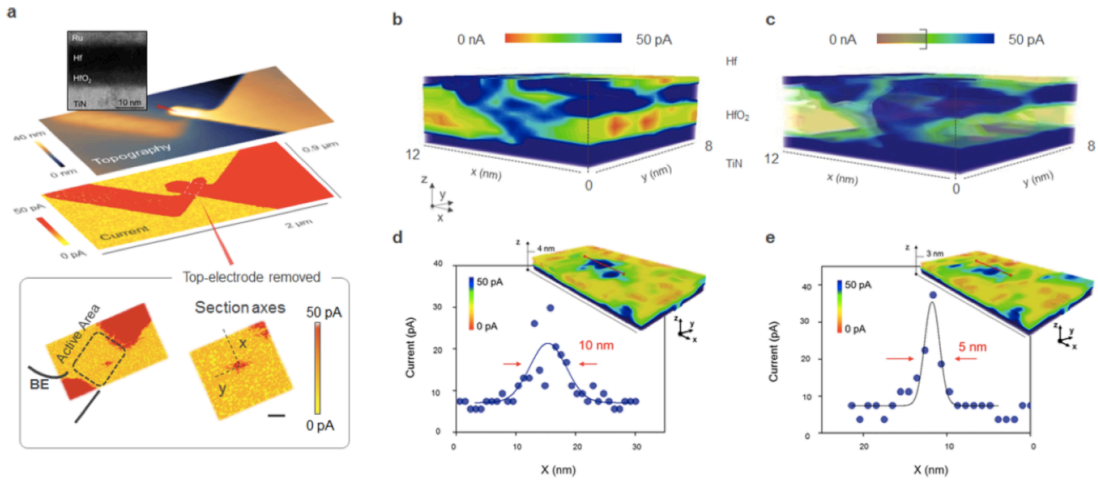

Figure 8.18. Recent example of CAFM tomography in an intrinsic switching material, reproduced from [201]. Similarly to earlier results on extrinsic switching devices,[189] the shape of the filament is very clear. However, little internal structural detail is apparent.

9. Project summary conclusions

9.1 Summary

In this report, I have presented data on the structural changes occurring in SiO_x-based RRAM devices under electrical bias. I began at the device scale and progressed to the scale of individual filaments. Firstly, I studied the changes occurring on the device surface, then the switching layer directly. Following these investigations, I studied the point of contact and finally explored a methodology for examining the changes occurring within the SiO_x.

My studies indicated that oxygen is lost from the switching layer under electrical stress. This produces filamentary conductive pathways, switching the device into a low resistance state. The oxygen likely progresses along correlated, intrinsic, structural and compositional defects, finally reaching the SiO_x surface to produce bubble-like distortions. These in turn deform the top electrode, rupturing the surface and causing staining.

9.2 List of novel achievements

In chapters **6**, **7**, and **8** I presented novel work relevant to the field of resistance switching in oxides and also to the use of CAFM in performing tomography. In summary, my contributions to the fields are:

1. The observation that top electrode stains can isolate the needle probe from electrical contact with top electrode.
2. A demonstration, with CAFM, that the bubble-like structure of stains on the surface of the top electrode is correlated with conductivity variations, particularly between bubbles.
3. Showing, with a combination of CAFM, SEM and XPS, that the surface of the top electrode is ruptured during staining, exposing the more conductive, bulk electrode material.
4. A demonstration, optically, that deformation occurs on the surface of the switching layer when using a mobile top electrode, both locally to the electrode and at greater distances from it.
5. Noting that there is not a well-defined dependence of the surface deformation size on the applied voltage and current compliance, though short voltage pulses and relatively low compliances reduce the size.
6. A confirmation, by XPS, that oxygen is lost from the bulk of the switching layer as a result of electroforming.

7. Support, from XPS, for the model of oxygen migration from peroxy linkages in silica-based devices.
8. Showing, by conductance tomography with CAFM, that the structure of conductive filaments in SiO_x-based devices conforms to the intrinsic columnar structure of the active layer.
9. A confirmation, by conductance tomography with CAFM, that multiple filamentary growth pathways can be present in an electroformed intrinsic switching device.
10. A confirmation of the feasibility of a conductance tomography method that is more practicable than previous methods.
11. A demonstration, by SEM and CAFM, that diamond-coated CAFM probes might be more robust than single-crystal diamond CAFM probes for conductance tomography measurements, at least for some sample materials.

9.3 Conclusions

My work demonstrates the crucial role of oxygen in resistance switching for silicon oxide-based RRAM devices. This is coupled with structural changes on a scale that implies an inherent limitation on functionality. Namely, that oxygen migration, when poorly controlled, can cause extreme deformation of the switching material. However, it is possible to impose measures that limit such damage, though it seems impossible to altogether remove morphological changes from the switching mechanics. Surely, device engineering is well placed to overcome this issue through novel fabrication methods and improved switching control systems.

I have shown that the intrinsic microstructure of the active layer is important in the formation of filaments. This does not appear problematic, though it does again imply that engineering approaches may be an ideal means of exploiting fabrication processes in order to optimise filament growth and operation. Filaments may be large, however, and this is an issue for downscaling devices. Confinement of the filamentary volume might be possible through engineering approaches, though this may best be achieved through microstructural control.

My findings on conductance tomography demonstrate that the method is applicable to intrinsic systems, as well as being practical in ambient conditions with unconventional probes and software packages. This suggests a huge scope for methodological development in the near future. I hope that, at some point and in some form, it becomes a common method, used and understood by many researchers and applicable in many fields of research.

9.4 Suggestions for further work

I will outline here a number of areas explored in this work that suggest further opportunities for investigation.

The switching discussed in this report was all performed using two-terminal measurements. While these are typically used in characterising resistance switching devices, the probes introduce lead and contact resistances that can affect the voltage applied to the device. In addition, the overshoot in the instrumental current compliance is difficult to manage, introducing a significant unknown into the electrical operation. One means of circumventing these issues would be to use instead four-point probe measurements. Rathen that applying a voltage and measuring the current with the same two probes, a current may be sourced while a different probe pair measures the resulting voltage. Notably, this has been done across devices, as in ref [54], where a constant current produces voltage spikes resembling the behaviour of biological neurons. Conversely, if the probing is performed on one electrode of the device then it might be possible to extract information on the interface between that electrode and the switching layer; as the interface properties change with device state, the conduction laterally across the electrode might be modified. For example, variations in the defect concentration at the interface might introduce some charge trapping under an applied current, creating a transient in the measured voltage.

In chapter **6.7**, I mentioned that I was unable to use XPS to perform depth profiling on used devices. It would be interesting to further pursue this, as a compositional analysis of a full set of device layers might give further insight into the fate of the oxygen that migrates from the switching layer. Perhaps a different instrument should be used, as I found the spectrometer that I used to be limited in its sampling alignment and bookable time. To my knowledge, there is a facility in Newcastle, called Nexus, which supports XPS studies for researchers funded by Engineering and Physical Sciences Research Council grants.

The orange bubbles discussed in chapter **7.4** did not persist in the vacuum environment of the XPS chamber, preventing an analysis of their composition. However, some techniques, notably Raman spectroscopy and matrix assisted laser desorption/ionisation mass spectrometry, are suitable for use in ambient conditions. Both approaches use laser illumination to generate sample information so there is a possibility that the bubbles would be disrupted by the relatively high energy of the incident photons. However, if the laser power may be tuned or spatially dispersed through focusing, it might be possible to operate below the threshold level required to burst the bubbles.

Focused ion beam milling and secondary ion mass spectroscopy depth profiling might be applicable to studying changes in the electrodes and switching layer as a result of electrical stress. Both of these techniques have a greater lateral resolution that XPS and so might be useful in further correlating structural changes with variations in composition. However, their instrumentation requires a vacuum, so they may not be suitable to further study of the orange bubbles, just to more robust features.

The issues arising in relation to the conductance tomography method in chapter **8.6** certainly require further investigation. The technique has the scope to become a powerful tool in study electronic devices, though the understanding of the influence of the measurement on the data must be better understood. This is not only relevant for understanding the current literature, but also for enabling more researchers to work with the method. In particular, studies must be carried out to determine the controllability of the etch rate, the consistency of measurements made with the same parameters and the influence of the probe type, instrument and local environment.

9.5 Impact statement

This work is important to the field of resistance switching as it improves our understanding of the mechanics of the switching process. In particular, the demonstration that oxygen migration is crucial for device performance indicates that steps must be taken toward the development of devices in which problematic oxygen loss may be minimised. In addition, the correlation between the intrinsic microstructure of the switching layer and the form of the filaments grown within it is significant. This observation indicates that the device fabrication process must be tailored to optimise the starting materials, such that the repeatability, efficiency and reliability of switching operation are enhanced. Furthermore, filaments may be large, as shown, which must be taken into account by the RRAM community. Although the filaments shown in this work may be oversized, the stresses used to produce them are not hugely dissimilar to those used in many literature reports. With the technological drive to produce smaller devices, fine control of filament size must be implemented in order to maintain device functionality at small scales.

The work presented here on conductance tomography is significant because, to some extent, it contradicts the established views on the technique. This indicates that there is much development yet to be made in the field, but also that the scope of the method is broad and may be applied to many systems. Further investigations must be made in order to bring the technique to a level at which it becomes a commonplace lab procedure, yet the community must be aware that a critical, exploratory and inventive approach is necessary.

10. List of publications

10.1 Journal articles

T. Sadi, A. Mehonic, L. Montesi, M. Buckwell, A. J. Kenyon, A. Asenov, "Investigation of resistance switching in SiO_x RRAM cells using a 3D multi-scale kinetic Monte Carlo simulator," *Journal of Physics: Condensed Matter*, vol. 30, pp. 084005, 2018.

W. H. Ng, A. Mehonic, M. Buckwell, L. Montesi and A. Kenyon, “High Performance Resistance Switching Memory Devices Using Spin-on Silicon Oxide,” *IEEE Trans. Nanotechnol.*, vol. PP, no. 99, pp. 1-1, 2018.

A. Mehonic, M. S. Munde, W. H. Ng, M. Buckwell, L. Montesi, M. Bosman, A. L. Shluger and A. J. Kenyon, “Intrinsic resistance switching in amorphous silicon oxide for high performance SiO_x ReRAM devices,” *Microelectron. Eng.*, vol. 178, pp. 98–103, 2017.

Y. Yang, Y. Takahashi, A. Tsurumaki-Fukuchi, M. Arita, M. Moors, M. Buckwell, A. Mehonic and A. J. Kenyon, “Probing electrochemistry at the nanoscale: in situ TEM and STM characterizations of conducting filaments in memristive devices,” *J. Electroceramics*, pp. 1–21, 2017.

M. S. Munde, A. Mehonic, W. H. Ng, M. Buckwell, L. Montesi, M. Bosman, A. L. Shluger and A. J. Kenyon, “Intrinsic Resistance Switching in Amorphous Silicon Suboxides: The Role of Columnar Microstructure,” *Sci. Rep.*, vol. 7, no. 1, p. 9274, 2017.

M. Duchamp, V. Migunov, A. Tavabi, A. Mehonic, M. Buckwell, M. Munde A. J. Kenyon, and R. E. Dunin-Borkowski, “Advances in in-situ TEM characterization of silicon oxide resistive switching memories,” *Resolut. Discov.*, vol. 1, pp. 27–33, 2016.

A. Mehonic, M. Buckwell, L. Montesi, M. S. Munde, D. Gao, S. Hudziak, R. J. Chater, S. Fearn, D. McPhail, M. Bosman, A. L. Shluger and A. J. Kenyon, “Nanoscale Transformations in Metastable, Amorphous, Silicon-Rich Silica,” *Advanced Materials*, vol. 28, no. 34. p. 7549, 2016.

D. Carta, P. Guttmann, A. Regoutz, A. Khiat, A. Serb, I. Gupta, A. Mehonic, M. Buckwell, S. Hudziak, A. J. Kenyon and T. Prodromakis, “X-ray spectromicroscopy investigation of soft and hard breakdown in RRAM devices,” *Nanotechnology*, vol. 27, no. 34, p. 345705, 2016.

L. Montesi, M. Buckwell, K. Zarudnyi, L. Garnett, S. Hudziak, A. Mehonic and A. J. Kenyon, “Nanosecond Analog Programming of Substoichiometric Silicon Oxide Resistive RAM,” *IEEE Trans. Nanotechnol.*, vol. 15, no. 3, pp. 1–1, 2016.

M. Buckwell, L. Montesi, S. Hudziak, A. Mehonic and A. J. Kenyon, “Conductance tomography of conductive filaments in intrinsic silicon-rich silica RRAM,” *Nanoscale*, vol. 7, no. 43, pp. 18030–5, 2015.

A. Mehonic, M. Buckwell, L. Montesi, L. Garnett, S. Hudziak, S. Fearn, R. Chater, D. McPhail and A. J. Kenyon, “Structural changes and conductance thresholds in metal-free intrinsic SiO_x resistive random access memory,” *J. Appl. Phys.*, vol. 117, p. 124505, 2015.

10.2 Conference papers

M. Buckwell, L. Montesi, A. Mehonic, S. Fearn, R. J. Chater, D. McPhail and A. J. Kenyon, “Structural investigation of resistance switching in silicon-rich silica films,” in *IEEE-NANO 2015 - 15th International Conference on Nanotechnology*, 2016, pp. 489–492.

M. Buckwell, K. Zarudnyi, L. Montesi, W. H. Ng, S. Hudziak, A. Mehonic and A. J. Kenyon, “Conductive AFM topography of intrinsic conductivity variations in silica based dielectrics for memory applications,” *ECS Trans.*, 2016, 75, 3–9.

M. Buckwell, L. Montesi, A. Mehonic, O. Reza, L. Garnett, M. Munde, S. Hudziak and A. J. Kenyon, “Microscopic and spectroscopic analysis of the nature of conductivity changes during resistive switching in silicon-rich silicon oxide,” *Phys. Status Solidi*, vol. 12, no. 1–2, pp. 211–217, Jan. 2015.

10.3 Conference presentations

M. Buckwell, S. Chen, L. Jiang, X, Jing, R. J. Chater, F. Iacoviello, L. Intilla, L. Montesi, W. H. Ng, S. Hudziak, A. Mehonic, F. Cacialli, P. Shearing, A. Aguadero, M. Lanza and A. J. Kenyon, “Tomography of conductive features in thin films with atomic force microscopy,” *UKSAF Coatings and Interface Analysis*, *2018*

M. Buckwell, L. Montesi, W. H. Ng, S. Hudziak, A Mehonic and A. J. Kenyon, “Conductance tomography of intrinsic SiO_x RRAM devices,” *ChinaRRAM, 2017*

M. Buckwell, L. Montesi, W. H. Ng, A. Mehonic, S. Hudziak and A. J. Kenyon, “Combined conductance tomography and Raman spectroscopy study of resistance switching in silica ReRAM devices,” *Materials Research Society Fall Meeting, 2016*

M. Buckwell, L. Montesi, W. H. Ng, A. Mehonic, S. Hudziak, M. Duchamp, R. E. Dunin-Borkowski and A. J. Kenyon, “Conductive AFM topography of intrinsic conductivity variations in silica based dielectrics for memory applications,” *Electrochemical Society PRiME Meeting, 2016*

M. Buckwell, L. Montesi, W. H. Ng, A. Mehonic, S. Hudziak, M. Duchamp, R. E. Dunin-Borkowski and A. J. Kenyon, “Tomography of intrinsic filamentation in silica based ReRAM devices with conductive atomic force microscopy,” *Electrochemical Society PRiME Meeting, 2016*

M. Buckwell, L. Montesi, L. Intilla, A. Mehonic, S. Hudziak, M. Duchamp, R. E. Dunin-Borkowski, F. Cacialli and A. J. Kenyon, “Conductance tomography as a simple way of examining nanoscale electro-structural changes in semiconductor devices,” *European Materials Research Society Spring Meeting, 2016*

M. Buckwell, L. Montesi, L. Intilla, A. Mehonic, S. Hudziak, F. Cacialli and A. J. Kenyon, “Conductance Tomography of Dielectric-Embedded conductivity variations with conductive atomic force microscopy,” *Materials Research Society Spring Meeting, 2016*

M. Buckwell, L. Montesi, S. Hudziak, A. Mehonic and A. J. Kenyon, “Conductance tomography of filamentation in intrinsic silica resistive RAM with conductive AFM,” (poster) *Materials Research Society Spring Meeting, 2016*

M. Buckwell, L. Montesi, A. Mehonic, S. Hudziak and A. J. Kenyon, “Tomography of conductive filaments in resistance switching memory with conductive atomic force microscopy,” *Materials Research Society Fall Meeting, 2015*

M. Buckwell, L. Montesi, S. Hudziak, A. Mehonic and A. J. Kenyon, “Observations of filamentation in silica resistive RAM by conductance tomography,” (poster) *Materials Research Society Fall Meeting, 2015*

M. Buckwell, L. Montesi (presenting author), S. Fearn, R. Chater, A. Mehonic, D. McPhail and A. J. Kenyon, “Structural investigation of resistance switching in silicon-rich silica films,” (poster) *IEEE International Conference on Nanotechnology, 2015*

M. Buckwell, L. Montesi, A. Mehonic, M. Munde, S. Hudziak, S. Fearn, R. Chater, D. McPhail and A. J. Kenyon, “Direct and real-time oxygen dynamics in silica resistance switches,” *European Materials Research Society Spring Meeting, 2015*

M. Buckwell, L. Montesi, A. Mehonic, S. Fearn, R. Chater, D. McPhail and A. J. Kenyon, “Intrinsic resistance switching in silica: the role of oxygen, “(poster) *European Materials Research Society Spring Meeting, 2015*

M. Buckwell, L. Montesi, A. Mehonic, S. Fearn, R. Chater, D. McPhail and A. J. Kenyon, “Oxygen-driven resistive switching in silica: Intrinsic mechanisms and challenges,” (poster) *Materials Research Society Spring Meeting, 2015*

M. Buckwell, L. Montesi, A. Mehonic, M. Munde, S. Hudziak, S. Fearn, R. Chater, D. McPhail and A. J. Kenyon, “Ionic- and defect-driven resistive switching in silicon suboxide,” *Materials Research Society Fall Meeting, 2014*

M. Buckwell, L. Montesi, A. Mehonic, M. Munde, S. Fearn, R. Chater, D. McPhail and A. J. Kenyon, “Reversible ionic- and defect-driven conductance changes in non-volatile, amorphous silica memory,” (poster) *European Materials Research Society Fall Meeting, 2014*

M. Buckwell, L. Montesi, A. Mehonic, M. Munde, S. Hudziak, S. Fearn, R. Chater, D. McPhail and A. J. Kenyon, “Resistive switching between non-volatile states of conductance in silicon suboxide,” *European Materials Research Society Fall Meeting, 2014*

M. Buckwell, L. Montesi, A. Mehonic, M. Munde, S. Hudziak, R. Chater, S. Fearn, D. McPhail and A. J. Kenyon, “An examination of the ionic and defect-driven changes which lead to the generation of discrete, reversible, non-volatile states of conductance in silicon-doped silica,” *European Materials Research Society Fall Meeting, 2014*

M. Buckwell, L. Montesi, O. Reza, A. Mehonic, M. Munde, S. Hudziak and A. J. Kenyon, “Microscopic and spectroscopic analysis of the nature of conductive filaments in silicon-rich silicon oxide,” *European Materials Research Society Fall Meeting, 2014*

11. References

[1] J. Yao, Z. Sun, L. Zhong, D. Natelson, and J. M. Tour, “Resistive switches and memories from silicon oxide.,” *Nano Lett.*, vol. 10, no. 10, pp. 4105–10, Oct. 2010.

[2] F. Pan, S. Gao, C. Chen, C. Song, and F. Zeng, “Recent progress in resistive random access memories: Materials, switching mechanisms, and performance,” *Mater. Sci. Eng. R Reports*, vol. 83, pp. 1–59, Sep. 2014.

[3] P. Pavan, R. Bez, P. Olivo, and E. Zanoni, “Flash memory cells-an overview,” *Proc. IEEE*, vol. 85, no. 8, pp. 1248–1271, 1997.

[4] F. Pan, C. Chen, Z. Wang, Y. Yang, J. Yang, and F. Zeng, “Nonvolatile resistive switching memories-characteristics, mechanisms and challenges,” *Prog. Nat. Sci. Mater. Int.*, vol. 20, pp. 1–15, Nov. 2010.

[5] G. E. Moore, “Cramming more components onto integrated circuits, Reprinted from Electronics, volume 38, number 8, April 19, 1965, pp.114 ff.,” *IEEE Solid-State Circuits Newsl.*, vol. 20, no. 8, pp. 33–35, 2006.

[6] R. R. Schaller, “Moore’s law: past, present and future,” *IEEE Spectr.*, vol. 34, 1997.

[7] G. Ghidini, a. Garavaglia, G. Giusto, R. Bottini, and D. Brazzelli, “Soft and hard breakdown: impact of annealing recovery on transistor performances,” *Microelectron. Eng.*, vol. 72, no. 1–4, pp. 5–9, Apr. 2004.

[8] C. M. . Osburn and D. W. Ormond, “Dielectric Breakdown in Silicon Dioxide Films on Silicon, I. Measurement and Interpretation,” *J. Electrochem. Soc.*, vol. 119, no. 5, pp. 591–597, 1972.

[9] C.-Y. Lu, K.-Y. Hsieh, and R. Liu, “Future challenges of flash memory technologies,” *Microelectron. Eng.*, vol. 86, no. 3, pp. 283–286, Mar. 2009.

[10] R. Waser and M. Aono, “Nanoionics-based resistive switching memories.,” *Nat. Mater.*, vol. 6, no. 11, pp. 833–40, Nov. 2007.

[11] K. M. Kim, D. S. Jeong, and C. S. Hwang, “Nanofilamentary resistive switching in binary oxide system; a review on the present status and outlook.,” *Nanotechnology*, vol. 22, no. 25, p. 254002, Jun. 2011.

[12] A. Mehonic, A. Vrajitoarea, S. Cueff, S. Hudziak, H. Howe, C. Labbé, R. Rizk, M. Pepper, and A. J. Kenyon, “Quantum conductance in silicon oxide resistive memory devices.,” *Sci. Rep.*, vol. 3, p. 2708, Jan. 2013.

[13] A. Mehonic, S. Cueff, M. Wojdak, S. Hudziak, O. Jambois, C. Labbé, B. Garrido, R. Rizk, and A. J. Kenyon, “Resistive switching in silicon suboxide films,” *J. Appl. Phys.*, vol. 111, no. 7, p. 74507, 2012.

[14] A. Mehonic, S. Cueff, M. Wojdak, S. Hudziak, C. Labbé, R. Rizk, and A. J. Kenyon, “Electrically tailored resistance switching in silicon oxide,” *Nanotechnology*, vol. 23, no. 45, p. 455201, Nov. 2012.

[15] J. Yao, L. Zhong, D. Natelson, and J. M. Tour, “Intrinsic resistive switching and memory effects in silicon oxide,” *Appl. Phys. A*, vol. 102, no. 4, pp. 835–839, Jan. 2011.

[16] L. Ji, Y. Chang, B. Fowler, and Y. Chen, “Integrated One Diode − One Resistor Architecture in Nanopillar SiOx Resistive Switching Memory by Nanosphere Lithography,” *Nano Lett.*, vol. 14, no. 2, pp. 813–818, 2014.

[17] G. Wang, A. C. Lauchner, J. Lin, D. Natelson, K. V Palem, J. M. Tour, and M, “High-performance and low-power rewritable SiOx 1 kbit one diode-one resistor crossbar memory array,” *Adv. Mater.*, vol. 25, no. 34, pp. 4789–93, Sep. 2013.

[18] R. Waser, R. Dittmann, G. Staikov, and K. Szot, “Redox-Based Resistive Switching Memories - Nanoionic Mechanisms, Prospects, and Challenges,” *Adv. Mater.*, vol. 21, no. 25–26, pp. 2632–2663, Jul. 2009.

[19] A. Mehonic, M. Buckwell, L. Montesi, L. Garnett, S. Hudziak, S. Fearn, R. Chater, D. McPhail, and A. J. Kenyon, “Structural changes and conductance thresholds in metal-free intrinsic SiOx resistive random access memory,” *J. Appl. Phys.*, vol. 117, p. 124505, 2015.

[20] Y. Wang, B. Fowler, Y.-T. Chen, F. Xue, F. Zhou, Y.-F. Chang, and J. C. Lee, “Effect of hydrogen/deuterium incorporation on electroforming voltage of SiOx resistive random access memory,” *Appl. Phys. Lett.*, vol. 101, no. 18, p. 183505, 2012.

[21] S. Lombardo, J. H. Stathis, B. P. Linder, K. L. Pey, F. Palumbo, and C. H. Tung, “Dielectric breakdown mechanisms in gate oxides,” *J. Appl. Phys.*, vol. 98, no. 12, p. 121301, 2005.

[22] N. Klein, “Electrical breakdown mechanisms in thin insulators,” *Thin Solid Films*, vol. 50, pp. 223–232, 1978.

[23] C. Zener, “A theory of the electrical breakdown of solid dielectrics,” *Proc. R. Soc. London. Ser. A, …*, vol. 145, no. 855, pp. 523–529, 1934.

[24] H. Fröhlich and B. Paranjape, “Dielectric breakdown in solids,” *… Phys. Soc. Sect. B*, vol. 21, 1956.

[25] M. Shatzkes, M. Av-Ron, and R. M. . Anderson, “On the nature of conduction and switching in SiO2,” *J. Appl. Phys.*, vol. 45, no. 5, p. 2065, 1974.

[26] L. Yang, “Resistive Switching in Pt/TiO2/Pt structures,” in *Resistive Switching in TiO2 Thin Films*, Forschungszentrum Jülich, 2011, pp. 37–53.

[27] R. Waser, “Resistive non-volatile memory devices (Invited Paper),” *Microelectron. Eng.*, vol. 86, no. 7–9, pp. 1925–1928, Jul. 2009.

[28] U. Celano and W. Vandervorst, “Scaning Probe Tomography for Advanced Material Characterization,” in *International Integrated Reliability Workshop*, 2014, pp. 1–5.

[29] J. Joshua Yang, F. Miao, M. D. Pickett, D. A. A. Ohlberg, D. R. Stewart, C. N. Lau, and R. S. Williams, “The mechanism of electroforming of metal oxide memristive switches.,” *Nanotechnology*, vol. 20, no. 21, p. 215201, May 2009.

[30] Y. F. Chang, B. Fowler, Y. C. Chen, Y. T. Chen, Y. Wang, F. Xue, F. Zhou, and J. C. Lee, “Intrinsic SiOx-based unipolar resistive switching memory. I. Oxide stoichiometry effects on reversible switching and program window optimization,” *J. Appl. Phys.*, vol. 116, no. 4, pp. 0–10, 2014.

[31] D. S. Jeong, H. Schroeder, U. Breuer, and R. Waser, “Characteristic electroforming behavior in Pt/TiO2/Pt resistive switching cells depending on atmosphere,” *J. Appl. Phys.*, vol. 104, no. 12, p. 123716, 2008.

[32] M. Lanza, G. Bersuker, M. Porti, E. Miranda, M. Nafría, and X. Aymerich, “Resistive switching in hafnium dioxide layers: Local phenomenon at grain boundaries,” *Appl. Phys. Lett.*, vol. 101, no. 19, p. 193502, 2012.

[33] S. M. Bishop, H. Bakhru, J. O. Capulong, and N. C. Cady, “Influence of the SET current on the resistive switching properties of tantalum oxide created by oxygen implantation,” *Appl. Phys. Lett.*, vol. 100, no. 14, p. 142111, 2012.

[34] C. Yoshida, K. Kinoshita, T. Yamasaki, and Y. Sugiyama, “Direct observation of oxygen movement during resistance switching in NiO/Pt film,” *Appl. Phys. Lett.*, vol. 93, no. 4, p. 42106, 2008.

[35] J. P. Strachan, M. D. Pickett, J. J. Yang, S. Aloni, a L. David Kilcoyne, G. Medeiros-Ribeiro, and R. Stanley Williams, “Direct identification of the conducting channels in a functioning memristive device.,” *Adv. Mater.*, vol. 22, no. 32, pp. 3573–7, Aug. 2010.

[36] J. Simmons and R. Verderber, “New conduction and reversible memory phenomena in thin insulating films,” *Proc. R. Soc. A*, vol. 301, pp. 77–102, 1967.

[37] D. P. Oxley, “ELECTROFORMING , SWITCHING AND MEMORY EFFECTS IN OXIDE THIN FILMS,” *Electrocompon. Sci. Technol.*, vol. 3, no. C, pp. 217–224, 1977.

[38] P. G. Lecomber, A. E. Owen, W. E. Spear, J. Hajto, A. J. Snell, W. K. Choi, M. J. Rose, and S. Reynolds, “The switching mechanism in amorphous silicon junctions,” *J. Non. Cryst. Solids*, vol. 77–78, no. PART 2, pp. 1373–1382, 1985.

[39] H. Pagnia and S. Sotnik, “Bistable Switching in Electroformed Metal-Insulator-Metal Devices,” vol. 11, 1988.

[40] Y. Wang, X. Qian, K. Chen, Z. Fang, W. Li, and J. Xu, “Resistive switching mechanism in silicon highly rich SiOx (x < 0.75) films based on silicon dangling bonds percolation model,” *Appl. Phys. Lett.*, vol. 102, no. 4, p. 42103, 2013.

[41] J. Yao, L. Zhong, Z. Zhang, T. He, Z. Jin, P. J. Wheeler, D. Natelson, and J. M. Tour, “Resistive switching in nanogap systems on SiO2 substrates.,” *Small*, vol. 5, no. 24, pp. 2910–5, Dec. 2009.

[42] D. S. Jeong, R. Thomas, R. S. Katiyar, J. F. Scott, H. Kohlstedt, A. Petraru, and C. S. Hwang, “Emerging memories: resistive switching mechanisms and current status.,” *Rep. Prog. Phys.*, vol. 75, no. 7, p. 76502, Jul. 2012.

[43] G. Dearnaley, A. M. Stoneham, and D. V. Morgan, “Electrical Phenomena in Amorphous

Oxide Films," *Rep. Prog. Phys.*, vol. 33, pp. 1129–1191, 1970.

[44] R. Waser, R. Bruchhaus, and S. Menzel, "Redox-based Resistive Switching Memories," in *Nanoelectronics and Information Technology*, 3rd ed., R. Waser, Ed. Wiley, 2012, pp. 683–710.

[45] M. P. Houng, Y. H. Wang, and W. J. Chang, "Current transport mechanism in trapped oxides: A generalized trap-assisted tunneling model," *J. Appl. Phys.*, vol. 86, no. May 2015, p. 1488, 1999.

[46] P. Blöchl and J. Stathis, "Hydrogen Electrochemistry and Stress-Induced Leakage Current in Silica," *Phys. Rev. Lett.*, vol. 83, pp. 372–375, 1999.

[47] M. Porti, M. Avidano, M. Nafria, X. Aymerich, J. Carreras, and B. Garrido, "Charge storage in Si nanocrystals embedded in SiO2 with enhanced C-AFM," *Proc. SPIE*, vol. 5838, pp. 43–51, Jun. 2005.

[48] D.-H. Kwon, K. M. Kim, J. H. Jang, J. M. Jeon, M. H. Lee, G. H. Kim, X.-S. Li, G.-S. Park, B. Lee, S. Han, M. Kim, and C. S. Hwang, "Atomic structure of conducting nanofilaments in TiO2 resistive switching memory.," *Nat. Nanotechnol.*, vol. 5, no. 2, pp. 148–53, Feb. 2010.

[49] G. Hwan Kim, J. Ho Lee, J. Yeong Seok, S. Ji Song, J. Ho Yoon, K. Jean Yoon, M. Hwan Lee, K. Min Kim, H. Dong Lee, S. Wook Ryu, T. Joo Park, and C. Seong Hwang, "Improved endurance of resistive switching TiO2 thin film by hourglass shaped Magnéli filaments," *Appl. Phys. Lett.*, vol. 98, no. 26, p. 262901, 2011.

[50] D. Carta, P. Guttmann, A. Regoutz, A. Khiat, A. Serb, I. Gupta, A. Mehonic, M. Buckwell, S. Hudziak, A. J. Kenyon, and T. Prodromakis, "X-ray spectromicroscopy investigation of soft and hard breakdown in RRAM devices," *Nanotechnology*, vol. 27, no. 34, p. 345705, 2016.

[51] M. Lanza, K. Zhang, M. Porti, M. Nafría, Z. Y. Shen, L. F. Liu, J. F. Kang, D. Gilmer, and G. Bersuker, "Grain boundaries as preferential sites for resistive switching in the HfO2 resistive random access memory structures," *Appl. Phys. Lett.*, vol. 100, no. 12, p. 123508, 2012.

[52] R. A. Street, "Doping and the Fermi Energy in Amorphous Silicon," *Phys. Rev. Lett.*, vol. 49, no. 16, pp. 1187–1190, 1982.

[53] M. S. Munde, A. Mehonic, W. H. Ng, M. Buckwell, L. Montesi, M. Bosman, A. L. Shluger, and A. J. Kenyon, "Intrinsic Resistance Switching in Amorphous Silicon Suboxides: The Role of Columnar Microstructure," *Sci. Rep.*, vol. 7, no. 1, p. 9274, 2017.

[54] A. Mehonic and A. J. Kenyon, "Emulating the electrical activity of the neuron using a silicon oxide RRAM cell," *Front. Neurosci.*, vol. 10, no. FEB, 2016.

[55] C. Baeumer, C. Schmitz, A. H. H. Ramadan, H. Du, K. Skaja, V. Feyer, P. Müller, B. Arndt, C.-L. Jia, J. Mayer, R. A. De Souza, C. Michael Schneider, R. Waser, and R. Dittmann, "Spectromicroscopic insights for rational design of redox-based memristive devices," *Nat. Commun.*, vol. 6, p. 8610, 2015.

[56] J. Yao, L. Zhong, D. Natelson, and J. M. Tour, “Etching-dependent reproducible memory switching in vertical SiO[sub 2] structures,” *Appl. Phys. Lett.*, vol. 93, no. 25, p. 253101, 2008.

[57] J. Yao, L. Zhong, D. Natelson, and J. M. Tour, “In situ imaging of the conducting filament in a silicon oxide resistive switch.,” *Sci. Rep.*, vol. 2, p. 242, Jan. 2012.

[58] Y. Y. Chen, B. Govoreanu, L. Goux, R. Degraeve, A. Fantini, G. S. Kar, D. J. Wouters, G. Groeseneken, J. A. Kittl, M. Jurczak, and L. Altimime, “Balancing SET/RESET Pulse for >1010 Endurance in HfO 2 1T1R Bipolar RRAM,” *IEEE Trans. Electron Devices*, vol. 59, no. 12, pp. 3243–3249, 2012.

[59] A. Belmonte, W. Kim, B. T. Chan, N. Heylen, A. Fantini, M. Houssa, M. Jurczak, and L. Goux, “A thermally stable and high-performance 90-nm Al2O3 \ Cu-based 1T1R CBRAM cell,” *IEEE Trans. Electron Devices*, vol. 60, no. 11, pp. 3690–3695, 2013.

[60] A. Bricalli, E. Ambrosi, M. Laudato, M. Maestro, R. Rodriguez, and D. Ielmini, “SiOx-based resistive switching memory (RRAM) for crossbar storage/select elements with high on/off ratio,” pp. 87–90, 2016.

[61] C. Li, L. Han, H. Jiang, M.-H. Jang, P. Lin, Q. Wu, M. Barnell, J. J. Yang, H. L. Xin, and Q. Xia, “Three-dimensional crossbar arrays of self-rectifying Si/SiO2/Si memristors,” *Nat. Commun.*, vol. 8, p. 15666, 2017.

[62] H. Y. Lee, Y. S. Chen, P. S. Chen, P. Y. Gu, Y. Y. Hsu, S. M. Wang, W. H. Liu, C. H. Tsai, S. S. Sheu, P. C. Chiang, W. P. Lin, C. H. Lin, W. S. Chen, F. T. Chen, C. H. Lien, and M. J. Tsai, “Evidence and solution of Over-RESET problem for HfOx Based Resistive Memory with Sub-ns Switching Speed and High Endurance,” *Tech. Dig. - Int. Electron Devices Meet. IEDM*, pp. 7–10, 2010.

[63] U. Celano, G. Giammaria, L. Goux, A. Belmonte, M. Jurczak, and W. Vandervorst, “Nanoscopic structural rearrangements of the Cu-filament in conductive-bridge memories,” *Nanoscale*, pp. 13915–13923, 2016.

[64] W. Yi, F. Perner, M. S. Qureshi, H. Abdalla, M. D. Pickett, J. J. Yang, M. X. M. Zhang, G. Medeiros-Ribeiro, and R. S. Williams, “Feedback write scheme for memristive switching devices,” *Appl. Phys. A Mater. Sci. Process.*, vol. 102, no. 4, pp. 973–982, 2011.

[65] S. Kumar, N. Davila, Z. Wang, X. Huang, J. P. Strachan, D. Vine, A. L. David Kilcoyne, Y. Nishi, and R. Stanley Williams, “Spatially uniform resistance switching of low current, high endurance titanium–niobium-oxide memristors,” *Nanoscale*, vol. 9, pp. 1793–1798, 2017.

[66] M.-J. Lee, C. B. Lee, D. Lee, S. R. Lee, M. Chang, J. H. Hur, Y.-B. Kim, C.-J. Kim, D. H. Seo, S. Seo, U.-I. Chung, I.-K. Yoo, and K. Kim, “A fast, high-endurance and scalable non-volatile memory device made from asymmetric Ta2O5−x/TaO2−x bilayer structures,” *Nat. Mater.*, vol. 10, no. 8, pp. 625–630, 2011.

[67] A. Chen, “Switching control of resistive switching devices,” *Appl. Phys. Lett.*, vol. 97, no. 26, p. 263505, 2010.

[68] T. Liu, Y. Kang, M. Verma, and M. Orlowski, “Switching and Mechanical Damage of

Cu/TaOx/Pt Resistive Devices under High Negative Voltage Stress," *Meet. Abstr.*, vol. 2762, no. 2007, p. 263505, 2012.

[69] J.-J. Huang, C.-W. Kuo, W.-C. Chang, and T.-H. Hou, "Transition of stable rectification to resistive-switching in Ti/TiO[sub 2]/Pt oxide diode," *Appl. Phys. Lett.*, vol. 96, no. 26, p. 262901, 2010.

[70] R. Nori, N. R. C. Raju, N. Thomas, N. Panwar, P. Kumbhare, G. Rao, S. Srivinvasan, N. Venketaramani, and U. Ganguly, "Conducting Oxide Electrode to Mitigate Mechanical Instability (Bubble Formation) during Operation of La1-xSrxMnO3 (LSMO) based RRAM," *MRS Symp. Proc.*, vol. 1507, no. Mi, 2013.

[71] Y. Yang, P. Gao, S. Gaba, T. Chang, X. Pan, and W. Lu, "Observation of conducting filament growth in nanoscale resistive memories," *Nat. Commun.*, vol. 3, p. 732, 2012.

[72] Keithley Instruments Inc., "4200-SCS Parameter Analyser," *Products Catalogue*, 2015. [Online]. Available: http://www.keithley.in/products/dcac/currentvoltage/4200scs. [Accessed: 26-Feb-2015].

[73] G. Binnig, C. Quate, and C. Gerber, "Atomic force microscopy," *Phys. Rev. Lett.*, vol. 53, pp. 53–55, 1986.

[74] P. Atkins and J. de Paula, "The Total Interaction," in *Atkins' Physical Chemistry*, 10th ed., Oxford, 2014, pp. 676–677.

[75] P. Atkins and J. de Paula, "Many-electron atoms," in *Atkins' Physical Chemistry*, 10th ed., Oxford, 2014, pp. 370–380.

[76] F. J. Giessibl, "Advances in atomic force microscopy," *Rev. Mod. Phys.*, vol. 75, no. July, 2003.

[77] C. Gerber and H. P. Lang, "How the doors to the nanoworld were opened.," *Nat. Nanotechnol.*, vol. 1, no. 1, pp. 3–5, Oct. 2006.

[78] Bruker Corporation, "Contact Mode AFM," *Guide to SPM and AFM modes*, 2011. [Online]. Available: http://blog.brukerafmprobes.com/category/guide-to-spm-and-afm-modes/page/3/. [Accessed: 26-Feb-2015].

[79] S. Hudziak, "Physcial Techniques in the Life Sciences, PTL: Atomic Force Microscopy." UCL EE, 2012.

[80] G. Binnig, C. Quate, and C. Gerber, "Atomic force microscope," *Phys. Rev. Lett.*, vol. 56, no. 9, pp. 53–55, 1986.

[81] P. Eaton and P. West, "AFM Modes," in *Atomic Force Microscopy*, 1st ed., Oxford University Press, 2010, pp. 49–81.

[82] UCL EE Department, "Experiment 6 : AFM Imaging of Biological Samples." pp. 1–2, 2012.

[83] Bruker Corporation, "PeakForce Tapping & QNM," *Guide to SPM and AFM modes*, 2011. [Online]. Available: http://blog.brukerafmprobes.com/guide-to-spm-and-afm-modes/peakforce-tapping-onm/. [Accessed: 26-Feb-2015].

[84] “Application Note # 128 Quantitative Mechanical Property Mapping at the Nanoscale with PeakForce QNM,” vol. im. Bruker, Santa Barbara, CA, 2012.

[85] W. Xu, P. M. Wood-Adams, and C. G. Robertson, “Measuring local viscoelastic properties of complex materials with tapping mode atomic force microscopy,” *Polymer (Guildf).*, vol. 47, no. 13, pp. 4798–4810, Jun. 2006.

[86] M. Lanza, S. O’Shea, and M. Welland, “Simultaneous force and conduction measurements in atomic force microscopy,” *Phys. Rev. B*, vol. 56, no. 23, pp. 15345–15352, 1997.

[87] J. B. Pethica and W. C. Oliver, “Tip Surface Interactions in STM and AFM,” *Phys. Scr.*, vol. T19A, pp. 61–66, Jan. 1987.

[88] J. Y. Park, S. Maier, B. Hendriksen, and M. Salmeron, “Sensing current and forces with SPM,” *Mater. Today*, vol. 13, no. 10, pp. 38–45, Oct. 2010.

[89] S. J. O’Shea, R. M. Atta, and M. E. Welland, “Characterization of tips for conducting atomic force microscopy,” *Rev. Sci. Instrum.*, vol. 66, no. 3, p. 2508, 1995.

[90] M. F. Tabet, “Deconvolution of tip affected atomic force microscope images and comparison to Rutherford backscattering spectrometry,” *J. Vac. Sci. Technol. B Microelectron. Nanom. Struct.*, vol. 15, no. 4, p. 800, Jul. 1997.

[91] Bruker Nano Inc., “RESP-20,” *Bruker AFM Probes*, 2017. [Online]. Available: http://www.brukerafmprobes.com/Product.aspx?ProductID=3929. [Accessed: 06-Oct-2017].

[92] Bruker Nano Inc., “SCM-PIC,” *Bruker AFM Probes*, 2017. [Online]. Available: http://www.brukerafmprobes.com/p-3390-scm-pic.aspx. [Accessed: 06-Oct-2017].

[93] M. Lanza, T. Gao, Z. Yin, Y. Zhang, Z. Liu, Y. Tong, Z. Shen, and H. Duan, “Nanogap based graphene coated AFM tips with high spatial resolution, conductivity and durability.,” *Nanoscale*, vol. 5, no. 22, pp. 10816–23, Nov. 2013.

[94] D. Tranchida, S. Piccarolo, and R. a C. Deblieck, “Some experimental issues of AFM tip blind estimation: the effect of noise and resolution,” *Meas. Sci. Technol.*, vol. 17, no. 10, pp. 2630–2636, Oct. 2006.

[95] K. Smith and C. Oatley, “The scanning electron microscope and its fields of application,” *Br. J. Appl. Phys.*, vol. 6, no. 11, pp. 391–399, 1955.

[96] M. Knoll, “Static potential and secondary emission of bodies under electron irradiation,” *Z. tech. Phys*, vol. 11, pp. 467–475, 1935.

[97] V. K. Zworkyin, “The Scanning Electron Microscope,” *Sci. Am.*, vol. 167, no. 3, pp. 111–113, 1942.

[98] B. Hafner, *Scanning Electron Microscopy Primer*, 1st ed. Twin Cities: Characterization Facility, University of Minnesota, 2007.

[99] J. I. Goldstein, D. E. Newbury, P. Echlin, D. C. Joy, A. Romig Jr., C. E. Lyman, C. Fiori, and E. Lifshin, “Evolution of the Scanning Electron Microscope,” in *Scanning Electron*

Microscopy and X-Ray Microanalysis: A Text for Biologists, Materials Scientists, and Geologists, 2nd ed., New York: Plenum Press, 1992.

[100] J. I. Goldstein, D. E. Newbury, P. Echlin, D. C. Joy, A. Romig Jr., C. E. Lyman, C. Fiori, and E. Lifshin, "Producing Minimum Spot Size," in *Scanning Electron Microscopy and X-Ray Microanalysis: A Text for Biologists, Materials Scientists, and Geologists*, 2nd ed., New York: Plenum Press, 1992, pp. 48–53.

[101] P. Royston, "XPS Theory." INRS-EMT.

[102] P. Atkins and J. de Paula, "Wave-particle duality," in *Atkins' Physical Chemistry2*, 7th ed., Oxford, 2002, pp. 299–304.

[103] H. Hertz, "On the Photoelectric Effect," *Ann Phys*, vol. 31, pp. 983–1000, 1887.

[104] A. Einstein, "On a heuristic point of view about the creation and conversion of light," *Ann. Phys.*, 1905.

[105] P. Atkins and J. de Paula, "Spectroscopy 2," in *Atkins' Physical Chemistry*, 7th ed., Oxford, 2002, pp. 568–571.

[106] A. Dane, U. K. Demirok, A. Aydinli, and S. Suzer, "X-ray photoelectron spectroscopic analysis of Si nanoclusters in SiO2 matrix.," *J. Phys. Chem. B*, vol. 110, no. 3, pp. 1137–40, Jan. 2006.

[107] Casa Software, "XPS Instrumentation," 2005. [Online]. Available: http://www.casaxps.com/help_manual/XPSInformation/XPSInstr.htm. [Accessed: 15-Jul-2013].

[108] H. Ishii and K. Seki, "Energy level alignment at organic/metal interfaces studied by UV photoemission: breakdown of traditional assumption of a common vacuum level at the interface," *IEEE Trans. Electron Devices*, vol. 44, no. 8, pp. 1295–1301, 1997.

[109] S. Hufner, *Photoelectron Spectroscopy: Principles and Applications*. Springer, 2003.

[110] D. R. Baer and M. H. Engelhard, "XPS analysis of nanostructured materials and biological surfaces," *J. Electron Spectros. Relat. Phenomena*, vol. 178–179, pp. 415–432, May 2010.

[111] D. R. Baer, M. H. Engelhard, D. J. Gaspar, a. S. Lea, and C. F. Windisch, "Use and limitations of electron flood gun control of surface potential during XPS: two non-homogeneous sample types," *Surf. Interface Anal.*, vol. 33, no. 10–11, pp. 781–790, Oct. 2002.

[112] A. Hohl, T. Wieder, P. A. van Aken, T. E. Weirich, G. Denninger, M. Vidal, S. Oswald, C. Deneke, J. Mayer, and H. Fuess, "An interface clusters mixture model for the structure of amorphous silicon monoxide (SiO)," *J. Non. Cryst. Solids*, vol. 320, no. 1–3, pp. 255–280, Jun. 2003.

[113] P. Atkins and J. de Paula, "Processes at Solid Surfaces," in *Atkins' Physical Chemistry*, 7th ed., Oxford, 2002, pp. 977–1005.

[114] Casa Software, "The Nature of X-ray Photoelectron Spectra," 2005. [Online]. Available:

http://www.casaxps.com/help_manual/XPSInformation/IntroductiontoXPS.htm. [Accessed: 15-Jul-2013].

[115] P. Atkins and J. de Paula, “The Solid State,” in *Atkins’ Physical Chemistry*, 7th ed., Oxford, 2002, pp. 767–812.

[116] P. Atkins and J. de Paula, “Molecular Structure,” in *Atkins’ Physical Chemistry*, 7th ed., Oxford, 2002, pp. 410–452.

[117] E. Dehan, P. Temple-Boyer, R. Henda, J. J. Pedroviejo, and E. Scheid, “Optical and structural properties of SiOx and SiNx materials,” *Thin Solid Films*, vol. 266, no. 1, pp. 14–19, 1995.

[118] T. P. Chen, “Application of Silicon Nanocrystal in Non-Volatile Memory Devices,” in *Nanocomposite Thin Films and Coatings: Processing, Properties and Performance*, 1st ed., S. Zhang and N. Ali, Eds. London: Imperial College Press, 2007, pp. 419–472.

[119] V. a. Terekhov, S. Y. Turishchev, K. N. Pankov, I. E. Zanin, E. P. Domashevskaya, D. I. Tetelbaum, a. N. Mikhailov, a. I. Belov, D. E. Nikolichev, and S. Y. Zubkov, “XANES, USXES and XPS investigations of electron energy and atomic structure peculiarities of the silicon suboxide thin film surface layers containing Si nanocrystals,” *Surf. Interface Anal.*, vol. 42, no. 6–7, pp. 891–896, Apr. 2010.

[120] S. Hofmann and J. H. Thomas, “An XPS study of the influence of ion sputtering on bonding in thermally grown silicon dioxide,” *J. Vac. Sci. Technol. B Microelectron. Nanom. Struct.*, vol. 1, no. 1, p. 43, 1983.

[121] F. Iacona, R. Kelly, and G. Marletta, “X-ray photoelectron spectroscopy study of bombardment-induced compositional changes in ZrO[sub 2], SiO[sub 2], and ZrSiO[sub 4],” *J. Vac. Sci. Technol. A Vacuum, Surfaces, Film.*, vol. 17, no. 5, p. 2771, 1999.

[122] O. A. Antony, “Technical aspects of ultrasonic cleaning,” *Ultrasonics*, vol. 1, no. 4, pp. 194–198, 1963.

[123] T. J. Mason, “Ultrasonic cleaning: An historical perspective,” *Ultrason. Sonochem.*, vol. 29, pp. 519–523, 2016.

[124] E. Maisonhaute, C. Prado, P. C. White, and R. G. Compton, “Surface acoustic cavitation understood via nanosecond electrochemistry. Part III: Shear stress in ultrasonic cleaning,” *Ultrason. Sonochem.*, vol. 9, no. 6, pp. 297–303, 2002.

[125] M. Buckwell, L. Montesi, A. Mehonic, A. J. Kenyon, S. Fearn, R. J. Chater, and D. McPhail, “Structural investigation of resistance switching in silicon-rich silica films,” in *IEEE-NANO 2015 - 15th International Conference on Nanotechnology*, 2016, pp. 489–492.

[126] The Mathoworks Inc., “MATLAB R2013a.” The Mathworks Inc., 2013.

[127] Microsoft, “Excel.” Microsoft, 2011.

[128] “NanoScope Analysis.” Bruker, 2014.

[129] http://www.slicer.org/, “3D Slicer.” [Online]. Available: http://www.slicer.org/. [Accessed:

24-Jun-2015].

[130] A. Fedorov, R. Beichel, J. Kalpathy-Cramer, J. Finet, J. C. Fillion-Robin, S. Pujol, C. Bauer, D. Jennings, F. Fennessy, M. Sonka, J. Buatti, S. Aylward, J. V. Miller, S. Pieper, and R. Kikinis, "3D Slicer as an image computing platform for the Quantitative Imaging Network," *Magn. Reson. Imaging*, vol. 30, no. 9, pp. 1323–1341, 2012.

[131] N. Fairley, *CasaXPS Manual - 2.3.15 Introduction to XPS and AES*, 1.2. Casa Software Ltd, 2009.

[132] N. Fairley, "CasaXPS." Casa Software Ltd, 2009.

[133] D. A. Shirley, "High-resolution x-ray photoemission spectrum of the valence bands of gold," *Phys. Rev. B*, vol. 5, no. 12, pp. 4709–4714, 1972.

[134] F. Jolly, J. L. Cantin, F. Rochet, G. Dufour, and H. J. Von Bardeleben, "Temperature effects on the Si/SiO2 interface defects and suboxide distribution," *J. Non. Cryst. Solids*, vol. 245, pp. 217–223, 1999.

[135] A. Mehonic, M. Buckwell, L. Montesi, M. S. Munde, D. Gao, S. Hudziak, R. J. Chater, S. Fearn, D. McPhail, M. Bosman, A. L. Shluger, and A. J. Kenyon, "Nanoscale Transformations in Metastable, Amorphous, Silicon-Rich Silica," *Advanced Materials*, vol. 28, no. 34. p. 7549, 2016.

[136] Y. Yang, Y. Takahashi, A. Tsurumaki-Fukuchi, M. Arita, M. Moors, M. Buckwell, A. Mehonic, and A. J. Kenyon, "Probing electrochemistry at the nanoscale: in situ TEM and STM characterizations of conducting filaments in memristive devices," *J. Electroceramics*, pp. 1–21, 2017.

[137] D. Ielmini, F. Nardi, and C. Cagli, "Universal reset characteristics of unipolar and bipolar metal-oxide RRAM," *IEEE Trans. Electron Devices*, vol. 58, no. 10, pp. 3246–3253, 2011.

[138] D. L. Sedin and K. L. Rowlen, "Influence of tip size on AFM roughness measurements," *Appl. Surf. Sci.*, vol. 182, no. 1–2, pp. 40–48, 2001.

[139] J. T. B. Degarmo and R. A. Kohser, "Surface Engineering," in *DeGarmo's Materials and Processes in Manufacturing*, Wiley, 2011, pp. 1032–1034.

[140] M. Porti, S. Meli, M. Nafria, and X. Aymerich, "Pre-breakdown noise in electrically stressed thin SiO2 layers of MOS devices observed with C-AFM," *Microelectron. Reliab.*, vol. 43, no. 8, pp. 1203–1209, Aug. 2003.

[141] S. Logothetidis and a. Barborica, "In-situ and real time room temperature oxidation studies of fcc TiN thin films," *Microelectron. Eng.*, vol. 33, no. 1–4, pp. 309–316, Jan. 1997.

[142] F. Truica-Marasescu, S. Pham, and M. R. Wertheimer, "VUV processing of polymers: Surface modification and deposition of organic thin films," *Nucl. Instruments Methods Phys. Res. Sect. B Beam Interact. with Mater. Atoms*, vol. 265, no. 1, pp. 31–36, Dec. 2007.

[143] H. a Girard, T. Petit, S. Perruchas, T. Gacoin, C. Gesset, J. C. Arnault, and P. Bergonzo,

"Surface properties of hydrogenated nanodiamonds: a chemical investigation.," *Phys. Chem. Chem. Phys.*, vol. 13, no. 24, pp. 11517–23, Jun. 2011.

[144] O. Park, J.-I. Lee, M.-J. Chun, J.-T. Yeon, S. Yoo, S. Choi, N.-S. Choi, and S. Park, "High-performance Si anodes with a highly conductive and thermally stable titanium silicide coating layer," *RSC Adv.*, vol. 3, no. 8, p. 2538, 2013.

[145] Thermo Scientific XPS, "Charge Compensation," *thermofisher.com*, 2016. [Online]. Available: https://xpssimplified.com/charge_compensation.php. [Accessed: 19-Sep-2017].

[146] T. L. Barr, "An XPS study of Si as it occurs in adsorbents, catalysts, and thin films," *Appl. Surf. Sci.*, vol. 15, no. 1–4, pp. 1–35, 1983.

[147] J. Zhao, E. G. Garza, K. Lam, and C. M. Jones, "Comparison study of physical vapor-deposited and chemical vapor-deposited titanium nitride thin films using X-ray photoelectron spectroscopy," *Appl. Surf. Sci.*, vol. 158, no. 3–4, pp. 246–251, May 2000.

[148] E. Galvanetto, F. P. Galliano, F. Borgioli, U. Bardi, and A. Lavacchi, "XRD and XPS study on reactive plasma sprayed titanium-titanium nitride coatings," *Thin Solid Films*, vol. 385, pp. 223–229, 2001.

[149] N. Fairley, "Peak Fitting in XPS," *casaxps.com*, 2006. [Online]. Available: http://www.casaxps.com/help_manual/manual_updates/peak_fitting_in_xps.pdf.

[150] F. Pagliuca, P. Luches, and S. Valeri, "Interfacial interaction between cerium oxide and silicon surfaces," *Surf. Sci.*, vol. 607, pp. 164–169, Jan. 2013.

[151] J. A. Leiro, M. H. Heinonen, T. Laiho, and I. G. Batirev, "Core-level XPS spectra of fullerene, highly oriented pyrolitic graphite, and glassy carbon," *J. Electron Spectros. Relat. Phenomena*, vol. 128, no. 2–3, pp. 205–213, 2003.

[152] V. V. Atuchin, V. G. Kesler, N. V. Pervukhina, and Z. Zhang, "Ti 2p and O 1s core levels and chemical bonding in titanium-bearing oxides," *J. Electron Spectros. Relat. Phenomena*, vol. 152, no. 1–2, pp. 18–24, 2006.

[153] N. C. Saha and H. G. Tompkins, "Titanium nitride oxidation chemistry: An x-ray photoelectron spectroscopy study," *J. Appl. Phys.*, vol. 72, no. 7, p. 3072, 1992.

[154] M. V. Kuznetsov, J. F. Zhuravlev, V. a. Zhilyaev, and V. a. Gubanov, "XPS study of the nitrides, oxides and oxynitrides of titanium," *J. Electron Spectros. Relat. Phenomena*, vol. 58, no. 1–2, pp. 1–9, Mar. 1992.

[155] N. White, A. L. Campbell, J. T. Grant, R. Pachter, K. Eyink, R. Jakubiak, G. Martinez, and C. V. Ramana, "Surface/interface analysis and optical properties of RF sputter-deposited nanocrystalline titanium nitride thin films," *Appl. Surf. Sci.*, vol. 292, pp. 74–85, 2014.

[156] C. M. Zgrabik and E. L. Hu, "Optimization of sputtered titanium nitride as a tunable metal for plasmonic applications," *Opt. Mater. Express*, vol. 5, no. 12, p. 2786, 2015.

[157] N. Jiang, H. J. Zhang, S. N. Bao, Y. G. Shen, and Z. F. Zhou, "XPS study for reactively sputtered titanium nitride thin films deposited under different substrate bias," *Phys. B Condens. Matter*, vol. 352, no. 1–4, pp. 118–126, Oct. 2004.

[158] C. Ernsberger, J. Nickerson, A. E. Miller, and J. Moulder, “Angular resolved x-ray photoelectron spectroscopy study of reactively sputtered titanium nitride,” *J. Vac. Sci. Technol. A Vacuum, Surfaces, Film.*, vol. 3, no. 6, p. 2415, 1985.

[159] Y. Du, A. Kumar, H. Pan, K. Zeng, S. Wang, P. Yang, and A. T. S. Wee, “The resistive switching in TiO2 films studied by conductive atomic force microscopy and Kelvin probe force microscopy,” *AIP Adv.*, vol. 3, no. 8, p. 82107, 2013.

[160] A. Sawa, “Resistive switching in transition metal oxides,” *Mater. Today*, vol. 11, no. 6, pp. 28–36, Jun. 2008.

[161] M. Lanza, U. Celano, and F. Miao, “Nanoscale characterization of resistive switching using advanced conductive atomic force microscopy based setups,” *J. Electroceramics*, 2017.

[162] G. E. Mcguire, “EFFECTS OF ION SPUTTERING ON SEMICONDUCTOR SURFACES,” *Surf. Sci.*, vol. 76, pp. 130–147, 1978.

[163] J. M. Chappé, N. Martin, J. Lintymer, F. Sthal, G. Terwagne, and J. Takadoum, “Titanium oxynitride thin films sputter deposited by the reactive gas pulsing process,” *Appl. Surf. Sci.*, vol. 253, no. 12, pp. 5312–5316, 2007.

[164] K. Szot, W. Speier, G. Bihlmayer, and R. Waser, “Switching the electrical resistance of individual dislocations in single-crystalline SrTiO3,” *Nat. Mater.*, vol. 5, no. 4, pp. 312–320, 2006.

[165] R. Waser, R. Dittmann, M. Salinga, and M. Wuttig, “Function by defects at the atomic scale – New concepts for non-volatile memories,” *Solid. State. Electron.*, vol. 54, no. 9, pp. 830–840, Sep. 2010.

[166] A. Mehonic, M. S. Munde, W. H. Ng, M. Buckwell, L. Montesi, M. Bosman, A. L. Shluger, and A. J. Kenyon, “Intrinsic resistance switching in amorphous silicon oxide for high performance SiOx ReRAM devices,” *Microelectron. Eng.*, vol. 178, pp. 98–103, 2017.

[167] N. Tomozeiu, E. . van Faassen, W. . Arnoldbik, a. . Vredenberg, and F. H. P. . Habraken, “Structure of sputtered silicon suboxide single- and multi-layers,” *Thin Solid Films*, vol. 420–421, pp. 382–385, Dec. 2002.

[168] T. Unagami, A. Lousa, and R. Messier, “Silicon Thin Film with Columnar Structure Formed by RF Diode Sputtering,” *Jpn. J. Appl. Phys.*, vol. 36, no. 2, pp. 737–739, 1997.

[169] M. T. P. M. McCann, D. A. Mooney, M. Rahman, D. D. P. Dowling, J. M. D. MacElroy, and J. Do MacElroy, “Novel, Nanoporous Silica and Titania Layers Fabricated by Magnetron Sputtering,” *ACS Appl. Mater. Interfaces*, vol. 3, no. 2, pp. 252–60, Feb. 2011.

[170] E. W. Müller, “Work Function of Tungsten Single Crystal Planes Measured by the Field Emission Microscope,” vol. 732, no. 1955, 2008.

[171] L. P. B. Lima, J. A. Diniz, I. Doi, and J. G. Fo, “Microelectronic Engineering Titanium nitride as electrode for MOS technology and Schottky diode : Alternative extraction method of titanium nitride work function,” *Microelectron. Eng.*, vol. 92, pp. 86–90, 2012.

[172] H. C. Day and D. R. Allee, “Selective area oxidation of silicon with a scanning force microscope,” *Appl. Phys. Lett.*, vol. 62, no. 21, p. 2691, 1993.

[173] a. E. Gordon, “Mechanisms of surface anodization produced by scanning probe microscopes,” *J. Vac. Sci. Technol. B Microelectron. Nanom. Struct.*, vol. 13, no. 6, p. 2805, Nov. 1995.

[174] I. Emmer, “Conducting filaments and voltage-controlled negative resistance in Al-Al2O3-Au structures with amorphous dielectric,” *Thin Solid Films*, vol. 20, no. 1, pp. 43–52, 1974.

[175] S. Privitera, G. Bersuker, S. Lombardo, C. Bongiorno, and D. C. Gilmer, “Conductive filament structure in HfO2 resistive switching memory devices,” *Solid. State. Electron.*, vol. 111, pp. 161–165, 2015.

[176] G. Bersuker, D. C. Gilmer, D. Veksler, P. Kirsch, L. Vandelli, a. Padovani, L. Larcher, K. McKenna, a. Shluger, V. Iglesias, M. Porti, and M. Nafría, “Metal oxide resistive memory switching mechanism based on conductive filament properties,” *J. Appl. Phys.*, vol. 110, no. 12, p. 124518, 2011.

[177] G. K. H. Pang, K. Z. Baba-Kishi, and A. Patel, “Topographic and phase-contrast imaging in atomic force microscopy,” *Ultramicroscopy*, vol. 81, no. 2, pp. 35–40, Mar. 2000.

[178] W. Walczyk and H. Schönherr, “The effect of PeakForce tapping mode AFM imaging on the apparent shape of surface nanobubbles,” *Langmuir*, vol. 29, no. 2, pp. 620–632, 2013.

[179] F. A. S. Al-Ramadhan and C. A. Hogarth, “Observation and compositional studies of the metallic conducting filaments in the low-resistance state (ON-state) of SiO/V2O5 thin films used as memory elements,” *J. Mater. Sci.*, vol. 19, no. 6, pp. 1939–1946, 1984.

[180] T. Eickhoff, V. Medicherla, and W. Drube, “Final state contribution to the Si 2p binding energy shift in SiO2/Si(1 0 0),” *J. Electron Spectros. Relat. Phenomena*, vol. 137–140, pp. 85–88, Jul. 2004.

[181] L. Khriachtchev, M. Pettersson, N. Runeberg, J. Lundell, and M. Rasanen, “A stable argon compound,” *Nature*, vol. 406, no. 6798, pp. 874–6, 2000.

[182] T. Laarmann, H. Wabnitz, K. Von Haeften, and T. Möller, “Photochemical processes in doped argon-neon core-shell clusters: The effect of cage size on the dissociation of molecular oxygen,” *J. Chem. Phys.*, vol. 128, no. 1, 2008.

[183] H. R. Philipp, “Optical and bonding model for non-crystalline SiOx and SiOxNy materials,” *J. Non. Cryst. Solids*, vol. 8–10, no. C, pp. 627–632, 1972.

[184] K. Prabhakaran, Y. Kobayashi, and T. Ogino, “Chemically prepared oxides on Si(001): an XPS study,” *Surf. Sci.*, vol. 290, no. 3, pp. 239–244, 1993.

[185] G. Hollinger, J. F. Morar, F. J. Himpsel, G. Hughes, and J. L. Jordan, “Si(111) surface oxidation: O 1s core-level study using synchrotron radiation,” *Surf. Sci.*, vol. 168, no. 1–3, pp. 609–616, 1986.

[186] L. Skuja, M. Hirano, H. Hosono, and K. Kajihara, “Defects in oxide glasses,” *Phys. Status Solidi C Conf.*, vol. 2, no. 1, pp. 15–24, 2005.

[187] D. Ricci, G. Pacchioni, M. Szymanski, A. Shluger, and A. Stoneham, “Modeling disorder in amorphous silica with embedded clusters: The peroxy bridge defect center,” *Phys. Rev. B*, vol. 64, pp. 3–6, 2001.

[188] R. Alfonsetti and G. De Simone, “SiOx surface stoichiometry by XPS: a comparison of various methods,” *Surf. …*, vol. 22, pp. 89–92, 1994.

[189] U. Celano, L. Goux, A. Belmonte, K. Opsomer, A. Franquet, A. Schulze, C. Detavernier, O. Richard, H. Bender, M. Jurczak, and W. Vandervorst, “Three-Dimensional Observation of the Conductive Filament in Nanoscaled Resistive Memory Devices.,” *Nano Lett.*, vol. 14, no. 5, pp. 2401–2406, Apr. 2014.

[190] S. Brivio, G. Tallarida, E. Cianci, and S. Spiga, “Formation and disruption of conductive filaments in a HfO2/TiN structure.,” *Nanotechnology*, vol. 25, no. 38, p. 385705, 2014.

[191] Y. Hou, U. Celano, L. Goux, L. Liu, A. Fantini, R. Degraeve, A. Youssef, Z. Xu, Y. Cheng, J. Kang, M. Jurczak, W. Vandervorst, Y. Hou, U. Celano, L. Goux, L. Liu, A. Fantini, R. Degraeve, and A. Youssef, “Sub-10 nm low current resistive switching behavior in hafnium oxide stack,” *Appl. Phys. Lett.*, vol. 123106, no. 108, pp. 1–6, 2016.

[192] T. R. Anthony, “Dielectric isolation of silicon by anodic bonding,” *J. Appl. Phys.*, vol. 58, no. 3, pp. 1240–1247, 1985.

[193] J. Frascaroli, S. Brivio, F. F. Lupi, G. Seguini, L. Boarino, M. Perego, and S. Spiga, “Resistive Switching in High-Density Nanodevices Fabricated by Block Copolymer Self-Assembly,” *ACS Nano*, vol. 9, no. 3, pp. 2518–2529, 2015.

[194] L. Montesi, M. Buckwell, K. Zarudnyi, L. Garnett, S. Hudziak, A. Mehonic, and A. J. A. Kenyon, “Nanosecond Analog Programming of Substoichiometric Silicon Oxide Resistive RAM,” *IEEE Trans. Nanotechnol.*, vol. 15, no. 3, pp. 1–1, 2016.

[195] D. Ielmini, “Resistive switching memories based on metal oxides: mechanisms, reliability and scaling,” *Semicond. Sci. Technol.*, vol. 31, no. 6, p. 063002–, 2016.

[196] B. H. Akinaga and H. Shima, “Resistive Random Access Memory (ReRAM) Based on Metal Oxides,” *Proc. IEEE*, vol. 98, no. 12, pp. 2237–2251, 2010.

[197] U. Celano, L. Goux, A. Belmonte, K. Opsomer, C. Detavernier, M. Jurczak, and W. Vandervorst, “Conductive filaments multiplicity as a variability factor in CBRAM,” in *Reliability Physics Symposium (IRPS), 2015 IEEE International*, 2015, pp. 1–3.

[198] U. Celano, L. Goux, A. Belmonte, K. Opsomer, R. Degraeve, C. Detavernier, M. Jurczak, and W. Vandervorst, “Understanding the Dual Nature of the Filament Dissolution in Conductive Bridging Devices,” *J. Phys. Chem. Lett.*, vol. 6, pp. 1919–1924, 2015.

[199] G.-S. Park, Y. B. Kim, S. Y. Park, X. S. Li, S. Heo, M.-J. Lee, M. Chang, J. H. Kwon, M. Kim, U.-I. Chung, R. Dittmann, R. Waser, and K. Kim, “In situ observation of filamentary conducting channels in an asymmetric Ta_2 O5-x/TaO2-x bilayer structure.,” *Nat.*

Commun., vol. 4, p. 2382, 2013.

[200] M. Duchamp, V. Migunov, A. Tavabi, A. Mehonic, M. Buckwell, M. Munde, A. J. Kenyon, and R. E. Dunin-Borkowski, “Advances in in-situ TEM characterization of silicon oxide resistive switching memories,” *Resolut. Discov.*, vol. 1, pp. 27–33, 2016.

[201] U. Celano, A. Fantini, R. Degraeve, M. Jurczak, L. Goux, and W. Vandervorst, “Scalability of valence change memory: From devices to tip-induced filaments,” *Appl. Phys. Rev.*, vol. 6, no. 8, 2016.

[202] M. Buckwell, L. Montesi, A. Mehonic, O. Reza, L. Garnett, M. Munde, S. Hudziak, and A. J. Kenyon, “Microscopic and spectroscopic analysis of the nature of conductivity changes during resistive switching in silicon-rich silicon oxide,” *Phys. Status Solidi*, vol. 12, no. 1–2, pp. 211–217, Jan. 2015.

[203] U. Celano, T. Hantschel, G. Giammaria, R. C. Chintala, T. Conard, U. Celano, T. Hantschel, G. Giammaria, C. Chintala, T. Conard, H. Bender, and W. Vandervorst, “Evaluation of the electrical contact area in contact-mode scanning probe microscopy,” vol. 214305, 2015.

[204] U. Celano, “Scanning Probe Tomography for the 3D-Observation of Conduction Paths in Advanced Memory Devices,” in *Materials Research Society Spring Meeting*, 2015.

[205] J. Weickert, “Anisotropic diffusion in image processing,” *Image Rochester NY*, vol. 256, no. 3, p. 170, 1998.

[206] K. Krissian and S. Aja-Fernández, “Noise-driven anisotropic diffusion filtering of MRI,” *IEEE Trans. Image Process.*, vol. 18, no. 10, pp. 2265–2274, 2009.

[207] J.-M. Mirebeau, J. Fehrenbach, L. Risser, and S. Tobji, “Anisotropic Diffusion in ITK,” pp. 1–9, 2015.

[208] K. L. Kaiser, “Resistance to Ground Formula,” in *Electromagnetic Compatibility Handbook*, CRC Press, 2004, pp. 28–33.

[209] B. J. Choi, D. S. Jeong, S. K. Kim, C. Rohde, S. Choi, J. H. Oh, H. J. Kim, C. S. Hwang, K. Szot, R. Waser, B. Reichenberg, and S. Tiedke, “Resistive switching mechanism of TiO[sub 2] thin films grown by atomic-layer deposition,” *J. Appl. Phys.*, vol. 98, no. 3, p. 33715, 2005.

[210] A. Sebastian, A. Pauza, C. Rossel, R. M. Shelby, A. F. Rodríguez, H. Pozidis, and E. Eleftheriou, “Resistance switching at the nanometre scale in amorphous carbon,” *New J. Phys.*, vol. 13, no. 1, p. 13020, Jan. 2011.

[211] Bruker Nano Inc., “DDESP-10,” *Bruker AFM Probes*, 2017. [Online]. Available: http://www.brukerafmprobes.com/Product.aspx?ProductID=3249. [Accessed: 06-Oct-2017].

[212] T. Hantschel, P. Niedermann, T. Trenkler, and W. Vandervorst, “Highly conductive diamond probes for scanning spreading resistance microscopy,” *Appl. Phys. Lett.*, vol. 76, no. 12, pp. 1603–1605, 2000.

[213] M. Buckwell, L. Montesi, S. Hudziak, A. Mehonic, and A. J. Kenyon, “Conductance tomography of conductive filaments in intrinsic silicon-rich silica RRAM.,” *Nanoscale*, vol. 7, no. 43, pp. 18030–5, 2015.

[214] U. Celano and W. Vandervorst, “Nanoscale Three Dimensional Characterization with Scalpel SPM,” in *Conductive Atomic Force Microscopy: Applications in Nanomaterials*, 1st ed., M. Lanza, Ed. Wiley, 2017, pp. 187–210.